DSRI

Danish Space Research Institute

DSRI Report 1/2004

ISSN 1602-527X

Swarm

End-to-End Mission Performance Simulator Study

Final Report

Nils Olsen and the
Swarm End-to-End Consortium

June 2005

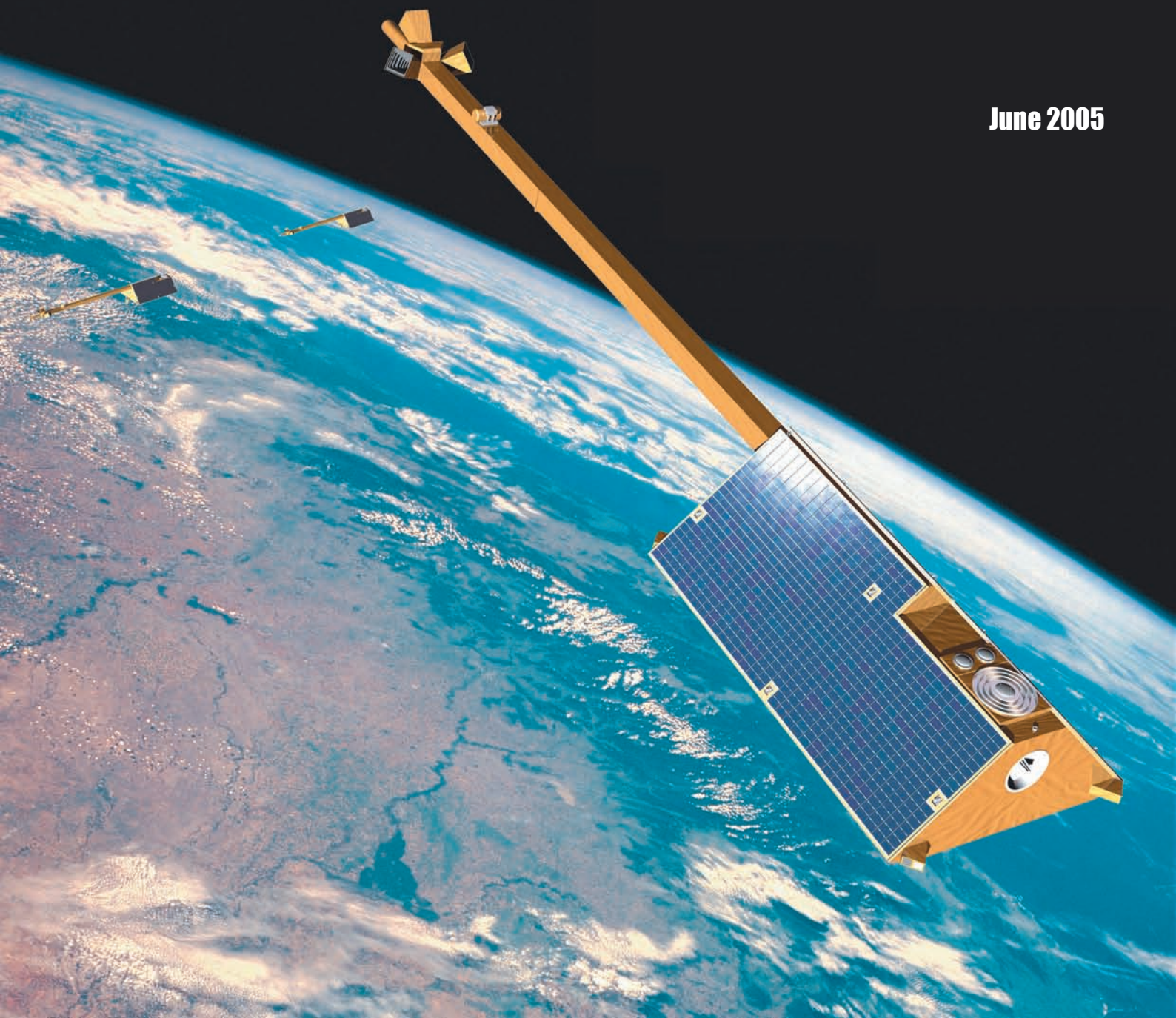

This page is intentionally left blank

Swarm End-to-End Mission Performance Simulator Study

Final Report

Doc. No. (Issue):	**SWE2E/DSRI/MIS/TN/0003 (2)**
Date:	**2005-06-06**
Prepared by:	**Nils Olsen**
Authorized by:	**Eigil Friis-Christensen**
Classification:	**Public**

This page is intentionally left blank

Classification Codes

Confidential	**The document shall be circulated only to those positively identified on the distribution list.**
Restricted	**The document may be circulated to anybody working on the project and, if deemed necessary, within the involved institutions or companies, but not outside.**
Open	**There are no restrictions in circulation, but the document will only be disseminated upon request to a named person.**
Public	**There are no restrictions in circulation, and the document will be made generally available on the World Wide Web.**

PAGE ISSUE RECORD

Document	Page	Issue	Filename and Format
SWE2E/DSRI/MIS/TN/0003	189	1	E2E-Final-Report_Draft.pdf
SWE2E/DSRI/MIS/TN/0003	190	2	E2E-Final-Report.pdf

DOCUMENT CHANGE LOG

Issue	Change References	Issue Date	Pages Affected	Remarks	Init.
1		2004-06-16	All	Initial Issue	NIO
2		2005-06-06	All	Final Issue	NIO

The Danish National Space Center (DNSC) is a new research center under the Ministry of Science, Technology and Innovation. The center is the result of the Danish Space Research Institute (DSRI) merging together with a part of The National Survey and Cadastre (KMS). The research activities include astrophysics, solar system physics, geodesy, and space technology.

This page is intentionally left blank

ESA STUDY CONTRACT REPORT

No ESA Study Contract Report will be accepted unless this sheet is inserted at the beginning of each volume of the Report.

ESA CONTRACT No **17263/03/NL/CB**	**SUBJECT** ***Swarm* End-to-End Mission Performance Simulator Study**		**CONTRACTOR** **Danish Space Research Institute**
*** ESA CR( )No** **17263**	*** STAR CODE**	**No of volumes 1** **This is Volume No 1**	**CONTRACTOR'S REFERENCE** **SWE2E/DSRI/MIS/TN/0003(2)**

ABSTRACT:

This report describes the *Swarm* End-to-End Mission Performance Simulator Study (ESTEC Contract No. 17263/03/NL/CB), which concerns the development and test of a forward scheme for creating synthetic data, and inversion schemes for recovery of the various field contributions.

The work described in this report was done under ESA Contract. Responsibility for the contents resides in the author or organisation that prepared it.

Names of authors: Nils Olsen, Eigil Friis-Christensen, Gauthier Hulot, Monika Korte, Alexei Kuvshinov, Vincent Lesur, Hermann Lühr, Susan Macmillan, Mioara Mandea, Stefan Maus, Michael Purucker, Christoph Reigber, Patricia Ritter, Martin Rother, Terence Sabaka, Pascal Tarits, Alan Thomson

**** NAME OF ESA STUDY MANAGER** **Roger Haagmans** **DIV: Science and Applications Department** **DIRECTORATE: Earth Observation Programmes**	**** ESA BUDGET HEADING**

This page is intentionally left blank

Contents

Chapter 1

Introduction

This report describes the results of activities performed during the *Swarm* End-to-End Mission Performance Simulator Study (ESTEC Contract No. 17263/03/NL/CB). The goal of the study is to analyze the key system requirements, particularly with respect to the number of *Swarm* satellites and their orbits related to the science objectives of *Swarm*.

This performance modeling include the space-craft and payload and the various relevant magnetic and electric fields in a forward modeling approach, followed by inversion (field recovery). Several inversion/data processing strategies, including effects of geophysical variability and noise caused by un-modeled sources, have been applied to reconstruct the input models. Also, the impact of random and systematic errors induced by the spacecraft and of the payload calibration has been analyzed.

The study has been organized in three main tasks and structured as indicated in Figure 1.1.

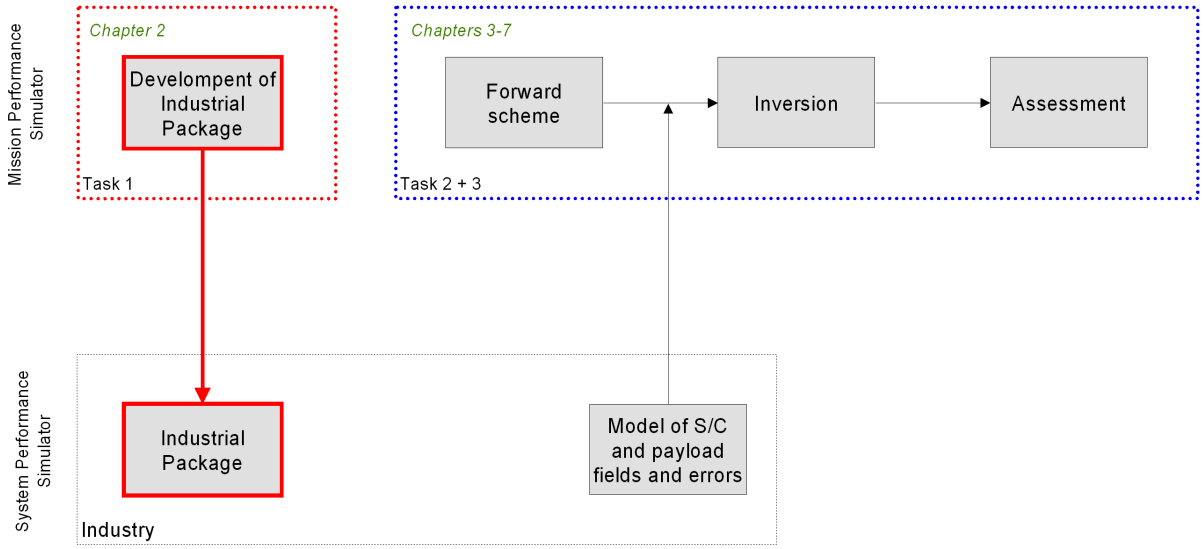

Figure 1.1: Study Logic

Task 1, described in chapter 2, concerns the construction of a software package to support the *Swarm* Industrial Phase A system study. These software modules allow the generation of magnetic field values at given satellite locations. The relationship between the *Swarm* End-to-End Mission Performance Simulator (this study) and the System Performance Simulator, done by industry, is indicated in red color in the Figure.

The main part of the study, Tasks 2 and 3 (chapters 3 - 7), are devoted to the End-to-End Mission Simulator Study. The purpose of this simulator is to build a virtual (simulated) mission of the external environment (magnetic and electric field model), of the environmental disturbances on the spacecraft, and on the dynamics of the spacecrafts (orbit and attitude). This End-To-End mission performance simulator, by adequate fine-tuning, will play an important role in the mission planning, implementation and operational phases of *Swarm* as follows:

- during the mission design phase, as a means for determining the expected scientific performance and for validating the error budget (and thus assess the criticability of the specifications for the various system elements),
- in parallel, to set up or improve realistic procedures for scientific data processing, based on representative 'raw' data

- during the mission implementation phase, to consolidate the expected scientific performances, given the measured performance of all the elements, as far as possible
- during the mission operation planning, as a means to test the in-flight operation sequences and of the instrument calibration
- during the mission itself, as a means for interpretation of the flight data.

The forward scheme, production of the synthetic data, is described in chapter 3. The results of an application of present single-satellite methods for in-flight calibration to simulated *Swarm* data is described in Chapter 4.

The various attempts for recovery of the various field contributions as per *Swarm* objectives are described in chapter 6. We have focused on the three prime science objectives of *Swarm*: investigation of the lithospheric field (sections 6.1 and 6.2), of the core field and secular variation (sections 6.1, 6.3, 6.4 and 6.5), and of 3-D mantle conductivity (sections 6.6 and 6.7). Recovery of the magnetic field caused by ocean flow, a secondary *Swarm* research objective, is discussed in section 6.8. The testplan for this source recovery is described in chapter 5.

Chapter 7 discusses the assessment of the field recovery approaches. Finally, chapter 8 summarizes the findings of the present study and discusses topics for future studies.

Meetings and Workshops The following meetings and workshops have been held in connection with the activities described in this report:

- **Kick-off meeting** at DSRI Copenhagen/Denmark, April 28, 2003
- **Progress Meeting 1** at ESTEC Noordwijk/The Netherlands, June 16, 2003
- **First Working Meeting** at GFZ Potsdam/Germany, September 28, 2003
- **Progress Meeting 2** at GFZ Potsdam/Germany, September 29, 2003
- **Mid Term Review** at DSRI Copenhagen/Denmark, November 11, 2003
- **Second Working Meeting** at IPG Paris/France, February 16, 2004
- **Progress Meeting 3** at IPG Paris/France, February 17, 2004
- **Final Presentation** at ESTEC Noordwijk/The Netherlands, June 18, 2004

Chapter 2

Construction of Industrial Modules (Task 1)

2.1 Introduction

This section describes activities performed during Task 1 of the *Swarm* End-to-End Mission Performance Simulator Study, which concerns the construction of a software package to support the *Swarm* Industrial Phase A system study. Involved in this task are WP 1100 (Design and Programming of Industrial Module – DC part), WP 1200 (Design and Programming of Industrial Module – AC part) and WP 1300 (Support of Transfer of Industrial Module). The package allows the generation of magnetic field values for a given satellite location and time, and are refined and augmented versions of the magnetic field models described in Section 5.3 of ECSS [2000].

It consists of 3 modules, as shown in Figure 2.1:

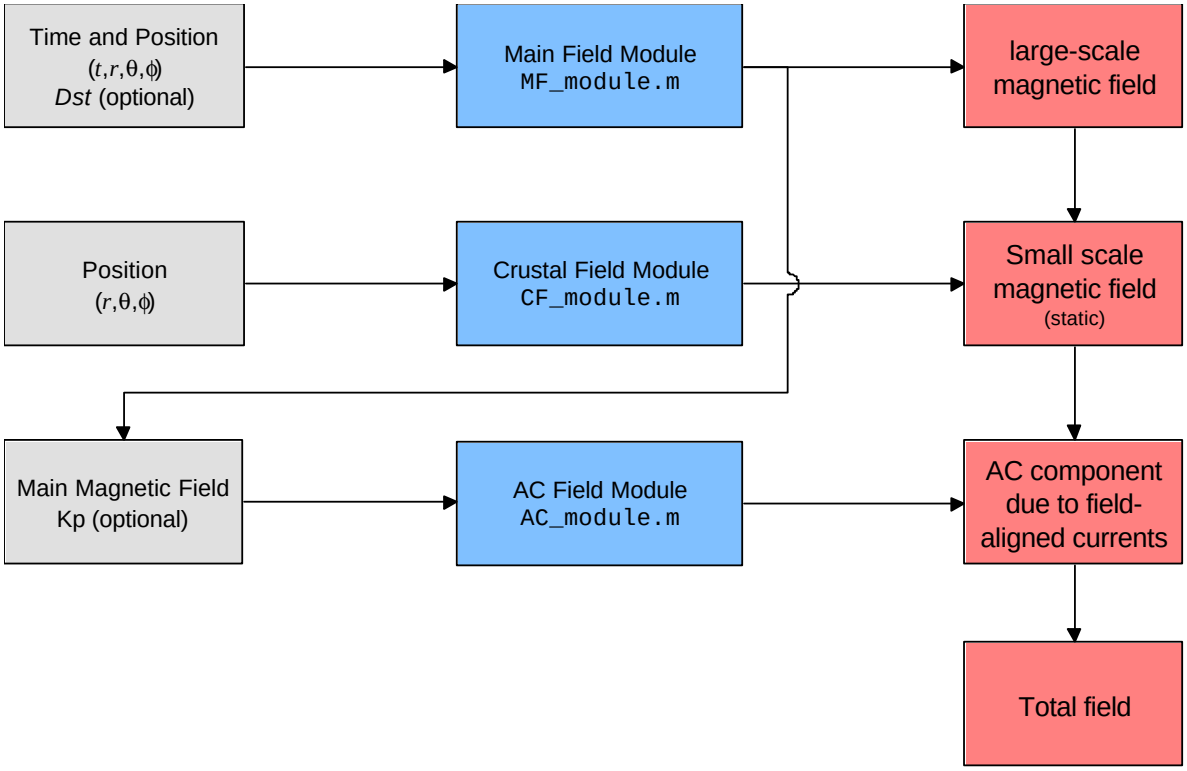

Figure 2.1: Schematic of industrial package

- **Main Field Module** (`MF_module.m`). This module describes the large-scale (a few thousands km scale length) contributions to the Earth's magnetic field. It is an extended version of the IGRF/DGRF models described in section 5.3.2 of ECSS [2000], considering spherical harmonic coefficients of degree n and order m up to 20 (rather than $n_{max} = k = 10$ for IGRF/DGRF, as described in Eq. 5.1 of ECSS [2000]). The module also describes the slowly varying field of internal origin (secular variation), assumed to vary linearly with time for the period for which the model is valid (1999.0 ± 3.0 yrs). Finally, the module delivers the large-scale external field of magnetospheric origin. Its time dependence is scaled by the *Dst*-index reflecting the magnetospheric activity.

- **Crustal Field Module** (`CF_module.m`). This module describes the high-degree (short wavelength) static field of internal origin (spherical harmonic coefficients of degree and

order between 21 and 120).

The magnetic field described by these two modules is static or quasi-static in the sense that changes due to the movement of the space-craft (with velocity of about 7-8 km/s) are much larger than the intrinsic time changes of the magnetic field.

- **AC Field Module** (`AC_module.m`). This module describes magnetic field fluctuations (frequency range 0.1-20 Hz) that are caused by the filamentation of currents through which the space-craft is flying.

2.2 Description of the Package

2.2.1 Contents of Package

Table 2.1 lists the files of the Industrial package. All files are available at ftp.spacecenter.dk/data/magnetic-satellites/Swarm/E2E/Industrial_Package/.

2.2.2 Definition of Input/Output Variables

In agreement with the definitions given in section 5.3.2 of ECSS [2000], the following variables are used as input/output variables of the modules:

- Time t (input parameter) is measured in days starting at January 1, 2000, 00:00 UT (Modified Julian Day 2000, MJD2000). Note that – although the start time of t is defined in UT – the time scale of t is continuous and does not include leap seconds. Note also that t is *not* Julian Day 2000 (which starts at January 1, 2000, 12:00 UT). The transformation between a given date and time `year, month, day, hour, minute, second` (in UT) and t can be done using standard Matlab functions:

```
t = datenum(year, month, day+hour/24+minute/1440+second/86400) - 730486;
[year, month, day, hour, minute, second] = datevec(t+730486);
```

  When calling the various Matlab modules time t is denoted as `t`. Note that `t` may be a scalar or a (row or column) vector `t(:)`.

- Position of the satellite is input parameter to the Main Field and Crustal Field modules and is given in geocentric coordinates (r, θ, ϕ), where r is geocentric distance in km, θ is geographic co-latitude in degrees (measured from geographic north pole) and ϕ is geographic longitude. $a = 6371.2$ km (mean radius of the Earth) is the radius of the reference sphere on which the expansion coefficients of the field model are defined. Co-latitude θ is connected to geographic latitude α by $\theta = 90^\circ - \alpha$. Position r, θ, ϕ is denoted as `r, theta, phi` and can be scalars or (row or column) vectors of equal length.

- The *Dst*-index (optional input argument to the Main Field Module) describes the level of (large-scale) magnetospheric current systems (see http://swdcwww.kugi.kyoto-u.ac.jp/dst2/onDstindex.html for the definition of *Dst*, and http://swdcdb.kugi.kyoto-u.ac.jp/dstdir/ for values of the index). Hourly values for the years 1997-2001 are provided in the file `Dst_1997-2001.mat` of this package.

Filename	Description
MF_module.m	Main Field module
CF_module.m	Crustal Field module
AC_module.m	AC Field module
tutorial.m	Tutorial describing the use of the package
synth_values.m	called by MF_module.m
design_SHA.m	called by synth_values.m
design_SHA.dll	called by design_SHA.m. This is the MEX version of design_SHA.f, compiled for MS Windows. design_SHA.m runs faster when a MEX version is available, but will also work without.
read_model.m	called by MF_module.m. Reads the spherical harmonic expansion coefficients of the model
swarm_02a_03.cof	File containing the spherical harmonic expansion coefficients of model swarm(02a/03), loaded by read_model.m
B_crust_grid_coarse.mat	File containing the 3-D grid of the crustal field, used by CF_module.m
AC_database.mat	File containing the coefficients of the AC-field, used by AC_module.m
Dst_1997-2001.mat	File containing hourly mean values of the *Dst*-index for the years 1997-2001. t_Dst is time (MJD2000) and Dst_all is the corresponding value of *Dst*.
Kp_1997-2001.mat	File containing 3-hourly values of the *Kp*-index for the years 1997-2001. t_Kp is time (MJD2000) and Kp_all is the corresponding value of *Kp*.
coastlines.mat	File with latitude and longitude of coastlines, used in tutorial.m
swarm1_1_990113.pos	Sample file containing one day (January 13, 1999) of simulated satellite positions (1 min sampling rate). Used in tutorial.m

Table 2.1: The files of the Industrial package

- The *Kp*-index (optional input argument to the AC Field Module) is a 3-hourly index of geomagnetic activity (see http://www.gfz-potsdam.de/pb2/pb23/GeoMag/niemegk/kp_index/ for more information on and actual values of the index). Values for the years 1997-2001 are provided in the file `Kp_1997-2001.mat` of this package.

- Output of each of the three modules is the three components of the magnetic field vector in spherical coordinates, $\mathbf{B} = (B_r, B_\theta, B_\phi)$ in units of nanoTesla (nT), where B_r, B_θ and B_ϕ are the radial, Southward and Eastward components, respectively. In Matlab $\mathbf{B}$ is denoted as `B(:,1:3)`, where `B(:,1)` denotes B_r, `B(:,2)` represents B_θ and `B(:,3)` stands for B_ϕ. The magnetic scalar field F can be calculated from the vector components by means of $F = \sqrt{B_r^2 + B_\theta^2 + B_\phi^2}$. In Matlab this transformation is done with the command `F=sqrt(B(:, 1).^2 + B(:, 2).^2 + B(:, 3).^2)`.

2.2.3 Calling statements

Model coefficients that are needed for the computation are loaded automatically during the first call of the module; these values are declared as `global` and hence are saved for future calls of the module. The needed files are: the list of spherical harmonic coefficients `swarm_02a_03.cof` used by `MF_module`; the 3-D grid of crustal field values `B_crust_grid_coarse.mat` used by `CF_module`, and `AC_database.mat` used by `AC_module`. By default these files are expected to be in the actual working directory; if this is not the case an error message is given and the module has to be called with explicit filename as last input argument.

Main Field module.

Input is time and position. Depending on the number of output variables, the module returns the main field vector only (1 output variable). `t`, `r`, `theta`, `phi`, and optionally `Dst` are scalars or vectors of equal length.

```
B_MF          = MF_module(t, r, theta, phi)
B_MF          = MF_module(t, r, theta, phi, [], filename_model)
```

or main and magnetospheric field vectors (2 output variables, and *Dst*-index as additional input)

```
[B_MF, B_Dst] = MF_module(t, r, theta, phi, Dst)
[B_MF, B_Dst] = MF_module(t, r, theta, phi, Dst, filename_model)
```

Crustal Field Module

Input is position; output is magnetic field vector.

```
B_CF = CF_module(r, theta, phi);
B_CF = CF_module(r, theta, phi, filename_3D_grid);
```

AC Field Module

Input is main field vector with 50 Hz sampling rate (and optionally *Kp*, the global index of magnetic activity); output is magnetic AC field vector. `Kp` has to be a scalar, describing the *Kp*-index for the whole period in consideration.

```
B_AC = AC_module(B_MF);
B_AC = AC_module(B_MF, Kp);
B_AC = AC_module(B_MF, Kp, filename_AC_database);
```

2.3 Tutorial on the use of the Package

The Matlab code of the following tutorial can be found in the file `tutorial.m`.

First we need some definitions, for later use:

```
clear         % clear workspace
a = 6371.2;   % mean Earth radius, in km
rad = pi/180; % factor for conversion from degree to radians
%
```

We also need to define time and position of a sample orbit. For the first examples we choose a satellite moving in a strictly polar orbit from North to South along the 110° E meridian at an altitude of 450 km above the mean radius $a = 6371.2$ km of the Earth; sampling rate is 1 Hz:

```
% create one half orbit of synthetic orbit: strictly polar, 110 deg longitude
% assuming an orbit period of 90 minutes
% 1 Hz sampling rate, i.e. 2700 secs for one half orbit
theta = linspace(0.01, 179.99, 2700)';  % geographic co-latitude, in deg
        % (0.01 ... 179.99 deg to avoid NaN in B_phi at poles)
r     = repmat(a+450, size(theta));     % geocentric radius, 450 km altitude
phi   = repmat(110,    size(theta));    % 100 deg longitude East
t = -364.5 + [0:length(theta)-1]/86400; % time in MJD2000, starting on Jan. 1, 1999, 12:00 UT
%
```

In the first example, `MF_module` is called to determine the main field only (magnetospheric fields are not considered). This is the simplest way of calling the Main field module.

```
% ********************** Example 1 **********************
% synthesize values, Main-field + SV
B_MF         = MF_module(t, r, theta, phi);
%
```

The second example deals with the calculation of both main field and magnetospheric fields. The strength of the latter is based on the *Dst*-index which is taken from the database file `Dst_1997_2001.mat`:

```
% ********************** Example 2 **********************
% synthesize values, Main-field + SV + Dst part of model
% with realistic value of Dst, based on input time t
load('Dst_1997-2001.mat'); % load database of Dst-values
Dst = interp1(t_Dst, Dst_all, t, 'spline'); % spline interpolation of Dst from database-values to time t
[B_MF, B_Dst] = MF_module(t, r, theta, phi, Dst);
B_total = B_MF + B_Dst; % add Dst-part to MF+SV
%
```

In the third example `CF_module` is called to calculate the crustal field, which is added to the magnetic field obtained in Example 2:

```
% ********************** Example 3 **********************
% calculate crustal field
%
B_CF = CF_module(r, theta, phi);
B_total = B_MF + B_Dst + B_CF; % add crustal field to MF+Dst field of example 2
%
```

The following lines create plots showing the θ-dependency of the main field (left), of the magnetospheric field (middle) and of the crustal field (right); the result is shown in Figure 2.2 (note the different scale used for the three constituents).

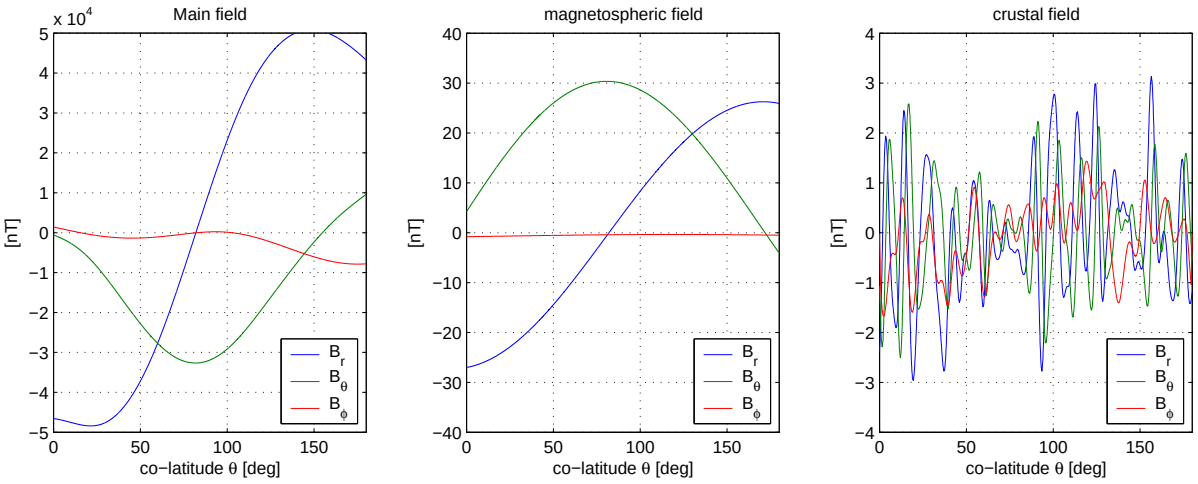

Figure 2.2: Magnetic fields along 110° E meridian, from Example 3 of the tutorial

```
% plot the various fields in dependency on co-latitude theta
clf
subplot(1,3,1)
plot(theta, B_MF, '-')
title 'Main field'
axis([0 180 -50000 50000])
legend('B_r', 'B_{\theta}', 'B_{\phi}', 4)
xlabel 'co-latitude \theta [deg]'
ylabel '[nT]'
grid on
subplot(1,3,2)
plot(theta, B_Dst, '-')
title 'magnetospheric field'
axis([0 180 -40 40])
legend('B_r', 'B_{\theta}', 'B_{\phi}', 4)
xlabel 'co-latitude \theta [deg]'
ylabel '[nT]'
grid on
subplot(1,3,3)
plot(theta, B_CF, '-')
title 'crustal field'
axis([0 180 -4 4])
legend('B_r', 'B_{\theta}', 'B_{\phi}', 4)
xlabel 'co-latitude \theta [deg]'
ylabel '[nT]'
grid on
%
```

It is not recommended to use `MF_module` and `CF_module` for creating time series with sampling rates higher than 1 Hz (although this is possible). If times series with sampling frequency higher than 1 Hz (for example 50 Hz) are needed, one should create 1 Hz values with `MF_module` and `CF_module`, followed by an spline-interpolation to the desired higher rate, as shown in the following example 4:

```
% ********************** Example 4 **********************
% Interpolate the 1 Hz values of Example 3 to obtain 50 Hz values
%
t_50Hz = [t(1):1/86400/50:t(end)];                          % time of the 50 Hz data
theta_50Hz = linspace(theta(1), theta(end), length(t_50Hz)); % theta of the 50 Hz data
B_total_50Hz = interp1(t, B_total, t_50Hz, 'spline');       % do the interpolation
%
```

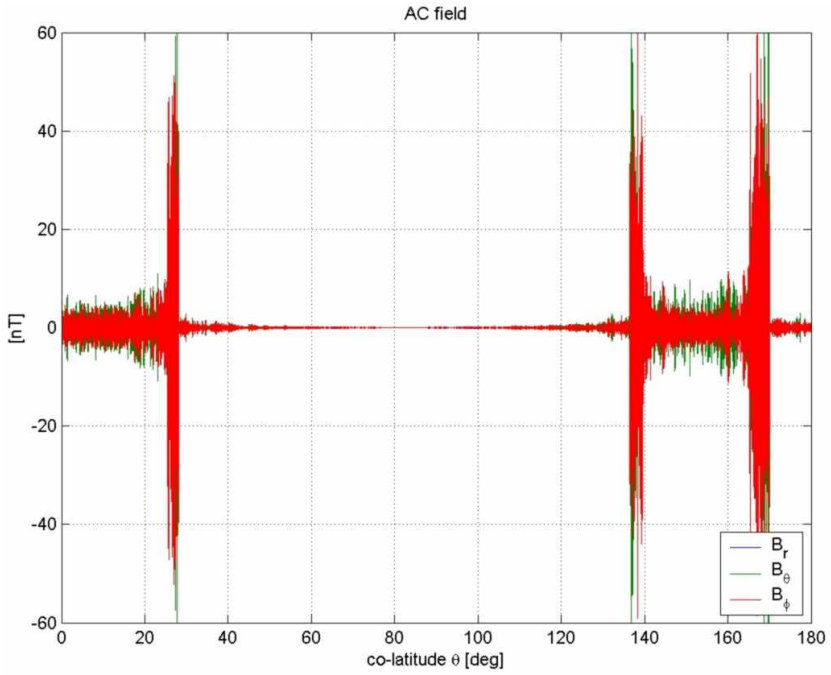

Figure 2.3: Magnetic AC contribution along 110° E meridian, from Example 5 of the tutorial.

In the next example we calculate and plot the AC contribution to the 50 Hz data of the previous example; Figure 2.3 shows the result (note that a randon number is used to determine the phase of the AC-signal in the program, and therefore the plot produced by the following lines of code will probably differ from the figure shown here)

```
% ********************** Example 5 **********************
% Calculate and plot AC disturbances for the values of the previous example
B_AC = AC_module(B_total_50Hz);     % calculate AC disturbances
B_total_50Hz = B_total_50Hz + B_AC; % add AC field to 50 Hz MF+SV+Dst+crustal field of example 4
clf
plot(theta_50Hz, B_AC, '-')
title 'AC field'
axis([0 180 -40 40])
legend('B_r', 'B_{\theta}', 'B_{\phi}', 4)
xlabel 'co-latitude \theta [deg]'
ylabel '[nT]'
grid on
%
```

In the last example we use one orbit of simulated positions (January 13, 1999, satellite swarm1, constellation #1 of the Missions simulator study). First we read the positions, convert them from ECEF Cartesian to (r, θ, ϕ) spherical coordinates and plot the ground track; the result is shown in Figure 2.4:

```
% ********************** Example 6 **********************
% Field values for January 13, 1999
%
% Read orbit data (1 min values, constellation #1) for swarm_1
% (synthetic orbit from the swarm E2E mission simulator study)
tmp = load('swarm1_1_990113.pos');
t_all = tmp(:,1); % time
X_all = tmp(:,2); Y_all = tmp(:,3); Z_all = tmp(:,4);        % ECEF cartesian coordinates
% convert to geocentric spherical coordinates
r_all = sqrt(X_all.^2 + Y_all.^2 + Z_all.^2);                % radius [km]
```

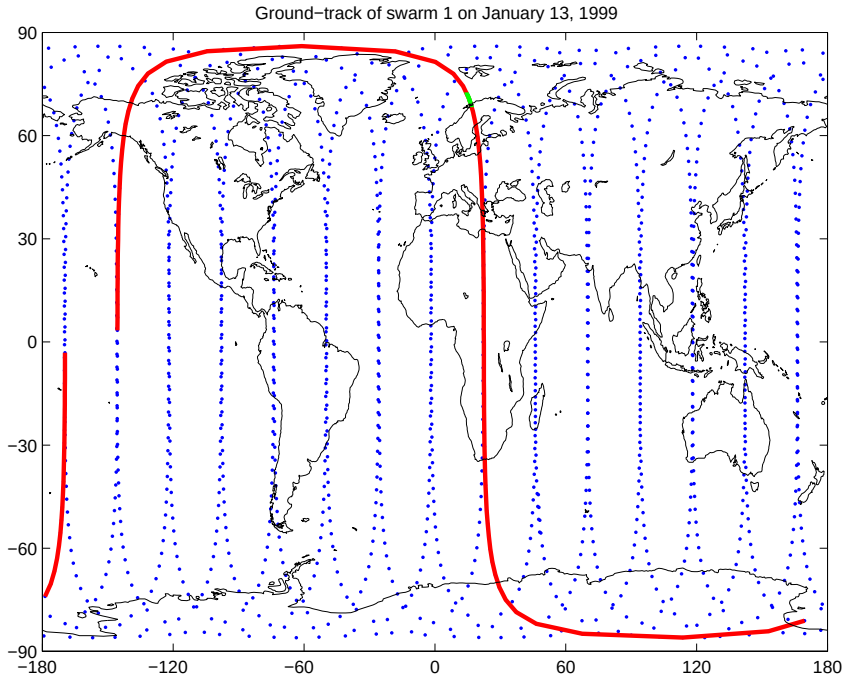

Figure 2.4: Ground track of one day of simulated orbit, from Example 6 of the tutorial. The red line shows the ground track of the first (complete) orbit of that day. (The green line segment just to the North-West of Norway shows the ground track of the data used in Figure 2.5. It is is not produced in Example 6.)

```
94  theta_all = atan2(sqrt(X_all.^2 + Y_all.^2), Z_all)/rad;     % co-latitude [deg]
95  phi_all = atan2(Y_all, X_all)/rad;                           % longitude [deg]
96  % Extract first (complete) orbit of that day
97  index = find(-352.97492648 < t_all & t_all < -352.90844219); % (orbit # 11158)
98  t = t_all(index); X = X_all(index); Y = Y_all(index); Z = Z_all(index);
99  % interpolate 1 Hz from the 1 min positions
100 t_1Hz = [t(1):1/86400:t(end)]'; % time of 1Hz time series
101 pos_1Hz = interp1(t, [X Y Z], t_1Hz, 'spline'); % interpolate the position (cartesian coordinates)
102 r_1Hz     = sqrt(pos_1Hz(:,1).^2 + pos_1Hz(:,2).^2 + pos_1Hz(:,3).^2);        % radius [km]
103 theta_1Hz = atan2(sqrt(pos_1Hz(:,1).^2 + pos_1Hz(:,2).^2), pos_1Hz(:,3))/rad; % co-latitude [deg]
104 phi_1Hz   = atan2(pos_1Hz(:,2), pos_1Hz(:,1))/rad;                           % longitude [deg]
105 %
106 % plot a map with satellite position;
107 % 1 min sampling (blue) for whole day, and 1 Hz sampling (red) for selected orbit
108 load coastlines % load coast-lines
109 clf
110 plot(phi_all, 90-theta_all, '.b', phi_1Hz, 90-theta_1Hz, '.r')
111 hold on; plot(long, lat, '-k'); hold off;
112 axis([-180 180 -90 90])
113 title 'Ground-track of swarm 1 on January 13, 1999'
114 set(gca, 'Xtick', [-180:60:810], 'Ytick', [-90:30:90])
115 %
```

We then interpolate the *Dst*-index from the data-base values (loaded already in Example 2), calculate 1 Hz values of the main field `B_MF`, magnetospheric field `B_Dst`, and crustal field `B_CF`. These three field constituents are summed to `B_total` and interpolated to obtain 50 Hz values `B_total_50Hz`. Next the value of the *Kp*-index corresponding to the first sample is extracted from the database. Then the AC field contribution `B_AC` is calculated (using *Kp* corresponding to the first sample) and added to `B_total_50Hz`. (Since *Kp* is a 3-hourly index, it can be

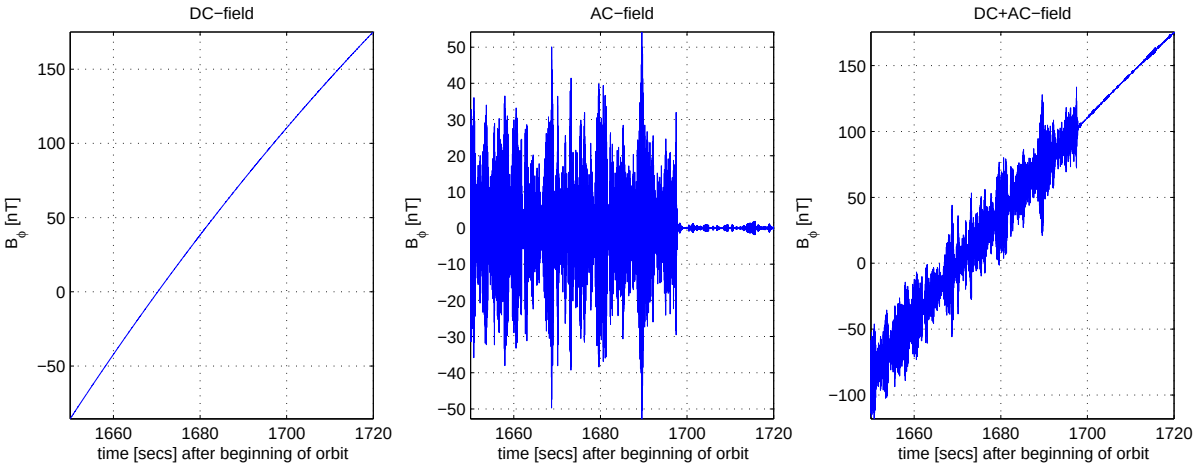

Figure 2.5: DC-part, AC-part and their sum for B_ϕ, as a function of time.

assumed that it is constant during the period in consideration, and therefore only the values corresponding to the first sample is used). Finally the DC- and AC-parts and their sum are plotted as a function of time for the interval 1650 s – 1720 s after orbit start for B_ϕ. (cf. Figure 2.5). During that time the satellite was just to the North-West of North-Norway, crossing the auroral oval where the contributions from field-aligned currents is largest.

```
Dst = interp1(t_Dst, Dst_all, t_1Hz, 'spline');                    % spline interpolation of
[B_MF, B_Dst]  = MF_module(t_1Hz, r_1Hz, theta_1Hz, phi_1Hz, Dst); % synthesize MF+Dst field
B_CF = CF_module(r_1Hz, theta_1Hz, phi_1Hz);                       % synthesize crustal field
B_total = B_MF + B_Dst + B_CF;                                     % add MF+Dst+crustal fields
%
t_50Hz = [t_1Hz(1):1/86400/50:t_1Hz(end)];                % time of the 50 Hz data
B_total_50Hz = interp1(t_1Hz, B_total, t_50Hz, 'spline'); % do the interpolation
load('Kp_1997-2001.mat');                                 % load database of Kp-index
Kp = interp1(t_Kp, Kp_all, t_1Hz, 'nearest');             % interpolation of Kp
Kp = Kp(1);                                               % use Kp corresponding to first sample
B_AC = AC_module(B_total_50Hz, Kp);                       % calculate AC disturbances
%
% plot the various fields in dependency on time t
clf
t_orbit = (t_50Hz-t_50Hz(1))*86400; %
index = find(t_orbit > 1650 & t_orbit < 1720);
subplot(1,3,1)
plot(t_orbit(index), B_total_50Hz(index,3), '-')
title 'DC-field'
xlabel 'time [secs] after beginning of orbit'
ylabel ' B_{\phi} [nT]'
axis([1650 1720 -Inf Inf])
grid on
subplot(1,3,2)
plot(t_orbit(index), B_AC(index,3), '-')
title 'AC-field'
axis([1650 1720 -Inf Inf])
xlabel 'time [secs] after beginning of orbit'
ylabel ' B_{\phi} [nT]'
grid on
subplot(1,3,3)
plot(t_orbit(index), B_total_50Hz(index,3)+B_AC(index,3), '-')
title 'DC+AC-field'
axis([1650 1720 -Inf Inf])
xlabel 'time [secs] after beginning of orbit'
ylabel ' B_{\phi} [nT]'
grid on
```

```
%
B_total_50Hz = B_total_50Hz + B_AC;  % add AC field to 50 Hz MF+SV+Dst+crustal field
%
```

2.4 Description of the Model Approaches

2.4.1 Model of Core Field and Secular Variation

We describe here briefly the model parameterization (for more details see Olsen [2002]). The magnetic field vector $\mathbf{B} = -\nabla V$ is presented as the gradient of a scalar potential V which (in extension to Eq. (5.1) of ECSS [2000]) is expanded according to

$$\begin{aligned} V = a\Bigg\{ & \sum_{n=1}^{N_{MF}} \sum_{m=0}^{n} \left(g_n^m \cos m\phi + h_n^m \sin m\phi\right) \left(\frac{a}{r}\right)^{n+1} P_n^m\left(\cos\theta\right) \\ & + \sum_{n=1}^{N_{SV}} \sum_{m=0}^{n} \left(\dot{g}_n^m \cos m\phi + \dot{h}_n^m \sin m\phi\right) \left(t - t_0\right) \left(\frac{a}{r}\right)^{n+1} P_n^m\left(\cos\theta\right) \\ & + \sum_{n=1}^{2} \sum_{m=0}^{n} \left(q_n^m \cos m\phi + s_n^m \sin m\phi\right) \left(\frac{r}{a}\right)^{n} P_n^m\left(\cos\theta\right) \\ & + D_{st} \cdot \left[\left(\frac{r}{a}\right) + Q_1 \left(\frac{a}{r}\right)^2\right] \times \\ & \left[\widetilde{q}_1^0 P_1^0\left(\cos\theta\right) + \left(\widetilde{q}_1^1 \cos\phi + \widetilde{s}_1^1 \sin\phi\right) P_1^1\left(\cos\theta\right)\right] \Bigg\}. \end{aligned} \tag{2.1}$$

The first line of this equation is identical to Eq. (5.1) of ECSS [2000] and describes the static field of internal origin (up to degree/order N_{MF}), the second line considers the linear time change (secular variation) of the internal field, and the remaining lines account for the static and Dst-dependent part of the large-scale external field of magnetospheric origin (plus its Earth-induced counterpart). (r, θ, ϕ) are the standard Earth-centered spherical coordinates (radius, colatitude, longitude), with a reference Earth radius of $a = 6371.2$ km, P_n^m are the associated Legendre functions of degree n and order m, t_0 is model epoch, $\{g_l^m, h_l^m\}$ are the internal Gauss coefficients (calculated to degree N_{MF}), $\{\dot{g}_l^m, \dot{h}_l^m\}$ the coefficients of main field secular variation (calculated to degree N_{SV}), and $\{q_l^m, s_l^m\}$ (calculated to degree 2) the large scale external field coefficients. The coefficients $\widetilde{q}_1^0, \widetilde{q}_1^1$ and $\widetilde{s}_1^1$ account for the variability of contributions from the magnetospheric ring current (parameterized for ease of use by the Dst-index) plus their internal, induced counterpart (considered by the factor $Q_1 = 0.27$). $n = 1, 2$, $m = 0$ terms incorporate an annual and semi-annual variation; the Values of all external coefficients are taken from the model described in Olsen [2002].

The coefficients are those of model swarm(02a/03) (`swarm_02a_03.cof`) the construction of which is described in Section 3.4.1. Terms up to degree/order $N_{MF} = 20$ are used for the static field (higher terms are considered in the Crustal Field Module) and up to $N_{SV} = 19$ for the secular variation. Model epoch t_0 is taken to be $t_0 = 1999.0$. It is not recommended to use this model outside the period range $t_0 \pm 3$ yrs (due to the approximation of secular variation by a linear time change).

2.4.2 Crustal Field Model

The crustal field module calculates the small-scale static magnetic field due to crustal magnetization, corresponding to spherical harmonic degree $n = 21 - 120$ of the first line of Eq. 2.1. However, instead of performing a spherical harmonic synthesis for each observation point, the module uses a 3-D linear interpolation from values pre-computed on a global grid. A grid spacing of $\Delta r = 60$ km, $\Delta\theta = \Delta\phi = 0.25°$ for $a + 300 \leq r \leq a + 600$ km ($a = 6371.2$ km), $0° \leq \theta \leq 180°$, $0° \leq \phi \leq 360°$, is recommended (see next section for an estimate of the interpolation error); the magnetic field vector of such a grid is available in the file `B_grid_coarse.mat`. The interpolation is done in Matlab using `interp3`.

Defining the grid for the interpolation of the crustal field

The evaluation of the magnetic field due to high-degree lithospheric sources is done by means of a linear interpolation using the Matlab functions `interp3`. The required grid-spacing $(\Delta r, \Delta\theta, \Delta\phi)$ of the 3D-grid used for the interpolation was found in the following way:

To estimate the error of the interpolation in radial direction, we recognize that the change with radius r of the magnetic field that is described by spherical harmonics of degree n is proportional to $(r_0/r)^{n+2}$, where r_0 is a reference radius. A Taylor-expansion of this dependency around r_0 yields a radial dependency proportional to

$$\left(\frac{r_0}{r_0+\delta}\right)^{n+2} = (1+\delta/r_0)^{-(n+2)} \approx 1 - \frac{(n+2)}{1}\frac{\delta}{r_0} + \frac{(n+2)^2}{2!}\left(\frac{\delta}{r_0}\right)^2 - \ldots$$

The first two terms on the right side are considered with a linear interpolation, and therefore the quadratic term $\frac{(n+2)^2}{2!}\left(\frac{\delta}{r_0}\right)^2$ is an estimate of the error introduced by using a linear interpolation. This error is maximal for $\delta = \Delta r/2$, i.e. in the middle between two nodes in radial direction, which leads to the following estimate of the maximum relative error of the radial interpolation

$$\text{rel. error}_{r\text{-interpol.}} \leq \frac{(n+2)^2}{8}\left(\frac{\Delta r}{r_0}\right)^2 . \tag{2.2}$$

For the longitudinal interpolation we notice that the dependence of the magnetic field (described by spherical harmonics of degree n) on longitude ϕ is given by $\cos m\phi$ or $\sin m\phi$ which have maximum variation for $m = n$. Taylor expansion of $\sin n\phi$ with $\phi = \phi_0 + \delta$ yields

$$\begin{aligned}\sin n\,(\phi_0+\delta) &\approx \sin n\phi_0 + (n\delta)\cos n\phi_0 - \frac{(n\delta)^2}{2!}\sin n\phi_0 - \ldots \\ &= \sin n\phi_0\left(1 + (n\delta)\cot n\phi_0 - \frac{(n\delta)^2}{2!} - \ldots\right) .\end{aligned}$$

Linear interpolation considers the first two terms in the brackets, hence $\frac{\delta^2}{2!}$ is an estimate of the error of the longitudinal interpolation. Choosing $\delta = \Delta\phi/2$ yields an estimate of the maximum relative error of

$$\text{rel. error}_{\phi\text{-interpol.}} \leq \frac{n^2}{8}\Delta\phi^2 . \tag{2.3}$$

A similar argumentation is used for the latitudinal interpolation: dependence of $\mathbf{B}$ on co-latitude θ is given (for $n \gg 1$) by $g(\theta)\cos n\theta$, where $g(\theta)$ varies slowly with θ and therefore

	`B_grid_coarse.mat` $\Delta r = 60$ km $\Delta\theta = \Delta\phi = 0.5°$ $6 \times 361 \times 721$	`B_grid_fine.mat` $\Delta r = 30$ km $\Delta\theta = \Delta\phi = 0.25°$ $11 \times 721 \times 1441$
$n = 60$	5.9%	1.5%
$n = 90$	13%	3.3%
$n = 120$	23%	5.9%
$n = 150$	37%	9.3%

Table 2.2: Maximal interpolation error for the grid spacings used in the *swarm* E2E Mission study, in dependency on degree n.

can be regarded as constant within a small latitude interval. This leads to the same functional dependency as for the longitudinal interpolation,

$$\text{rel. error}_{\theta\text{-interpol.}} \leq \frac{n^2}{8}\Delta\theta^2 \ , \tag{2.4}$$

as an estimate of the maximum relative error of the latitudinal interpolation.

Requiring equal relative errors, and using $(n+2)^2 \approx n^2$ for $n \gg 1$, leads to the condition

$$r_0\Delta\phi \approx r_0\Delta\theta \approx \Delta r \tag{2.5}$$

for the selection of the grid spacings. (This condition follows also directly from a scaling analysis.) Using this relationship, and adding the three errors yields an average (maximum) error of the 3D interpolation (for a given grid-spacing and for magnetic field contributions due to terms of spherical harmonic degree n) of

$$\Delta_{3D} = \frac{\sqrt{3}}{8}n^2\Delta\theta^2$$

Table 2.2 lists this error for the two grid spacing used in the *swarm* E2E Mission study. Note that these numbers are worst-case estimates; the result of a closed-loop analysis indicates that the actual error is much smaller.

2.4.3 Model used for the AC Field Module

The purpose of the AC module is to generate a representative time series of the magnetic field signal in the frequency range 0.1 to 20 Hz. It produces not just random fluctuations, but takes into account the orientation of the AC field with respect to the background field and considers the latitude dependence of its intensity.

Design of the Module

Presently there are no standard models available representing the magnetic AC characteristics on a global scale. Our approach is thus to make use of available high-resolution satellite measurements for constructing a module which generates representative AC signals. In order to keep this task manageable, a number of simplifications have been introduced.

- The signal power is in principle constant in time. There is no diurnal or seasonal variation considered. The amplitude is scaled linearly with the magnetic index Kp.
- For the description of the latitude dependence the module is structured in one degree wide blocks, ranging from the equator to the pole. These latitude classes are identical for the northern and southern hemisphere and there is no longitudinal dependency.
- The part of the magnetic field spectrum considered here is caused almost exclusively be field-aligned currents. We therefore limit the generated AC signals to the components perpendicular to the ambient magnetic field. Also the intensity of these currents strongly depends on the magnetic latitude. In order to have a simple interface with the other modules the appropriate latitude classes are selected according to the actual dip latitude β, which depends only on the inclination of the ambient magnetic field.

For each latitude class there exist three independent sets of Fourier coefficients for the three vector components. The spectral power distribution within each class is only dependent on the magnetic activity. An inverse Fourier transform is used for generation the time series of the AC field data.

In spite of these apparent simplifications important features of the global AC magnetic field distribution are reflected quite well (see Figure 2.7). Outstanding are the signal peaks at auroral latitudes. Furthermore, the expected dependence of signal power with latitude is clearly seen.

Analysis

For the construction of the AC signal generator we make use of the high resolution CHAMP vector magnetic field measurements. Corrected and calibrated data sampled at 50 Hz are employed. Since an attitude correction with the help of the star camera readings is adding undesired noise to the vector readings, the transformation into the North-East-Centre (NEC) system is based on the smooth nominal attitude angles. (The NEC system is a local frame with the origin in the geometric center of the vector magnetometer (VFM). The radial component points from the centre of the VFM towards the centre of the Earth (defined in ITRF). The North (N) and East (E) components point from the center of the VFM towards North and East, i.e. along the local tangent to the meridian, respectively the parallel, of the sphere (defined in ITRF) with radius from the center of the Earth to the center of the instrument.) This method is adding some long periodic angular biases, but this biases can be ignored, because it does not add signal to the higher frequency range of interest.

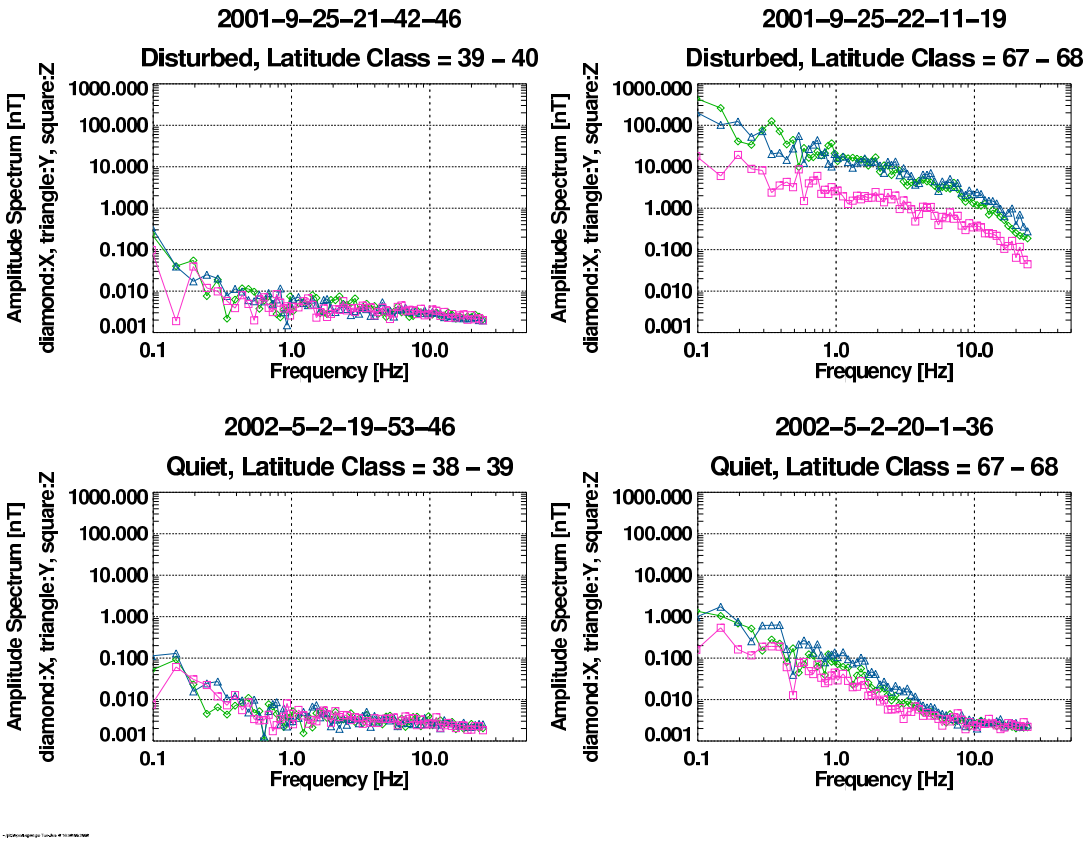

Figure 2.6: Examples of amplitude spectra for disturbed and quiet days taken at low and high dip latitudes.

The data are blocked according to their geomagnetic dip latitude. The blocks have a fixed latitude range of one degree. For each block a typical spectrum is derived from CHAMP data. After a trend removal and cosine-tapering the time series is transformed into the frequency domain by an *FFT*. The coefficients are set to zero for all frequencies greater than 20 Hz and less than 0.1 Hz. After collection of typical samples for each block in the [0...90] degree latitude range both for a quiet and a disturbed day all Fourier coefficients are stored into a matlab binary file. See Figure 2.6 for four typical examples of spectra for a quiet and disturbed day.

The spectral power content of each block is kept constant, only the phase information is randomized each time the synthesis of that block is activated. For the sake of processing speed the *FFT* is used for both the analysis and synthesis of the field vectors.

Synthesis

As an input of the model for the synthesis of the AC data the geomagnetic dip latitude is needed. The dip latitude, β, is computed from the components of the field model

$$\beta = \arctan\left(\frac{1}{2} \cdot \frac{B_z}{\sqrt{B_x^2 + B_y^2}}\right), \tag{2.6}$$

where B_x, B_y and B_z are the North, East and Center components of the geomagnetic field. Here $|\beta|$ is used to select the set of coefficients for the appropriate block. All intervals with the same dip latitude classification are filled with values created by inverse FFT using the same set of coefficients, but with randomized phases.

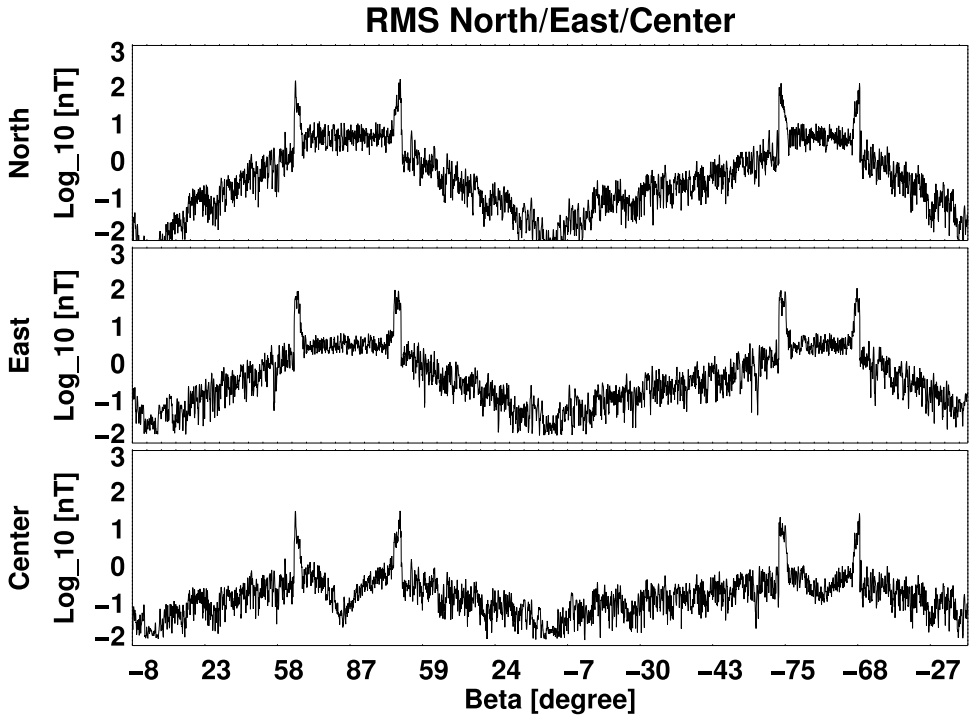

Figure 2.7: Variance of North, East and Center components for one orbit.

The final step is the orthogonalization of the synthetic AC field vector $\mathbf{B}_{\mathrm{AC}}$ to the model magnetic field $\mathbf{B}_{\mathrm{M}}$ by

$$\mathbf{B}_{\perp,\mathrm{AC}} = \frac{\mathbf{B}_{\mathrm{M}} \times (\mathbf{B}_{\mathrm{AC}} \times \mathbf{B}_{\mathrm{M}})}{|\mathbf{B}_{\mathrm{M}}|^2}. \tag{2.7}$$

This ensures that the AC signal is confined to the direction perpendicular to the ambient field, as is the case in reality.

The magnetic activity is accounted for by the parameter Kp of the AC module. Kp is used in the floating point range [0...9] selecting between the quiet and disturbed sets of coefficients.

The global Kp index is obtained as the mean value of the disturbance levels in the two horizontal field components, observed at 13 selected, mid-latitude observatories. The

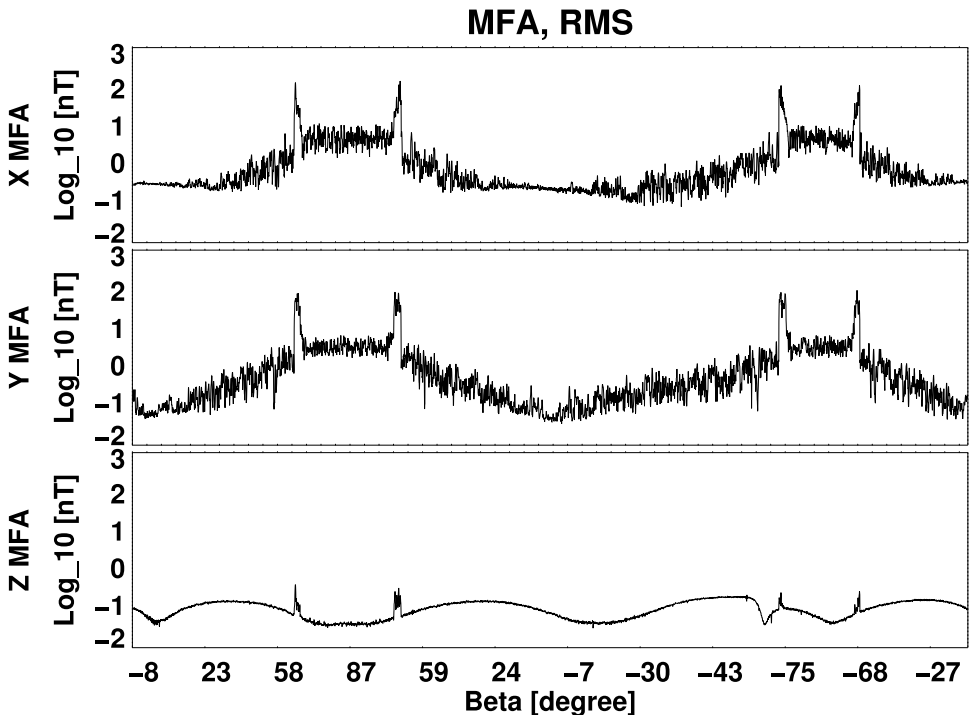

Figure 2.8: Standard deviation over whole orbit of synthetic magnetic field in MFA coordinate system.

name *Kp* originates from "planetarische Kennziffer" (planetary index), see http://www.gfz-potsdam.de/pb2/pb23/GeoMag/niemegk/kp_index/.

As mentioned in section 2.3, the optional parameter *Kp* can be passed to the AC module by a floating point parameter or as a string argument in the classical Kp notation, see http://www.gfz-potsdam.de/pb2/pb23/GeoMag/niemegk/kp_index/kptab.html or ftp://ftp.gfz-potsdam.de/pub/home/obs/kp-ap for sources in tabular format. If the *Kp* parameter is missing, a default value of 3 is used.

Validation

A set of magnetic field vectors computed for a whole orbit, including northern and southern polar regions, the AC signal has been generated. There appear two pairs of activity maxima when passing the auroral ovals, as expected. Since the inclination of the magnetic field vector itself is controlling the selection of blocks, it is of course not synchronized with the geographic latitude. Figure 2.7 contains the three components in the NEC (North/East/Center) coordinate system. The moving window variance calculation is using a time window of three seconds. The obtained AC activity variation with latitude reflects rather well the real conditions.

As mentioned before, the expected high frequency disturbances are confined to the perpendicular components. This can be tested by transforming the synthesized field into a MFA (Mean-Field-Aligned) coordinate system, where the Z component is locally aligned with the main field and the X and Y components are pointing approximately eastward and northward, respectively. As is evident from Figure 2.8, the AC disturbances of the Z component in the MFA system are much weaker then the ones in the perpendicular components.

Chapter 3

Forward Scheme: Production of Synthetic Data

3.1 Introduction

This section describes the production of synthetic data for a simulated mission. Involved in this task are the working packages WP-2100 "Orbit Determination", WP-2200 "Magnetic and Electric Field Generation", and WP-2300 "Magnetic and Electric Field Generation, Support". Figure 3.1 shows a flow chart of the forward scheme. Table 3.1 lists the different data products. Here and in the following the naming convention is only shown for data of Constellation #1.

data product	contents	described in	available at ftp.spacecenter.dk/data/magnetic-satellites/Swarm/E2E/constellation_1/
1 min position values	daily files of satellite position of the	section 3.2	./orbits/
1 min magnetic field values	separate contributions from core ($n = 1 - 19$), crust ($n = 14 - 120$), ionosphere (primary), ionosphere (induced), magnetosphere (primary), magnetosphere (induced), toroidal	section 3.5.1	./1min/
5 secs values	dto.	section 3.5.1	./5sec/
ionospheric currents and electric fields	ionospheric sheet current density and electric fields(5 secs values)	section 3.5.5	./currents_and_E-field/
oceanic magnetic field	separate magnetic field contribution (1 min values) due to 10 tidal modes	section 3.5.3	./ocean_tides
magnetospheric SH terms	time series (1 hour sampling rate) of magnetospheric expansion coefficients $\epsilon_n^m(t)$	section 3.6	./indices/
observatory data	observatory hourly mean values, using all main sources of CM4	section 3.6	./synthetic_obs_data/

Table 3.1: The various data products

3.2 Orbit Design

3.2.1 Constellation #1

In Task 2 we have used the orbit parameters presented in the *Swarm* proposal [Friis-Christensen et al., 2002]. We call this Constellation #1. It covers the following points:

- The orbits of all spacecraft shall be circular and near-polar.
- Two of the satellites shall fly as low as possible, but high enough to support a 4-year in-orbit life-time. They shall follow each other at a distance of about 1000 km.
- The remaining two satellites shall fly at least 100 km higher, separated along the orbit by about 180°.

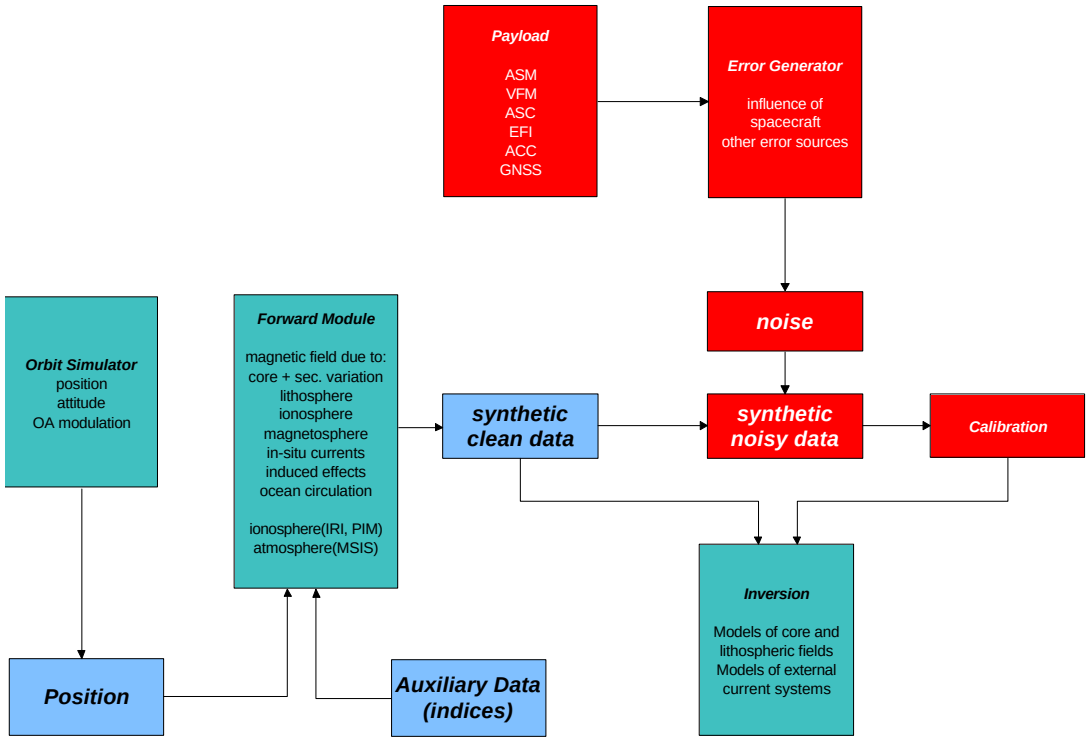

Figure 3.1: Forward Scheme.

- The two orbital planes shall have slightly different inclinations giving rise to a difference in nodal drift by some 90° in 3 years.

The sensitivity of the mission performance on any of these requirements will be assessed as part of the end-to-end simulation.

The characteristics of this constellation, denoted as Constellation #1, are shown in Figure 3.2 and Table 3.2. For our simulation we assumed a launch of the *Swarm* satellites on January 1, 1997, 00:00 UT, i.e. one solar cycle (11 years) before the anticipated launch in 2008. This was done in order to have similar ambient conditions, but have access to actual input values to parameterize e.g. the atmospheric drag model, the Earth rotation variations, etc.

3.2.2 Options for Constellation #2

In Task 3 of the study an optimized orbit constellation has been determined which is, however, consistent with the performance of the spacecraft as outlined in the conducted industry Phase A studies.

To obtain larger flexibility in the assessment of favorable measurement conditions to select Constellation #2, data for initially 6 satellites with different orbit parameters are generated. For any simulation run up to 4 out of the 6 available synthetic data sets can be used in the inversion analysis. The choice of orbital parameters was based primarily on the experience gained during the Task 2 studies. A major change in concept is to have two spacecraft flying side-by-side separated in the east/west direction instead of two satellites following each other. This constellation promises to provide more uncorrelated information. Another point is to increase the orbit inclination slightly in order to reduce the size of the polar gaps. Finally, the

Swarm 1	
Inclination	$i_1 = 86.0°$
RAAN	$\Omega_1 = 0°$
Eccentricity	$\epsilon_1 = 0$
Argument of Perigee	$\omega_1 = 0°$
Mean Anomaly at Epoch	$M_1 = 90°$
Mean Motion	$n_1 = 15.05490756$ rev/day
Altitude	$h_1 = 550$ km
Semi-Major Axis	$a_1 = 6928.137$ km
Period	$T_1 = 95.6499$ min $= 5738.9924$ sec
Swarm 2	
Inclination	$i_2 = 86.0°$
RAAN	$\Omega_2 = 0°$
Eccentricity	$\epsilon_2 = 0$
Argument of Perigee	$\omega_2 = 0°$
Mean Anomaly at Epoch	$M_2 = 270°$
Mean Motion	$n_2 = 15.05490756$ rev/day
Altitude	$h_2 = 550$ km
Semi-Major Axis	$a_2 = 6928.137$ km
Period	$T_2 = 95.6499$ min $= 5738.9924$ sec
Swarm 3	
Inclination	$i_3 = 85.4°$
RAAN	$\Omega_3 = 0°$
Eccentricity	$\epsilon_3 = 0$
Argument of Perigee	$\omega_3 = 0°$
Mean Anomaly at Epoch	$M_3 = 0°$
Mean Motion	$n_3 = 15.38684059$ rev/day
Altitude	$h_3 = 450$ km
Semi-Major Axis	$a_3 = 6828.137$ km
Period	$T_3 = 93.5865$ min $= 5615.19$ sec
Swarm 4	
Inclination	$i_4 = 85.4°$
RAAN	$\Omega_4 = 0°$
Eccentricity	$\epsilon_4 = 0$
Argument of Perigee	$\omega_4 = 0°$
Mean Anomaly at Epoch	$M_4 = 8.3911°$ (1000 km separation)
Mean Motion	$n_4 = 15.38684059$ rev/day
Altitude	$h_4 = 450$ km
Semi-Major Axis	$a_4 = 6828.137$ km
Period	$T_4 = 93.5865$ min $= 5615.19$ sec

Table 3.2: Kepler elements used for Constellation #1, for epoch January 1, 1997, 00:00 UT (launch).

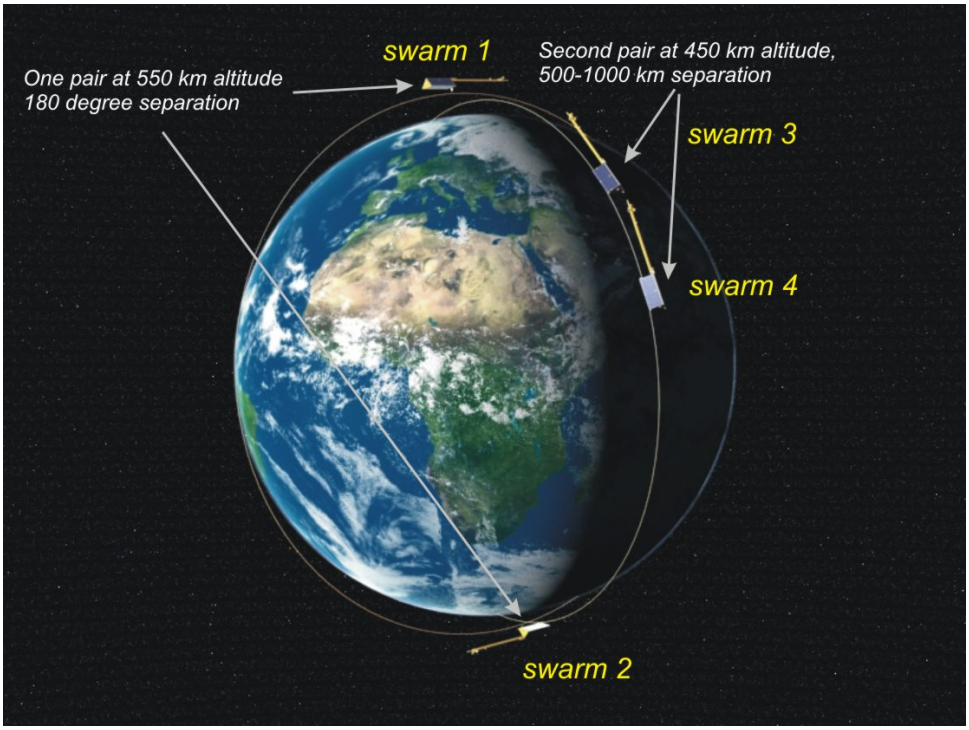

Figure 3.2: Definition of *Swarm* Constellation #1.

initial altitude was adjusted according to the presently best guesses of spacecraft properties like mass and cross-section area, as resulting from the two industry studies.

Details of the orbit elements of Constellation #2 are listed in Table 3.3. The main features of the initial Constellation #1 are preserved. There are pairs of satellites at a lower and a higher altitude. The lower pair is dedicated to support the high-degree lithospheric magnetization studies and thus calls for small separations. For this study we have selected separations for the lower pair in east/west direction of 1.5° and optional 11.25° in longitude.

One of the results of this study is that the combination consisting of the three satellites *Swarm* 4, 5 (lower pair) and *Swarm 1* (higher satellite) turned out to be optimal. These three satellites have been renamed, and the new names *Swarm A, B* and *C* are used in some of the figures and in the final assesment (chapter 7) and yield Constellation # 2.

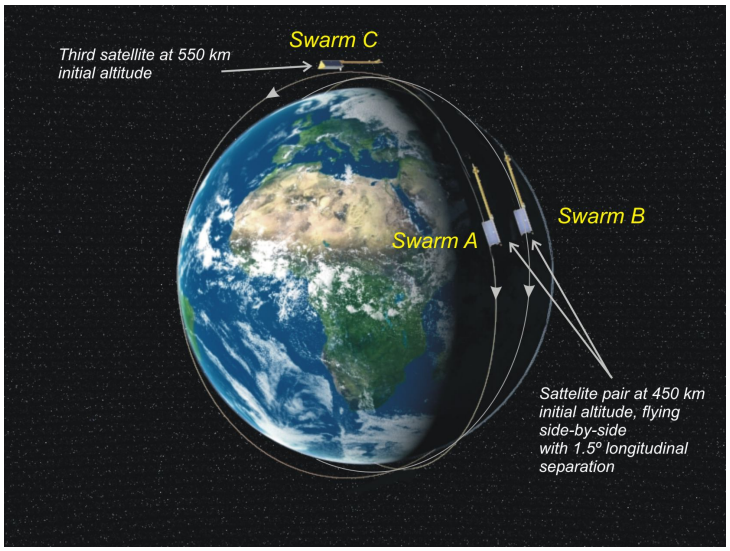

Figure 3.3: Definition of *Swarm* Constellation #2

Prerequisites

Epoch for simulations	1997.0 (Launch expected at 2008.0)
Reference radius for altitudes	R = 6371.2 km
Earth gravitational constant	$\mu = 3.986004418 \cdot 10^{14}$ m^{3}s^{-2} (IERS Conventions 2003)
Drag coefficients	$c_D = 2.2$
Cross-section area	A = 0.82 m^{-2} (0.75 m^{-2} + 10% margin)
Satellite mass	m = 400 kg

High Satellites

Swarm **1** = *Swarm* **C**	
Inclination	$i_1 = 87.3°$
RAAN	$\Omega_1 = 0°$
Eccentricity	$\epsilon_1 = 0$
Argument of Perigee	$\omega_1 = 0°$
Mean Anomaly at Epoch	$M_1 = 90°$
Mean Motion	$n_1 = 15.07754714$ rev/day
Mean Altitude	$h_1 = \sim 550$ km
Semi-Major Axis	$a_1 = 6921.2$ km
Period	$T_1 = 95.5063$ min $= 5730.38$ sec

Swarm **2**	
Inclination	$i_2 = 87.3°$
RAAN	$\Omega_2 = 0°$
Eccentricity	$\epsilon_2 = 0$
Argument of Perigee	$\omega_2 = 0°$
Mean Anomaly at Epoch	$M_2 = 270°$
Mean Motion	$n_2 = 15.07754714$ rev/day
Mean Altitude	$h_2 = \sim 550$ km
Semi-Major Axis	$a_2 = 6921.2$ km
Period	$T_2 = 95.5063$ min $= 5730.38$ sec

Swarm **3**	
Inclination	$i_3 = 87.3°$
RAAN	$\Omega_3 = 348°(= -12°)$
Eccentricity	$\epsilon_3 = 0$
Argument of Perigee	$\omega_3 = 0°$
Mean Anomaly at Epoch	$M_3 = 90°$
Mean Motion	$n_3 = 15.07754714$ rev/day
Mean Altitude	$h_3 = \sim 550$ km
Semi-Major Axis	$a_3 = 6921.2$ km
Period	$T_3 = 95.5063$ min $= 5730.38$ sec

Table 3.3: Kepler elements used for satellites to select Constellation #2, for epoch January 1, 1997, 00:00 UT (launch).

Low Satellites

Swarm **4** = *Swarm* **A**	
Inclination	$i_4 = 86.8°$
RAAN	$\Omega_4 = 0°$
Eccentricity	$\epsilon_4 = 0$
Argument of Perigee	$\omega_4 = 0°$
Mean Anomaly at Epoch	$M_4 = 0°$
Mean Motion	$n_4 = 15.41031864$ rev/day
Mean Altitude	$h_4 = \sim 450$ km
Semi-Major Axis	$a_4 = 6821.2$ km
Period	$T_4 = 93.4439$ min $= 5606.63$ sec
Swarm **5** = *Swarm* **B**	
Inclination	$i_4 = 86.8°$
RAAN	$\Omega_4 = 358.5°(= -1.5°)$
Eccentricity	$\epsilon_4 = 0$
Argument of Perigee	$\omega_4 = 0°$
Mean Anomaly at Epoch	$M_4 = 0°$
Mean Motion	$n_4 = 15.41031864$ rev/day
Mean Altitude	$h_4 = \sim 450$ km
Semi-Major Axis	$a_4 = 6821.2$ km
Period	$T_4 = 93.4439$ min $= 5606.63$ sec
Swarm **6**	
Inclination	$i_4 = 86.8°$
RAAN	$\Omega_4 = 348.75°(= -11.25°)$
Eccentricity	$\epsilon_4 = 0$
Argument of Perigee	$\omega_4 = 0°$
Mean Anomaly at Epoch	$M_4 = 0°$
Mean Motion	$n_4 = 15.41031864$ rev/day
Mean Altitude	$h_4 = \sim 450$ km
Semi-Major Axis	$a_4 = 6821.2$ km
Period	$T_4 = 93.4439$ min $= 5606.63$ sec

Table 3.3: *Swarm* satellites for selection of Constellation #2, continued

The higher pair is dedicated more towards supporting the recovery of the larger scale features. The two options considered here are two satellites in one orbital plane separated by about 180° in phase. The other set consists of two satellites flying side-by-side separated in east/west direction by 12° in longitude.

The characteristics of the selected constellation, denoted as Constellation #2, are shown in Figure 3.3. The epoch chosen for the start of the orbit modeling is again 1 Jan. 1997 in order to have similar environmental conditions as for the anticipated launch date in early 2008.

On the longitudinal separation of the lower satellite pair

The retrieval of the high-degree lithospheric field can be improved by considering gradients in the inversion algorithm. This concept of emphasing the small-scale structures is widely used in gravity missions, e.g. GRACE. Optimal spacecraft separations for deriving the gradients depend on signal spectrum, instrument resolution, and on the smallest scales that should be resolved during the mission. In order to find the optimal longitudinal separation of the lower pair of satellites for crustal field studies, we consider the following scenario: The scalar potential describing the crustal field $\mathbf{B}_{\rm cr} = -\mathrm{Re}\{\mathrm{grad}\ V\}$, is given as

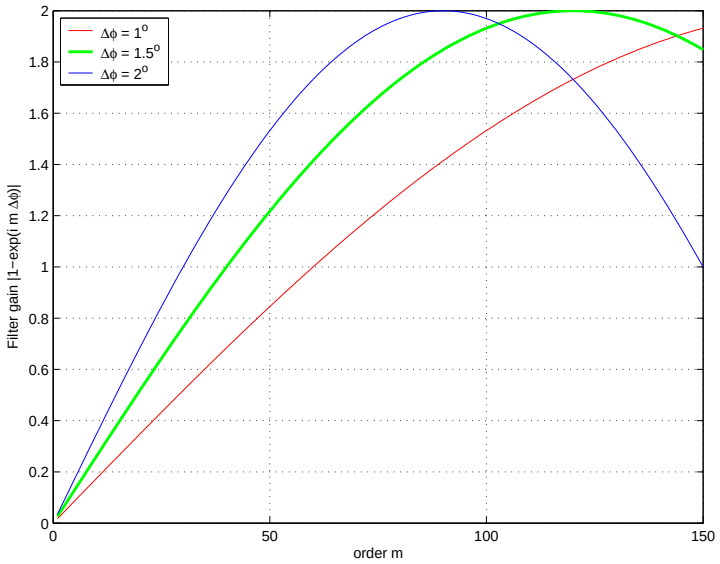

Figure 3.4: Relative sensitivity of the gradient method versus spherical harmonic order m, for three different longitude separations, $\Delta\phi$, of the spacecraft.

a spherical harmonic expansion,

$$V_{\rm cr} = a \sum_{n=1}^{n_{\max}} \sum_{m=0} \left(\frac{a}{r}\right)^{n+1} \gamma_n^m P_n^m e^{im\phi}.$$

This is the complex form of the usual spherical harmonic summation used in geomagnetism, cf. Eq. 2.1, with $\gamma_n^m = g_n^m - ih_n^m$.

The difference of the magnetic field measured by two satellites flying simultaneously with a longitudinal separation $\Delta\phi$ is $\Delta\mathbf{B}_{\rm cr} = \mathbf{B}_{\rm cr}(r,\theta,\phi) - \mathbf{B}_{\rm cr}(r,\theta,\phi+\Delta\phi) = -{\rm Re}\{{\rm grad}\,\Delta V\}$, where ΔV is a spherical harmonic expansion with coefficients $\Delta\gamma_n^m = \gamma_n^m \left(1 - e^{im\Delta\phi}\right)$. Hence by analysing the difference of the magnetic field measured by the two satellites the crustal field coefficients γ_n^m are multiplied with some filter factors, and the filter gain is $|\left(1 - e^{im\Delta\phi}\right)| = \sqrt{2(1-\cos m\Delta\phi)}$. Figure 3.4 shows the filter gain for three different values of longitudinal separation, $\Delta\phi$, of the satellites. Since *Swarm* aims at the determination of the lithospheric field up to spherical harmonics of degree and order 133 (spatial scale of 300 km), the optimal longitudinal separation of the lower satellites is about 1.4°.

Figure 3.5 shows the lithospheric field components (top) and the East-West gradient (bottom). Altitude is 400 km.

3.3 Orbit Generation

This section describes the efforts to do an orbit propagation for each of the *Swarm* satellites using state-of-the-art modelling software and realistic spacecraft properties. These activities relate to WP 2001 "Orbit Determination".

3.3.1 Performance Requirements

One characteristic of the *Swarm* mission, which is important for achieving the scientific goals, is a dedicated orbital constellation. For this reason it is indispensable that the orbital development be as realistic as possible. The obtained mission performance, tested with this simulator, may critically depend on the finally selected separation between the spacecraft.

Basic requirements of the orbit characteristics are given in the System Requirement Document (EOP-FP/2002-07-685/V1.1):

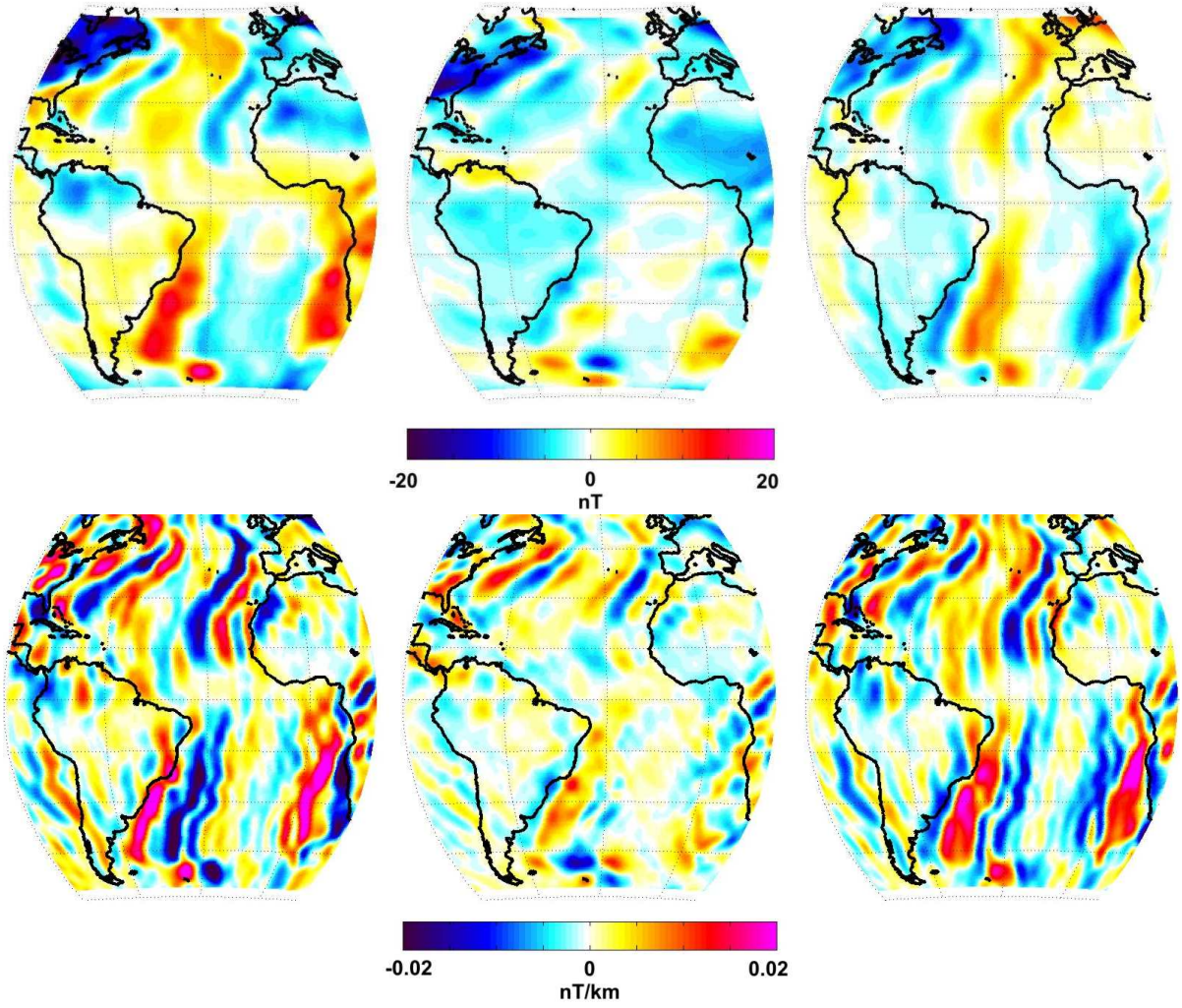

Figure 3.5: Lithospheric field components (top) and its East-West gradient (bottom), at 400 km altitude. Left to right shows B_r, B_θ, B_ϕ (resp. their gradients).

1. *The Swarm baseline constellation shall consist of 4 satellites in two different orbits.*
2. *Two satellites (the lower pair) shall be placed in an orbit as low as possible that allows an orbit lifetime of 4 years, separated by 500 to 1000 km.*
3. *The other two satellites (the higher pair) shall be placed in an orbit that is approximately 100 km higher than the one of the lower satellite pair, with an orbital arc separation of 180 degrees.*
4. *Both orbital inclination shall be close to 90 degrees, but the two orbits shall have slightly different inlcinations to obtain different precession rates leading to a separation of the two orbit planes.*

3.3.2 Approach of Orbit Modeling

The simulation has been performed by numerical integration of the equations of motion as they are programmed in the EPOS (Earth Parameter & Orbit System) software developed by GFZ Potsdam over more than 10 years. The central module EPOS-OC (Orbit Computation) has been used for the analysis of satellite tracking data of more than a dozen different satellites as well as for the integration of orbits and simulation of tracking data.

Integration The integration is done numerically, the integrator being of the type Cowell. For the integration a step size of 60 s has been chosen. This step is larger than the value operationally used for the precise orbit determination of the CHAMP satellite mission (15 s), but for CHAMP the required orbit accuracy is much higher (less than 20 cm), related to other applications. Tests have shown that the selected step size of 60s will be sufficient for the required interpolation accuracy.

Reference System The integration has been performed in the true-of-date reference system (TDS) and later on rotated into the International Conventional Terrestrial Reference System (ICTS). The Earth Orientation parameters have been taken from the IERS Bulletin B (http://hpiers.obspm.fr/eop-pc). The nutation and precession models have been taken from IERS Conventions 1996 [Mc Carthy, 1996]. The International Conventional Inertial Reference System (ICIS) is based on the mean equator and equinox of J2000.0 [Mc Carthy, 1996].

Dynamical Models The greatest dynamical force acting on a satellite is the terrestrial gravity field. For the simulation a newly computed model EIGEN-2SP, making use of CHAMP data, has been used. The spherical harmonic expansion up to degree and order 70 has been considered. For the ocean tides the FES2002 model has been selected with spherical harmonic coefficients up to degree 50 and order 39. The modeling of the Earth tides is done according to the IERS Conventions 1996 [Mc Carthy, 1996]. The ephemerides for the Sun, the Moon and 5 planets (Mercury, Venus, Mars, Jupiter, Saturn) are coming from the JPL Planetary and Lunar Ephemerides DE405/LE405. The Schwarzschild relativistic effect has been taken into consideration.

For all non-conservative forces the *Swarm* satellites have been modeled as cannonballs, since the final geometry and surface properties of the satellites are not yet accurately known. In this case of pure orbit integration (prediction) this assumption should be justified, compared to other types of uncertainties (e.g., solar flux ($F10.7$) predictions).

After the gravity field the second largest force acting on a satellite at this altitude is the atmospheric drag. The modeling of the atmospheric density is based on the MSIS-86 model [Hedin, 1987] making use of the 3-hourly geomagnetic indices (Ap), as well as the daily solar flux ($F_{10.7}$) and the average solar flux over 3 solar rotations (81 days). The solar radiation model is using umbra, penumbra and a regularisation function. Earth radiation pressure effects in the visible part (albedo) and in the infrared domain are modeled according to Knocke et al. [1988].

Constellation The orbit integration was performed over intervals of three months. To avoid jumps at the interfaces the periods overlap by one day. In the post-processing a continuous data stream sampled at one minute is generated. The start epoch is defined by the initial conditions and the orbit integrations were stopped when the altitude of the lower pair approached 250 km.

Rather than integrating the orbit developments for all four spacecraft, in the case of Constallation #1 only one in each plane was calculated. The ephemerides of the two companion satellites are derived by delaying the orbital phase accordingly and assuming a somewhat enhanced air drag, which is based on experience from the GRACE mission. This leads to a continuous increase of the distance between the satellites in a pair. In the case of Constellation #2 additional measures are required to maintain the required separation (see Sec. 3.3.7).

3.3.3 Data Products Generated

The prime data products are daily files with the ephemerides separately for each of the four spacecraft. The naming convention of these files is:

SW-OG-3-PSO+CTS-CL1-SW1_1997_01_01_01_00.dat

where SW is the *Swarm* project, OG stands for Orbit and Gravity, 3 is the level of data processing, PSO is Precise Orbit, CTS for the Conventional Terrestrial System, CL1 is the number of *Swarm* constellation, SW1 is number of the spacecraft, 1997_01_01 is epoch of data, 01 is a code for used orbit modeling, 00 is the version of the data. These orbit files are available at ftp.spacecenter.dk/data/magnetic-satellites/Swarm/E2E/constellation_1/orbits.

The data are preceded by 25 header lines. Each data line starts with the time in MJD2000 (Modified Julian Day, starting at 1 Jan. 2000, 00:00 UTC), followed by three component of the position and the velocity, both are given in the CTS frame, which is consistent with the GPS-based WGS-84 frame to a level of 0.1 m. A short printout of the data is shown below.

```
% DSIDP  SW-OG-3-PSO+CTS-CL1-SW1_1997_01_01_01_00.dat
% COMENT SWARM_1 PRECISE ORBIT (01.01.1997 - 02.04.1997)
% COSPAR 1997-001A
% PERIOD  -1095.0000  -1094.0007
% INIREV 1
% PARAMS
% QUALCO Sta_Dev_Initial_Elements = 0 0 0 mm, 0 0 0 mu/s
% TFRAME UTC
% RFRAME CTS
% MRELAT  Post Newtonian
% MNUTAT  VLBI-Korrektur 1997
% MPOTER  eigen2sp_grasse2002.
% MPOLUN  Point Mass
% METID   IERS-Conv. (1996)
% MOTID   Marees FES2002 up to
% MATMOS  CIRA 86 von Hedin
% MALBED  Knocke CSR
% MEPHEM  DE200/LE200
% COMENT The ORBIT line marks end of the header and start of the trajectory records
% COMENT The trajectory records end at the end of file
% ORBIT
%
% ------------------------------------------------------------------------------------------
%   MJD [d]          X [km]       Y [km]       Z [km]      Vx [m/s]       Vy[m/s]       Vz [m/s]
% ------------------------------------------------------------------------------------------
-1095.00000000   474.882936   -89.594495  6906.200918  1399.7206904  7419.2976140     0.0035838
-1094.99930556   559.735878   355.067524  6891.313687  1427.6693081  7397.4391636  -496.0674499
-1094.99861111   646.074354   797.460428  6846.715325  1449.1739555  7343.6964733  -990.0137407
-1094.99791667   733.500424  1235.679033  6772.596869  1463.8632356  7258.3549378 -1479.7191124
-1094.99722222   821.594823  1667.839381  6669.275815  1471.3977178  7141.8358643 -1963.0861790
-1094.99652778   909.918924  2092.086778  6537.194742  1471.4720882  6994.6932046 -2438.0436000
-1094.99583333   998.016880  2506.603702  6376.919572  1463.8181106  6817.6116544 -2902.5529511
```

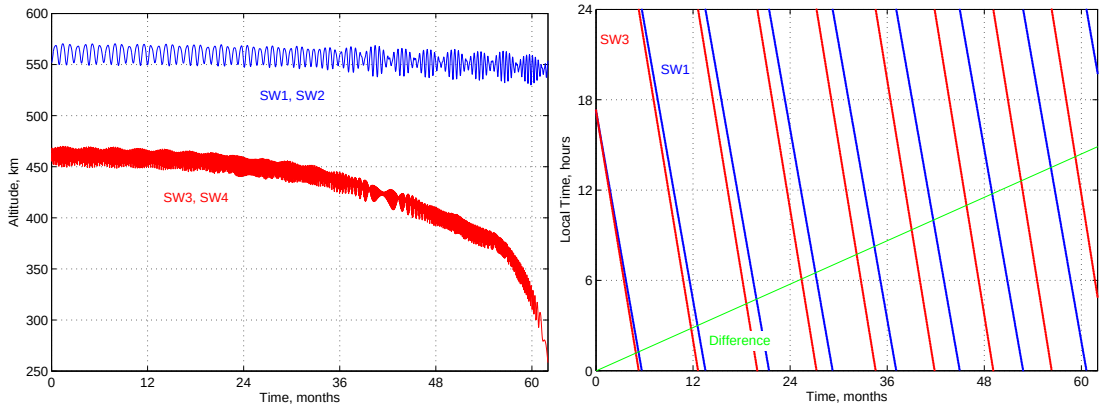

Figure 3.6: Left: Orbital decay of the high and low *Swarm* pairs. Right: Local time development of the *Swarm* satellites SW1(high) and SW3 (low).

A second data product is the orbit counter generated for each of the four spacecrafts. These files are available at ftp.spacecenter.dk/data/magnetic-satellites/Swarm/E2E/constellation_1/tools/swarm1_1_orbit-numbers.dat (and corresponding filenames for swarm2, swarm3 and swarm4, respectively).

The three columns of this file contain the orbit number, as well as the time (MJD2000) and the longitude of the northbound equator crossing. An example of the Orbit Number file is given below.

```
% DSIDP  SW_ORBIT_NUMBER_CL1_SW1_1997_01_01_01_00.dat
%
% ----------------------------------
% Orbit#   MJD [d]    long.asc.node
% ----------------------------------
1 -1094.95009028     -118.72581
2 -1094.88357820     -142.77064
3 -1094.81706674     -166.81534
4 -1094.75055571      169.13991
5 -1094.68404477      145.09581
6 -1094.61753278      121.05218
```

3.3.4 Obtained Orbit Evolution, Constellation #1

In this section the prime characteristics of the orbital evolution of the first *Swarm* constellation are presented. The left part of Figure 3.6 shows the orbital decay over the 62 months considered here. The altitude is defined as height above the reference sphere with radius r = 6371.2 km. The higher pair, SW1 and 2, experiences only a small decrease of some 15 km in altitude over the displayed period of 5 years. Clearly visible is a modulation giving rise to a 20 km altitude variation at a period of about 28 days in the beginning rising to about 30 km at a period of 12 days in the end.

The development is a little different for the lower pair. Here we find a rather continuous decay during the first 4 years by some 60 km, but towards the end of the fifth year a rapid decrease is observed. This is caused by the high solar activity and its influence on the atmospheric density during autumn and winter 2001.

Another parameter of interest is the local time of the orbital plane. As can be seen in the right part of Figure 3.6, a precession through all local times takes about 8 months for both pairs. Therefore the orbital planes are wrapping around several time during the mission. In the constellation simulated here SW1 flies in a plane with a constant offset of about 45 min towards later local time with respect to SW2. Since the upper pair of satellites is flying at a somewhat higher inclination, its nodal drift is a

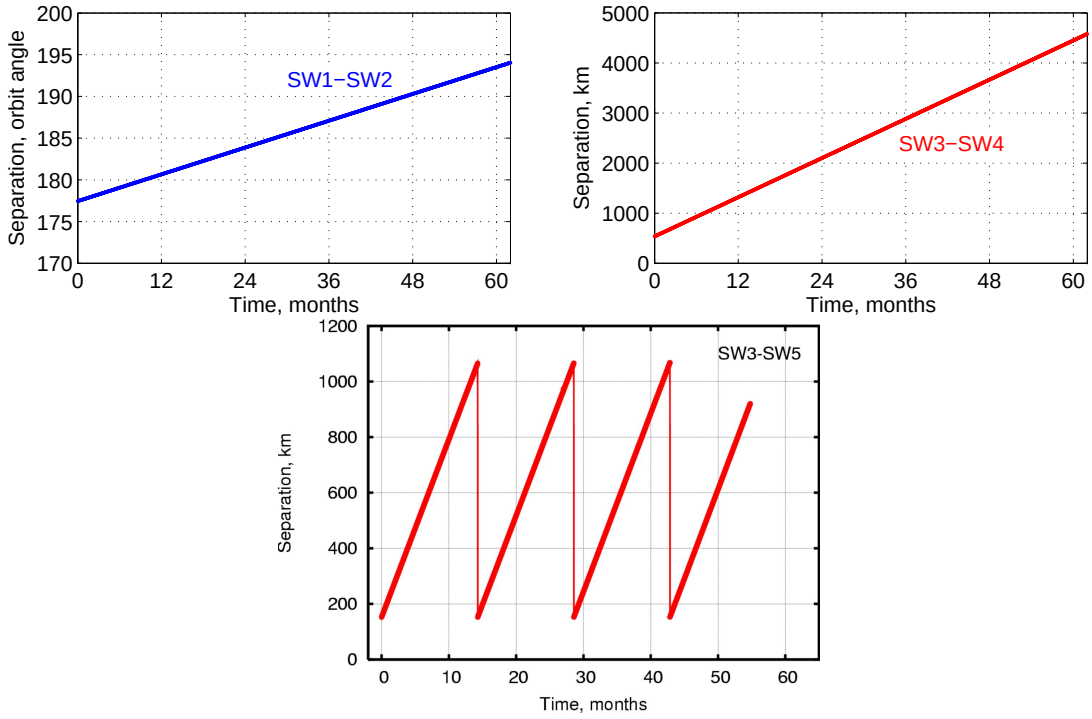

Figure 3.7: Development of the distance between the upper (left) and the lower (right) satellite pairs, another option of the lower pair with controlled distance (bottom)

little slower than that of the lower pair. Starting in the same plane the local time difference builds up to almost 15 hours over the 62 months mission time, as can be seen in the figure.

Finally we have a look at the spacecraft separations in the constellation. The upper pair is intended to sample the antipodes simultaneously. As can be seen in Figure 3.7 (left), this is attained quite well during the mission. At the beginning of the mission the orbital phase angle difference is slightly below 180°. Due to a somewhat slower SW2 the angle increases to 194° at the end of the mission. The lower pair is intended to stay closer together. As shown in Figure 3.7 (right), the satellites SW3 and SW4 start at a separation of about 500 km and gradually drift apart due to a slightly different air drag. After 62 months the distance has grown to 4600 km. This is probably somewhat more than desired for the lower pair.

3.3.5 Summary of Orbits, Constellation #1

The orbital development of the *Swarm* satellites has been modeled using a constellation as presented in the project proposal. Most of the primary results compare favorably with the requirements stated in the MRD. Some conclusions can be drawn from the obtained results.

1. The orbital life-time of the lower pair exceeds the projected 4 years by about 14 months. This means one could have started at an altitude about 10 km lower.

2. The two orbital planes have a slightly different nodal drift. Over the 62 months a difference in local time of almost 15 hours builds up. This is clearly higher than the anticipated 6 hours in 3 years. A smaller separation between the inclinations could be selected.

3. The development of the separation between accompanying satellites is well within the range of expectations for the pair, SW1/SW2. Here the 180° in orbital angle is maintained close enough through all the years. The lower pair, SW3/SW4, drifts apart much further than the desired

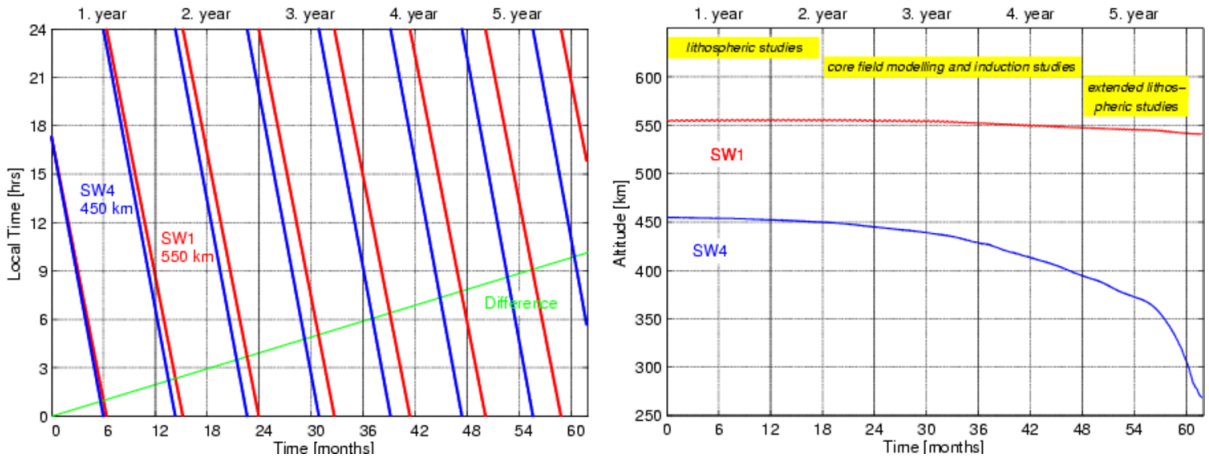

Figure 3.8: Orbit evolution of the higher and lower satellite pairs. (top) Precession of the orbital planes through local time. The lower satellites drift slightly faster. (bottom) Orbital decay of the higher and lower satellite pairs.

1000 km. To maintain the range of distance, some kind of orbit manoeuvres would have to be included in the orbit simulation.

To solve the problem of drift between SW3 and SW4, which is the largest violation of the formation concept,an additional satellite, called SW5, was introduced. This one started at a distance of 160 km from SW3 and drifted apart at the know rate. When the distance reached 1000 km an orbit manoeuvre was simulated and the separation brought back to 160 km (cf. Fig. 3.7, bottom).

3.3.6 Obtained Orbit Evolution, Constellation #2

The studies of Task 2 were based on the Constellation #1. A slightly modified set of satellites to select Constellation #2 was designed from the experience gained there as a basis for the Task 3 study. Main orbital elements are listed in Table 3.3

The computation of the orbit data for the second constellation was performed in the same way as described above. The data products, daily files of the position and velocity sampled at one minute intervals and the orbit number files, also have the same formats as before. The different spacecraft have been assigned SW1 through SW6. The higher ones are SW1 to SW3 and the lower SW4 to SW6. For the two altitudes SW1 and SW4 are chosen as reference satellites.

We obtained the following orbit evolutions from our calculations. The orbital decay is almost identical for the three spacecraft with the same initial altitude. For that reason only the decay of SW1 and SW4 over the mission period is shown in Figure 3.8. We have stopped the orbit integration at the time when SW4 reached the altitude of 250 km. This occurred after 61 months. The satellites at altitudes of 550 km (SW1-SW3) come down only a little within the mission period.

In order to obtain a separation between the orbital planes, the upper and lower spacecraft have been given a slightly different inclination (cf. Table 3.3). The precession of the orbital planes of the upper and lowers sets is also shown in Figure 3.8. The drift rate of the lower satellites is slightly faster. This results in a local time difference of 6 hours after 36 months, as required.

Another parameter of interest for a constellation is the spatial separation between two accompanying spacecraft. These separations have been set at the beginning to a desired value but may vary over the course of the mission. The evolution of the higher and lower pairs is shown in Figure 3.9. SW4 and SW5 are initially set up with an east/west spacing of 165 km at the equator. Due to slight differences in orbit decay the satellites slowly drift apart. To keep the spacecraft within the desired range, five orbit manoeuvres had to be simulated. These events manifest themselves as discontinuous changes in the separation (cf. middle panel of Fig. 3.9). Orbit adjustments were initiated when the difference in

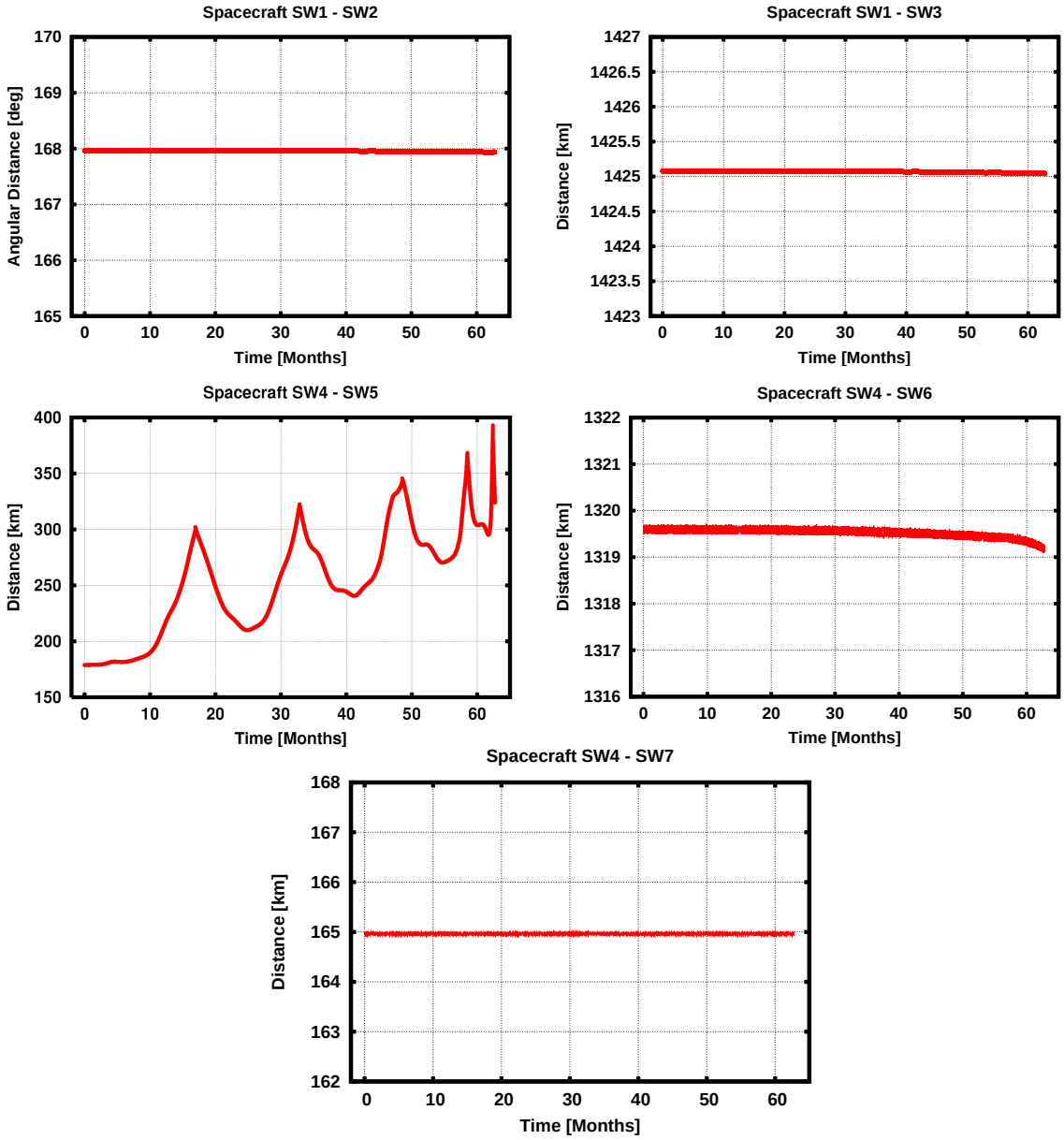

Figure 3.9: Separation between satellite pairs at the higher (top), and lower (middle and bottom) orbits.

latitudes between SW4 and SW5 exceeded 2°. The behavior of SW4 and SW6 is very much the same as for SW1 and SW3.

3.3.7 Summary of Constellation #2

In Section 3.3.1 it has been stated that a close spacing of the two lower satellites in the east-west direction is advantageous for resolving small lithospheric features. From Fig. 3.9 we see that the separation of the pair SW4-SW5 is slowly increasing, thus degrading the optimal spacing (cf. Fig. 3.4). To solve the problem of drift an additional satellite, termed SW7, was introduced. This spacecraft is forced to have a constant separation in longitude of 1.5° at the equator (cf. Fig. 3.9). The purpose of the satellite pair SW4-SW7 is to demonstrate and test the potential of the gradient method in resolving small-scale features.

Orbit ephemerides of seven satellites for a period of 61 months have been generated. The orbital evolution of the spacecraft pairs SW1/2 and SW4/5 was quite smooth, as expected. On the other hand, the spacecraft pairs SW1/3 and SW4/6 initially showed quite large relative drifts, even though identical spacecraft were used in the orbit propagation. The difference in environment experienced by two spacecraft separated by 12° in longitude seems to be quite significant. A dedicated tuning of the the accompanying spacecraft SW3 and SW6 was required to keep them at constant distance. In case such an east/west separation should be implement in the *Swarm* mission a special study of the expected orbit dynamics would be recommended.

For the closely spaced pair SW4-SW7 we have not paid any attention to the critical approaches at the orbital cross-over points. The assessment of collision risk at minimum separation definitely requires special attention.

The orbit computation presented here takes for a period of 4 years about one day per satellite for the integration and another day for the joining of the individual arcs and the formatting to daily files. The latter requires a lot of manual interaction. The *Swarm* orbits have been computed on a SunFire 880, 8x750 Mhz, 16 GB RAM.

3.4 Design of the Input Models

3.4.1 Construction of the Core and Crustal Field models swarm(02a/03) and swarm(11a/03)

Constellation #1: model swarm(02a/03) The spherical harmonic model swarm(02a/03) was used for creating synthetic data for Constellation #1. It consists of static spherical harmonic expansion coefficients g_n^m, h_n^m up to $n, m = 120$ and linear secular variation coefficients $\dot{g}_n^m, \dot{h}_n^m$ up to $n, m = 19$.

The static terms g_n^m, h_n^m are found by the following procedure: Coefficients for the lowest degrees (up to $n = 40$) are taken from a snapshot (at epoch 1997.0) of the latest version of the *Comprehensive Model* [Sabaka et al., 2002] called CM4 (version CM3e-J_2, [Sabaka and Olsen, 2003]). This model is also used to create synthetic data for Tasks 2 and 3 of the *Swarm* E2E Mission Simulator study. Medium degree coefficients ($n = 40 - 70$) are taken from the field model MF-2 derived by Maus *et al.* (see Maus et al. [2002] and www.gfz-potsdam.de/pb2/pb23/SatMag/litmod2.html); a smooth transition (cosine bell) has been used for coefficients with n between 35 and 45. The high degree coefficients ($n = 71 - 120$) are taken from a synthetic model, based on an extrapolation of the MF-2 spectrum (linear fit to $\log(R_n)$ for $n = 25 - 70$) and assuming that the amplitudes of all coefficients for a given n are from a common Gaussian distribution. Coefficients with $n > 110$ are tapered to zero at $n = 120$. Figure 3.10 shows the Mauersberger-Lowes Spectrum of the merged model (blue line) and of its constituents.

Coefficients $\dot{g}_n^m, \dot{h}_n^m$ of the linear secular variation are taken from a snapshot of CM4 at epoch 1997.0 for $n = 1 - 13$. Higher terms ($n = 14 - 19$) are created from a fitted spectrum in the same way as described above for the crustal field; the spectrum was found from the difference of a Field model for epoch 2000.0 (IDEMM-low, see www.dsri.dk/Oersted/Field_models/IDEMM/) and a snapshot of CM4 for epoch 1980.0, divided by 20 years (2000.0-1980.0).

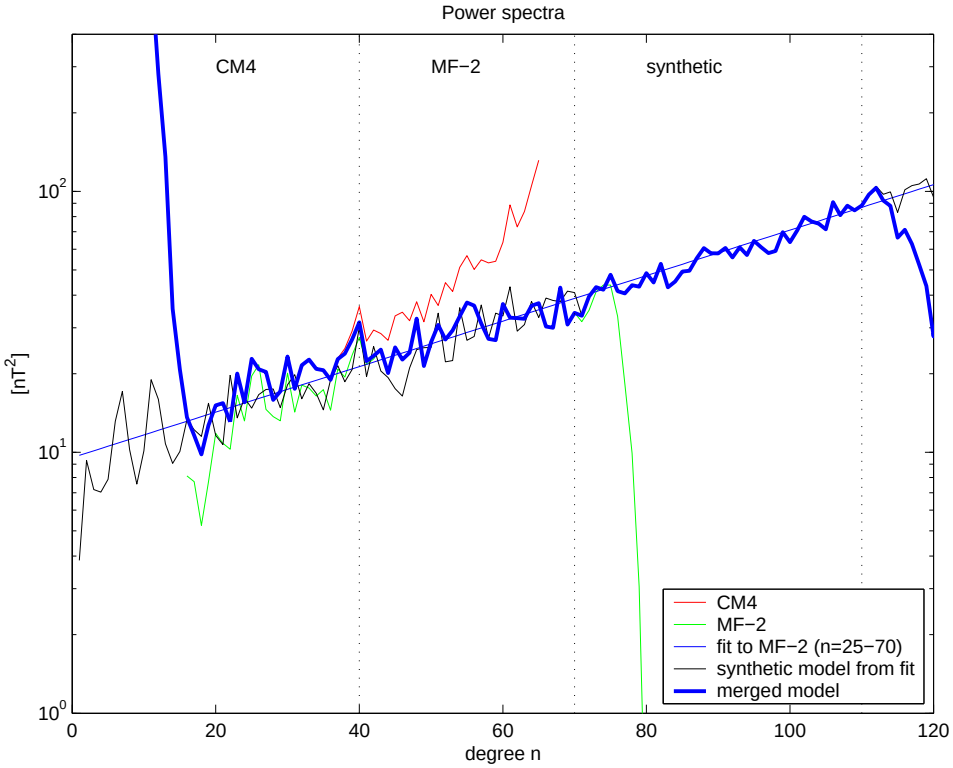

Figure 3.10: Power-spectrum of the crustal field part of the magnetic field model swarm(02a/03) used in this study

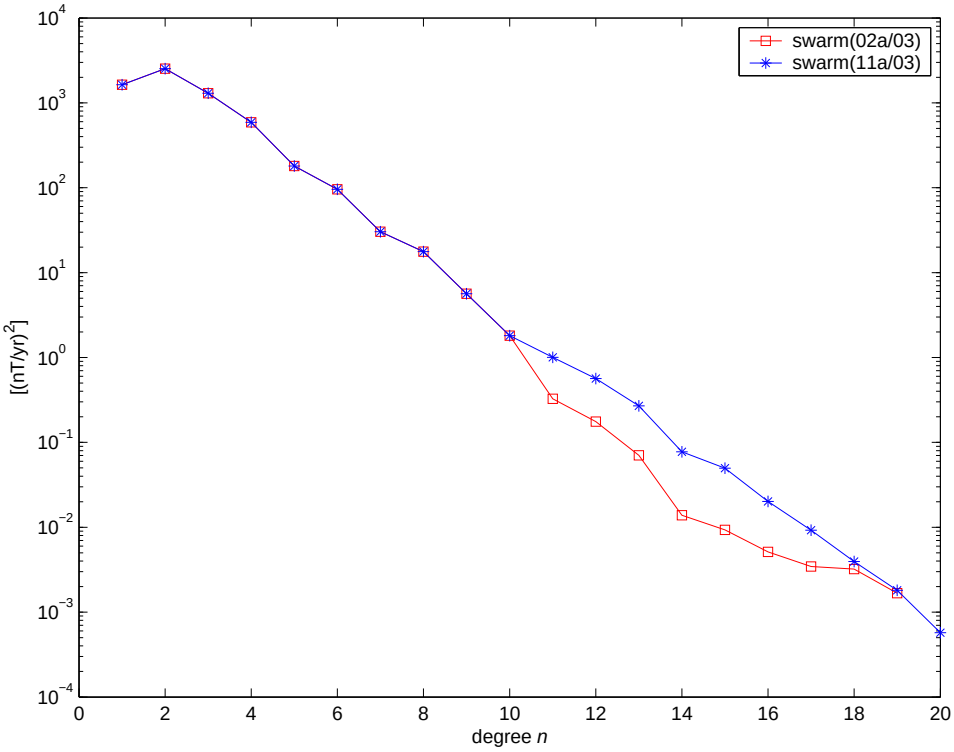

Figure 3.11: Power-spectrum of the secular variation model swarm(11a/03) used in Task 3 and of model swarm(02a/03) used in Task 2.

Constellation #2: model swarm(11a/03) Based on the experience gained with data of Constellation #1 (Task 2) we have modified the secular variation model for Constellation #2. The revised model, called `swarm_11a_03.cof`, was derived in a similar way as the model `swarm_02a_03.cof`; however, the amplitude of the secular variation was increased. Figure 3.11 shows the Mauersberger-Lowes Spectrum of the secular variation of the new model in comparison with the previous model.

3.4.2 Design of a realistic high-degree crustal field model (model swarm(06a/04))

This section describes results obtained by Michael Purucker, NASA/GSFC, in collaboration with Jerome Dyment (IPGP) and Nils Olsen (DSRI).

Concept

The recovery of lithospheric field signals past degree 100 by the GFZ Group suggests that it is possible to recover signals to even higher degree. But our current model goes only to degree 110, and hence is inadequate for complete testing of these recovery techniques. Therefore, we have produced three new 'realistic' high-degree lithospheric field models, up to degree and order 199 that can be used to better assess ultimate signal recovery. There are two additional reasons for producing such high-degree models. First, such models can be used to determine the optimum E-W separation for satellites flying side-by-side. Second, these models can be used in the World Digital Magnetic Anomaly Map in areas of inadequate data coverage. The three models presented here are: 1) DAHP149, a degree 149 model of the oceanic remanence field, 2) DAHP199, a degree 199 model of the oceanic remanence field, and 3) COAP199, a degree 199 model of the induced and remanent magnetic fields of the oceans and continents, constrained by MF-3.

Model building

DAHP149 We begin with a 1/2 degree grid (721x361) of vertically integrated remanent magnetization (A). This grid was developed by Dyment and Arkani-Hamed [1998] and was developed for oceanic crust based on an age map of the oceans, the relative motion of the plates, and the African Apparent Polar Wander Path. Neither satellite, shipborne, or aeromagnetic data was used in this initial compilation. However, the grid was subsequently calibrated against observations of the satellite anomaly field in the North Atlantic, and subsequently, in the South Atlantic [Purucker and Dyment, 2000]. Because the magnetization grid is not global, and continental crust is assigned a zero magnetization, ringing is a problem. The gridded data set is first Fourier-analyzed along lines of latitude, then longitude. A taper is applied to correct for latitudinal distribution, and the spherical harmonic coefficients are calculated. This is facilitated with a pre-existing look-up table which contains the Schmidt functions for all degrees of n and order m at a given colatitude. For this case, the calculation of the lookup table took several minutes, and the conversion to spherical harmonic coefficients look less than a minute. These spherical harmonics can then be recast in terms of a potential function V and the g's and h's extracted. This recasting operation again is facilitated by the creation of a lookup table of integrals (Schmidt function related), but on a finer mesh than the earlier lookup table. Calculation of this lookup table consumes in excess of 2 hours, and its application takes a few minutes/component. The procedures have been detailed in Appendix A of Dyment and Arkani-Hamed [1998], portions of which are extracted here.

The magnetic potential $V(\mathbf{r})$ at a point $\mathbf{r}$ with spherical coordinates r, θ, and ϕ (the radial distance from the Earth center, geographic colatitude, and east longitude) is given by

$$V(\mathbf{r}) = \int \mathbf{M}(\mathbf{r_o}) \cdot \nabla_o \frac{1}{|\mathbf{r} - \mathbf{r_o}|} d\mathbf{r_o}, \qquad \text{(A1)}$$

where $\mathbf{r_o}$ is a source point with spherical coordinates r_o, θ_o, and ϕ_o; ∇_o is the gradient operator in the $\mathbf{r_o}$ domain; and $\mathbf{M}(\mathbf{r_o})$ is the magnetization at $\mathbf{r_o}$ described by its components M^r, M^θ, and M^ϕ. Terms in (A1) are expanded in spherical harmonics as

$$\begin{bmatrix} M^r \\ M^\theta \\ M^\phi \end{bmatrix} = \sum_{n=0}^{N} \sum_{m=0}^{n} \left(\begin{bmatrix} M_{nm}^{r,e} \\ M_{nm}^{\theta,e} \\ M_{nm}^{\phi,e} \end{bmatrix} \cos m\phi_o + \begin{bmatrix} M_{nm}^{r,o} \\ M_{nm}^{\theta,o} \\ M_{nm}^{\phi,o} \end{bmatrix} \sin m\phi_o \right) P_n^m(\cos\theta_o), \qquad \text{(A2)}$$

$$\frac{1}{|\mathbf{r}-\mathbf{r_o}|} = \sum_{n=0}^{N} \sum_{m=0}^{n} \frac{r_o^n}{r^{n+1}} (\cos m\phi_o \cos m\phi + \sin m\phi_o \sin m\phi) P_n^m(\cos\theta_o) P_n^m(\cos\theta), \qquad \text{(A3)}$$

where N is the highest degree of harmonics retained and P_n^m is the Schmidt normalized associated Legendre function (the Schmidt function) of degree n and order m [*Chapman and Bartels*, 1962]. $M_{nm}^{r,e}$, $M_{nm}^{r,o}$, $M_{nm}^{\theta,e}$, $M_{nm}^{\theta,o}$, $M_{nm}^{\phi,e}$, and $M_{nm}^{\phi,o}$ are the spherical harmonic coefficients of M^r, M^θ, and M^ϕ. Here e denotes the "even" and o denotes the "odd" coefficients. Using these expressions and the orthogonality relations of the Schmidt functions, (A1) becomes

$$V(r,\theta,\phi) = \sum_{n=0}^{N} \sum_{m=0}^{n} \frac{1}{r^{n+1}} (V_{nm}^e \cos m\phi + V_{nm}^o \sin m\phi) P_n^m(\cos\theta), \qquad \text{(A4)}$$

where V_{nm}^e and V_{nm}^o are the spherical harmonic coefficients of V, defined as

$$\begin{bmatrix} V_{nm}^e \\ V_{nm}^o \end{bmatrix} = \frac{4\pi n}{2n+1} \int r_o^{n+1} \begin{bmatrix} M_{nm}^{r,e} \\ M_{nm}^{r,o} \end{bmatrix} dr_o + \sum_{k=0}^{N} \left(\begin{bmatrix} \xi_{nk}^{m,e} \\ \xi_{nk}^{m,o} \end{bmatrix} \int r_o^{n+1} \begin{bmatrix} M_{km}^{\theta,e} \\ M_{km}^{\theta,o} \end{bmatrix} dr_o \right) + \sum_{k=0}^{N} \left(m \begin{bmatrix} -\eta_{nk}^{m,o} \\ \eta_{nk}^{m,e} \end{bmatrix} \int r_o^{n+1} \begin{bmatrix} M_{km}^{\phi,o} \\ M_{km}^{\phi,e} \end{bmatrix} dr_o \right) \qquad \text{(A5)}$$

and $\xi_{nk}^{m,e}$, $\xi_{nk}^{m,o}$, $\eta_{nk}^{m,e}$, and $\eta_{nk}^{m,o}$ are defined as

$$\begin{bmatrix} \xi_{nk}^{m,e} \\ \xi_{nk}^{m,o} \end{bmatrix} = \pi \int_0^\pi P_k^m(\cos\theta_o) \left[\frac{d}{d\theta_o} P_n^m(\cos\theta_o) \right] \sin\theta_o d\theta_o \begin{bmatrix} 1+\delta^{m,0} \\ 1-\delta^{m,0} \end{bmatrix}, \qquad \text{(A6)}$$

$$\begin{bmatrix} \eta_{nk}^{m,e} \\ \eta_{nk}^{m,o} \end{bmatrix} = \pi \int_0^\pi P_k^m(\cos\theta_o) \left[\frac{1}{\sin\theta_o} P_n^m(\cos\theta_o) \right] \sin\theta_o d\theta_o \begin{bmatrix} 1+\delta^{m,0} \\ 1-\delta^{m,0} \end{bmatrix},$$

with $\delta^{n,m} = 0$ if $n \neq m$, $\delta^{n,m} = 1$ if $n = m$. The functions

$$\frac{d}{d\theta_o} P_n^m(\cos\theta_o), \quad \frac{1}{\sin\theta_o} P_n^m(\cos\theta_o)$$

are related to Schmidt functions of neighboring degrees and orders by recursion formulas [*Chapman and Bartels*, 1962]. The integrals in (A6) are computed by standard trapezoidal method, using a 0.1° interval

Figure 3.12: Details of procedure for producing high-degree models [Dyment and Arkani-Hamed, 1998].

DAHP199 Details of the DAHP199 model are identical with the DAHP149 model. The lookup table of integrals took in excess of 7 hours to compute, and the application to individual components takes about 20 minutes.

COAP199 The COAP199 model includes the oceanic remanence model as above. We also wanted to determine whether adding continental magnetizations would suppress the ringing in the DAHP models. So we added an induced magnetization model determined on a 0.5 degree grid to the oceanic remanent magnetization model. The induced magnetization model is based on 11562 dipoles located on an icosahedral tesselation, with an average spacing of 1.89 degrees (210 km), the current version of which is documented in Fox Maule et al. [2005]). The model is determined by iteration from a starting model defined by the crustal thickness and heat flow of the seismic tomography model 3SMAC [Nataf and Ricard, 1996]. After three iterations, residuals with respect to the MF-3 model [Maus et al., 2005] are generally less than 1 nT. This crustal thickness model is then converted to an integrated magnetization and added vectorially to the oceanic remanent model. The oceanic remanent model had first been removed from the MF-3 model prior to this iterative process.

Model evaluation

Power spectra of the new models, and of MF-3, are shown below. All of the new models have less power than MF-3, and hence may be scaled to fit its average power if desired. Our models have power at degrees less than 16, the MF-3 cutoff. In the case of the remanent magnetization model, this is because of the long-wavelengths associated with the Cretaceous quiet zone. In the case of the induced magnetization model, this is because of the long-wavelengths associated with the 3SMAC seismic tomographic model. The DAHP149 and DAHP 199 models are indistinguishable on the plot out through degree 75, then exhibit some divergence. The induced and remanent magnetization models do not fit seamlessly together, as shown by the dip in the spectra near Degree 90. The induced magnetization model is considerably less detailed than the remanent model, and we believe that this dip is a manifestation of that difference in detail between the models. Finally, it is believed that the lithospheric spectra should turn over somewhere in the degree range between 150 and 250. This may be what is seen around degree 180.

The COAP199 model captures many of the details of continental anomalies as seen from the MF-3 model at 400 km altitude.

Little difference can be seen in the fidelity of the oceanic stripes seen in the DAHP149 and DAHP199 model. A mask has been placed over the continental regions. Both models show striping well into the continents, reflecting the oceanic striping, and a consequence of the absence of magnetizations on the continents in these two models.

Finally, the coefficients of model COAP199 have been scaled up by a factor of 1.4 to bring its power in the degree range between $n = 20$ and 80 to the same level as model MF-3; the scaled model is called swarm(06a/04). Coefficients for $n < 30$ are taken from CM4.

Conclusions

The three models, when appropriately scaled, represent 'realistic' high degree lithospheric models which can be used to validate lithospheric recovery techniques, determine optimum separation distances for the constellation, and fill in holes in the Digital Magetic Anomaly Map of the World. Profitable areas of further work would involve further minimization of the ringing produced by the linear oceanic stripes, and minimizing any discontinuities and inconsistencies between the induced and remanent models.

3.4.3 Design of the Model of Mantle Conductivity

For considering induced field contributions in Constellation #1, a radially symmetric (1D) model of mantle conductivity was used, as described in Sabaka et al. [2002].

For Constellation #2 a more realistic model of mantle conductivity has been used for considering induced contributions due to magnetospheric sources (for induced contributions due to ionospheric sources the same model was used as for Constellation #1). The model includes the conductivity of the seawater and of some inhomogenities in the deep mantle. The model consists of: 1) an inhomogeneous conducting

surface shell; 2) three local conductors of 0.04 S/m running from the bottom of the shell down to 400 km depth; 3) a deep-seated regional conductor of 1 S/m running from 400 km depth down to 700 km. The local and regional conductors reside in a radially symmetric 1D section which consists of a relatively resistive 400 km layer of 0.004 S/m, a 300 km thick transition layer of 0.04 S/m, and an inner uniform sphere of 2 S/m.

The surface shell approximates the nonuniform distribution of the conductance in the oceans and at the continents. The conductance of the shell is chosen to be as realistic as possible and includes contributions from sea water and from sediments. The conductance of the sea water has been derived from the global $5' \times 5'$ NOAA ETOPO map of bathymetry, multiplying the water depth by a mean seawater conductivity. Note that the seawater conductivity varies between 3 and 4 S/m, depending for example on salinity and temperature. We used a mean value of 3.2 S/m; the errors introduced by deviations from that value are considered to be smaller than those due to insufficient knowledge of mantle conductivity. The conductance of the sediments has been derived from the global sediment thickness given by the $1° \times 1°$ map of Laske and Masters [1997] by using a heuristic procedure similar to that described in Everett et al. [2003]. Figure 3.16 shows the various layers of the adopted conductivity model. The top panel presents the adopted surface shell conductance. It is seen that the conductance varies from tens of S inland up to 35000 S in the oceans.

Two local conductors of horizontal size 600×1200 km^2 describe hypothetic plumes under the Baikal rift and under Hawaii [Constable and Heinson, 2004]; the third conductor of size of 600×3000 km^2 represents a hypothetical subduction zone along the western margin of South America. This part of the model is shown in the middle panel of the Figure.

Finally, the deep-seated large scale structure describing the hypothetical conductor beneath the Pacific Ocean plate is shown in the bottom panel of the Figure.

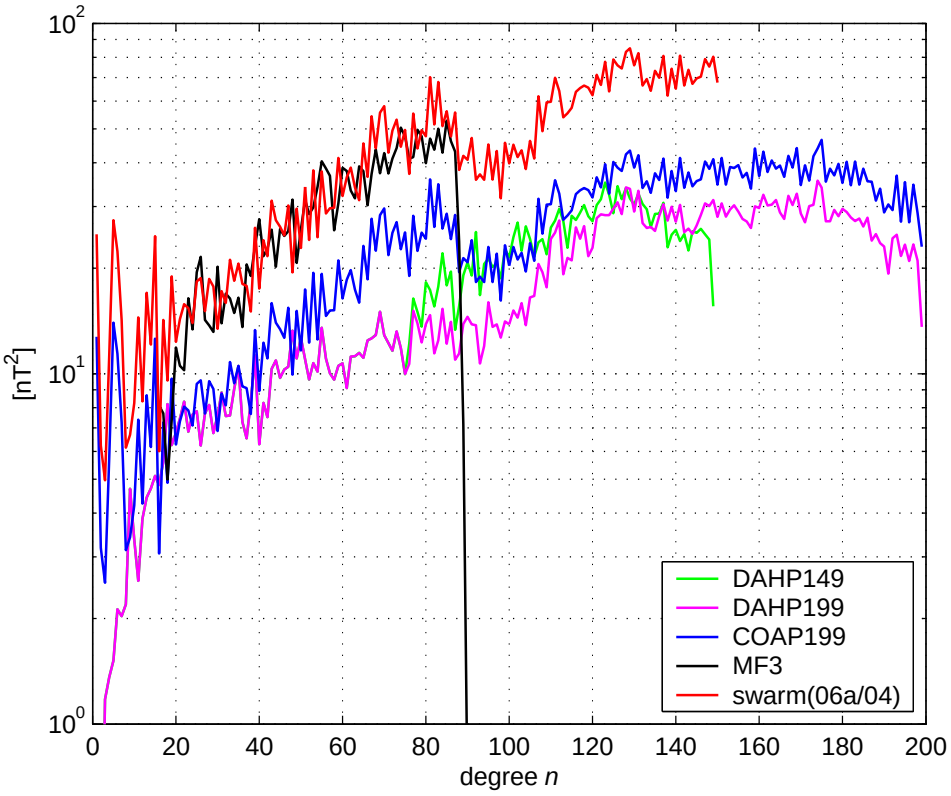

Figure 3.13: Power spectra of the three new high degree models (DAHP149 and DAHP199 are in green and magenta, respectively, COAP199 is in blue), in comparison with MF-3 (in black) and the final model swarm(06a/04) (in red).

The model was discretized in vertical direction into 4 inhomogeneous spherical sublayers of thickness 1 km, 150, 250, and 300 km, respectively. Each spherical sublayer was discretized in horizontal direction in 180×90 cells of size $2^\circ \times 2^\circ$.

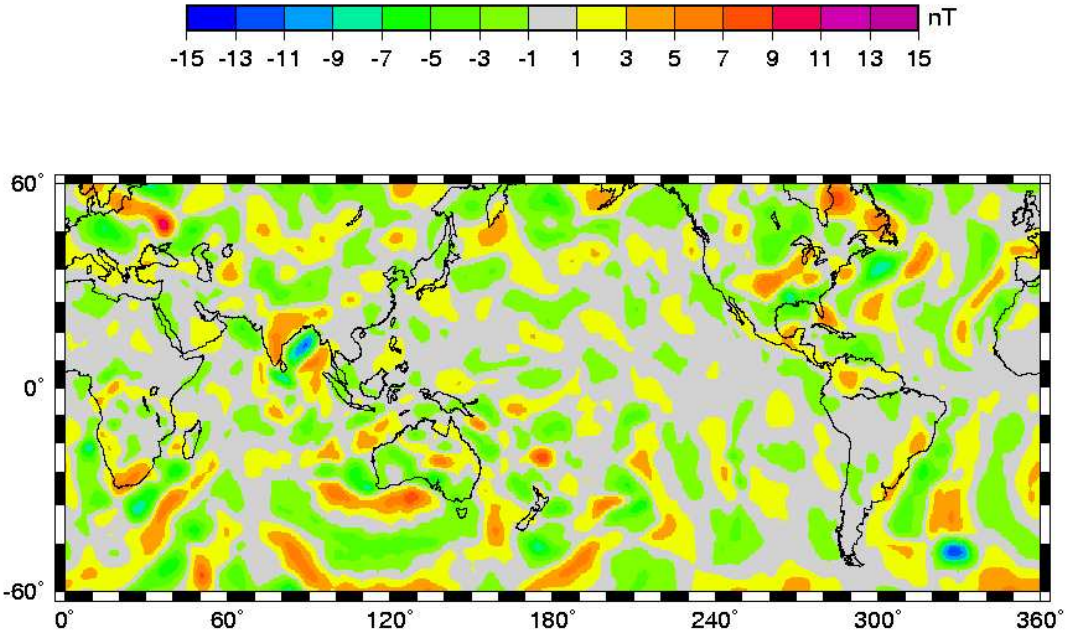

Figure 3.14: Vertical (Z) field from degrees 16-200 for COAP199 high degree model at 400 km altitude.

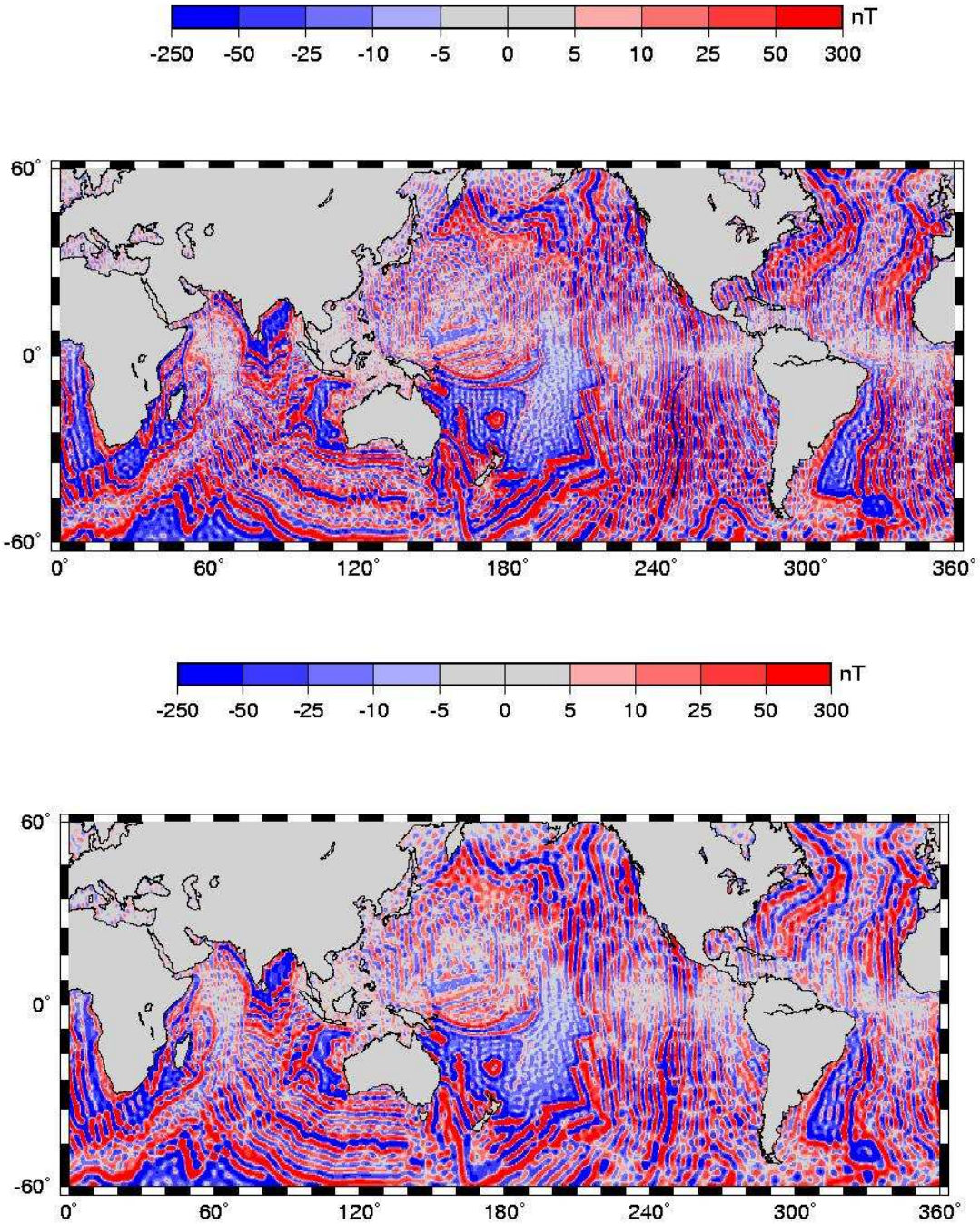

Figure 3.15: Vertical(Z) field from all degrees for DAHP149 (top) and DAHP149 (bottom) high degree models at 5 km altitude.

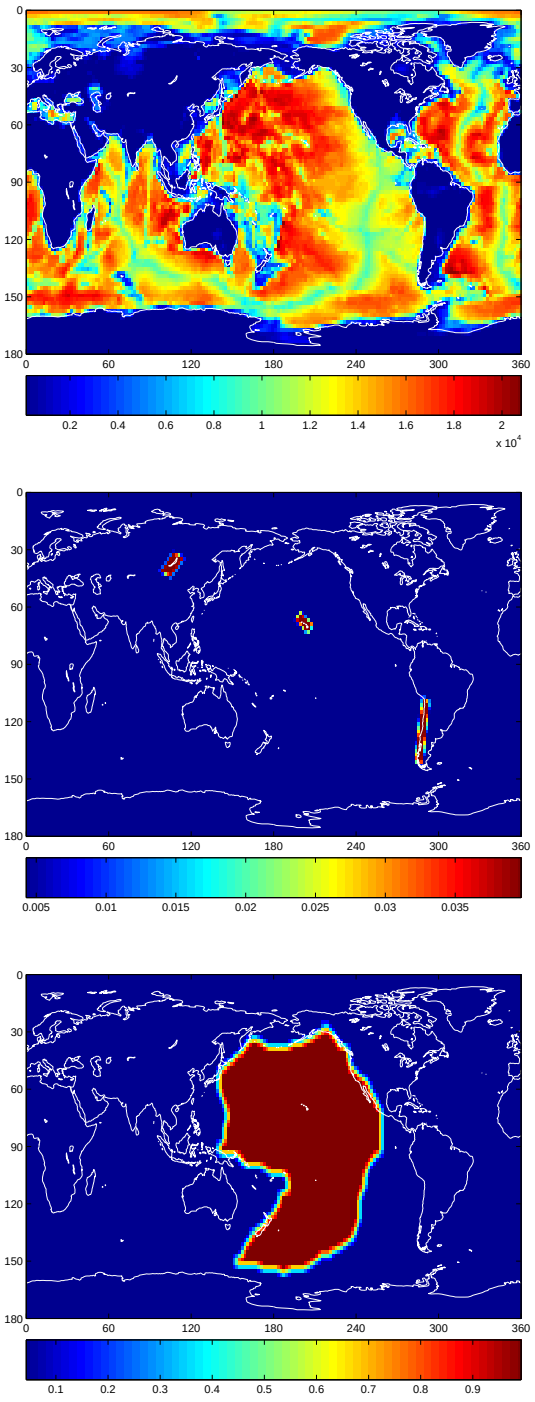

Figure 3.16: Top: Surface shell conductance in units of S. Middle: Conductivity [S/m] at depths from 1 km down to 400 km. Bottom: Conductivity [S/m] at depths from 400 km down to 700 km.

3.5 Magnetic and Electric Field Generation

Figure 3.17 shows a flow chart of the magnetic and electric field generation.

3.5.1 Magnetic Field due to Main Sources – Constellation #1

Magnetic field values are calculated at the time (1 min sampling rate) and satellite positions of the orbit files generated as described in the previous section. We used the 4th generation of the *Comprehensive Model* (CM4) for this task [Sabaka et al., 2002, Sabaka and Olsen, 2003], called CM4 (version CM3e-J_2). This model provides the magnetic field contribution of the core (up to spherical harmonic degree/order $n = 13$), crust (static field, up to $n = 65$), ionosphere, magnetosphere, coupling currents (coupling the ionosphere and magnetosphere) and secondary, Earth-induced contributions.

In order to include magnetic field contributions of smaller scale than currently modeled by CM4, the core and lithospheric field parts of CM4 are augmented by contributions from a synthetic model, as described below.

In following we summarize the various field contributions and how they are parameterized; details can be found in Sabaka et al. [2002], Sabaka and Olsen [2003]:

Core Field and Secular Variation

The core field and its time change is described in CM4 by Spherical Harmonics up to $n = 13$, the time variation of the Gauss coefficients is described by means of Cubic B-splines with a knot separation of 2.5 years. Secular variation for $n = 14 - 19$ is assumed to vary linearly in time and is taken from the synthetic model `swarm_02a_03.cof`, as described in section 3.4.1.

Crustal Field

We do not directly use the crustal field as given by CM4 (which covers $n = 14{-}65$), but use the coefficients of the merged model `swarm_02a_03.cof`, described in Section 3.4.1. Crustal field contributions up to $n = 29$ are found by a spherical harmonic synthesis for each satellite position, while contributions from $n = 30 - 120$ are found using linear three-dimensional interpolation from a $\Delta r = 30$ km $\times \Delta\theta = 0.25° \times \Delta\phi = 0.25°$ grid, as described in Section 2.4.

Magnetospheric Field

The primary magnetospheric field is described in CM4 by a spherical harmonic expansion in dipole-latitude and magnetic local time (MLT) using terms up to $n = 12$ (but not all corresponding orders m are included). Each coefficient has daily (24 h, 12 h, 8 h and 6 h) and seasonal (annual and semi-annual) variations. In addition, coefficients with $n = 1$ are modulated by the Dst index; values of Dst for the period of the simulated *Swarm* mission (1997-2001) are available at ftp.spacecenter.dk/data/magnetic-satellites/Swarm/E2E/indices/Dst_1997-2001.dat.

Magnetospheric Field, induced contribution

Secondary, induced, contributions are considered using a 1D model of electrical conductivity of the mantle.

Ionospheric Field

The primary ionospheric field is described by a spherical harmonic expansion in Quasi-Dipole (QD) coordinates [Richmond, 1995], to take into account the influence of the main field on ionospheric currents. As for the magnetospheric field, each coefficient contains daily (24 h, 12 h, 8 h and 6 h) and seasonal (annual and semi-annual) variations. In addition, all coefficients are scaled by daily values of solar flux $F_{10.7}$ (daily values are used to introduce some day-to-day variability of the ionospheric field); these values are available at ftp.spacecenter.dk/data/magnetic-satellites/Swarm/E2E/indices/F10.7_daily_1996-2002.dat.

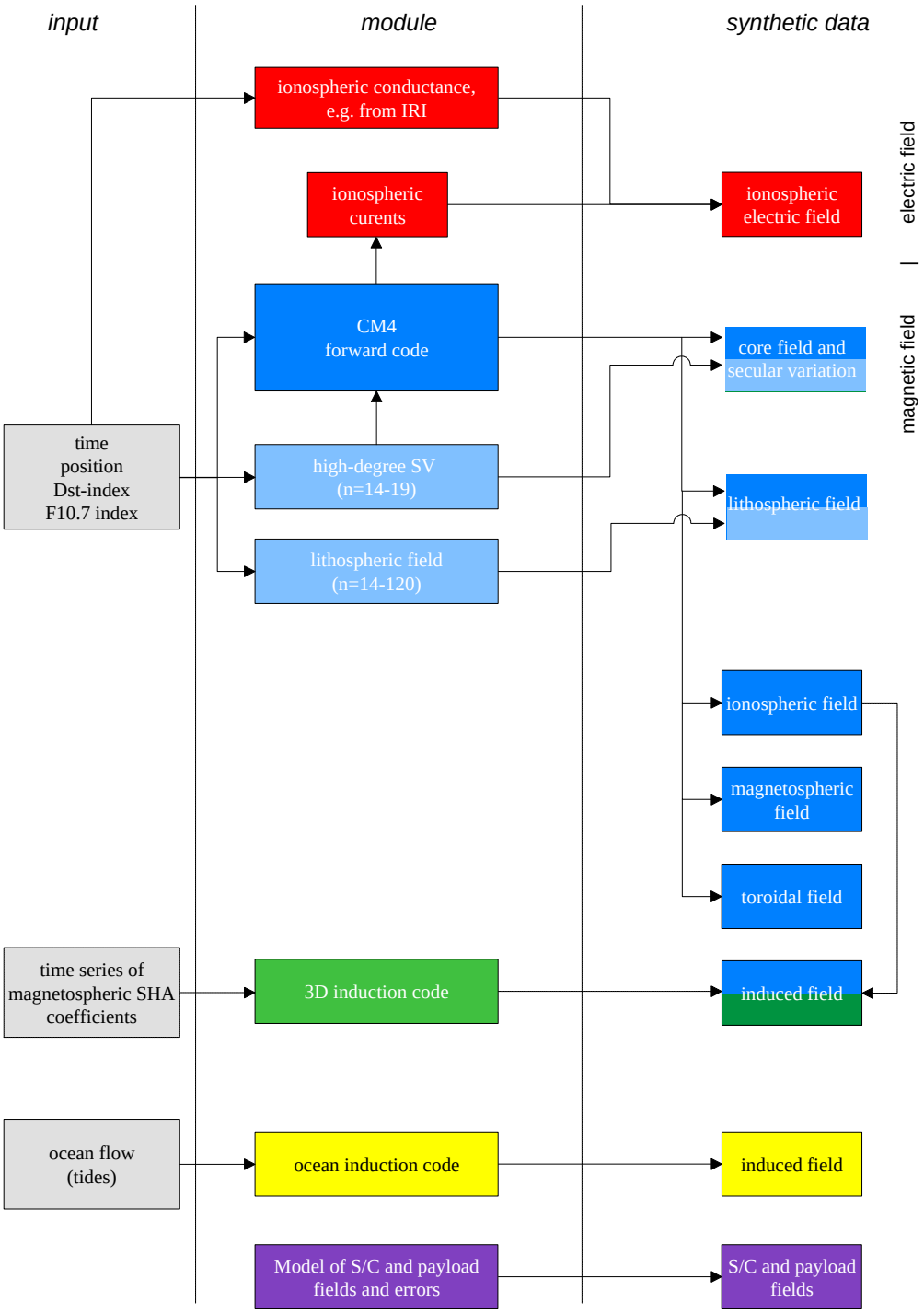

Figure 3.17: Generation of synthetic magnetic and electric field data. The different colors refer to the various data generation modules and data products.

Ionospheric Field, induced contributions

These are considered using a 1D model of mantle conductivity.

Toroidal field

The toroidal field is due to electric currents at satellite altitude. As for the ionospheric contribution, the toroidal field is modeled by a spherical harmonic expansion in QD coordinates, and contains a seasonal and LT dependency. Note that B_r of the toroidal field is zero by design.

Data availability

1 min values Synthetic data for the first constellation (1 min sampling rate) are available as daily files (each containing a header of 5 lines plus 1440 data lines corresponding to the 1440 minutes of one day) at ftp.spacecenter.dk/data/magnetic-satellites/Swarm/E2E/constellation_1/1min/; data for other constellations will be added at a later time. The filename follows the naming scheme `swarm4_1_971201.dat` which means data of satellite swarm4, Constellation #1, and for December 1, 1997. The contents of the various columns is shown in Table 3.4. To get a realistic magnetic field reading all these contributions have to be added up.

column 1	time [MJD2000]	t
2-4	position [km, degrees, degrees]	(r, θ, ϕ)
5-7	main field + SV [nT]	(B_r, B_θ, B_ϕ)
8-10	crustal field [nT]	(B_r, B_θ, B_ϕ)
11-13	magnetospheric field [nT]	(B_r, B_θ, B_ϕ)
14-16	field induced by magnetospheric contributions [nT]	(B_r, B_θ, B_ϕ)
17-19	ionospheric field [nT]	(B_r, B_θ, B_ϕ)
20-22	field induced by ionospheric contributions [nT]	(B_r, B_θ, B_ϕ)
23-25	toroidal field [nT]	$(B_r = 0, B_\theta, B_\phi)$
26-28	unit vector of flight direction	(n_r, n_θ, n_ϕ)

Table 3.4: Contents of the daily files with synthetic magnetic field data

5 secs values At the *Swarm* working meeting on September 5, 2003, it was decided to provide 5 secs values in addition to the 1 min values, since it was found that lithospheric studies require a higher sampling rate. Synthetic data at 5 secs sampling rate are available at ftp.spacecenter.dk/data/magnetic-satellites/Swarm/E2E/constellation_1/5secs/. The naming scheme and file format follows that used for the 1 minute values.

3.5.2 Magnetic Field due to Main Sources – Constellation #2

The forward scheme of calculating synthetic values of the electric and magnetic field at *Swarm* positions follows closely that used for Constellation #1. However, there are four modifications:

- The amplitude of the secular variation signal has been increased;
- The magnetospheric field is described more realistically by determing its time-space structure on an hour-by-hour basis from worldwide distributed observatory data;
- A realistic 3D model of electrical conductivity of the crust and mantle is used to calculate the effect of secondary, Earth-induced, magnetic field contributions;
- Magnetic noise due to the space-craft and payload has been included.

In the following we discuss these changes to the forward scheme compared to the approach used for Task 2.

Core Field and Secular Variation

is taken from CM4 for Spherical Harmonics up to $n = 10$, the time variation of the Gauss coefficients is described by means of Cubic B-splines with a knot separation of 2.5 years. Secular variation for $n = 11 - 19$ is assumed to vary linearly in time and is taken from the synthetic model `swarm_11a_03.cof` that was derived in a similar way as the model `swarm_02a_03.cof` (cf. section 3.4.1).

Magnetospheric Field

The time-space structure of the magnetospheric field is described by a hour-by-hour spherical harmonic analysis of world-wide distributed observatory hourly mean values in dipole-latitude and magnetic local time (MLT). After removal of main field, secular variation and ionospheric (primary and induced) contributions as predicted by CM4 from the observatory hourly mean values, a spherical harmonic expansion of the horizontal components is performed and expansion coefficients of the external (magnetospheric) potential, $q_{n_\alpha}^{m_\alpha}(t)$ and $s_{n_\alpha}^{m_\alpha}(t)$ are estimated for $n_\alpha = 1 - 3$ and $m_\alpha = 0 - 1$. Separation of external and induced fields is done using a 1D model of electrical conductivity. These time series were then used as input for the calculation of secondary, induced, contributions, as described in the next section.

Magnetospheric Field, induced contribution

Secondary, induced, contributions are considered using a 3D model of electrical conductivity of the mantle. The procedure shown in Figure 3.18 has been used to produce magnetic fields due to magnetospheric sources at the orbits of the *Swarm* satellites for a given three-dimensional (3-D) spherical conductivity model of the Earth and for a given time series of hourly mean values of external (inducing) coefficients of the magnetic potential. It consists of the following steps:

1. Electromagnetic (EM) induction simulations are performed using a 3-D model of electrical conductivity (a description of the used model is given below) in the frequency domain for N_s logarithmically spaced frequencies, $f_j, j = 1, 2, ...N_s$, covering the frequency range from $f_1 = \frac{1}{P}$, where P is the mission duration (here P is equal to 5 years) to $f_{N_s} = \frac{1}{2\Delta t}$ (here Δt is equal to 1 hour). For each frequency the simulations are performed for a set of preselected elementary harmonics, $1_{n_\alpha}^{m_\alpha}, \alpha = 1, 2, ..., N_\epsilon$, of the external field (in our case $N_\epsilon = 9$ with $n_\alpha = 1 - 3, m_\alpha = 0 - 1$, as described in the previous section). To simulate the magnetic fields the frequency domain 3-D numerical solution, which is based on the fast integral equation approach, is used. Details of the solution can be found in Kuvshinov et al. [2002], Kuvshinov and Olsen [2005], Kuvshinov et al. [2005].

2. The external coefficients, $q_{n_\alpha}^{m_\alpha}(t)$ and $s_{n_\alpha}^{m_\alpha}(t)$ of the previous section are transformed from geomagnetic to geographic coordinates;

3. The time series of the resulting SHA coefficients are Fourier transformed to obtain complex coefficients $\epsilon_{n_\alpha}^{m_\alpha}(f_i)$ at a set of frequencies, $f_i, i = 1, 2, ..., N_d$, where $N_d = \frac{P}{2\Delta t}$.

4. For each elementary harmonic, $1_{n_\alpha}^{m_\alpha}$, and each frequency, f_j, a spherical harmonic analysis of B_r of the simulated induced part (from step 1) is performed, resulting in arrays of coefficients of the induced part of the potential, $I_{n_\alpha k}^{m_\alpha l}(f_j)$ for all harmonics up to degree N_ι (where N_ι is determined from the cosen horizontal discretization of the 3-D model. Here we used a value of $N_\iota = 45$).

5. The arrays $I_{n_\alpha k}^{m_\alpha l}(f_j)$ are spline interpolated from the coarse logarithmically spaced frequency set f_j to the actual (denser) frequency set f_i, and the resulting coefficients arrays $\iota_k^l(f_i)$ are calculated as

$$\iota_k^l(f_i) = \sum_{\alpha=1}^{N_\epsilon} I_{n_\alpha k}^{m_\alpha l}(f_i)\epsilon_{n_\alpha}^{m_\alpha}(f_i), \tag{3.1}$$

   for $k = 1, ..., N_\iota, l = -k, k + 1, ..., k$. This step gives frequency domain coefficients of the induced part of the potential produced by given external coefficients.

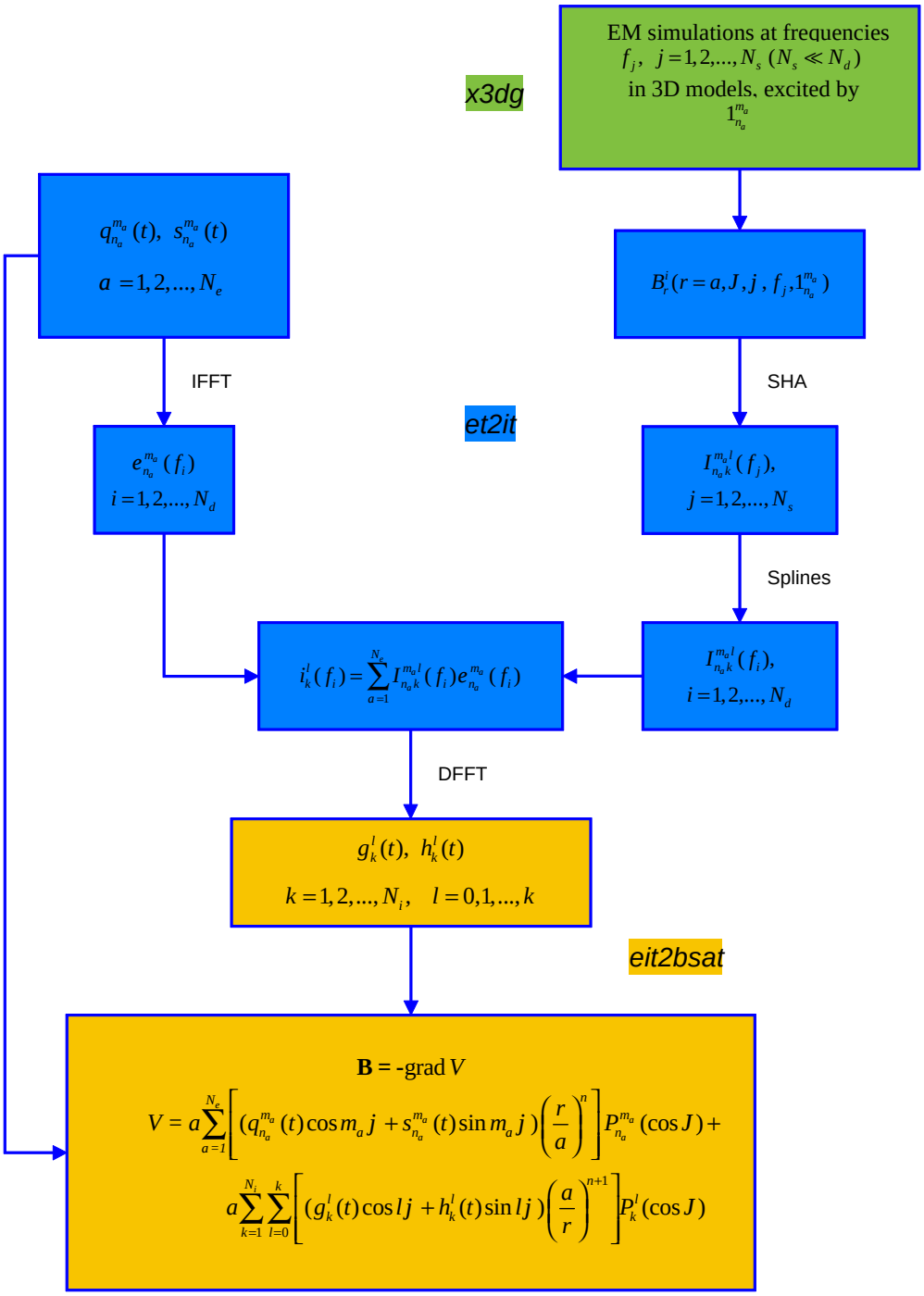

Figure 3.18: Scheme describing the calculation of induced field contributions. The different color refer to the various programs.

6. The coefficients $\iota_k^l(f)$ are Fourier transformed to the time domain, resulting in time series of hourly mean values of the coefficients g_k^l and h_k^l of the induced part of the potential at the surface of the Earth.

7. The obtained hourly mean values of coefficients of external and induced parts of the potential, $q_{n_\alpha}^{m_\alpha}$, $s_{n_\alpha}^{m_\alpha}$ and g_k^l and h_k^l, are linearly interpolated to obtain time series with sampling rate of 1-min and 5-secs, respectively.

8. Finally the magnetic fields at the position of the *Swarm* satellites, $r_i, \theta_i, \phi_i, t_i$, are obtained from the scalar magnetic potential as $\mathbf{B} = -\text{grad}\ V$, where the potential V is approximated by a spherical harmonic expansion

$$\begin{aligned} V &= a\sum_{\alpha=1}^{N_\epsilon}\left[(q_{n_\alpha}^{m_\alpha}(t_i)\cos m_\alpha\phi_i + s_{n_\alpha}^{m_\alpha}(t_i)\sin m_\alpha\phi_i)\left(\frac{r_i}{a}\right)^{n_\alpha}\right]P_{n_\alpha}^{m_\alpha}(\cos\theta_i) \\ &\quad + \sum_{k=1}^{N_\iota}\sum_{l=0}^{k}\left[(g_k^l(t_i)\cos l\phi_i + h_k^l(t_i)\sin l\phi_i)\left(\frac{a}{r_i}\right)^{k+1}\right]P_k^l(\cos\theta_i), \end{aligned} \tag{3.2}$$

with a= 6371.2 km as the mean Earth's radius, θ and ϕ as geographic colatitude and longitude and $P_{n_\alpha}^{m_\alpha}$, P_k^l as the associated Legendre functions.

Computational loads Three programs, **x3dg**, **et2it**, **eit2bsat**, have been implemented. They run successively. The first program, the 3D induction code **x3dg**, performs EM simulations (step 1 of the approach; see previous paragraph). Input for the code is a 3-D model of electrical conductivity (described below), a given frequency and spherical harmonic degree n and oder m (i.e., an elementary spherical harmonic excitation). Output is the magnetic field at the surface of the Earth.

This is the most complicated and time consuming part of the approach. Note that, if the calculations of the elementary spherical harmonics and frequencies have been done for a given 3-D conductivity model, one can calculate the magnetic signals for any *Swarm* constellation scenario.

Each simulation (for a given frequency and elementary spherical harmonic) takes about 1.1 hours of CPU on one processor of a SunFire V8800 and a mesh of ($N_\theta \times N_\phi \times N_r = 90 \times 180 \times 4$; see details of discretization in the next paragraph). Since the simulations were performed for $N_s = 41$ frequencies (9 frequencies per decade), and N_ϵ=9 elementary harmonics, the overall time for this part of the approach on one processor takes 1.1 hours $\times 41 \times 9 = 405$ hours. 5 CPU were used, so this task was done in about 80 hours.

Steps (2)-(6) are done using the program **et2it**. Input is mission life time (5 years), time series of hourly mean values of external coefficients, $q_{n_\alpha}^{m_\alpha}$ and $s_{n_\alpha}^{m_\alpha}$, for the whole mission, maximum degree of harmonics, N_ι, of the induced part, and the simulated vertical magnetic field on the surface of the Earth as given by **x3dg**. Output is time series of hourly mean values of the internal, induced, coefficients, g_k^l and h_k^l.

The production of 5 years of time series of i_k^l up to degree $N_\iota = 45$ the code **et2it** took 12 hours of CPU on one processor of a SunFire V8800.

Steps (7)-(8) are done using the program **eit2bsat**. Input is time series of hourly mean values of the external coefficients, $q_{n_\alpha}^{m_\alpha}$ and $s_{n_\alpha}^{m_\alpha}$, and of the induced coefficients g_k^l and h_k^l. Output is the three components of the magnetic fields at each point of the orbits of the *Swarm* satellites with 1 min or 5 sec sampling rate.

To produce magnetic fields for 6 satellites and for a 5 year mission time with the program **eit2bsat** takes 6 hours of CPU for 1 min discretization and 72 hours of CPU for 5 sec discretization on one processor of a SunFire V8800.

Data availability

Data of Constellation #2 are available as daily files at ftp.spacecenter.dk/data/magnetic-satellites/Swarm/E2E/constellation_2/. Data with 1 min sampling rate are provided as text files (gzipped) and in Common Data Format (CDF) at ./1min. 5-second values are distributed in CDF

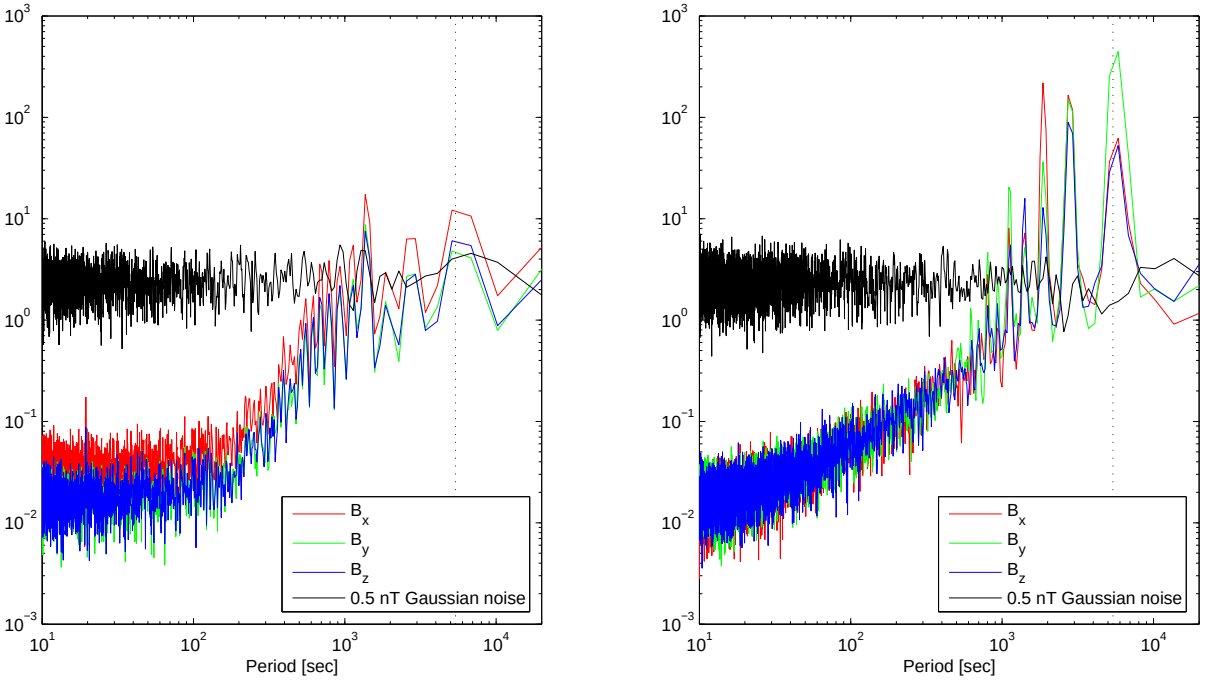

Figure 3.19: Sample spectrum of space-craft and payload noise. Also shown is the spectrum of a sample of Gaussian noise of 0.5 nT amplitude. The vertical dashed line indicates orbit period. Left: Noise model used in this study, based on scaled CHAMP data. Right: Noise model from one of the two *Swarm* System Simulator Studies.

only at ./5sec The filename follows the naming scheme `swarm4_2_971201.cdf` which means data of satellite swarm4, Constellation #2, and for December 1, 1997.

Computation takes about 1.5 hours of CPU on a SunFire V8800 (with 4 Ultra Sparc 3 CPU's and 8 GB RAM) per satellite and year for the 1 minute sampling rate, and about 30 hours CPU for the 5 second values. The data are provided as text files (gzipped) and in Common Data Format (CDF).

3.5.3 Magnetic Field due to Ocean Tides

Data are provided as daily files (1-min sampling rate) with 34 columns, containing time t [MJD2000] in the first column, position (r, θ, ϕ), and the magnetic field components (B_r, B_θ, B_ϕ) for the 10 tidal modes $(M_2, S_2, N_2, K_2, K_1, O_1, P_1, Q_1, M_f$ and $M_m)$ provided by Erofeeva and Egbert [2002]. These files will be made available at ftp.spacecenter.dk/data/magnetic-satellites/Swarm/E2E/constellation_1/ocean_tides/.

These magnetic fields are derived by model calculations that were performed using the models of water transports ($1/4° \times 1/4°$ resolution) of TPXO.6.1 [Erofeeva and Egbert, 2002]. The 3D model of electrical conductivity consists of a inhomogeneous surface shell with a 1-D mantle underneath. The calculations were performed on a $1° \times 1°$ grid using the scheme described in Kuvshinov and Olsen [2005]. Upward propagation from ground to satellite was done using a spherical harmonic expansion up to $n = 45$.

3.5.4 Space-craft and Payload Noise

Models of payload and S/C noise provided by the industrial teams were not yet of the desired accuracy when the production of the synthetic data of Constellation #2 started (December 2003). As a work-around, we decided to use synthetic noise based on CHAMP experience and *Swarm* specifications. We designed random noise that is correlated in time, but uncorrelated among the components. The standard

deviation of the noise is (0.1, 0.07, 0.07) nT for (B_r, B_θ, B_ϕ), in agreement with *Swarm* performance requirements. The left panel of Figure 3.19 shows a sample spectrum of the noise; the right part shows the spectrum of the noise model that was provided by industry in Spring 2004. The close agreement between the two spectra confirm the validy of using the scaled CHAMP spectra for the present study.

3.5.5 Electric Currents and Fields

Swarm will also measure the electric field, helping to better separate the effects of ionospheric currents from contributions of internal magnetic sources.

In the forward modelling we have to make sure that the generated electric fields are consistent with the magnetic field values caused by ionospheric currents, as described in section 3.5.1. For that reason we make use of the ionospheric current systems, on which the associated magnetic field part in CM4 is based. The basic equation for the currents density, $\mathbf{j}$, in the ionosphere is:

$$\mathbf{j} = \underline{\underline{\sigma}}(\mathbf{E} + \mathbf{v} \times \mathbf{B}) \tag{3.3}$$

where $\underline{\underline{\sigma}}$ is the conductivity tensor, $\mathbf{E}$ the electric field, $\mathbf{v}$ the plasma velocity and $\mathbf{B}$ the ambient magnetic field. The sum of both terms in the parenthesis, the intrinsic electric field and the part caused by plasma motion can be considered as the effective electric field. The conductivity is highly anisotropic. In the direction along the field lines the conductivity is almost perfect. For that reason we may consider the lines of forces as equipotential lines. In the ionospheric E-layer (centred around 110 km) we find the Pedersen conductivity, σ_P, which supports currents along the direction of the electric field and the Hall conductivity, σ_H, allowing currents to flow perpendicular to the electric and the magnetic field. It is just this Hall current which is of interest here. Under the reasonable assumption that conductivity gradients are not too large, Hall currents close entirely in the ionosphere thus producing a poloidal magnetic field. The combined field-aligned – Pedersen current circuit, on the other hand, gives rise to toroidal magnetic fields. Only the former field can be described in terms of a scalar potential. Since the magnetic field part in CM4 related to ionospheric currents (Sec. 3.5.1) is derived from a scalar potential, it is justified to conclude that the underlying currents are of the Hall type.

Hall currents are confined in the ionosphere to a layer of some 20 km in vertical thickness. Since the satellites are more than 300 km above the E-layer, we may use height-integrated quantities for the current density, $\mathbf{J}$, and the conductivity, Σ. The basic equation for the Hall current density, $\mathbf{J}_H$, is:

$$\mathbf{J}_H = -\Sigma_H \frac{\mathbf{E} \times \mathbf{B}}{B}. \tag{3.4}$$

Hereafter we drop the subscript $_H$ and consider only the Hall current and conductance. The above equation can be solved for the electric field, $\mathbf{E}$:

$$\mathbf{E} = \frac{1}{B\Sigma}\mathbf{J} \times \mathbf{B}. \tag{3.5}$$

The current density is given in the NEC system. Since the currents are confined to the E-layer, the vertical component, J_Z, is zero. From the above equation we can derive the electric field in the NEC frame. For the mapping of the electric field from the ionosphere to the satellite altitude it is more appropriate to have it in the Mean-Field-Aligned (MFA) frame. This transformation comprises two successive rotations

$$E_{MFA} = R_y(-\beta) \cdot R_z(\alpha) \cdot E_{NEC} \tag{3.6}$$

with $\alpha = \text{atan2}(B_y, B_x)$ and $\beta = \text{atan}(\sqrt{B_x^2 + B_y^2}/B_z)$. The components of the E-field in the MFA frame (which is a right handed coordinate system) are termed E_Ψ, E_λ, $E_\parallel$. The third component is aligned with the magnetic field and is identically zero. The second component is pointing toward magnetic east and the first one completes the triad pointing outward.

A quantity in the equations that has not been considered so far is the Hall conductance, Σ. There are models for the spatial distribution of the ionospheric conductivity. For the purpose of this simulator it is, however, not recommended to make use of such sophisticated conductivity distributions, since the employed current patterns do not match, as expected, the patches of enhanced conductivity. For

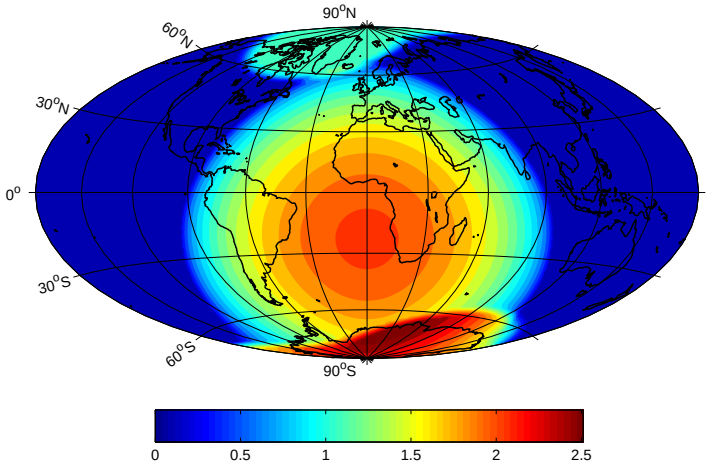

Figure 3.20: Distribution of height-integrated Hall conductivity in Siemens (S). In this representation local noon is in the centre of the map and the season is beginning of January.

that reason a rather general conductivity model is used. At mid and low latitudes the conductivity is controlled by the photo-ionisation, modulated in intensity by the short-wavelength solar flux. At polar regions, an additional ionisation by precipitating electrons has to be considered. The basic equation is, according to Robinson and Vondrak [1984]:

$$\Sigma = a\sqrt{c\cos\chi} + b \tag{3.7}$$

where χ is the solar zenith angle, a is a scaling factor, c represents the modulation of conductivity by the solar flux as given by the index F10.7 and b is an additive term. For $|\chi| > 90°$ (sun below horizon) the square root is set to zero. The factor $a = 0.2$ is chosen to get a representative conductance value at daytime. On the night side we take a value $b_n = 0.1$ S. The enhanced conductance at high latitude is accounted for by the additive term b_p. This term increases for dipole latitudes above 65° and stays constant towards the pole:

$b_p = 0$ to 1S	for 65° to 70° dip-latitude
$b_p = 1S$	for 70° to 90° dip-latitude.

The total additive term is $b = b_n + b_p$. Figure 3.20 shows the conductance distribution for northern winter conditions. At the sub-solar point we have the high conductivity. Even higher conductances are obtained during this season at the continuously sun-lit south pole where in addition ionisation by precipitating electrons is effective.

Electric Field Processing Steps We have described above how to determine the electric field in the ionosphere. For this study we want to generate the E-field readings at satellite orbit level. To obtain that we use the following procedure (cf. Figure 3.21):

- For a given satellite position we identify the intersecting magnetic field line and trace it down to the ionospheric E-layer. Since the orbits are fairly low, it is justified to use a dipole geometry for the mapping. The employed dipole has its pole at 11.2° colatitude and 289.3°E longitude.
- The satellite position has to be converted from geocentric into dipole coordinates. The footprint in the ionosphere of the intersecting field line can be found with the help of the equation

$$\sin^2\theta_{di} = \frac{r_i}{r_s}\sin^2\theta_{ds} \tag{3.8}$$

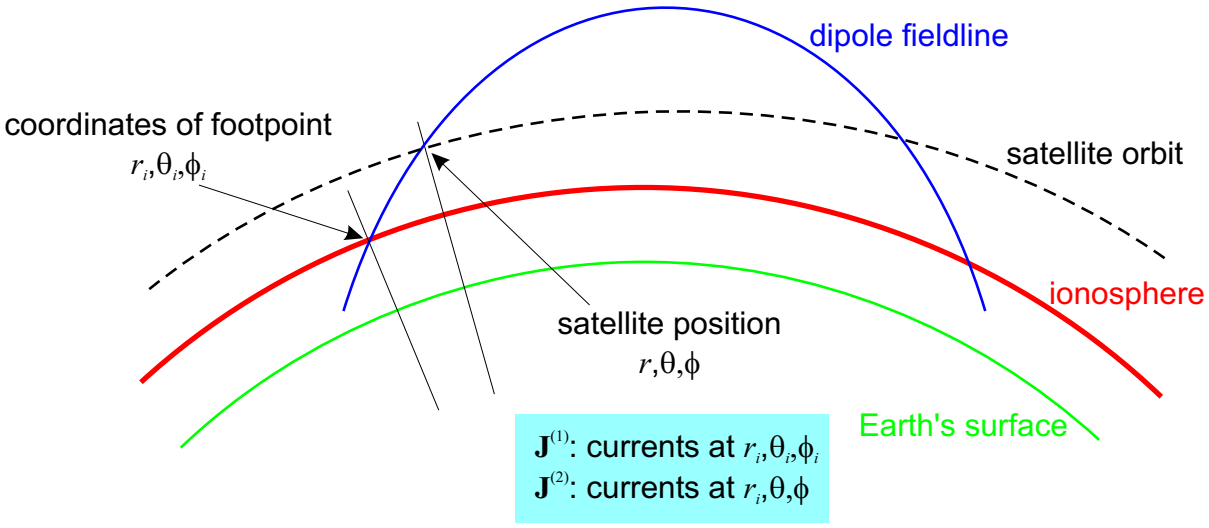

Figure 3.21: Scheme of the geometry used for calculating ionospheric currents

where θ_{di} and θ_{ds} are the dipole colatitudes in the ionosphere and at the satellite, and r_i and r_s the radial distances of the ionosphere and the satellite, respectively. The dipole longitude is the same at both levels. For the ionospheric radius we have taken into account the ellipsoidal shape of the Earth,

$$r_i = (a + 110\text{km})(1 - f\cos^2\theta) \tag{3.9}$$

with $a = 6378$km and $f = 1/298.25$.

- At the ionosphere the coordinates are converted back to geometric and the sheet current density, $\mathbf{J^{(1)}}$, is calculated according to the CM4 model. In addition, the sheet current density $\mathbf{J}^{(2)}$ of the location that crosses the ionosphere when going in radial direction from satellite position downward is provided, too.
- The calculation of the electric field, $\mathbf{E}$, in the ionosphere follows the procedure outlined above.
- Finally, the E-field from the ionosphere has to be mapped up to the satellite level. Since field lines are considered as equipotential lines, the orientation of the E-field in the MFA frame does not change. But due to the inflation of the magnetic field with altitude, also the E-field becomes weaker. The decrease is proportional to the increasing distance between adjacent field lines from the ionosphere to the satellite. For the eastward component we get:

$$E_{\lambda s} = E_{\lambda i}\left(\frac{\sin\theta_{di}}{\sin\theta_{ds}}\right)^3 \tag{3.10}$$

and for the outward component

$$E_{\Psi s} = E_{\Psi i}\cdot 2\left(\frac{\sin\theta_{di}}{\sin\theta_{ds}}\right)^3. \tag{3.11}$$

With the help of the described procedure the electric field components along the satellite track can be computed. The sheet current densities and E-field components are provided as daily files (5 secs sampling rate), with time t [MJD2000], position (r,θ,ϕ), $(J_r^{(1)}, J_\theta^{(1)}, J_\phi^{(1)})$, $(J_r^{(2)}, J_\theta^{(2)}, J_\phi^{(2)})$, $(E_{\Psi s}, E_{\lambda s})$ and will be made available at ftp.spacecenter.dk/data/magnetic-satellites/Swarm/E2E/constellation_1/currents_and_E-field/.

The electric field distribution calculated for the beginning of January 1997 is shown in Figure 3.22 on a world map. Results are presented independently for the ascending (left) and the descending (right) tracks. In the left plot, which is for a local time of 1700 hours, high electric fields occur in the northern

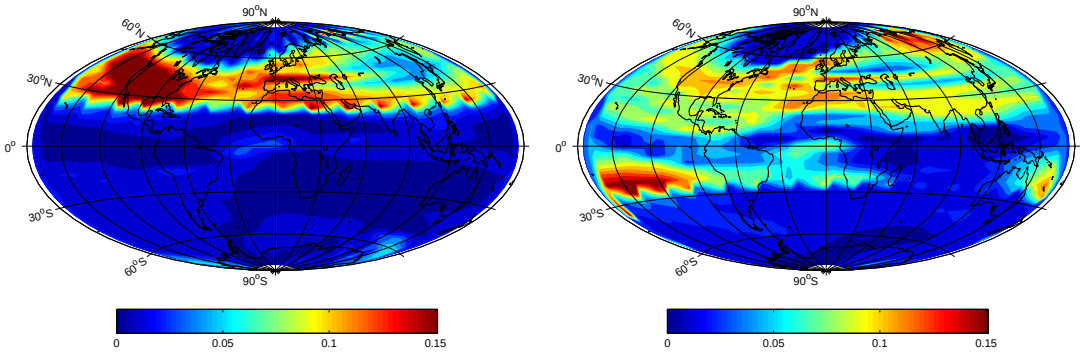

Figure 3.22: Global distribution of the derived electric field (in V/m), as seen by the satellite SW1 during the first days of January 1997. Left: ascending tracks, 1700 local time. Right: descending tracks, 0500 local time.

hemisphere where the conductivity is already quite low during that time of the day in winter, but the currents still have sizable strength. On the right plot, which is for 0500 LT, the E-field distribution is more homogeneous. In the polar regions CM4 does not represent the currents appropriately. Therefore, only insignificant E-fields appear at both poles.

3.6 Auxiliary Data

Geomagnetic indices Kp (three hourly values), Dst (hourly values), and solar flux $F_{10.7}$ (daily values) for the period of the simulated mission (1997-2001) are made available at ftp.spacecenter.dk/data/magnetic-satellites/Swarm/E2E/indices/. Since hourly mean values of the Dst-index have been used for generating the synthetic data as described in section 3.5.1, we decided *not* to use Dst in the inversion, but to estimate an equivalent to Dst, called RC, from the synthetic observatory data. Therefore hourly values of RC have been calculated from the synthetic observatory data using the approach described in Olsen [2002] and are available at ftp.spacecenter.dk/data/magnetic-satellites/Swarm/E2E/indices/RC_swarm.dat. Figure 3.23 shows the difference between Dst (obtained from the "true" observatory data) and RC (obtained from the synthetic observatory data) for the years 1997-2001. The reason for the difference is the fact that any daily variation, and modulation of the daily variation with season, has been subtracted from the observatory data prior to the calculation of Dst, since it is assumed that such variations are of ionospheric (i.e., non-magnetospheric) origin. This, however, is only partly true (about 10-20% of the daily variation is now believed to be of magnetospheric origin), and hence RC is probably a better description of magnetospheric contributions, at least in the night-side sector.

Synthetic observatory hourly mean values of 88 observatories are available at ftp.spacecenter.dk/data/magnetic-satellites/Swarm/E2E/synthetic_obs_data/ and are provided as yearly files in the usual WDC hourly mean values format. All source contributions as predicted by CM4 have been used.

These hourly values are calculated at the center of the UT hour and are thus representative for 00:30 UT, 01:30 UT, 02:30 UT,...23:30 UT. The locations of the 'synthetic' observatories are the same as those which were collecting and reporting data for the 1997-2001 period, and for which biases can be calculated. `swarm_02a_03.cof` was used to evaluate high degree secular variation ($n = 14 - 19$). The J_2 coefficient set (coefficient file: `umdl.CM3e-J_2`) of the Comprehensive model was used for all other fields (static through degree $n = 65$, observatory biases, ionospheric primary and induced, magnetospheric primary and induced). The output is local magnetic components X, Y, and Z in the geodetic coordinate frame. As for the synthetic satellite data, daily values of $F_{10.7}$ are used to modulate the ionospheric field. The time range of the data is from January 1, 1997 to December 31, 2001.

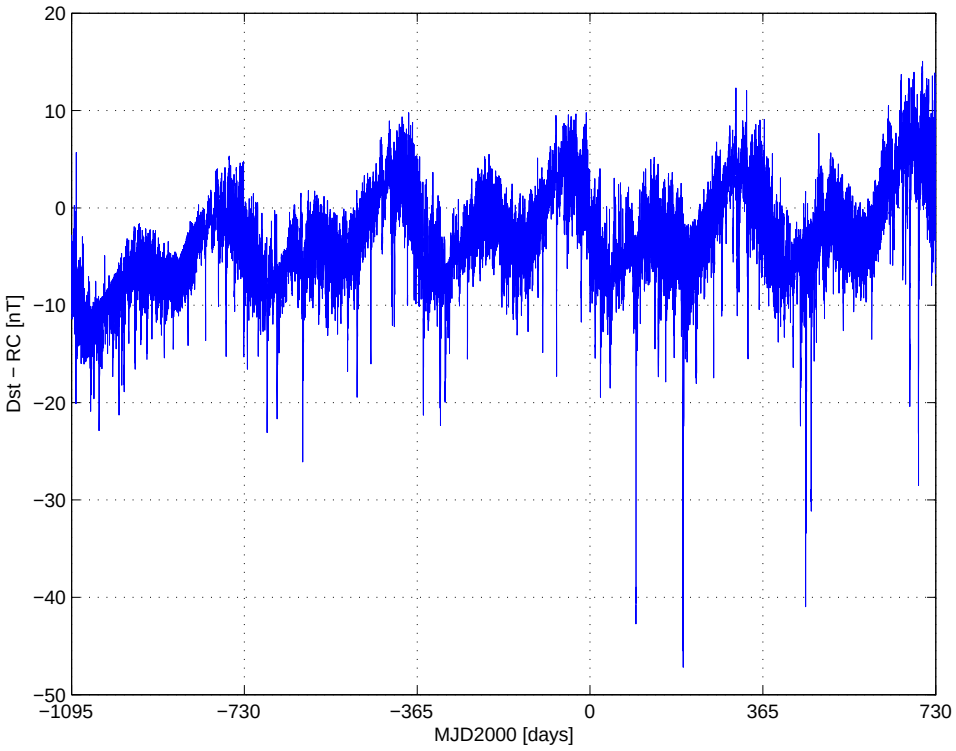

Figure 3.23: Difference between Dst and RC.

Magnetospheric expansion coefficients Times series (1 hour sampling rate) of magnetospheric expansion coefficients $\epsilon_n^m(t)$, to be used in the induction part of this study, are available at ftp.spacecenter.dk/data/magnetic-satellites/Swarm/E2E/indices/magnetospheric_coefficients_1997-2000.dat.gz. These coefficients describe the magnetospheric magnetic field $\mathbf{B}^{\text{mag}} = -\text{grad}\, V^{\text{mag}}$ with

$$V^{\text{mag}}(t) = a \sum_{n,m} \left(q_n^m(t) \cos m\phi_d + s_n^m(t) \sin m\phi_d\right) \left(\frac{r}{a}\right)^n P_n^m(\cos\theta_d)$$

where θ_d and ϕ_d are dipole co-latitude and longitude, respectively.

Main field coefficients Time series (1997 - 2002 in steps of 1 month) of the main field coefficients ($n = 1 - 19$) that were used to create the data are available at ftp.spacecenter.dk/data/magnetic-satellites/Swarm/E2E/tools/swarm_MF_models.txt. Crustal field coefficients (terms with $n > 13$) and the linearly changing secular variation terms (for $n = 14 - 19$) are provided in the file ftp.spacecenter.dk/data/magnetic-satellites/Swarm/E2E/tools/swarm_02a_03.cof.

Chapter 4

In-flight Calibration and Alignment of the Vector Magnetometer

This section describes the in-flight calibration and alignment of the *Swarm* magnetometers. Involved in this task is the working package WP-3100 "In-Flight Calibration".

Section 4.1 describes the the calibration of the Vector Fluxgate Magnetometer (VFM) by comparing its output with the level 1b scalar field data of the Absolute Scalar Magnetometer (ASM). Section 4.2 presents the alignment of the magnetometer, i.e., the determination of the rotation between the coordinate frame of the magnetometer and that of the attitude sensor. The approaches described here follow closely those developed for the Ørsted and CHAMP missions [Olsen et al., 2003a, cf.]. However, only single-satellite approaches have been used; the development of multi-satellite approaches for satellite-satellite inter-calibration is beyond the topic of the present study but is suggested for future work.

4.1 In-Flight Calibration of the VFM

4.1.1 The VFM vector magnetometer – a linear instrument

Experienced with Ørsted and CHAMP has shown that the VFM vector magnetometer is a linear instrument. Hence, the magnetometer output $\mathbf{F} = (F_1, F_2, F_3)^T$ (in engineering units, eu) is connected to the applied magnetic field $\mathbf{B}_{\rm VFM} = (B_1, B_2, B_3)^T$ (in the orthogonal magnetometer coordinate system) according to

$$\mathbf{F} = \underline{\underline{\mathbf{S}}} \cdot \underline{\underline{\mathbf{P}}} \cdot \mathbf{B}_{\rm VFM} + \mathbf{b} \tag{4.1}$$

where

$$\mathbf{b} = \begin{pmatrix} b_1 \\ b_2 \\ b_3 \end{pmatrix} \tag{4.2}$$

is the offset vector (in eu),

$$\underline{\underline{\mathbf{S}}} = \begin{pmatrix} S_1 & 0 & 0 \\ 0 & S_2 & 0 \\ 0 & 0 & S_3 \end{pmatrix} \tag{4.3}$$

is the (diagonal) matrix of sensitivities (in eu/nT), and

$$\underline{\underline{\mathbf{P}}} = \begin{pmatrix} 1 & 0 & 0 \\ -\sin u_1 & \cos u_1 & 0 \\ \sin u_2 & \sin u_3 & \sqrt{(1 - \sin^2 u_2 - \sin^2 u_3)} \end{pmatrix} \tag{4.4}$$

is a matrix which transforms a vector from the orthogonal magnetic axes coordinate system to the non-orthogonal magnetic sensor axes coordinate system. The left part of Figure 4.1 shows the geometry used for this definition of the non-orthogonalities.

Knowledge of the 9 parameters b_i, S_i, u_i, $i = 1, \ldots, 3$ are sufficient for describing the magnetometer. However, three additional parameters, the Euler angles α, β, γ, are necessary to transform the magnetic field vector from the (unknown) orthogonal coordinate system of the VFM to a (known) orthogonal coordinate system, which here is taken as the Common Reference Frame (CRF) of the attitude sensor (ASC). This transformation is a "1-2-3" rotation:

$$\underline{\underline{R}} = \begin{pmatrix} 1 & 0 & 0 \\ 0 & \cos\alpha & -\sin\alpha \\ 0 & \sin\alpha & \cos\alpha \end{pmatrix} \begin{pmatrix} \cos\beta & 0 & \sin\beta \\ 0 & 1 & 0 \\ -\sin\beta & 0 & \cos\beta \end{pmatrix} \begin{pmatrix} \cos\gamma & -\sin\gamma & 0 \\ \sin\gamma & \cos\gamma & 0 \\ 0 & 0 & 1 \end{pmatrix} \tag{4.5}$$

Once the 12 calibration parameters are known, the magnetic field in the VFM and CRF coordinate system, respectively, can be determined from the sensor output according to

$$\mathbf{B}_{\rm VFM} = \underline{\underline{\mathbf{P}}}^{-1} \cdot \underline{\underline{\mathbf{S}}}^{-1} \cdot (\mathbf{F} - \mathbf{b}) \tag{4.6}$$

$$\mathbf{B}_{\rm CRF} = \underline{\underline{\mathbf{R}}}^{-1} \cdot \mathbf{B}_{\rm VFM} = \underline{\underline{\mathbf{R}}}^{-1} \cdot \underline{\underline{\mathbf{P}}}^{-1} \cdot \underline{\underline{\mathbf{S}}}^{-1} \cdot (\mathbf{F} - \mathbf{b}) \tag{4.7}$$

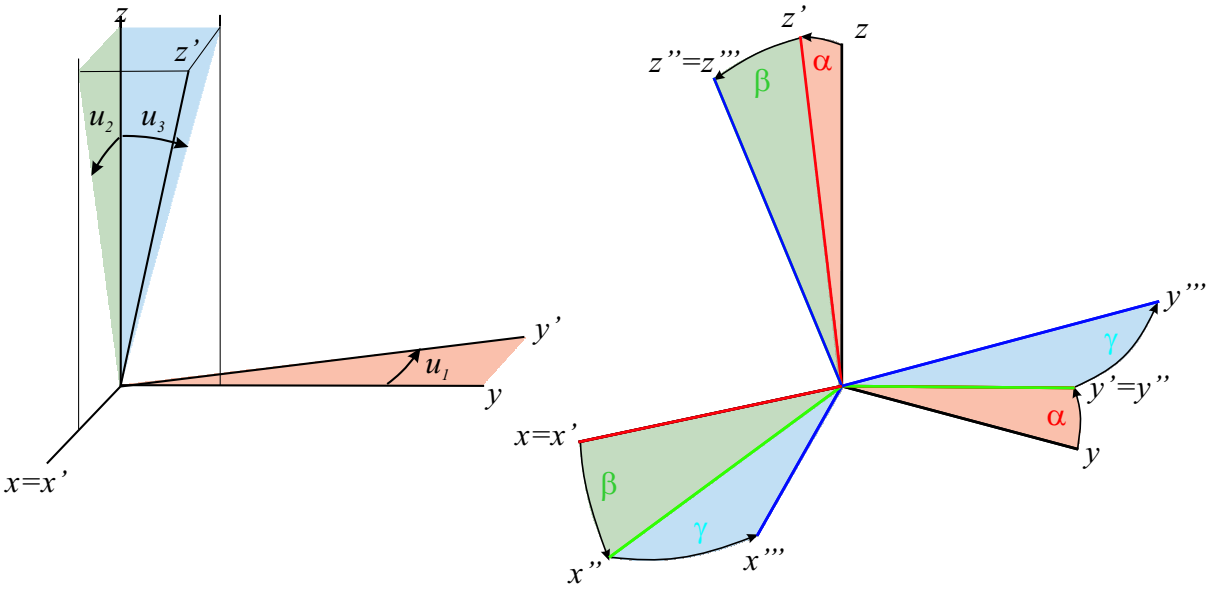

Figure 4.1: Left: Definition of the non-orthogonalities. The matrix $\mathbf{B}' = \underline{\underline{\mathbf{P}}} \cdot \mathbf{B}$ transforms a vector $\mathbf{B}$ whose components are given in the orthogonal coordinate system to the vector $\mathbf{B}'$ whose components are given in the (primed) non-orthogonal coordinate system.
Right: Definition of the three Euler angles α, β, γ defining the "1-2-3" rotation.

where $\underline{\underline{\mathbf{R}}}^{-1} = \underline{\underline{\mathbf{R}}}^{T}$ and

$$\underline{\underline{\mathbf{P}}}^{-1} = \begin{pmatrix} 1 & 0 & 0 \\ \frac{\sin u_1}{\cos u_1} & \frac{1}{\cos u_1} & 0 \\ -\frac{\sin u_1 \sin u_3 + \cos u_1 \sin u_2}{w \cos u_1} & -\frac{\sin u_3}{w \cos u_1} & \frac{1}{w} \end{pmatrix} \tag{4.8}$$

with $w = \sqrt{1 - \sin^2 u_2 - \sin^2 u_3}$.

4.1.2 Temperature dependence of the calibration constants

To account for sensor and electronics temperature effects, the VFM sensor output has to be transformed to a reference temperature, which is taken to 0° C. This will be done using pre-flight determined values; for this study we assume that the temperature dependencies are perfectly known. See Risbo [1996], Merayo et al. [2000] and Risbo et al. [2003] for pre-flight calibration of the Ørsted vector magnetometer, and Olsen et al. [2003a] for its in-flight calibration, including verification of the temperature dependencies. The following section describes how to correct the VFM magnetometer sensor output before performing the in-flight calibrations.

Let E_i be the raw VFM magnetometer output (in eu and uncorrected for temperature) for the ith VFM sensor, $i = 1 - 3$. T_A (in °C) is the temperature of the electronics (ADC-temperature), T_S (in °C) is the sensor temperature, and F_i is the VFM output (in eu) transformed to the reference temperature 0° C, for both the ADC- and the sensor temperature. Finally, B_i is the calibrated sensor output in the (non-orthogonal) coordinate system defined by the magnetic axes. The index i which denotes the axis will be dropped in the following.

In this approximation it is assumed that the sensitivities S and the offsets b depend on T_A and T_S; that this temperature dependence is linear and that the non-orthogonalities (as well as the rotation between the VFM and the CRF coordinate systems) are temperature independent. This is based on experience from Ørsted and CHAMP, and has been confirmed by the *Swarm* System Simulator Study

done by Industry. Hence

$$\begin{aligned} S &= S_0 + S_A T_A + S_S T_S \\ b &= b_0 + b_A T_A + b_S T_S \end{aligned}$$

The magnetic field B (in nT) is connected to the raw sensor output E according to

$$B = \frac{E-b}{S}.$$

Combining these equations yields

$$\begin{aligned} B &= \frac{E - b_0 - b_A T_A - b_S T_S}{S_0 \left[1 + \frac{S_A}{S_0} T_A + \frac{S_S}{S_0} T_S\right]} \\ &\approx \frac{E - b_0 - b_A T_A - b_S T_S}{S_0} \left[1 - \frac{S_A}{S_0} T_A - \frac{S_S}{S_0} T_S\right] \end{aligned}$$

(In this approximation it has been used that $S_A, S_S = O(10^{-6}) \ll S_0 = O(10^0)$ and $T_A, T_S = O(10^1)$). This has to be equal to the calibration of the temperature corrected sensor output F

$$B = \frac{F - b_0}{S_0}$$

from which the temperature corrected sensor output F follows as

$$F = E - b_A T_A - b_S T_S - \left(\frac{S_A}{S_0} T_A + \frac{S_S}{S_0} T_S\right)(E - b_A T_A - b_S T_S - b_0) \tag{4.9}$$

This equation is used for correcting the sensor output for temperature effects.

4.1.3 In-flight scalar calibration – comparison of the VFM scalar field with the ASM

It follows from Eq. (4.6) that the scalar intensity B_{VFM} of the VFM magnetometer as a function of the (temperature corrected) VFM output $\mathbf{F}$ is given by

$$B_{\mathrm{VFM}} = |\mathbf{B}_{\mathrm{VFM}}| = \sqrt{\mathbf{B}_{\mathrm{VFM}}^T \cdot \mathbf{B}_{\mathrm{VFM}}} \tag{4.10}$$

$$= \sqrt{(\mathbf{F}-\mathbf{b})^T \cdot \underline{\underline{\mathbf{S}}}^{-1} \cdot \left(\underline{\underline{\mathbf{P}}}^{-1}\right)^T \cdot \underline{\underline{\mathbf{P}}}^{-1} \cdot \underline{\underline{\mathbf{S}}}^{-1} \cdot (\mathbf{F}-\mathbf{b})}. \tag{4.11}$$

To estimate the 9 "intrinsic" parameters of the VFM magnetometer, arranged in the model vector $\mathbf{m} = (b_1, b_2, b_3, S_1, S_2, S_3, u_1, u_2, u_3)^T$, a linearized least-squares approach is used and the model parameters are chosen such that the χ^2- misfit is minimized:

$$\chi^2 = \sum \left(\frac{B_{\mathrm{VFM}}(\mathbf{F}, \mathbf{m}) - B_{\mathrm{ASM}}}{\sigma_B}\right)^2 = \mathrm{Min!} \tag{4.12}$$

where $B_{\mathrm{VFM}}(\mathbf{F}, \mathbf{m})$ depends nonlinearly on the model vector $\mathbf{m}$ and on the VFM sensor output $\mathbf{F}$. σ_B is the combined VFM and ASM maesurement error, which is assumed to be equal for all data points, and hence the data weights ($\propto 1/\sigma_B$) are set to unity for simplicity. The summation is taken over a given set of data. The connection between data residuals $\delta\mathbf{d} = (B_{\mathrm{VFM}}(\mathbf{F}, \mathbf{m}) - B_{ASM})$, and the model vector is (in linear approximation)

$$\delta\mathbf{d}^i = \underline{\underline{\mathbf{G}}}^i \cdot \delta\mathbf{m}^i \tag{4.13}$$

where the superscript i denotes the ith iteration and the elements of the kernel matrix $\underline{\underline{\mathbf{G}}}$ are given by

$$\underline{\underline{\mathbf{G}}}^i = \left.\frac{\partial \mathbf{d}(\mathbf{m})}{\partial \mathbf{m}}\right|_{\mathbf{m}=\mathbf{m}_i} \tag{4.14}$$

The ith iteration of the Gauss least-squares estimator may be written as

$$\mathbf{m}_{i+1} = \mathbf{m}_i + \delta\mathbf{m}_i \tag{4.15}$$

$$\delta\mathbf{m}_i = \left[\left(\underline{\underline{\mathbf{G}}}_i\right)^T \cdot \underline{\underline{\mathbf{W}}} \cdot \underline{\underline{\mathbf{G}}}_i\right]^{-1} \left[\left(\underline{\underline{\mathbf{G}}}_i\right)^T \cdot \underline{\underline{\mathbf{W}}} \cdot (\mathbf{d} - \mathbf{d}(\mathbf{m}_i))\right] \tag{4.16}$$

where $\underline{\underline{\mathbf{W}}}$ is a weight matrix to account for outliers (Huber weights, Hogg [1979]). The kernel matrix $\underline{\underline{\mathbf{G}}}$ contains derivatives of the inverse matrix of non-orthogonalities, which are given by

$$\frac{d\underline{\underline{\mathbf{P}}}^{-1}}{du_1} = \begin{pmatrix} 0 & 0 & 0 \\ \frac{1}{\cos^2 u_1} & \frac{\sin u_1}{\cos^2 u_1} & 0 \\ -\frac{\sin u_3}{w\cos^2 u_1} & -\frac{\sin u_1 \sin u_3}{w\cos^2 u_1} & 0 \end{pmatrix}$$

$$\frac{d\underline{\underline{\mathbf{P}}}^{-1}}{du_2} = \begin{pmatrix} 0 & 0 & 0 \\ 0 & 0 & 0 \\ -\cos u_2 \frac{\cos u_1 \cos^2 u_3 + \sin u_2 \sin u_1 \sin u_3}{w^3 \cos u_1} & -\frac{\sin u_3 \sin u_2 \cos u_2}{w^3 \cos u_1} & \frac{\sin u_2 \cos u_2}{w^3} \end{pmatrix}$$

$$\frac{d\underline{\underline{\mathbf{P}}}^{-1}}{du_3} = \begin{pmatrix} 0 & 0 & 0 \\ 0 & 0 & 0 \\ -\cos u_3 \frac{\sin u_1 \cos^2 u_2 + \sin u_3 \cos u_1 \sin u_2}{w^3 \cos u_1} & -\frac{\cos u_3 \cos^2 u_2}{w^3 \cos u_1} & \frac{\sin u_3 \cos u_3}{w^3} \end{pmatrix}$$

4.1.4 Application to synthetic *Swarm* data

The method has been applied to synthetic data calculated using the *Swarm* System Simulator developed by the industrial teams during Phase A.

We used time series of 2 days length and 1 sec sampling rate of the raw VFM sensor output, $E_i, i = 1-3$, temperature of the VFM sensor and electronics, and the level 1b ASM scalar intensity, B_{ASM}. Using the temperature dependencies S_A, S_S, b_A, b_S (assumed to be exactly known) the sensor output were transformed to zero reference temperature, cf. Eq .4.9.

Experience from Ørsted and CHAMP indicate that relative timing errors between the two magnetometers have influence on the calibration parameters, and that such timing errors can be detected by analyzing the rms misfit (Eq. 4.12). To study this, the time series of the ASM instrument has been shifted in time by $\Delta t = -30, -25, -20, \ldots, 30$ ms and the minimization has been performed for each of these time delays. The left part of Figure 4.2 shows this misfit in dependence on Δt. Relative timing errors between the two magnetometers down to a few ms can be found in that way.

Also, recent analysis of Ørsted and CHAMP data indicate that the absolute instrument of both missions (both satellites carry almost identical Overhauser proton precession magnetometers) has a bias, which has been estimated independently with Ørsted and CHAMP data to be -0.5 nT. We therefore also looked for a bias in the ASM instrument model. The result of this analysis is shown in the right panel of the Figure. Since a bias is not foreseen in the instrument model that was used for creating the synthetic data (at time of developing these models the existence of such a bias in the Ørsted and CHAMP data was not yet known), minimum misfit is achieved for zero bias, as expected.

Figure 4.3 shows the residual $\Delta B = B_{\mathrm{VFM}} - B_{\mathrm{ASM}}$ of the scalar field between the two magnetometers before (top) and after (bottom) optimization of the calibration parameters; the former is calculated from the difference of Level 1b ASM and VFM data as provided by the System Simulator. The in-flight parameter optimization reduces the orbital period that is clearly seen in the upper panel; the rms misfit is reduced from 0.14 nT to 0.08 nT.

The influence of a relative timing error on the calibration parameters is shown in Figure 4.4. Fixing the non-orthogonalities to the pre-flight values results in larger variability of the other 6 parameters; however, the minimum in the misfit-Δt-curve is more pronounced. as can be seen in the bottom part of the Figure.

4.1.5 Conclusion and Recommendations

The described in-flight scalar calibration is based on experienced gained from present single-satellite missions Ørsted and CHAMP and was found to be a very stable and robust method to estimate the 9

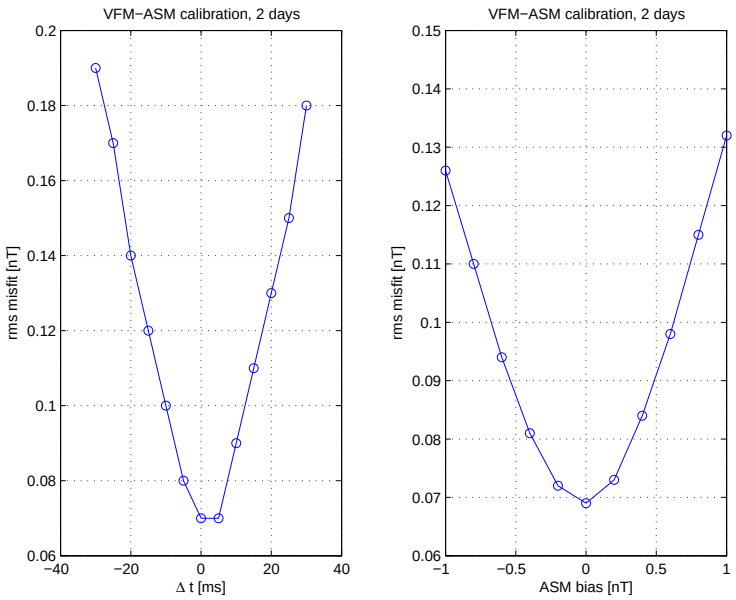

Figure 4.2: Rms misfit between scalar field of the ASM and the (calibrated) VFM, in dependence on relative timing error Δt (left) and bias of the ASM (right).

"intrinsic" magnetometer parameters of the vector magnetometer. This is confirmed from the present analysis of synthetic *Swarm* data. Since two instruments measuring the magnetic field strength at the same time instant and at the same space-craft are compared, the method does neither require data from the other *Swarm* satellites (i.e. this calibration is performed for each satellite separately, not taking advantage of the constellation) nor data taken during geomagnetic quiet conditions – contrary to the in-flight vector alignment described in the next section.

However, the study confirms the strong influence of timing errors between the instruments on the results, which has already been found from the analysis of Ørsted and CHAMP data. relative timing errors of 5 msec can be found in-flight with the described method; however, it is strongly recommended that attention is paid to possible timing errors during the design of payload and spacecraft.

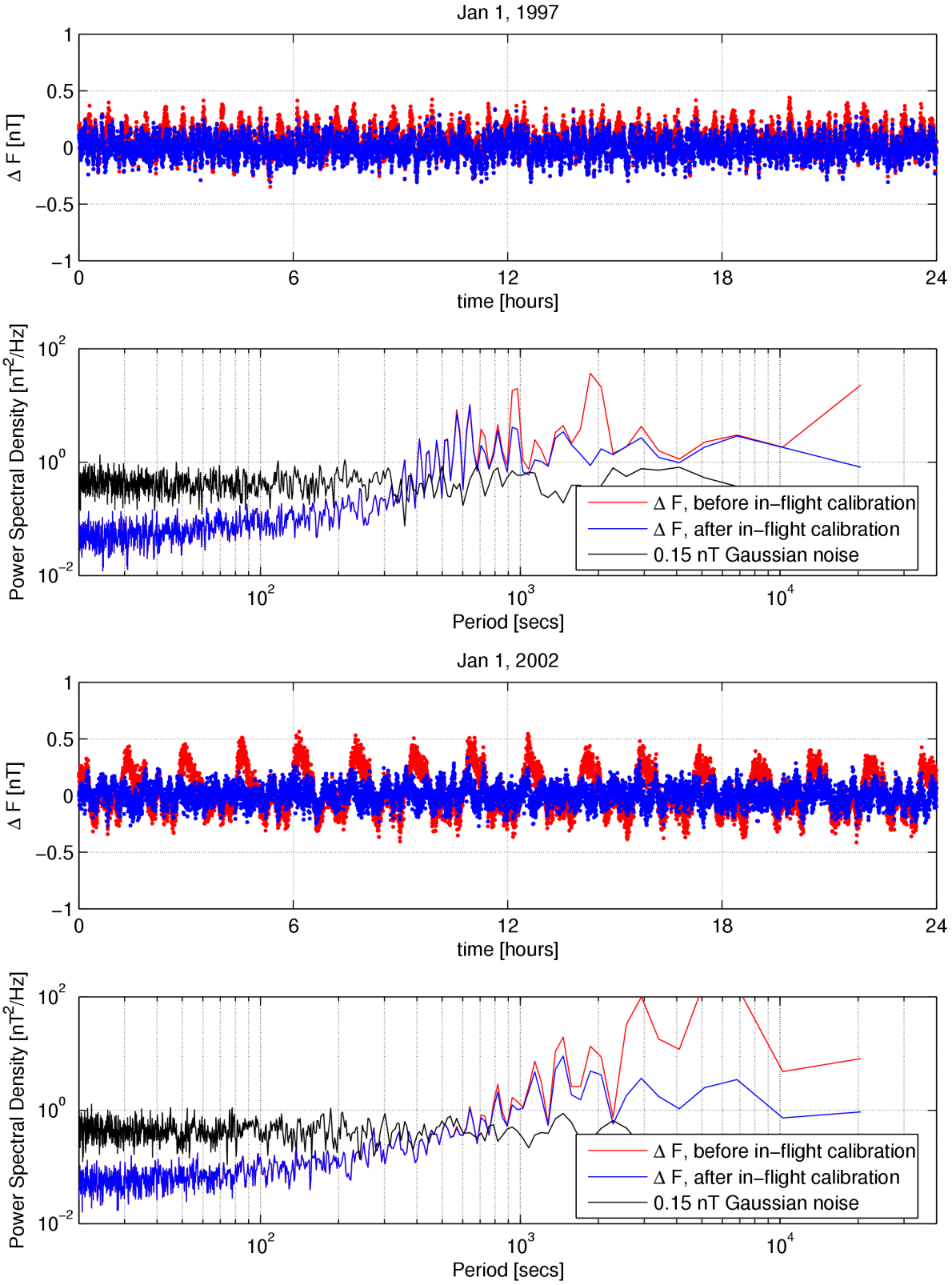

Figure 4.3: Time series and power spectral density of the residual $B_{\mathrm{VFM}} - B_{\mathrm{ASM}}$ before (red) and after (blue) in-flight calibration, for January 1, 1997 (top) and 2002 (bottom), respectively.

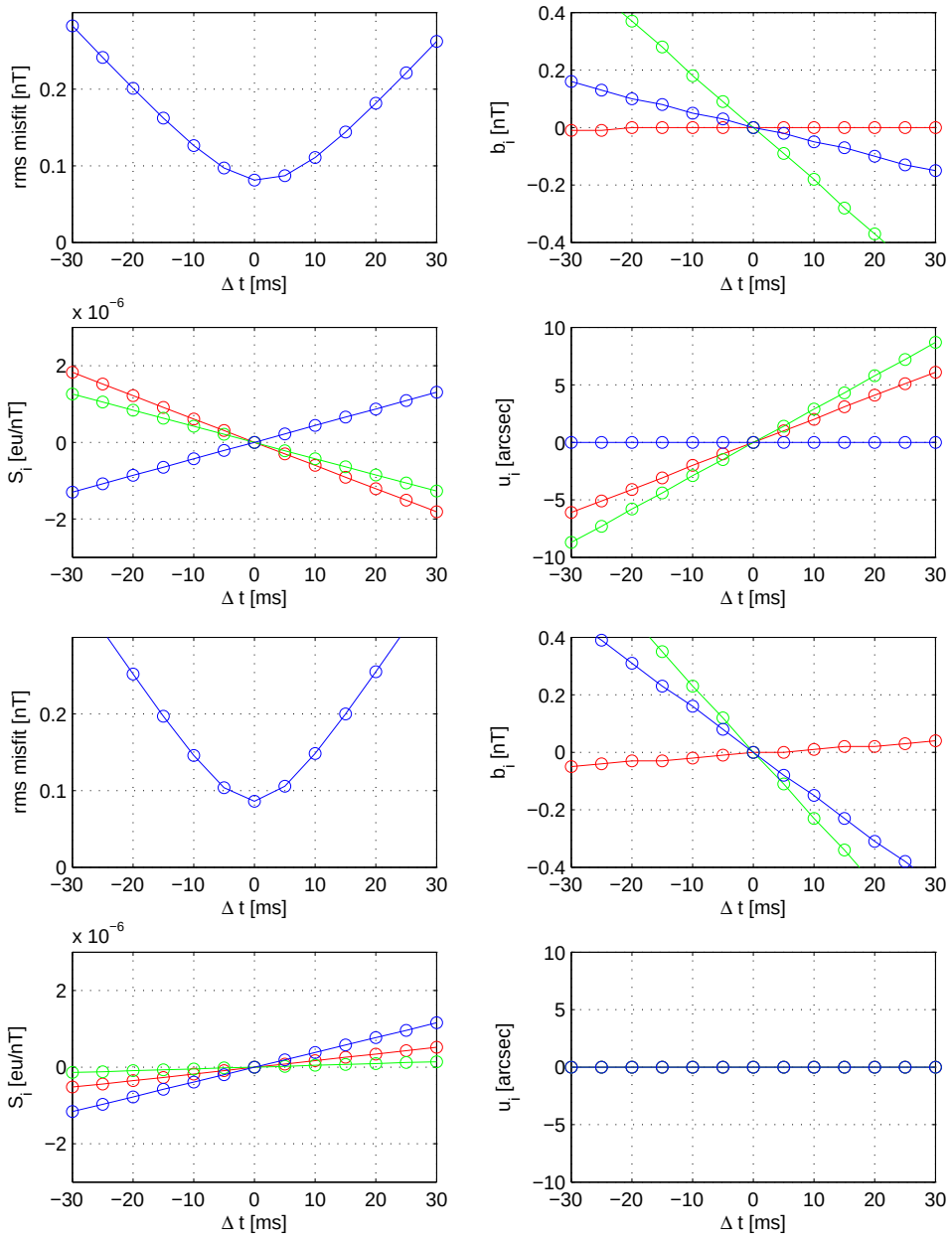

Figure 4.4: Change of the calibration parameters as a function of relative timing Δt (the values for $\Delta t = 0$ have been used as reference). Red, green and blue refer to VFM sensor axes 1, 2 and 3, respectively. Top: Estimation of all 9 parameters. Bottom: non-orthogonalities u_i fixed to the pre-flight values.

4.2 Alignment of the ASC and VFM

This section deals with the in-flight determination of the transformation between the vector magnetometer (VFM) and the star camera (ASC). This transformation is described by means of three Euler angles (α, β, γ), and their estimation is called "alignment". An in-flight determination of these Euler angles is essential because it is hardly possible to perform a pre-flight determination with the required accuracy of a few arcsecs (5 arcsecs is probably the best that can achieved at ground). In the following, simplistic analytic examples as well as synthetic data of the *Swarm*1 satellite and constellation #2 are used to investigate the impact of the various field contributions and flight scenario on the in-flight determination of the Euler angles.

To obtain the magnetic field in the North-East-Center (NEC) coordinate system, the VFM magnetometer readings (given in the VFM frame) are combined with attitude measured by the ASC. The latter measures the rotation between the International Celestial Reference Frame (ICRF) and the Common Reference System (CRF) of the optical bench; attitude is deliverd in the CRF (the merging of the attitude of the individual camera heads to the CRF will not be discussed here), and therefore rotation between the CRF and the ICRF is straightforward. Likewise, transformation from the ICRF to the International Terrestrial Reference Frame (ITRF), and further to the North-East-Center Frame (NEC) is straightforward, too. Hence the following steps are required in the processing of the level 1b data:

$$\mathbf{B}_{\mathrm{VFM}} \longrightarrow \mathbf{B}_{\mathrm{CRF}} \longrightarrow \mathbf{B}_{\mathrm{ICRF}} \longrightarrow \mathbf{B}_{\mathrm{ITRF}} \longrightarrow \mathbf{B}_{\mathrm{NEC}}$$

Note that no knowledge of space-craft attitude is required in this scheme; only the attitude of the optical bench (CRF) is required.

4.2.1 Description of the Simulation

Since a siumulation of the star camera was not included in the present study (this is part of the *Swarm* System Simulation Studies performed by industry), ASC attitude data (i.e., attitude of the CRF) were not available. Thus we had to rely on other ways of obtaining the attitude of the optical bench (CRF). We did this by assuming that CRF and S/C frame co-incide; and derived the latter from the unit vector of the along-track velocity, but allowing for rotation between the CRF (=S/C frame) and the orbit frame (OF). Note that this approach is only used for this simlation since no real ASC attitude data were available; for the real processing of level 1b data neither S/C nor OF attitude is required.

To calculate synthetic data in the VFM frame, various rotations (between orthogonal coordinate systems) are necessary. In particular:

Rotation of the magnetic field from the NEC system to the orbit frame (OF) This rotation is given by

$$\mathbf{B}_{\mathrm{OF}} = \underline{\underline{R}}_1 \mathbf{B}_{\mathrm{NEC}} \tag{4.17}$$

with

$$\underline{\underline{R}}_1 = \begin{pmatrix} \hat{x}_r & \hat{x}_\theta & \hat{x}_\phi \\ \hat{y}_r & \hat{y}_\theta & \hat{y}_\phi \\ \hat{z}_r & \hat{z}_\theta & \hat{z}_\phi \end{pmatrix} \tag{4.18}$$

$\hat{\mathbf{x}} = (\hat{x}_r, \hat{x}_\theta, \hat{x}_\phi)$ is the unit vector of the x-direction in the OF system. Figure 4.5 defines the coordinate system used here.

We assume that $\hat{\mathbf{x}}$ is in the (nominal) flight direction, so $\hat{\mathbf{x}} = \mathbf{v}/|\mathbf{v}|$ is determined from the instantaneous spacecraft velocity vector. Assuming that $\hat{\mathbf{z}}$ is in the plane spanned by $\hat{\mathbf{x}}$ and the radial direction (no roll misalignment of the space-craft), we find

$$\hat{\mathbf{y}} = \frac{\hat{\mathbf{x}} \times \hat{\mathbf{r}}}{|\hat{\mathbf{x}} \times \hat{\mathbf{r}}|} = \frac{1}{\sqrt{x_\theta^2 + x_\phi^2}} \begin{pmatrix} 0 \\ x_\phi \\ x_\theta \end{pmatrix}$$

$$\hat{\mathbf{z}} = \frac{\hat{\mathbf{x}} \times \hat{\mathbf{y}}}{|\hat{\mathbf{x}} \times \hat{\mathbf{y}}|} = \frac{1}{\sqrt{x_\theta^2 + x_\phi^2}} \begin{pmatrix} -\left(x_\theta^2 + x_\phi^2\right) \\ x_r x_\phi \\ x_r x_\theta \end{pmatrix}$$

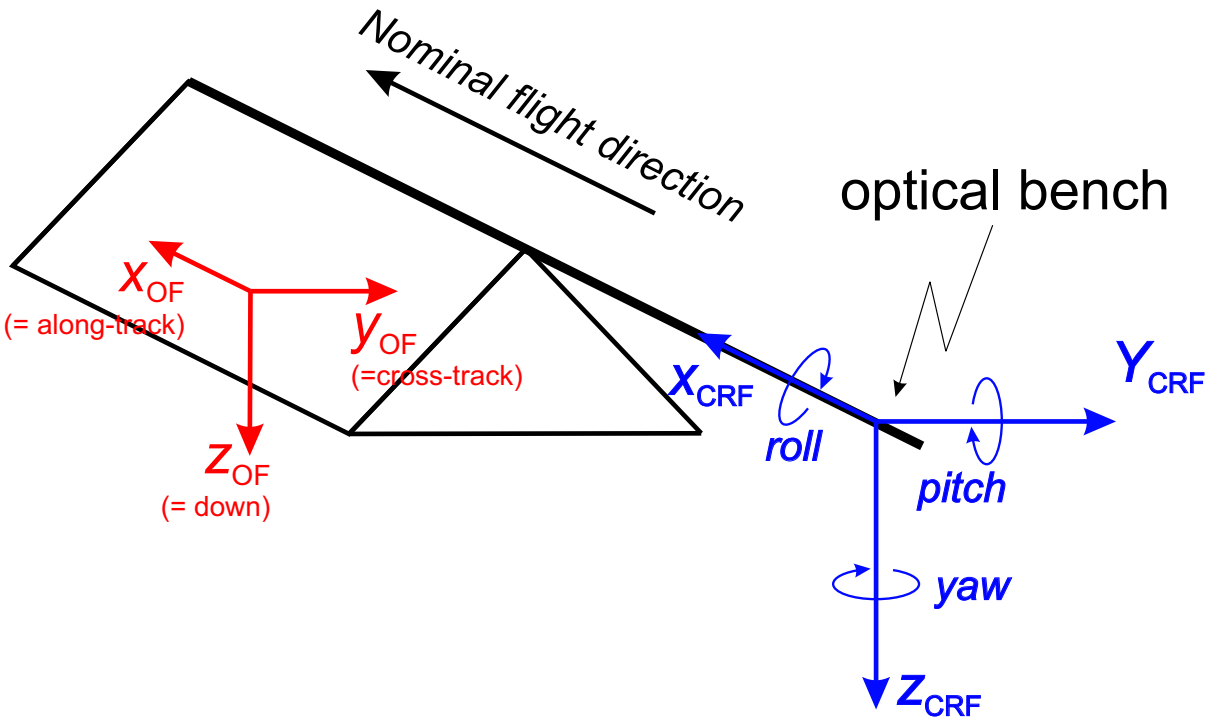

Figure 4.5: Definition of coordinate systems.

Rotation of the magnetic field from the Orbital Frame (OF) to the Common Reference Frame (CRF)

This rotation is given by

$$\mathbf{B}_{\mathrm{CRF}} = \underline{\underline{R}}_2 \mathbf{B}_{\mathrm{OF}} \tag{4.19}$$

The Common Reference Frame (CRF) is the coordinate system of the optical bench that contains ASC and VFM, and is defined by the merged attitude information of all three camera heads. Nominally the CRF is (approximately) equal to the orbit frame (OF) and hence $\underline{\underline{R}}_2$ is a 3×3 identity matrix; however, since we are interested in the effect of rotating the optical bench wrt. the nominal flight direction we parameterize $\underline{\underline{R}}_2$ by three Euler angles defining a 1-2-3 rotation.

Rotation of the magnetic field from CRF to the VFM system

This rotation is given by

$$\mathbf{B}_{\mathrm{VFM}} = \underline{\underline{R}}_3 \mathbf{B}_{\mathrm{CRF}} \tag{4.20}$$

where $\underline{\underline{R}}_3$ is parameterized by the three Euler angles (α, β, γ) of a 1-2-3 rotation as given in Eq. 4.5.

Estimation of the Euler angles

The Euler angles are estimated by comparing the observed magnetic vector components with those of a field model (that may or may not be co-estimated with the Euler angles). This approach is for instance described in Olsen et al. [2003a]. Here we used a fixed field model $\mathbf{B}_{\mathrm{NEC}}$ consisting of the core field plus a correction of the large-scale magnetospheric field. (α, β, γ) are estimated using an iteratively re-weighted Least-Squares approach by minimizing

$$|\Delta \mathbf{B}_{\mathrm{VFM}}| = \left| \mathbf{B}^{\mathrm{obs}}_{\mathrm{VFM}} - \mathbf{B}^{\mathrm{mod}}_{\mathrm{VFM}} \right|,$$

with

$$\mathbf{B}^{\rm obs}_{\rm VFM} = \underline{\underline{\widehat{R}}}_3\underline{\underline{R}}_2\underline{\underline{R}}_1\mathbf{B}^{\rm obs}_{\rm NEC}$$
$$\mathbf{B}^{\rm mod}_{\rm VFM} = \underline{\underline{R}}_3\underline{\underline{R}}_2\underline{\underline{R}}_1\mathbf{B}^{\rm mod}_{\rm NEC}$$

Here $\underline{\underline{R}}_3$ is the "true" CRF/VFM rotation (given by the true Euler angles) and $\underline{\underline{\widehat{R}}}_3$ is its estimate.

The ability of the method to determine unbiased Euler angles depends on the approximation of the observed magnetic field $\mathbf{B}^{\rm obs}_{\rm VFM}$ by the model field $\mathbf{B}^{\rm mod}_{\rm VFM}$. However, not only the field difference, $\Delta\mathbf{B}_{\rm VFM} = \mathbf{B}^{\rm obs}_{\rm VFM} - \mathbf{B}^{\rm mod}_{\rm VFM}$, but also the *properties* (nature) of this difference has impact on the Euler angles. Even a relatively large difference field $\Delta\mathbf{B}_{\rm VFM}$ will only have minor influence on the estimation of the Euler angles if $\Delta\mathbf{B}_{\rm VFM}$ is a potential field, $\Delta\mathbf{B}_{\rm VFM} = -\text{grad}\,\Delta V$. Also, a $\Delta\mathbf{B}_{\rm VFM}$ with a *distribution* in the VFM-frame that does not show a preferred direction will not harm the estimation of the Euler angles. It is therefore important to consider the following aspects:

- Use of a good model field (i.e., $||\Delta\mathbf{B}_{\rm VFM}||$ should be small). Compared to present state-of-the-art models, the *Swarm* mission will lead to significantly improved models, for instance by taking advantage of the constellation.
- Data selection that minimizes any preferred direction of $\Delta\mathbf{B}_{\rm VFM}$ in the VFM coordinate system. Combining data from different parts of the mission, and taken during special space-craft maneuvers will help to fulfill this.

4.2.2 Analytic examples: how do unmodeled non-potential fields disturb the estimation of Euler angles?

Before analyzing synthetic data we will discuss the influence of certain *properties* of $\Delta\mathbf{B}_{\rm VFM}$ on the estimation of the Euler angles. This is done by studying simplified examples.

Unmodeled fields in the VFM coordinate system (i.e., non-zero $\Delta\mathbf{B}_{\rm VFM}$) may result in a mismatch (bias) of the estimated Euler angles. Of special importance are unmodeled non-potential fields, which means that $\Delta\mathbf{B}_{\rm VFM}$ can *not* be derived from a scalar potential. There are two types of unmodeled fields: poloidal and toroidal. Both are "non-potential" fields (since they are not describable in the potential approach used for the "model" field). However, curl $\mathbf{B} = 0$ for the poloidal field, whereas curl $\mathbf{B} \neq 0$ for the toroidal field.

In this section we investigate, using analytic examples, how the existence of non-potential fields due to (unmodeled) LT dependency (curl $\mathbf{B} = 0$) or (unmodeled) toroidal field (curl $\mathbf{B} \neq 0$) may result in a misalignment of the CRF/VFM rotation (i.e. wrong determination of the Euler angles describing this rotation).

Consider an unmodeled magnetic field caused by a potential of the form

$$\begin{aligned}\Delta V &= \text{Re}\left\{a\left(\frac{r}{a}\right)^n \varepsilon_n^{m,p} P_n^m \exp\left(ipt + m\phi\right)\right\} \\ &= a\left(\frac{r}{a}\right)^n P_n^m \left[q_n^{m,p}\cos\left(pt + m\phi\right) + s_n^{m,p}\sin\left(pt + m\phi\right)\right]\end{aligned} \tag{4.21}$$

with $\varepsilon_n^{m,p} = q_n^{m,p} - is_n^{m,p}$. UT dependent coefficients are those with $p = 0$; local time dependent coefficients are those with $p = m$. In the latter the longitude/time dependency is $mt + m\phi = mT$ with local time $T = t + \phi$. Assume that the satellite samples the magnetic field at midnight ($T = 0$) and set $q_n^{m,m} = 0$ (for other local times the following argumentation can be modified by using a suitable combination of $q_n^{m,m}$and $s_n^{m,m}$). In that case the magnetic vector components (for $T = 0$) are given by

$$\begin{aligned}B_r &= 0 \\ B_\theta &= 0 \\ B_\phi &= \frac{m}{\sin\theta}\left(\frac{r}{a}\right)^{n-1} s_n^{m,m} P_n^m\end{aligned} \tag{4.22}$$

Note that B_ϕ is independent on longitude, which means incompatible with the usual spherical harmonic expansion of a potential field (that does not include local-time effects).

This magnetic field, although measured in a current-free region ($\mathrm{curl}\,\mathbf{B} = 0$), is identical to the toroidal magnetic field produced by a radial current density given by

$$J_r = \frac{1}{\mu_0 a}\frac{m}{\sin\theta} s_n^{m,m}\frac{dP_n^m}{d\theta} \tag{4.23}$$

where $r = a$ has been chosen for simplicity, and $\frac{1}{\mu_0 a}$ is approximately equal to $\frac{1}{8}\frac{\mathrm{nA/m^2}}{\mathrm{nT}}$. Therefore the magnetic effects of currents at satellite altitude and of a non-UT dependent potential field are indistinguishable if data from a fixed local time are used.

However, a similar magnetic field can produced by a mismatch of the Euler angles, as will be demonstrated now.

For $n = 2, m = p = 1$ this yields

$$B_\phi = s_2^{1,1}\sqrt{3}\cos\theta.$$

Consider now a south-going polar satellite track in a dipolar main-field, and a mismatch of the yaw Euler angle γ. This yields an East-West magnetic field

$$B_\phi = -\gamma g_1^0 \sin\theta, \tag{4.24}$$

which, again, is independent on longitude. $-\gamma g_1^0 = +3$ nT for $\gamma = 20$ arcsecs and $g_1^0 = -30000$ nT. The magnetic field due to this form of misalignment can be described exactly by (4.21-4.24) if the coefficient is chosen to $s_2^{2,2} = -\frac{1}{\sqrt{3}}\gamma g_1^0$ (≈ 1.7 nT for $\gamma = 20$ arcsecs). Physically probably more important is the term with $n = 1, m = p = 1$. According to the Tsyganenko model, the amplitude of $q_1^{1,1}$ is about 3 nT during solstices and vanishing during equinoxes (annual variation: -3 nT $\cos(\tau)$, where τ is season starting at Dec. 21). (Since q_n^m rather than s_n^m is considered the above argumentation holds for a dawn-dusk orbit rather than a profile along the midnight meridian.) Such a coefficient produces a latitude-independent magnetic field $B_\phi = s_1^{1,1}$. If vector data for the analysis are restricted to latitudes $\pm 50^o$, $\sin\theta$ varies only between 0.64 and 1.00, and Eq. 4.2.2 can be approximated by a latitude independent mean value of $B_\phi = -\gamma g_1^0 \overline{\sin\theta} \approx 2.5$ nT for $\gamma = 20$ arcsecs. Hence an unmodeled local-time dependent potential field (as predicted by the Tsyganenko model) may lead to spurious annual variation of the Euler angles of about 20 arcesc amplitude.

Misalignment of the roll angle α in a dipole field gives

$$B_\phi = 2\alpha g_1^0 \cos\theta,$$

which corresponds to a field produced by $s_2^{1,1} = \frac{2}{\sqrt{3}}\alpha g_1^0$. A roll misalignment of $\alpha = 20$ arcsecs thus produces $s_2^{1,1} = 3.36$ nT. The corresponding (equivalent) radial current density is $J_r = \frac{1}{\mu_0 a} s_2^{1,1}\frac{\cos 2\theta}{\sin\theta}$.

4.2.3 In-flight alignment using simulated data

The approach described in the previous section has been applied to data of the *Swarm*1 satellite and the second constellation. We selected the data according to the usual criteria for field modeling (geomagnetic quiet times: the global index of geomagnetic activity $Kp \leq 1^+$ for the time of observation and $Kp \leq 2^o$ for the previous three hour interval; the index of magnetospheric ring-current strength, Dst, is within ± 10 nT and $|d(Dst)/dt| < 3$ nT/hr. Only night-side data (local time T between 19 and 7) equatorwards of 60^o dipole latitude are used. The consequences of this data selection (restriction to $< 60^o$ dipole latitude, and of the fact that the satellites fly in a preferred direction, which both leads to non-uniform and spatially insufficient covering of the magnetic field direction on the unit sphere) should be analysed in a future study.

Test: Closed-loop analysis

Figure 4.6 shows the recovery of the Euler angles if the synthetic data only contain contributions from the core and crust (no external contributions). For the model field $\mathbf{B}^{\mathrm{mod}}$ we only used contributions from the core (up to spherical harmonic degree/order 13). Using data segments containing 30000 data points each we estimated the Euler angles α, β, γ (the true values that have been used for synthesizing the

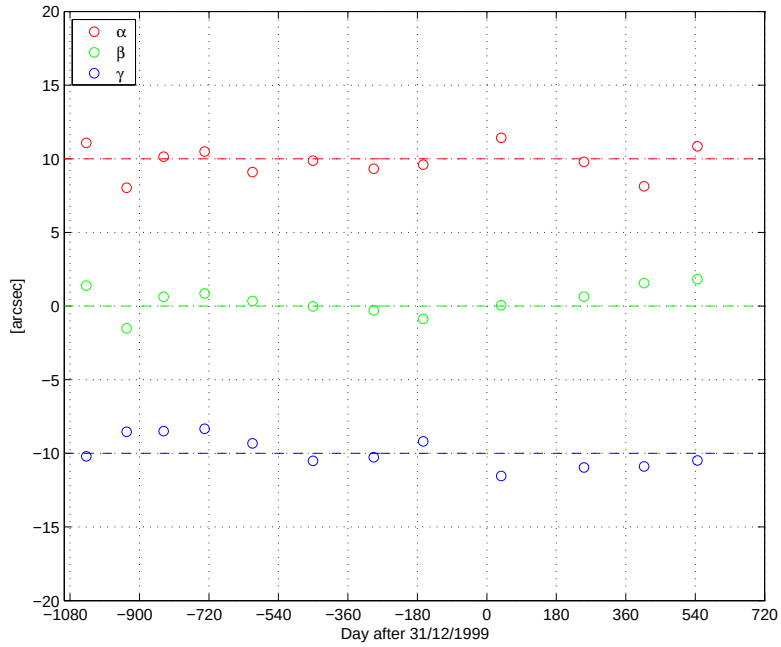

Figure 4.6: Estimation of Euler angles: closed-loop test. The dashed line present the true values.

data are: $\alpha^{\text{true}} = +10$ arcsecs, $\beta^{\text{true}} = 0$ arcsecs, $\gamma^{\text{true}} = -10$ arcsecs). By averaging the 12 individual estimates we obtain mean values $\overline{\alpha} = 9.8 \pm 0.3$ arcsecs, $\overline{\beta} = 0.4 \pm 0.3$ arcsecs, $\overline{\gamma} = -9.9 \pm 0.3$ arcsecs, in very good agreement with the true values. This demonstrates that a determination of the VFM-CRF transformation at sub-arcsecond level is possible in-flight, provided that a good model of the magnetic field is available.

Results of some experiments

In order to study the influence of an imperfect knowledge of the true magnetic field vector we performed a series of experiments. We assumed time-varying Euler angles and tried to recover this time variation. Although this will not be the case for the *Swarm* mission (for which the Euler angles of the optical bench are required to be stable within 5 arcsecs, according to the *System Requirements Document*), we introduced time-changing true values to investigate the robustness of the solution. For α we assumed a linear time dependence of $\alpha^{\text{true}} = 20$ $(t/1000$ days) arcsecs (where t is time in days after January 1, 2000); $\beta^{\text{true}} = 10$ arcsecs (no time dependence); and a quadratic dependence for γ according to $\gamma^{\text{true}} = 30$ $(t/1000$ days$)^2$ arcsecs. Based on our experience with the calibration of Ørsted and CHAMP, we applied the above described approach to data segments of 10000 data points each. Figure 4.7 shows the result. The true values are shown with dashed lines, whereas our estimates are presented with symbols. The lower panel of the figure shows the (weighted) rms misfit (the rms difference between the model value and the aligned true value, blue) and the rms alignment error (the rms difference between the true value and the aligned true value, red).

As is obvious from the Figure, the estimated values are off by tens of arcsecs and vary with time. This time variation is due to seasonal and LT variation of the field; the order of magnitude of these variations are as found with real data from the present geomagnetic missions.

To investigate *which* part of the unmodeled field produces the variations of the Euler angles, we re-did the analysis for the case that the observed field only contains a poloidal part (i.e. no toroidal field contribution) and only a toroidal part (i.e. no unmodeled potential contribution), respectively. The results, shown in the bottom part of Figures 4.7, indicate almost equal disturbances introduced by unmodeled poloidal and toroidal fields.

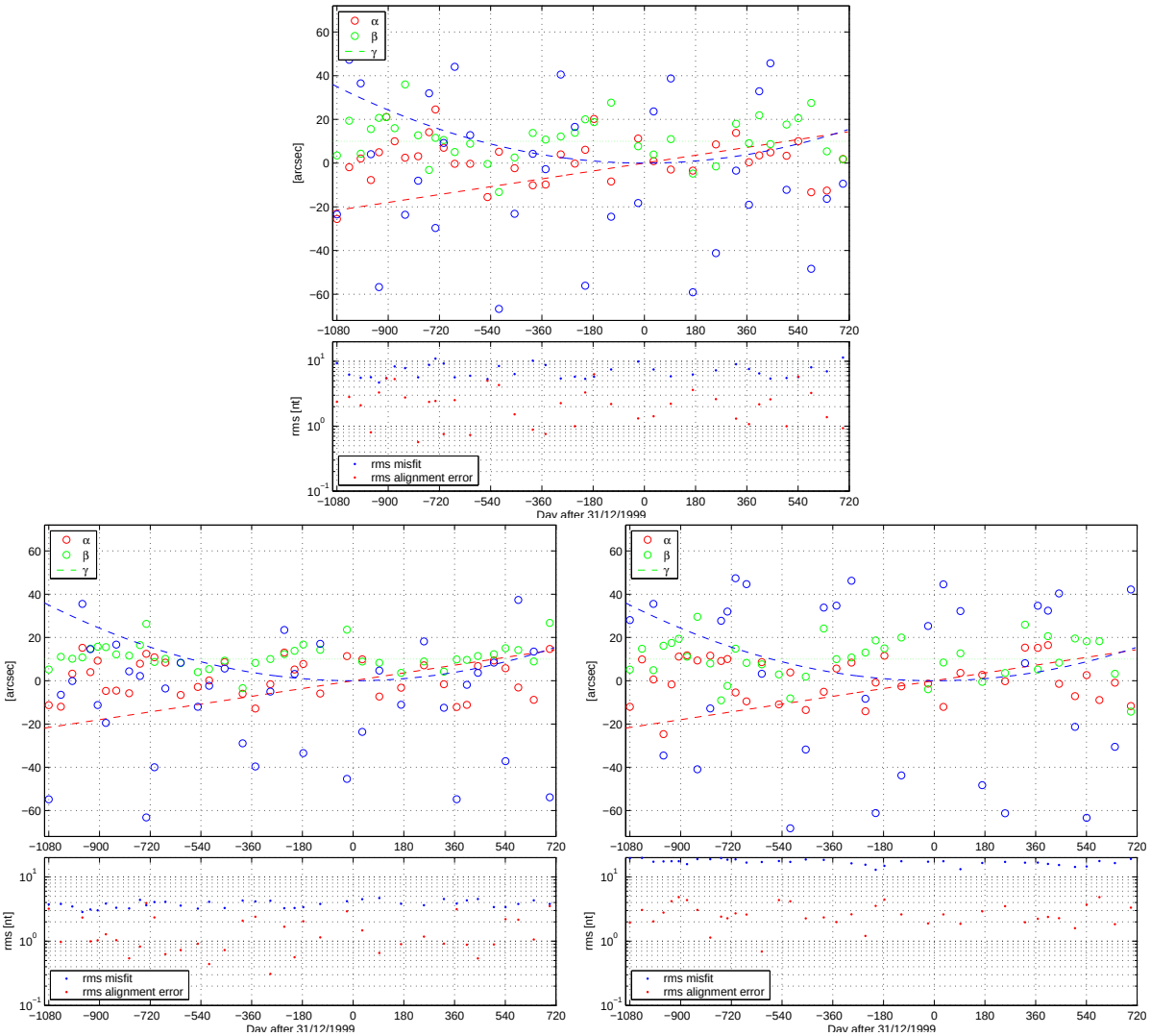

Figure 4.7: Estimation of Euler angles. Top: contributions from all sources. Bottom left: using potential field contributions only (i.e. curl $\mathbf{B} = 0$). Bottom right: using the toroidal field contribution only.

Rotation of the satellite helps to increase the estimation of the Euler angles. To investigate the impact of a rotation around a specific axis, we used a satellite that spins around its z axis (here we used a spinning rate of a few turns per minute, but the results are not dependent on the exact value). The left top part of Figure 4.8 shows that this scenario allows a very good recovery of α and β, but leaves γ badly determined. In contrary, a satellite that spins around its x axis allows a good determination of β and γ but leaves α undetermined, the right top part of the Figure. From this we conclude that rotation around a specific axis does not help to improve the determination of the Euler angle describing the rotation around that axis!

The reason for this are biases which are perpendicular to the field in the plane of rotation (that is, these biases are not described by a simple rotation in the plane). Let's say we are trying to find α around the x axis from two identical vector observations $B_m = B_{\rm rot} + e$, where $B_{\rm rot}$ is the field B_0 after rotation by alpha from the true and e (the bias error) is perpendicular to $B_{\rm rot}$ in the $y-z$ plane. The vector $dB/d\alpha$ will also be perpendicular to $B_{\rm rot}$ in the $y-z$ plane (either parallel or anti-parallel to e). The analysis will render a biased estimate of α since e has non-trivial influence. Now let's say that we rotate B_0 by $\gamma = 90°$ about the z axis for the second observation (that is, the second B_0 is mirrored across the z axis). For the second observation the relative orientation of e and $dB/d\alpha$ is *opposite* to that of the first observation. The dot products of B_m and $dB/d\alpha$, which make up the right-hand side of the normal equations will now be absent of contamination from e (they have canceled). The same argument is true if we rotate by beta about the y axis. This is why when one rotates about one axis one get good results about the other two, i.e., one basically canceled out more of the bias e in the B_m vectors. This is a simple example, but as one swings back and forth across the field with the rotations one effectively averaging out the components of e which are symmetric wrt the oscillation center.

We have tested this with two simple simulations: In the first we fit α (true value 20 degrees) from 2 redundant pairs of observations on the positive y half-plane. The estimate is -32 degrees. In the second example we mirrored the pairs of observations across the z plane. The estimate of α is 19.999 degrees, very close to the true value of 20 degrees.

As demonstrated in the bottom part of Figure 4.8, a reliable determination of all three Euler angles is possible from a fully tumbling satellite.

We conclude from these experiments that only a fully spinning (tumbling) satellite allows to estimate time-varying Euler angles.

Application to simulated *Swarm* data

From the results of the previous section it is clear that rotation of the satellite around a specific axis does not improve the determination of the Euler angle around that axis.

We therefore tried to answer the following questions

1. Does an analysis of data from the whole *Swarm* mission (taken during various seasons and local-time conditions) allow for a stable estimation of the Euler angles?
2. Do attitude maneuvers improve the stability of the solution? What is the minimum attitude maneuvers, if any, needed to obtain reliable estimates?

In this study we rely on the single-satellite approach that has been derived for the present missions. However, the natural next step in the analysis should be to take advantage of the constellation and to do a simultaneous determination of the Euler angles of all *Swarm* satellites. This is beyond the topic of the present investigations but is recommended for future studies

A very important system requirement for *Swarm* is the mechanical stability of the optical bench carrying VFM and ASC. This implies time independent Euler angles, which allows the use of long data periods in the analysis. The hope is that seasonal and LT variations will be averaged out if data spanning several years are used. In following we present "accumulated" results, which means that the value shown for time t is obtained by using all data from mission start until t.

The top left part of Figure 4.9 shows the result for a single satellite flying always in nominal direction. While a determination of α and β is possible within a few arcsecs if data of several years are used, the estimate of γ is biased by about 18 arcsecs. Since this is due to unmodeled magnetic fields it is hoped that the situation will improve after more sophisticated magnetic field models become available.

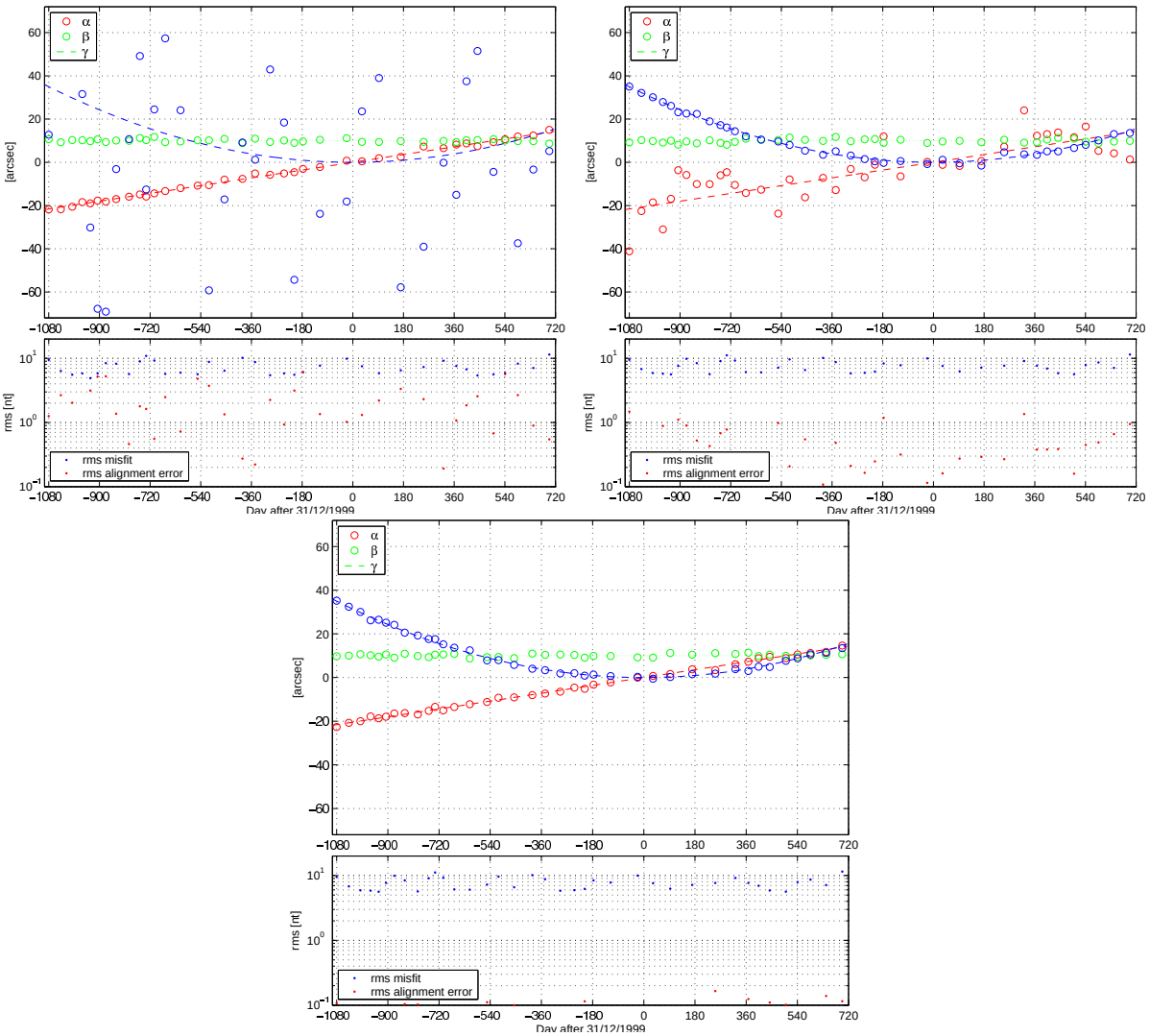

Figure 4.8: Estimation of Euler angles, all source contributions, but assuming a satellite spinning around the z (top left) and x (top right) axis, respectively. Bottom: Same, but for a satellite that spins (tumbles) around its x and z axes.

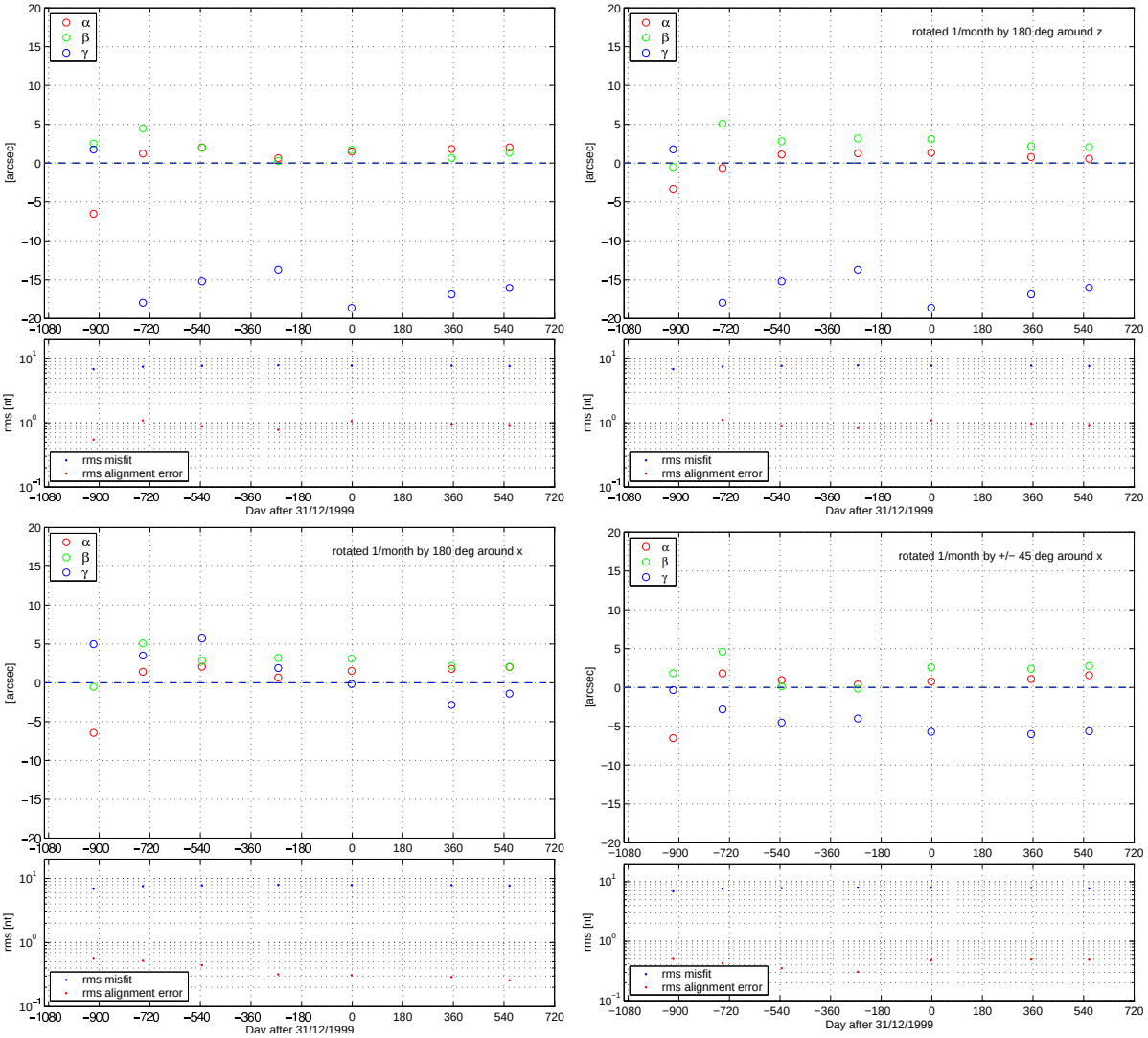

Figure 4.9: Estimation of Euler angles. All source contributions. Shown are accumulated values, i.e. the for time t is obtained by using all data until t. Top left: satellite flying always in nominal direction. Top right: Satellite turned by 180° around its z axis every month. Bottom left: Satellite turned by 180° around its x axis every month. Bottom right: Satellite turned by $\pm 45°$ around its x axis every month.

Although the results obtained in the last section indicate that rotation around z will probably not improve this situation, we investigated the effect of swapping the satellite around its z axis by 180° every month (e.g. a boom in flight-direction during even months and in anti-flight direction during odd months). As expected, and as shown in the top right part of the Figure, even such a severe maneuver does not improve the determination of γ.

We next rotated the satellite around its x axis once a month by 180° (which is of course equivalent to rotating the boom by 180° around boom axis). The bottom left part of the Figure demonstrates that this allows a determination of all three Euler angles within 5 arcsecs.

Finally we rotated the satellite once a month by $\pm 45°$. Although this yields a significantly improved determination of γ compared to the nominal flight configuration (top left panel), the value is still biased by more than 5 arcsecs, as shown in the bottom right part of Figure 4.9.

4.2.4 Conclusion and Recommendations

From the present studies the following conclusions can be drawn:

1. An in-flight determination of the three Euler angles parameterizing the VFM-ASC transformation is possible with sub-arcsec accuracy, provided that a magnetic field model of sufficient accuracy (differences less than a few nT, and direction evenly distributed on the unit sphere of the VFM) is available. However, mechanical stability of the optical bench (i.e., time independent Euler angles) is required for this.
2. If there are deficiencies in the magnetic model (resulting in magnetic field residuals larger than a few nT, and with uneven distribution on the unit sphere), reliable in-flight estimates of the two angles α, β are possible from data covering several years without satellite maneuvers. However, γ is biased (by 15-20 arcsecs).
3. Rotation of the satellite around its z-axis does not improve this. (Such maneuvers, however, may be needed for the VFM/ASM calibration.)
4. Rotation around x (flight direction) of $\pm 180^\circ$ once a month yields stable estimates of all three Euler angles. Even a rotation of $\pm 45^\circ$ improves the solution significantly, but is (alone) not sufficient to get γ with an accuracy of less than 5 arsecs. Not the *number* of satellite maneuvers (rotations of the optical bench), but the *amount of data* sampled in the rotated configuration is important.

Based on these results, The following recommendations are made:

- Of crucial importance is the mechanical stability of the VFM-ASC assembly (i.e., time independent Euler angles).
- Methods should be developed (improved) for a reliable pre-flight determination of the Euler angles.
- Methods should be developed for a simultaneous determination of the Euler angles of all *Swarm* satellites (multi-satellite approach). This could for instance be done in connection with comprehensive modeling of all relevant magnetic field contributions. It should be analyzed how a-priori (e.g., pre-flight) knowledge of a certain set of Euler angle (for instance knowledge of α and γ of satellite 1 and 3), help to stabilize the determination of *all* Euler angles.

Chapter 5

Testplan

Important requirements concerning the scope and functionality of the Mission Performance Simulator are given in the related *Statement of Work for the Swarm End-to-End Mission Performance Simulator Study [ESA-EOP-FS/0752, Sept. 2002]*:

The initial design, implementation and tests shall be done in deterministic sense, without observational noise, in order to be able to check the "closed loop", and to allow to analyze the effects of specific space and time sampling on the aforementioned separated field components.

The main goal of the Swarm mission performance simulator is to reconstruct internal field coefficients with accuracy's of better than 1 nT and to determine which constellation is optimal for the various science objectives. This implies that the second part of this task shall focus on the inclusion of propagated noise coming from the payload/satellite system and the calibration in level 1b data into the inversion process. This will allow analyses and judgment of the influence of these errors on the scientific objectives as a part of task 3.

The verification of all the various processing steps requires a dedicated test strategy involving all levels of complexity. In the following sections the anticipated test strategy is outlined.

5.1 Verification of the Synthetic Dataset

An important part of the Task 2 activities is the generation of representative datasets for magnetic field, electric field and other environmental conditions. Particular emphasis is put on a high-quality magnetic field representation. In this study we thus will focus on testing that quantity.

As mentioned above, the ambient magnetic field comprises contributions from various sources. In the simulator many of them are generated separately and have to be added up to give the complete magnetic field reading at the position of the satellite. For the verification of the synthetic data the individual contributions shall be tested separately. The proposed approach is to invert the "clean" (noise-free) data and determine the corresponding spherical harmonic (SH) coefficients. The derived model can be synthesized again and directly compared with the input data and/or the input model. This first "closed-loop" test is regarded as a verification of the calculated dataset and of the inversion algorithm.

5.2 Test Quantities and Criteria

There are different ways to demonstrate the quality of the achieved model. We plan to use the following criteria:

Difference in Spectra Let g_n^m and h_n^m be the (internal) Gauss coefficients of a spherical harmonic model. The Mauersberger-Lowes Spectrum R_n (at Earth's surface) is defined as

$$R_n = (n+1)\sum_{m=0}^{n}\left[(g_n^m)^2 + (h_n^m)^2\right] \tag{5.1}$$

We will use the spectrum of the differences of the coefficients, $\Delta g_n^m, \Delta h_n^m$, in combination with the spectrum of the original model, to evaluate a recovered model.

Degree correlation ρ between two models given by their expansion coefficients $(g_n^{m,(1)}, h_n^{m,(1)})$ and $(g_n^{m,(2)}, h_n^{m,(2)})$, respectively, is defined as [Langel and Hinze, 1998, eq. 4.23]

$$\rho_n = \frac{\sum_{m=0}^{n}\left[g_n^{m,(1)} g_n^{m,(2)} + h_n^{m,(1)} h_n^{m,(2)}\right]}{\sqrt{\sum_{m=0}^{n}\left[\left(g_n^{m,(1)}\right)^2 + \left(h_n^{m,(1)}\right)^2\right]\sum_{m=0}^{n}\left[\left(g_n^{m,(2)}\right)^2 + \left(h_n^{m,(2)}\right)^2\right]}} \tag{5.2}$$

Models are considered compatible up to that degree n where the degree correlation drops below 0.7.

Sensitivity matrix For the determination of systematic errors it is recommended to determine the sensitivity matrix which gives the relative error of each coefficient in a degree versus order matrix. The difference of all the coefficients is determined and these are subsequently normalised by the mean spectral amplitude of the associated degree n. Let k_n^m be the estimated Gauss coefficient, with $k_n^m = g_n^m$ for $m \geq 0$ and $k_n^m = h_n^{-m}$ for $m < 0$, and let c_n^m be the corresponding coefficient of the original model. The elements of the sensitivity matrix are defined as

$$S(n,m) = 100 \frac{k_n^m - c_n^m}{\sqrt{\frac{1}{2n+1} \sum_{m=-n}^{n} (c_n^m)^2}} \tag{5.3}$$

Maps of differences Finally, we plan to investigate the local differences (for instance of B_r) between the original and the recovered model, on a global map. This helps to find geographically confined deficiencies.

5.3 Inversion of Noise-Free Data

In a next step the complete magnetic signal shall be used, but still noise-free, and from this the individual source terms have to be recovered. Within the Task 2 activity we are going to focus on the main *Swarm* objectives, recovery of core field with secular variation (SV) and the lithospheric magnetic field. For the task of field separation advantage of the multi-satellite constellation shall be taken.

The results obtained here shall help to find suitable sampling strategies both in the space and time domain. The constellation and its temporal evolution shall be optimized for the recovery of the above mentioned source parts, main field + SV and lithospheric field.

5.4 Data Calibration Approaches

The core objective of the End-to-End simulator is to demonstrate the performance which can be achieved in resolving the various parts of geomagnetic field with the help of a suitable constellation of satellites. Within the Task 3 activity quasi-realistic data have to be used in the simulation. This implies that the synthetic data are distorted by propagated noise coming from the payload and satellite systems. An additional task resulting from the distortion is that the data have to be calibrated before they can be used in the inversion process.

Based on the experience of current magnetic field missions approved calibration procedures will be implemented. In addition dedicated techniques suitable for multi-satellite missions have to be developed. Utilizing a constellation of spacecraft places on the one hand higher demands on the quality of the calibrations, but offers on the other hand new possibilities of separating parameters which cannot be resolved in a single satellite approach. Highest priority shall have a precise inter-calibration of the payloads on the various spacecraft. This is the prerequisite for obtaining reliable estimates for the vector gradients from the differences of measurements taken by adjacent satellites. Including gradients in the interpretation helps in several respects to improve the separation of source terms. It shall be determined which orbit and attitude configurations are most favorable for the inter-calibration of the payloads.

Finally, an approach for an absolute calibration of the complete constellation shall be developed. This again shall be optimized in a way that the prime objectives main field + SV and lithospheric field models are most accurate. Calibration success has to be demonstrated by comparison with the clean input data. The obtained residuals have to be checked against the Level 1b data requirements, as stated in the System Requirement Document (ESA, EOP-FP/2002-07-685, Issue 1.1, October 2002).

5.5 Inversion of Quasi-Real Data

The calibrated data have the Level 1b quality. These are the basis for modeling efforts. For the retrieval of the various magnetic field source terms different approaches shall be tested. One of which is the

comprehensive approach, solving for all contributions in one run. An alternative approach performs a successive removal of superimposed components and a final inversion of the cleaned data set. The latter may be applied in an iterative way.

For assessing the quality of the obtained results the retrieved models shall be compared with the input models on source term level. The same tests as described in Section 5.2 shall be applied, i.e. the coherence between input and output models. The obtained model is considered valid up to the degree n where the degree correlation drops below 0.7. Also the other comparisons which look for systematic differences shall be applied.

One important aim of the simulator is to find the best satellite configuration for achieving the scientific goals. Besides that also scenarios with a reduced number of satellites have to be considered. In particular, the increase in performance shall be shown when upgrading from two to three satellites and from three to four. This will help in justifying the selection of mission options.

Chapter 6

Inversion: Recovery of the Various Field Contributions

Since modeling of the core field (plus secular variation) and of the lithospheric field is the main objective of *Swarm*, we will demonstrate the ability to recover these two field contributions using data from constellation #1.

The results of closed-loop inversions (using "clean" data, which means that the data only contain field contributions we are inverting for) are discussed in Section 6.1.1 (Figures 6.2 to 6.8) for the comprehensive inversion (inverting for all sources using data containing all sources), and in the first part of Section 6.2 (Figures 6.23 to 6.25) for a inversion of the high-degree lithospheric field alone (using data that only contain lithospheric field contributions). As demonstrated in these sections, we achieve an almost perfect recovery of the high-degree secular variation and lithospheric field.

6.1 Comprehensive Inversion

This section describes the application of Comprehensive Inversion (CI) to simulated *Swarm* mission data in order to recover both the core secular variation (SV) and lithospheric or crustal fields, i.e., per WP 4100 "Comprehensive Inversion". This work was carried out by Terence J. Sabaka of NASA/Goddard Space Flight Center and Nils Olsen of the Danish Space Research Institute.

6.1.1 Task 2: Closed-loop simulation

The premise of Task 2 is to recover the target core SV and crustal fields from clean or perfect data from a variety of methods. These data contain not only the target fields but also well-known extraneous or contaminating fields. Some methods rely upon stringent data selection criteria in mitigating the effects of the contaminates, while others build these effects into an error analysis, while still others attempt to parameterize and coestimate the contaminating fields along with the targets. The CI may be classified in the last category; it attempts to recover the target fields using minimal selection criteria and focuses rather on describing natural data variations with detailed parameterizations of the various constituent fields. Since significant spatial and temporal overlap exists between these fields, they are coestimated in a weighted least-squares sense for optimal signal partitioning. This work follows closely that of Sabaka et al. [2002].

It is expected that external field contamination will be one of the major impediments to the successful recovery of the target fields from the actual mission data. Therefore, this task has been developed in three stages according to how external field variability is introduced and treated. However, only the first stage is of particular importance since it is here that internal consistency within the simulation is established. The later two stages, while of some interest in how they illuminate the problems of external field contamination, do not present optimal methods of dealing with the problem. Hence, they will only be briefly summarized in anticipation of superior methods presented later in Task 3.

Recall that for this task all data are synthesized from comprehensive model (CM) CM3e-J_2 (J_2), which is a prototype to the CM4 model of Sabaka et al. [2004]. These models were derived using an external field dipole which is linearly dependent on the $D_{\rm st}$ index in all travelling modes as a proxy for ring-current variability. In addition, the dependence of primary ionospheric currents in the E-region dynamo on solar activity (particularly EUV radiation) has been assumed to be scalar. That is, all basis functions are equally scaled by a function of the 3-monthly means of the $F10.7$ cm solar radio flux ($F10.7_{\rm 3m}$), such that the E-region currents "breathe" with this flux.

Specifically, data were synthesized using the $D_{\rm st}$ index and the daily $F10.7$ value ($F10.7_{\rm d}$) to obtain magnetospheric and ionospheric contributions, respectivley. The first stage, or the "Perfect Indices" (PI) stage, provides a consistency check or a "closed-loop" simulation in which the data are analyzed with the same indices used in the synthesis, i.e., $D_{\rm st}$ and $F10.7_{\rm d}$. The second stage, or the "Imperfect Indices" (II) stage, introduces external field variability which is not directly modelled and provides insight into the robustness of the CI. The $F10.7_{\rm 3m}$ flux is used in place of $F10.7_{\rm d}$, and the RC index of Section 3.6 replaces $D_{\rm st}$. The RC index is the coefficient associated with an axial external dipole which has been derived every hour from synthesized observatory hourly means (OHMs) data residing in a specified nightside sector. It is expected that RC will reflect some of the $D_{\rm st}$ variability, particularly the hourly, but will also exhibit additional seasonal and perhaps more long-term behavior from the seasonal and seasonal/$D_{\rm st}$ modulations built into J_2. This suggests a third stage, or the "Adjusted Indices" (AI) stage, in which the same "imperfect" indices are used in the analysis, but an additional parameter modification is implemented in an attempt to correct for these external perturbations.

Spherical harmonic models from the II stage show severe degradation in parameter recoverability in SV for degrees $n \geq 14$ and in the crustal field above $n = 89$. Most of the contamination can be traced to leakage from uncompensated long-term trends in magnetospheric induction and biases in unmodelled ionospheric induced, and maybe primary, signal. This is not unexpected given that RC and $D_{\rm st}$ are most different at long wavelengths. Correcting for these long-term discrepancies between RC and $D_{\rm st}$ in the AI stage via simple polynomials brings great improvement in SV recovery up through $n = 19$. Trouble still exists in the crustal recovery above $n = 90$, but recovery has improved below this. However, this method is still dependent upon the availability of proxy indices which are not estimated consistently with the

whole model. In addition, the simple functional forms which employ these indices may be inadequate for more complicated, i.e., realistic external and induced fields. Hence, this approach is replaced in Task 3 by a less empirical method which is consistent with all data types.

The remainder of this section will describe the data, parameterization, estimation, and results of the PI stage or "closed-loop" simulation.

6.1.2 Data Type and Selection

In this study, all available synthesized data were considered over the entire mission envelope, 1997-2002. This not only includes the four *Swarm* satellites from constellation #1, but also the OHMs synthesized at the 88 observatory locations considered in this study. This latter data set is essential to the CI approach in that it helps, among other things, to resolve the field from ionospheric E-region currents. The only restriction placed on the data was that they occur during magnetically quiet conditions as defined by $K_p(t) \leq 1^+$, $K_p(t-3\text{h}) \leq 2^0$ and $|D_{\text{st}}| \leq 20$ nT being true at time t of the measurement. The vector OHMs are synthesized in local ellipsoidal (geodetic) coordinates as $(North, East, Down)$ or (X, Y, Z) components, while satellite vector components are in local spherical coordinates. Note that the same OHM and satellite data sets were used at each stage.

The top panel of Fig. 6.1 shows the locations of the 88 observatories and the bottom panel shows a histogram of the number of vector OHMs provided by all observatories during quiet conditions on a given day (identified by its Modified Julian day (MJD)) during the mission. Clearly, the observatory spatial distribution is far from uniform with a high concentration in Europe and low concentrations in the oceans and S. hemisphere, which will have implications later. The temporal distribution shows a slightly higher density of quiet-times early in the mission. The resulting data total is 1,296,680 vector OHMs.

The *Swarm* satellite data used has been synthesized once per minute from constellation #1. The density of this data from each of the four satellites is of course very uniform and dense, except for the polar holes, which range from a 4° to 4.6° half-angle for the upper (1 and 2) and lower (3 and 4) satellite pairs, respectively. Each satellite provides about 879,702 vector measurements during quiet periods. When combined with the OHMs, the total number of vector measurements analyzed in this study is about 4,815,488.

6.1.3 Model Parameterization and Inversion

Given that the synthesizing model J_2 is a CM, we have an opportunity in this study to investigate a "closed-loop" simulation in which not only the target fields, but all fields are successfully recovered. Thus, in this stage, we exactly reproduce the parameterization of J_2, where applicable, such that the constituent fields are represented following Sabaka et al. [2004]. This deviation from J_2 is found in the internal field parameterization where, for instance, the spherical harmonic (SH) truncation level has been increased from the J_2 value of $n = 65$ to the new value of $n = 120$. Since J_2 spanned 1960-2002, the core SV temporal representation has also changed; cubic B-splines are still employed, but for all harmonics of $n \leq 20$ as opposed to $n \leq 13$ in J_2, and such that their domain is now 1997-2002 with a single interior knot placed at 1999.5 (the main field epoch). This gives a total of six temporal coefficients (including the static term at epoch) for each harmonic of $n \leq 20$ and of course one coefficient per harmonic for $21 \leq n \leq 120$. The internal SH expansion is done in geographic coordinates. As in J_2, local crustal anomalies are modelled as vector biases at the 88 observatory locations.

The external and associated induced fields were analyzed exactly as in J_2, except for differences in the proxy indices stated earlier. The primary magnetospheric field is represented by an external SH expansion in dipole coordinates having both local and non-local diurnal time modes and annual and semi-annual seasonal time modes. Ring-current variability is built in as previously discussed. Ignoring diurnal modes and induced coupling coefficients, the magnetospheric external dipole terms in this stage

have the form

$$q_1^m(t) = q_{1,0}^m + \sum_{k=1}^{2}(q_{1,k,\mathrm{c}}^m \cos k\phi_\mathrm{s}(t) + q_{1,k,\mathrm{s}}^m \sin k\phi_\mathrm{s}(t)) + D_\mathrm{st}\left[q_{1,0,\mathrm{d}}^m + \sum_{k=1}^{2}(q_{1,k,\mathrm{cd}}^m \cos k\phi_\mathrm{s}(t) + q_{1,k,\mathrm{sd}}^m \sin k\phi_\mathrm{s}(t))\right], \text{ for } m = 0 \text{ and } 1, \quad (6.1)$$

where $\phi_\mathrm{s}(t)$ is the fundamental season angle and t is the UT fraction of year. Induced contributions are linked with the primary coefficients via coupling coefficients derived from the *a priori* 1-D (radially varying) conductivity of Olsen [1998].

The field from the primary ionospheric E-region currents is represented by an internal SH expansion for satellites and an external expansion for observatories in Quasi-dipole (QD) coordinates. The two

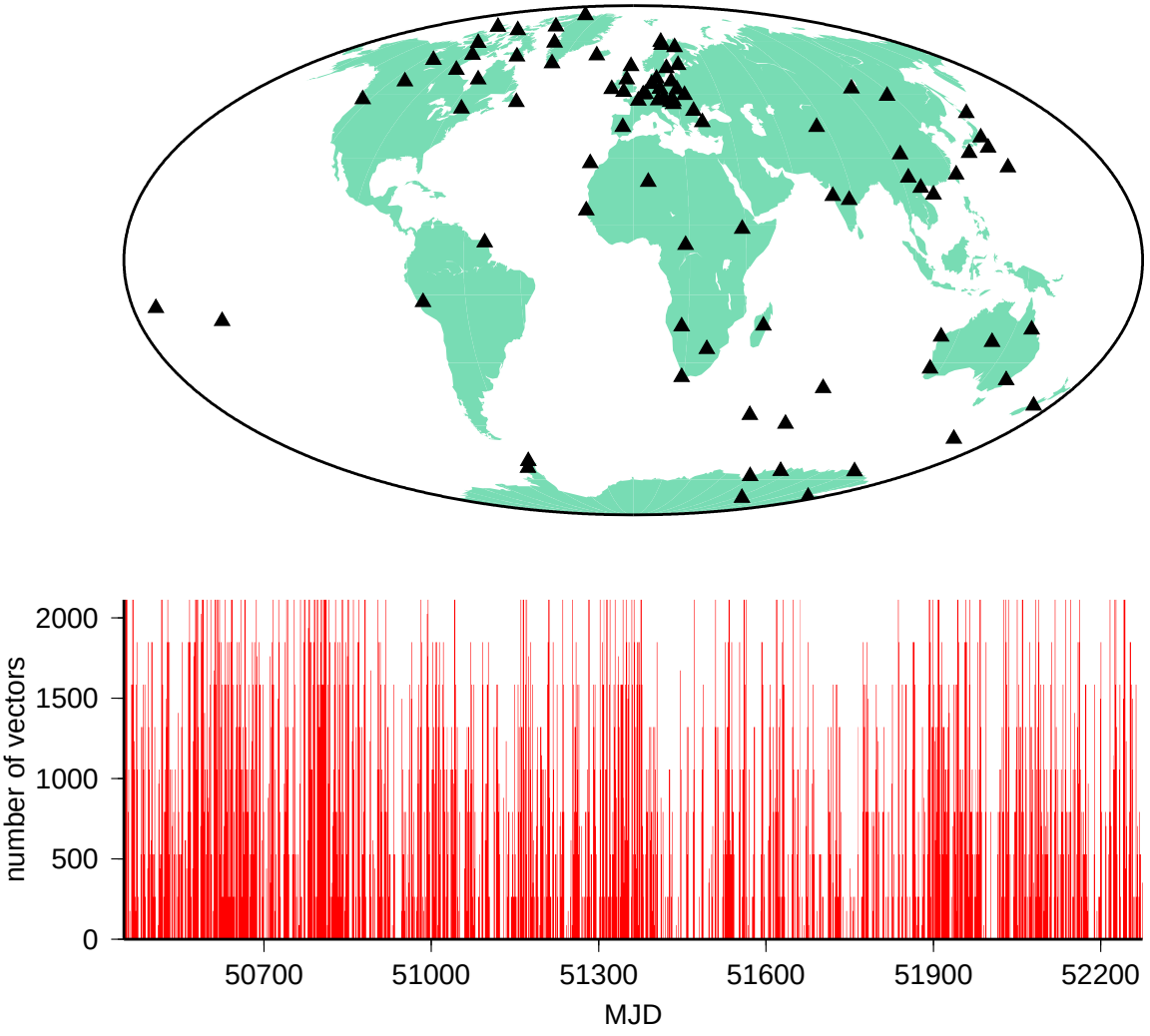

Figure 6.1: Top: Locations (triangles) of the 88 observatories providing hourly-means during the mission. Bottom: Histogram of the number of hourly-mean vectors provided by all observatories during quiet conditions on a given day (identified by MJD) during the mission.

Field source	Number of parameters
OHM biases	264
Core/lithosphere	16,840
Ionosphere	5,520
Magnetosphere	800
Satellite coupling currents	6,120
Total	29,544

Table 6.1: Number of parameters in each field source for PI stage.

expansions are related by the radial continuity of the field across an assumed sheet current shell at 110 km altitude. The QD coordinate chart lines conform to the contours of the main field and reflect the true conductivity structure of the E-region. These expansions also possess local and non-local diurnal time modes and annual and semi-annual seasonal time modes. Solar activity influence is built in as previously discussed via $F10.7_{\mathrm{d}}$. Induction is treated as in the magnetospheric case.

The fields discussed so far are generated from current systems far from the measurement regions. Thus, they are treated as gradients of potential functions. There are, however, insitu currents present in the satellite sampling shells. These fields connect electrical circuits between the magnetosphere and ionosphere and between hemispheres within the ionosphere. Fields from these coupling currents cannot be represented by gradients of potential functions. In the CMs, they are represented by toroidal field expansions and are thus horizontal fields. In J_2, the underlying poloidal current densities are considered to flow in QD meridional planes; QD coordinates are again employed here for similar arguments about conductivity. This model contains three separate representations of toroidal fields from the Magsat satellite sampling shell at dawn and dusk local time and from the Ørsted satellite shell at all local times. Toroidal contributions have been synthesized for this simulation from the Ørsted model since it contains continuous diurnal time modes as well as annual and semi-annual seasonal time modes. Hence, this is the parameterization we use in this study. Table 6.1 shows the number of parameters used to model each field source and the total parameter number.

For the inversion, a weighted least-squares estimator was used which seeks to minimize the function

$$L(\mathbf{x}) = (\mathbf{d} - A\mathbf{x})^T W(\mathbf{d} - A\mathbf{x}), \tag{6.2}$$

where $\mathbf{d}$ is the data vector, $\mathbf{x}$ is the model parameter vector, A is the Jacobian matrix, and W is the inverse data covariance matrix. In this study, W is treated as a diagonal matrix whose diagonal entries are unity for OHM data and $\sin\theta$ for satellite data, where θ is the colatitude of the satellite position, such that the satellites have effectively an equal-area distribution. Because $\mathbf{d}$ is a linear function of $\mathbf{x}$, the minimizer of $L(\mathbf{x})$, $\tilde{\mathbf{x}}$, is given by

$$\tilde{\mathbf{x}} = (A^T W A)^{-1} A^T W \mathbf{d}. \tag{6.3}$$

6.1.4 Task 2: Results and Discussion

Two models were derived during the PI stage; both contain data from all four *Swarm* satellites from constellation 1, but differ in whether OHM data were included ("OHM-Satellite Perfect Indices" - OSPI) or not ("Satellite Perfect Indices" - SPI). This was done in order to see just what can and cannot be resolved by the satellites. Figures 6.2, 6.3 and 6.4 compare the original and recovered SPI SV at 1997.5, 1998.5, 1999.5, 2000.5 and 2001.5 and the core and lithosphere (C/L) at 1999.0 at Earth's surface. The comparisons are made on the basis of the R_n spectrum, degree correlation, and sensitivity matrix of eqs. 5.1, 5.2 and 5.3, respectively, and also a difference of coefficients. Clearly, the target fields are being well recovered, which is somewhat of a surprise when using just satellite data. It says that over the duration of the mission and in the configuration of constellation 1 the CM parameterization is quite observable, i.e., the data derived normal matrix $A^T W A$ is not badly conditioned. As for the details of

SPI, it can be seen that there is very slight degradation of the SV near the ends of the mission envelope and that most of the coefficient discrepancies occur near the $n > 14$ sectoral regime. As for the C/L, there is generally a slight increase in coefficient difference with increased n with peculiar spikes at $n = 30$ and $n = 90$. This latter jump also corresponds with the lower edge of a circular pattern of discrepancies in the sensitivity matrix.

To illuminate the C/L discrepancies, difference maps were made of the B_r, B_θ and B_ϕ components from SPI and the truth model for degrees $1 - 120$ and are shown in Figure 6.5. First, the differences are of magnitude less than 0.1 nT, but what is surprising is the broad-scale nature of the pattern. There is a clear $n = 2$, $m = 1$ mode in the differences which happens to be the major constituent of the ionospheric baseline field included in the forward model. This baseline serves to eliminated low-mid latitude nightside current in the ionosphere and will easily map into the lithospheric field in the absence of surface data such as the OHMs. Evidently, these differences, although dominant, represent a very small *relative* coefficient error and are consequently not detectable in the sensitivity matrix.

A similar comparison between the original and recovered fields is shown in Figures 6.6, 6.7 and 6.8 for the OSPI model. In general, there is noticably more degradation in this model than in SPI, particularly in the C/L fields where the degree correlation at $n = 120$ has dropped to almost 0.9. However, this "degraded" model is still well within acceptable limits of observability for all target parameters. The SV sensitivity matrices show much more deviation across all orders m at high n values and the C/L matrix shows an enhancement of the pattern seen earlier in SPI. The lower quality of the OSPI solution is probably due to the poor spatial distribution of the observatories, which may not be able to sustain an accurate global solution much above $n = 8$. The OHM influence is distorting the otherwise highly accurate resolving power of the satellites, and this is perturbing the SV (since the biases effectively remove any direct OHM influence on the static field parameters), which will indirectly affect the rest of the solution space.

There is, however, one major improvement seen in the OSPI model which cannot be overstated; the resolution of the very low degree SV and C/L terms (especially $n = 1$) is greatly enhanced when OHMs are added. For example, there is much less scatter in the $n = 1$ and $n = 2$ C/L terms and the g_1^0 coefficient difference has gone from about 0.03 nT in SPI to about 0.005 nT in OSPI. Difference maps like those in Figure 6.5 are shown in Figure 6.9 for OSPI. The overall differences are now reduced compared to SPI, at least at non-polar latitudes where there does seem to be a slight enhancement. However, differences still have magnitudes of less than 0.17 nT. There is now a strong zonal content to these maps aligned with a dipole coordinate system which indicates that although the major modes of the ionospheric baseline, such as $n = 2$, $m = 1$, have been resolved with the inclusion of OHM data, perhaps their uneven distribution is slightly perturbing higher degree zonal modes of this baseline.

In summary, we have seen that in the case of "perfect indices", whether using all the data or satellites only, the recovered fields match the original field to very high accuracy using a number of metrics. Thus, the "closed-loop" simulation has been demonstrated.

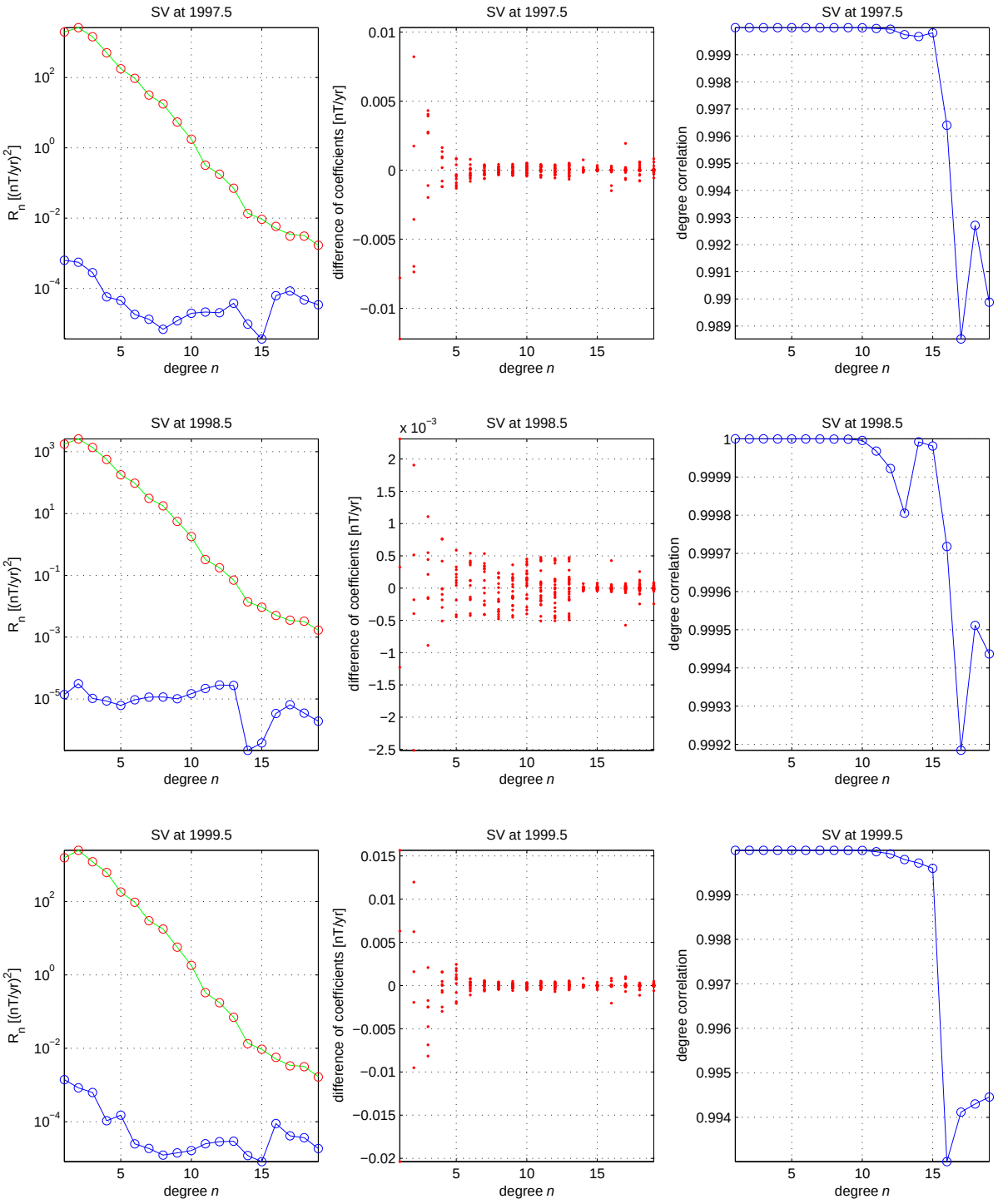

Figure 6.2: Comparision of original and recovered SPI secular variation (SV) at 1997.5, 1998.5 and 1999.5 at Earth's surface. Left: R_n spectra of the original (green), recovered (red) and difference (blue) models. Middle: Difference of the coefficients, in dependency on degree n. Right: Degree correlations between recovered and original model.

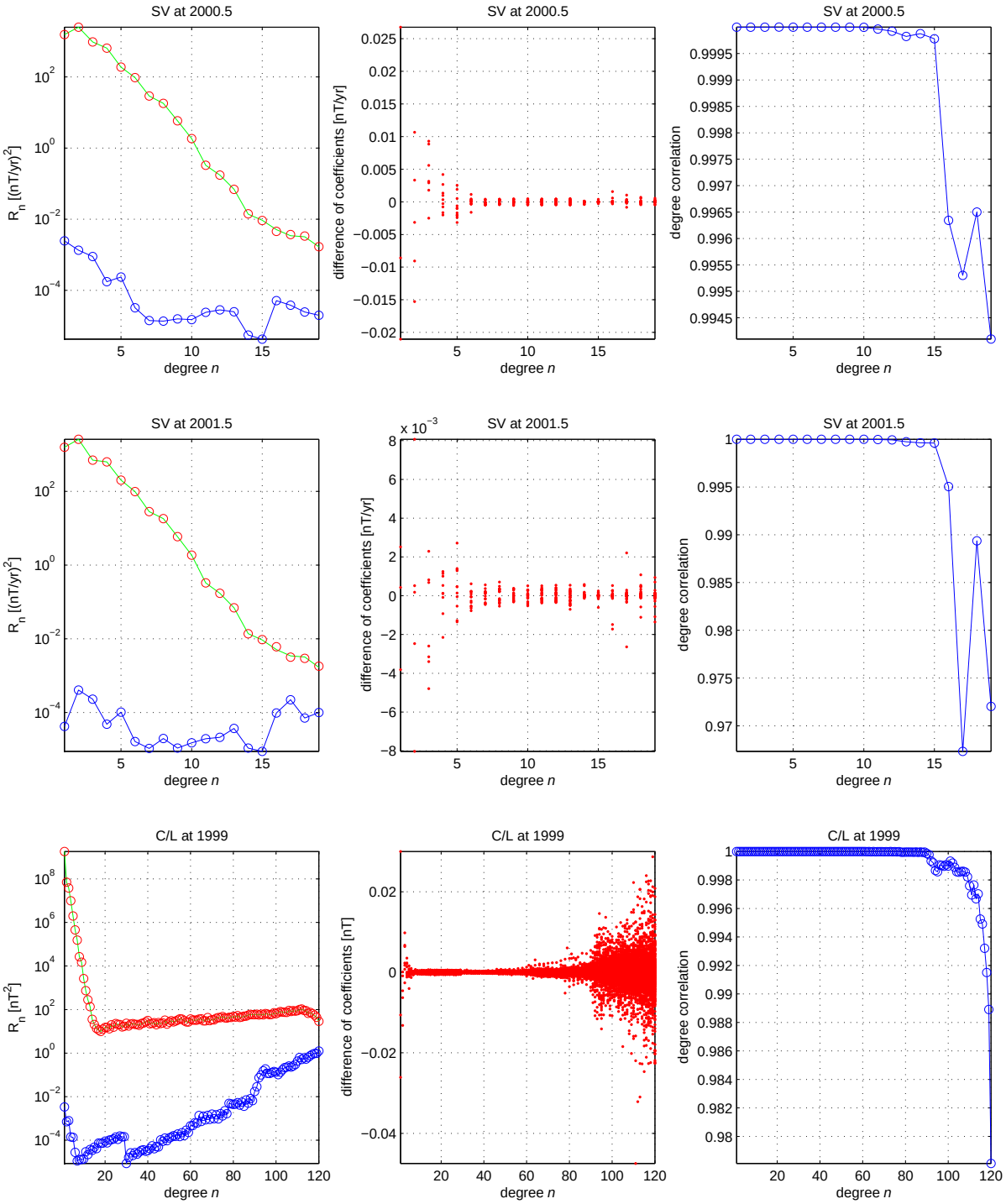

Figure 6.3: Same as Fig. 6.2, but for SV at 2000.5 and 2001.5 and for the core and lithosphere (C/L) at 1999.0 at Earth's surface.

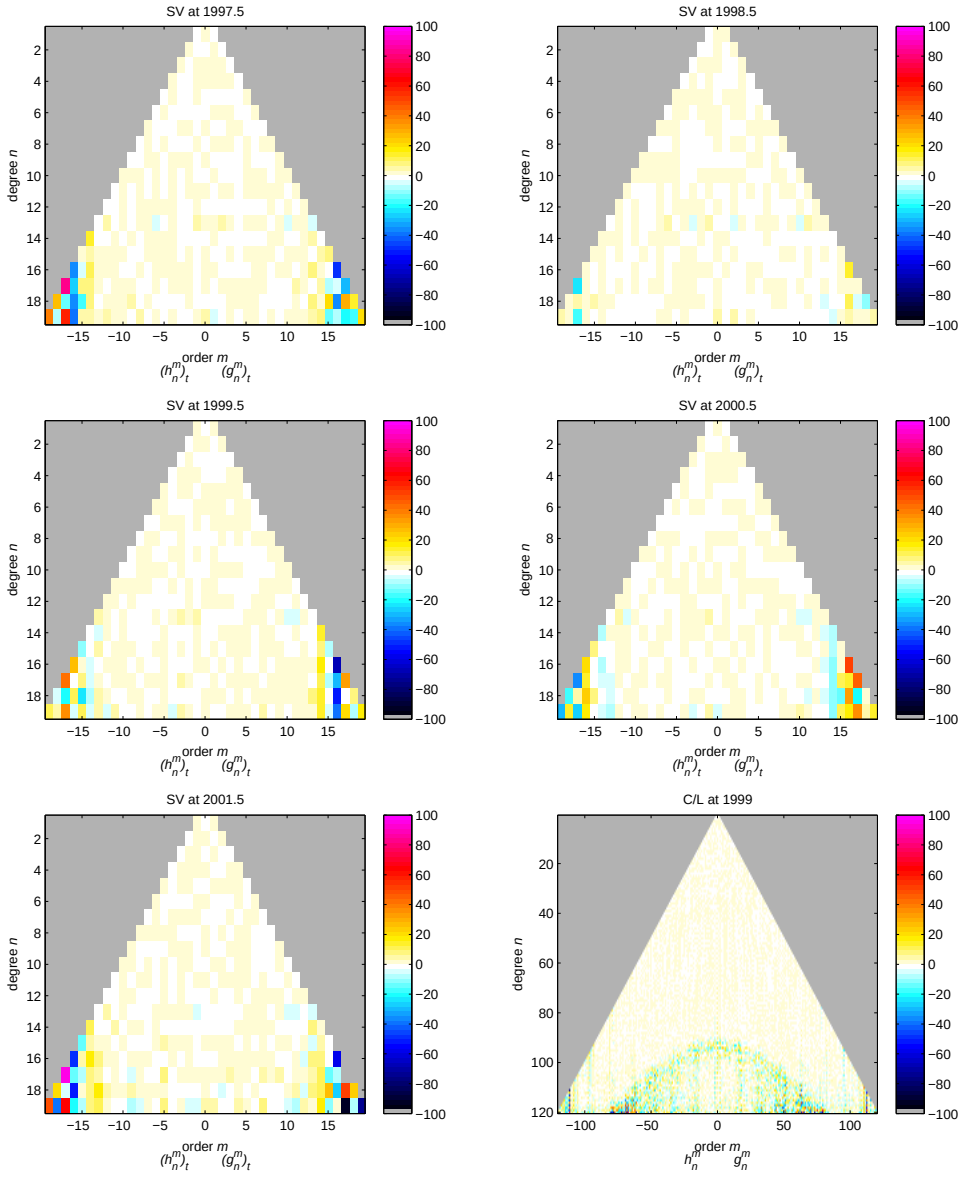

Figure 6.4: Sensitivity matrices for the SPI SV and C/L models corresponding to those in Figs. 6.2 and 6.3.

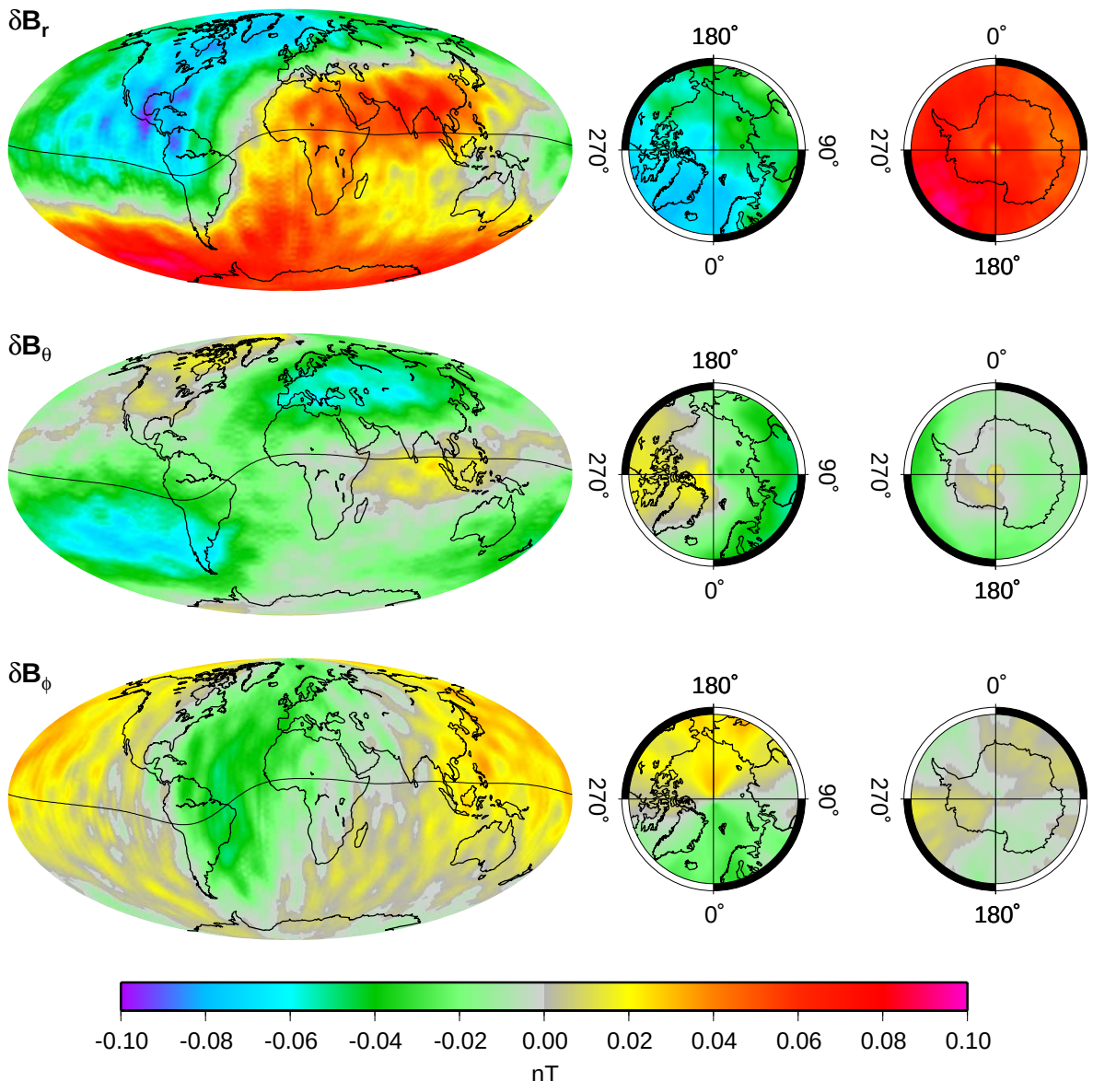

Figure 6.5: C/L difference maps in the B_r, B_θ and B_ϕ components from SPI and the truth model for degrees $1 - 120$.

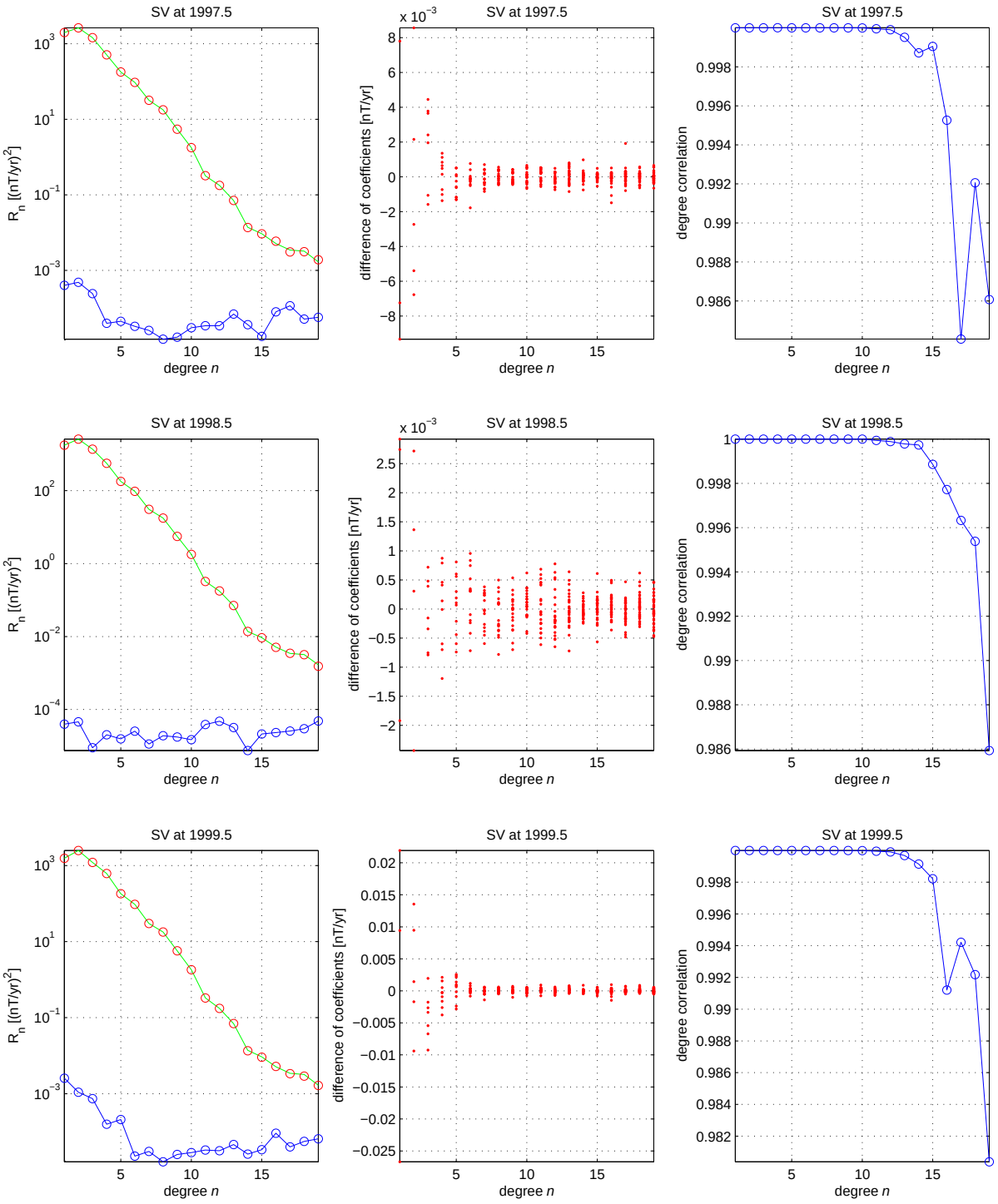

Figure 6.6: Same as Fig. 6.2, but for the OSPI model.

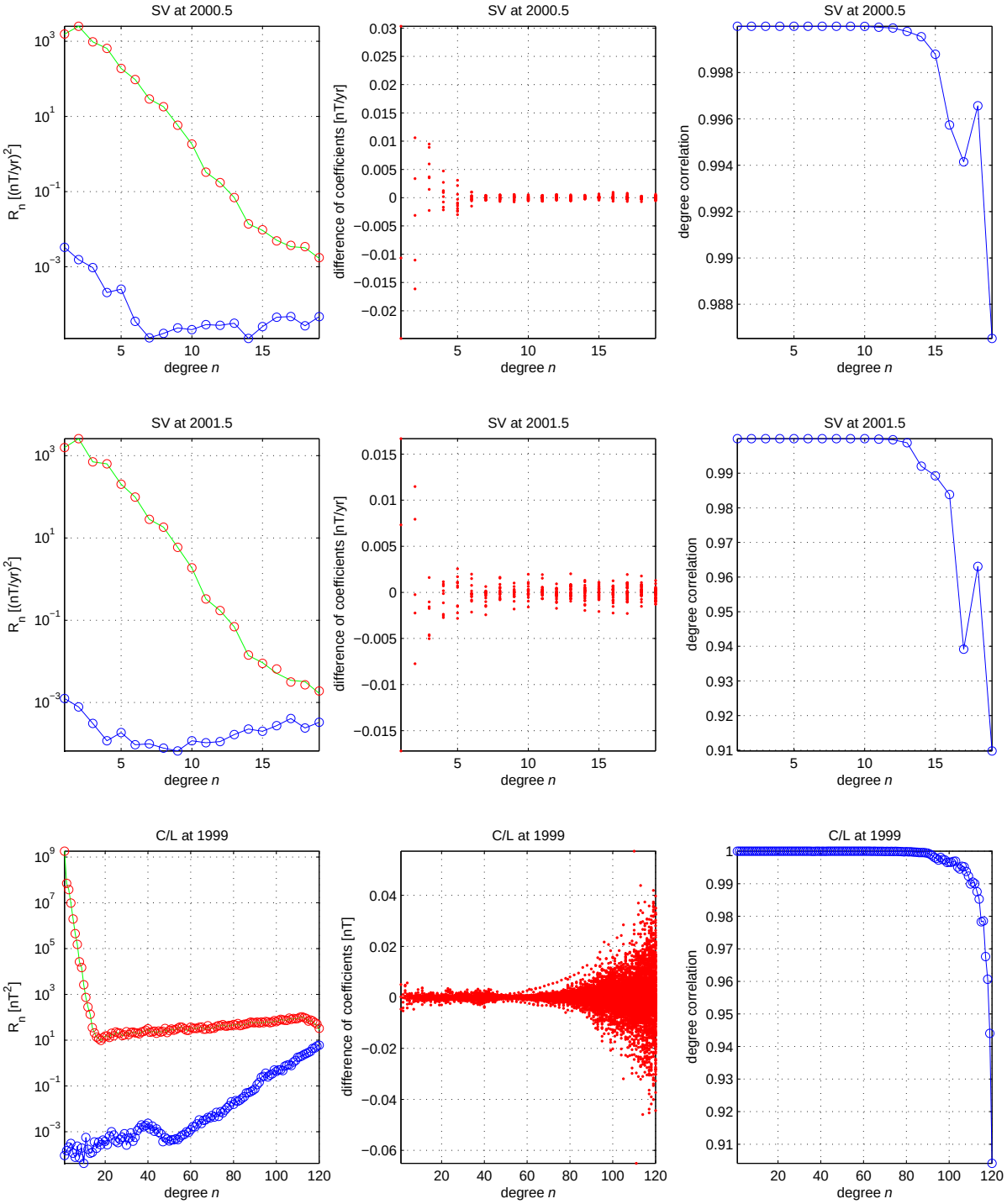

Figure 6.7: Same as Fig. 6.3, but for the OSPI model.

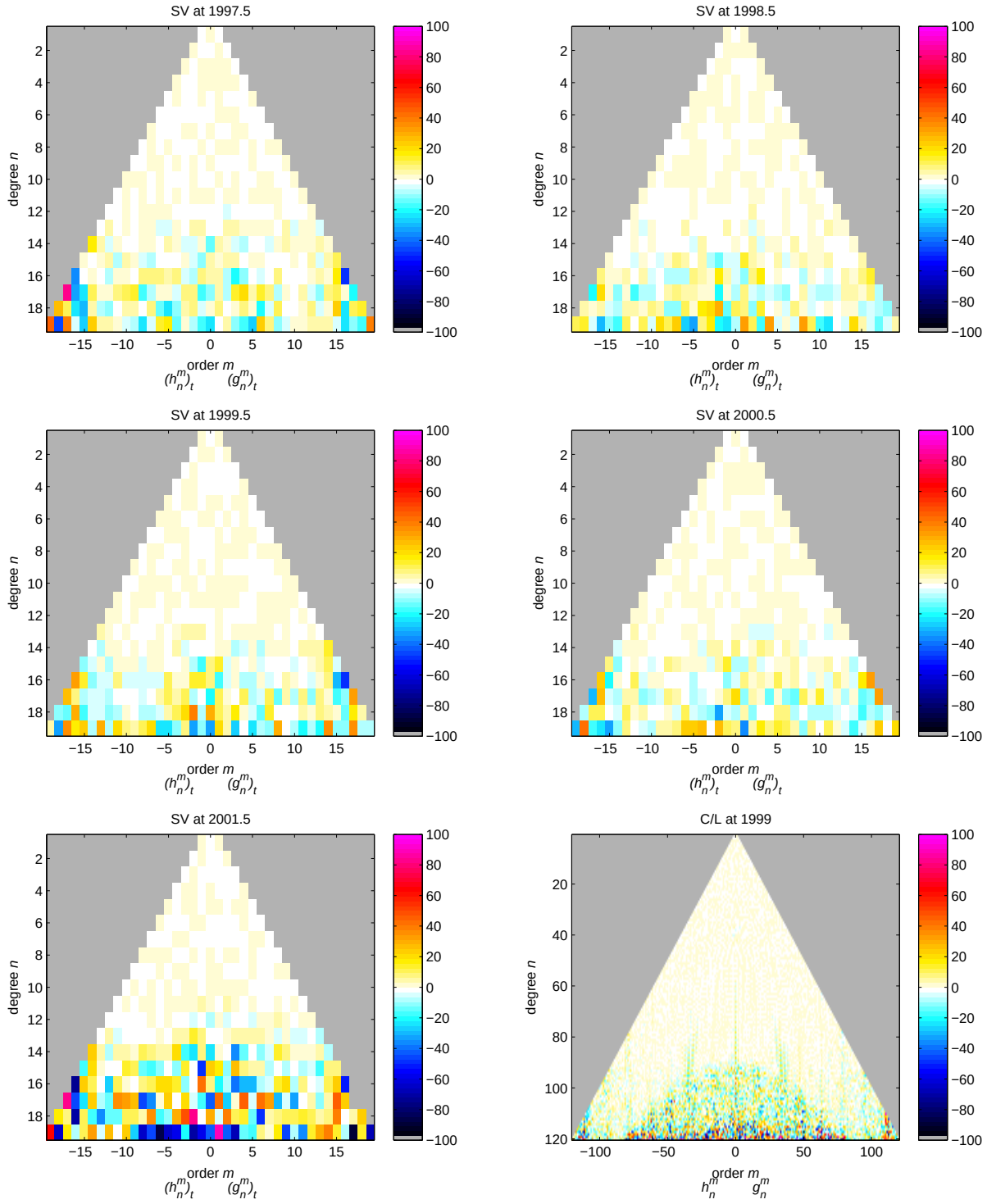

Figure 6.8: Same as Fig. 6.4, but for the OSPI model.

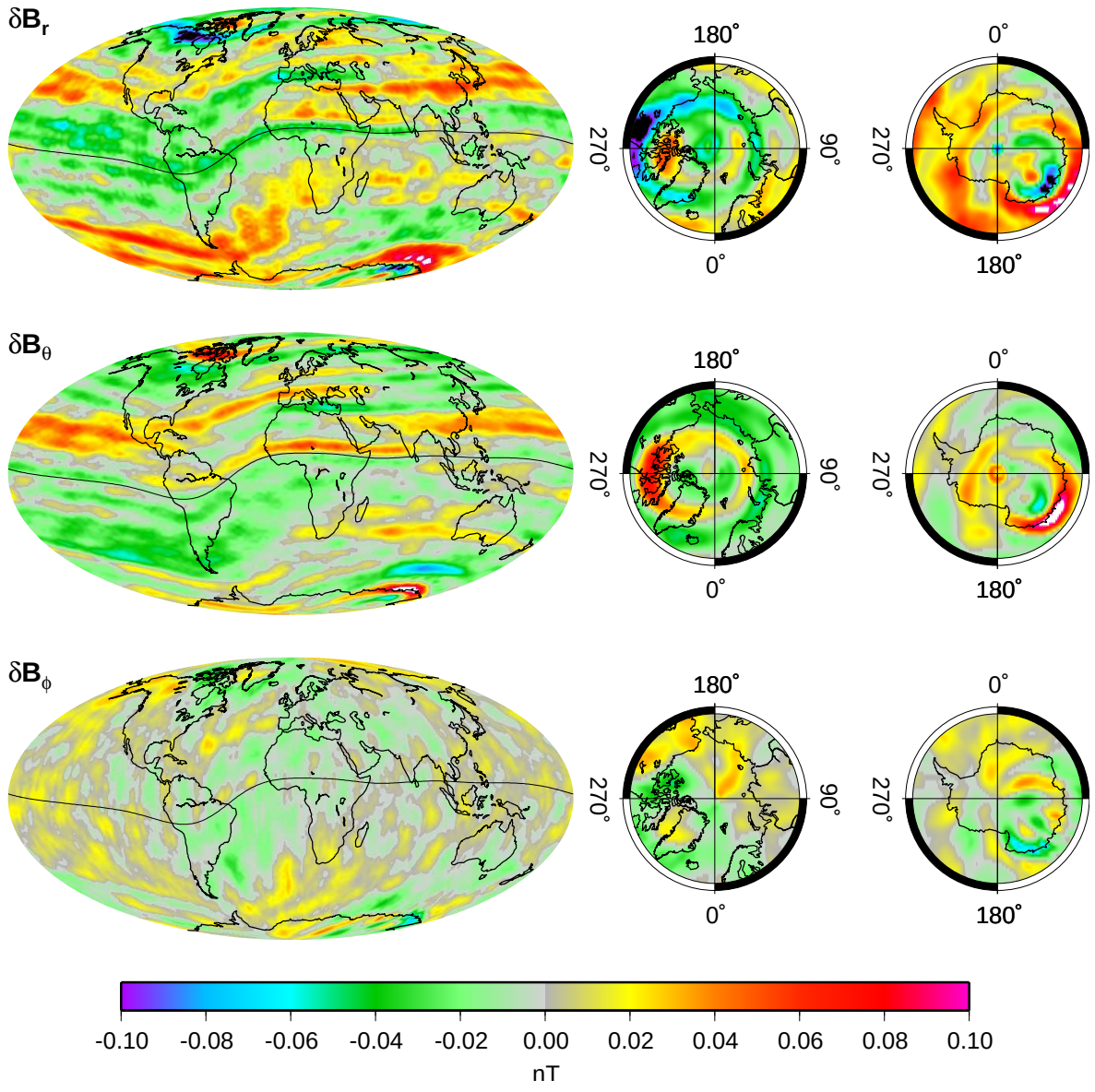

Figure 6.9: Same as Fig. 6.5, but for OSPI.

6.1.5 Task 3: Inversion of noisy data

Task 3 differs from Task 2 in that now realistic instrument noise has been added to the system, as well as more realistic complexity in the magnetosphere and its associated induced contribution. It should be noted that the toroidal field used in Task 2 is not considered realistic at the altitudes of the lower satellites, and so has been excluded all together from this study. One of the major deficiencies of the CI approach in Task 2 was the use of magnetic indices to track the temporal fluctuations of the Ring current and solar flux indices to track that of the ionosphere. Therefore, the estimation algorithm has been redesigned in an attempt to make it independent of these indicators. However, even with these enhancements, it is still reasonable to select data that is more likely to behave in more predictable ways. In this study, all quiet-time 1-min *Swarm* data from all satellites available for the selection of constellation #2 were considered over the entire mission envelope, 1997-2002. Quiet conditions imply $K_p(t) \leq 1^+$, $K_p(t - 3\text{h}) \leq 2^0$, $|D_{\text{st}}| \leq 20$ nT, and $|\Delta D_{\text{st}}/\Delta t| \leq 3$ nT/hr being true at time t of the measurement.

The remainder of this section will describe the new algorithm and its application to cases in which simultaneous measurements from *Swarm* satellites 1, 2, 4 and 5 are used (sw1245), from satellites 2, 4 and 5 only (sw245), from satellites 4 and 5 only (sw45), and only from 4 (sw4). It will be shown that satellites in at least two well-separated orbit planes provide the best resolution of the core secular variation (SV).

6.1.6 Estimation Algorithm used in Task 3

Since the magnetospheric field is generally broad-scale and quickly varying, the new algorithm models it as static snapshots within 1-hr bins. These static fields are represented as spherical harmonic (SH) expansions in dipole coordinates of maximum degree $N_{max} = 3$ and order $M_{max} = 1$. A single *Swarm* satellite traverses roughly 2/3 of an orbit in one hour, which appears to be quite sufficient for resolving these truncation levels. However, the associated induced field is a function of a 3-D conductivity structure and requires a more complicated spatial representation. In this case, an $N_{max} = M_{max} = 3$ SH expansion is used. It will be seen that in order to resolve these features, one should have satellites in at least two well-separated orbit planes.

A similar approach was initially used to model the ionospheric E-region field and its associated induced contribution. Near the Earth the ionosphere has much smaller-scale spatial structure than the magnetosphere, particularly under daylight conditions. However, since the ionospheric contributions are synthesized from a quiet-time field model, the temporal variation is much more regular and long-period. These two conditions suggest that a longer bin width could be used to model ionospheric fields. If no relationship between the primary (E-region) and secondary (induced) is assumed, then one must rely heavily upon surface data, e.g., observatories, to facilitate separation of the primary field from the core/SV field. Initial tests using data from *Swarm* constellation #2 and observatory hourly-means (OHM) data to solve for the ionosphere over 3-hr bins were unsuccessful because neither the two orbit planes of this constelltion nor the OHM stations distribution were able to resolve the small-scale structure in these fields. Thus, for purposes of this study, the ionosphere and its induced contribution are modelled as in Task 2 using a known 1-D conductivity model and tracking solar activity influence via 3-monthly means of the $F10.7$ cm solar radio flux ($F10.7_{3\text{m}}$).

The core field is parameterized as in Task 2 such that secular variation is described in terms of cubic B-splines with a single interior knot at 1999.5, which also serves as the model epoch. Recall that the magnetospheric field and its induced contribution do not have a simple relationship, and thus, they are not coupled in the model. Recall also that the CI approach attempts to invert for all sources simultaneously, which would clearly lead to colinearities between this induced portion and the core SV. However, it is expected that a large percentage of the power in the induced field will be high-frequency and may provide a way of separation. To this end, the broad-scale, high-frequency portion of the induced field is constrained to be orthogonal to the core SV over the mission envelope. Clearly, this does not offer separation between core SV and long-period induction effects (but this is impossible anyways without additional knowledge of the conductivity structure being introduced), but it will be seen to provide quite good estimates of the high-frequency induced field.

The model parameters were coestimated in a weighted least-squares sense using equal-area weighting for each satellite, and the instrument noise was treated as being stationary and isotropic. Orthogonality between SV and induced fields was introduced as a set of linear equalities.

6.1.7 Task 3: Results and Discussion

Case sw1245 In this case data from all four *Swarm* satellites were used to derive a model designated sw1245. The number of 1-hr snapshot bins was about 14,000, each of which contain 24 parameters; the number of core/SV+ionospheric parameters was about 24,500; the number of linear orthogonalization constraints was 90. Figures 6.10, 6.11 and 6.12 compare the original and recovered sw1245 SV at 1997.5, 1998.5, 1999.5, 2000.5 and 2001.5 and the core and lithosphere (C/L) at 1999.0 at Earth's surface. The comparisons are made on the basis of the R_n spectrum, degree correlation, and sensitivity matrix defined in section 2.2 of the Task 2 Report, respectively. Also shown is the difference of coefficients. The quality of the high-degree SV recovery varies over the life of the mission, being a bit better towards the middle of the mission. Degrees $1-14$ are recovered consistently above the 0.7 correlation threshold, but degrees up to 16 are recovered at this level during certain times. It is expected that recovery of degrees $1-2$ will be enhanced if OHM data are used. The sensitivity matrices show a gradual degradation across all orders with increasing degree. It should be noted that there do exist long-term trends in the magnetospheric induced contributions (up to about 0.2 nT/yr for B_θ) whose power is commensurate with that of the high-degree SV. Hence this power would be folded into the SV estimation by design and could be the cause of the observed deterioration.

The crustal field is being recovered adequately from degrees $20-90$; the degree correlations are above 0.97 through degree 80. The sensitivity matrix shows a nice uniform recovery that is roughly independent of order and which very gradually deteriorates with increasing degree. However, as seen in Task 2, there is a peculiar sharp decline in recoverability centered on $m = 0$ for $n > 90$, which appears as a hemispherical pattern. The exact cause is unknown, but it is related to ionospheric contributions and could be compensation by the crustal field for the quasi-static ionospheric baseline which exists in the synthesizing model.

Case sw245 Here, data from one high, 2, and two low *Swarm* satellites, 4 and 5, were used to derive model sw245. Because orbit planes in essentially two distinct local times are maintained in this case, the same parameterization of external and high-frequency induced fields has been successfully used as in the sw1245 case. Comparing Figures 6.13 - 6.15 for sw245 with the same Figures 6.10 - 6.12 for sw1245 shows very minor degradation in the SV specta, most notably for $n > 16$. For lower degrees the results are actually mixed as to which model does better. The crustal field recovery quality is also very close, but there is a slight improvement for sw245 for degree 89 and 90. As for the sensitivity matrices, they indeed confirm the closeness of the SV and crustal models. In fact, the crustal matrices for the two cases are practically indistinguishable by eye.

These two cases suggest a very salient point in that the sw1245 case does only marginally better than sw245, and even this is not absolutely true in all comparisons. Hence, for SV and crustal recovery using CI in Task 3, it appears that mission specifications can be met with three satellites (the 4-5 low pair and one of the high pair), if necessary.

Case sw45 In this case data from the two low *Swarm* satellites, 4 and 5, were used to derive a model designated sw45. Initially, the high-frequency induced field was modelled with an $N_{max} = M_{max} = 3$ SH expansion, but this proved to be unseparable. Evidently, the orbit planes of these two satellites were not separated sufficiently in local-time. Thus, the final sw45 model employed an $M_{max} = 1$, which was well resolved by this orbit configuration. Figures 6.16 and 6.17 are similar to Figures 6.10 and 6.11, respectively, and show that there has indeed been a degradation in SV recoverability for the current configuration. The sw1245 model does a consistently better job at recovering the SV field in the range of $n > 1$, except possibly for $n > 17$ at 2000.5. The greatest difference in model performance appears to be in the mid-range of the expansion ($4 < n < 18$), and given that there is known contamination of the high-degree SV by long-period induction effects, then this is quite a strong argument for multiple

satellites in well-separated orbits. The sensivitiy matrices do not show much difference between the two models and so they are not included for sw45.

As for crustal field recovery, sw45 actually does a slightly better job than sw1245 for high-degrees. However, this is easily explained by the fact that the high-altitude data of satellites 1 and 2 is less sensitive to the high-degree crust, but still exerts influence on the estimation. In practice, crustal fields should either be determined from the low satellites exclusively or from a proper weighting of all satellites.

As a final comparison of the recovery capability between the two, three and four satellite constellation cases, coefficients corresponding to the various field sources for individual harmonics have been plotted. Figure 6.18 shows the h_2^1, $(h_2^1)_t$, b_2^1 (induced) and s_2^1 coefficients plotted over the time of the mission from the sw45 (red), sw245 (green), sw1245 (blue) models and h_2^1 and $(h_2^1)_t$ from the true (black) model. One sees generally good recovery of h_2^1 and $(h_2^1)_t$ for each satellite model, but with the sw45 case clearly degraded. The three and four satellite cases show good recovery over the middle portion of the envelope, but degraded slightly near the edges. The recovery of b_2^1 and S_2^1 is fairly consistent amongst the models over the bins, but with sw45 showing the most scatter.

Figure 6.19 is similar to Fig. 6.18 except it is for the h_1^1 family of coefficients. Here the recovery performance is different between sw45 (blue), sw245 (red) and sw1245 (green). The sw1245 still appears superior to the others, e.g., the recovery of the inflection point in $(h_1^1)_t$ near 200.5 which is absent in the other models. However, sw245 shows a distinct bias in h_1^1 and is more degraded in $(h_1^1)_t$ recovery near the edges of the mission envelope than sw45. In addition, one notices large oscillations in the sw245 and sw1245 b_1^1 and s_1^1 coefficients at the beginning of the mission, which attenuate to a minimum amplitude around 2000, and then slightly increase towards the end of the mission (note how the orthogonality constraints leave b_1^1 with no long-term trend, whereas s_1^1 has a clear long-term trend). These oscillations are enhanced in the sw245 case. This corresponds well to the observed discepancies between the true and recovered $(h_1^1)_t$. However, what is most intriguing is that this correlates extremely well with the evolution of the local-time separation between the two orbit planes as seen in Figure 3.8 and the velocity direction in these planes. At the begining of the mission the two planes are coincident and the satellites are co-rotating within the planes. The separation increases to a maximum 6 hr separation three years into the mission. Near the end of the mission the oribit planes again come to within 2 hr of each other, but the satellites are now counter-rotating.

Recall that $M_{max} = 3$ for sw245 and sw1245, but $M_{max} = 1$ for sw45. At the beginning of the mission all orbit planes are coincident and all satelliets are co-rotating in them. Thus, sw245 and sw1245 have no advantage over sw45 in resolving external and induced structure initially . However, sw245 and sw1245 are asked to resolve more complicated structure regardless and this leads to colinearity between the parameters manifested as spurious oscillations. It is believed that the combination of orbit plane separation and counter-rotation work to resolve this aliasing as the mission progresses, thus leading to a decrease in oscillations 18 months into the mission. Clearly, multiple satellite orbits allow for better resolution of complicated spatial structure over short periods of time, but only after an initial phase. However, certain coefficient families such as h_2^1 appear to be resolved in a consistent fashion over the entire mission.

Case sw4 Only data from low *Swarm* satellite 4 was used in this case to derive a model designated as sw4. A SH expansion with $N_{max} = 3$ and $M_{max} = 1$ was used to model the high-frequency induced field, as in the sw45 model. It was found that the magnetospheric and the high-frequency induced fields, and consequently the SV field, were not well resolved when using 1-hr bins. Therefore, the bins were increased to 3-hr duration where the resulting observability was quite good. Figures 6.20 and 6.21 again illustrate the trio of metrics used to evaluate these models. The model is recovering the SV spectrum well for $n < 14$, especially in the mid-range of $3 < n < 14$, but not as well as the sw1245 model did. The recovery is significantly degraded for $n > 13$, as can be seen in the SV sensitivity matrices in Figure 6.22. This shows that although the modelled parameters were observable, i.e., the system matrices were very well-conditioned, they were insufficient in describing the actual signal. Indeed, the combination of spatial complexity and high-frequency variation present in the external field contributions could not be resovled adequately with a single satellite; increasing the bin duration allows more complicated spatial structure to be modelled, but this longer averaging window evidently looses critical information, especially about high-degree SV.

This behavior also affects the crustal field recovery, as can be seen in the trio of metric plots. Only coefficients in the $n < 78$ regime have degree correlations roughly above 0.7. The sensitivity matrix indicates that much of the degradation is occurring when n and m are both above about 40. This is interesting since the problem of multiple satellite altitudes mentioned earlier does not apply here. It suggests that perhaps some portion of the induced signal not modelled by the longer 3-hr bins is contaminating the crustal field. Thus, the lack of mutlitple satellites in well-separated orbits can be seen to degrade not only the SV recovery, but also that of the crustal field.

6.1.8 Summary

The *Swarm* satellite data of Task 3 now include more complicated magnetospheric and associated induced contributions as well as realistic instrument noise. The 1-min data of constellation #2 have been analyzed using the CI approach in order to capture the SV and crustal coefficients. In order to demonstrate the advantage of using a *Swarm* constellation of well-separated orbit planes to recover these fields, four combinations of satellites were compared: 1, 2, 4 and 5 (sw1245), 2, 4, and 5 (sw245), 4 and 5 (sw45), and 4 only (sw4). The ability to model the magnetospheric and high-frequency induced fields is a function of the number of distinct, well-separated orbital planes and the distribution of satellites within these planes. For sw1245 and sw245, which consist of two planes, as well as a 180° separation in plane $1-2$ for the former, this induced field could be resolved to $M_{max} = 3$ over 1-hr bins, but for sw45, which consists of two slightly separated planes, $M_{max} = 1$ was used over 1-hr bins. For sw4, $M_{max} = 1$ was used, but the bin duration had to be increased to 3-hr. Given the transient nature of the magnetospheric and its associated induced field, sw1245 and sw245 clearly performed best. Although both sw1245 and sw245 contain data from both high and low satellites, their crustal recovery was still considered excellent up to about $n = 90$. Comparisons between sw1245 to sw245 find only a marginal improvement of the four satellites over the three, and even this is not a consistent improvement, e.g., the highest degree crustal terms are better resolved in the sw245 case. However, the critical point is that the mission specifications can still be met using the sw245 case, and presumably an sw145 case, if necessary.

Recall that because of the limited instantaneous sampling of local-times by constellation #2, the possibility of modelling the time evolution of the more spatially complicated ionospheric field and its associated induced contribution in bins had to be forgone. However, this study suggests that a constellation of satellites in orbits equally spaced in local-time could provide for maximum spatial resolution in the least amount of time. This would allow for a model which is independent of proxy functions that track solar activity such as ($F10.7_{3m}$), just as the use of D_{st} was eliminated from the magnetospheric parameterization here. In addition, the successful extraction of the high-frequency induced contribution in this study could allow for a much more realistic transfer function to be developed which could then aid surface data in separating the ionosphere from its induced contribution.

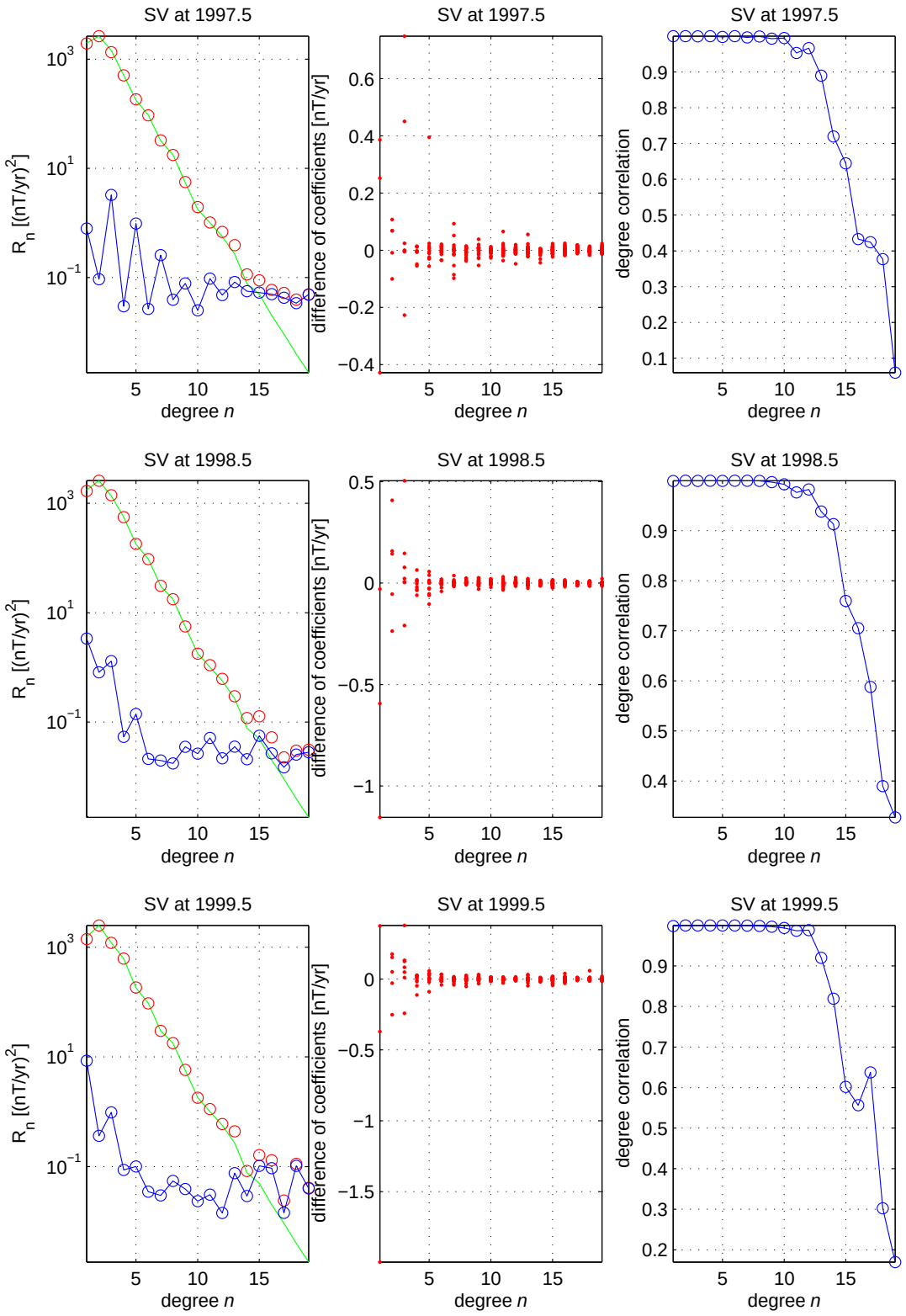

Figure 6.10: Comparision of original and recovered sw1245 secular variation (SV) at 1997.5, 1998.5 and 1999.5 at Earth's surface. Left: R_n spectra of the original (green), recovered (red) and difference (blue) models. Middle: Difference of the coefficients, in dependency on degree n. Right: Degree correlations between recovered and original model.

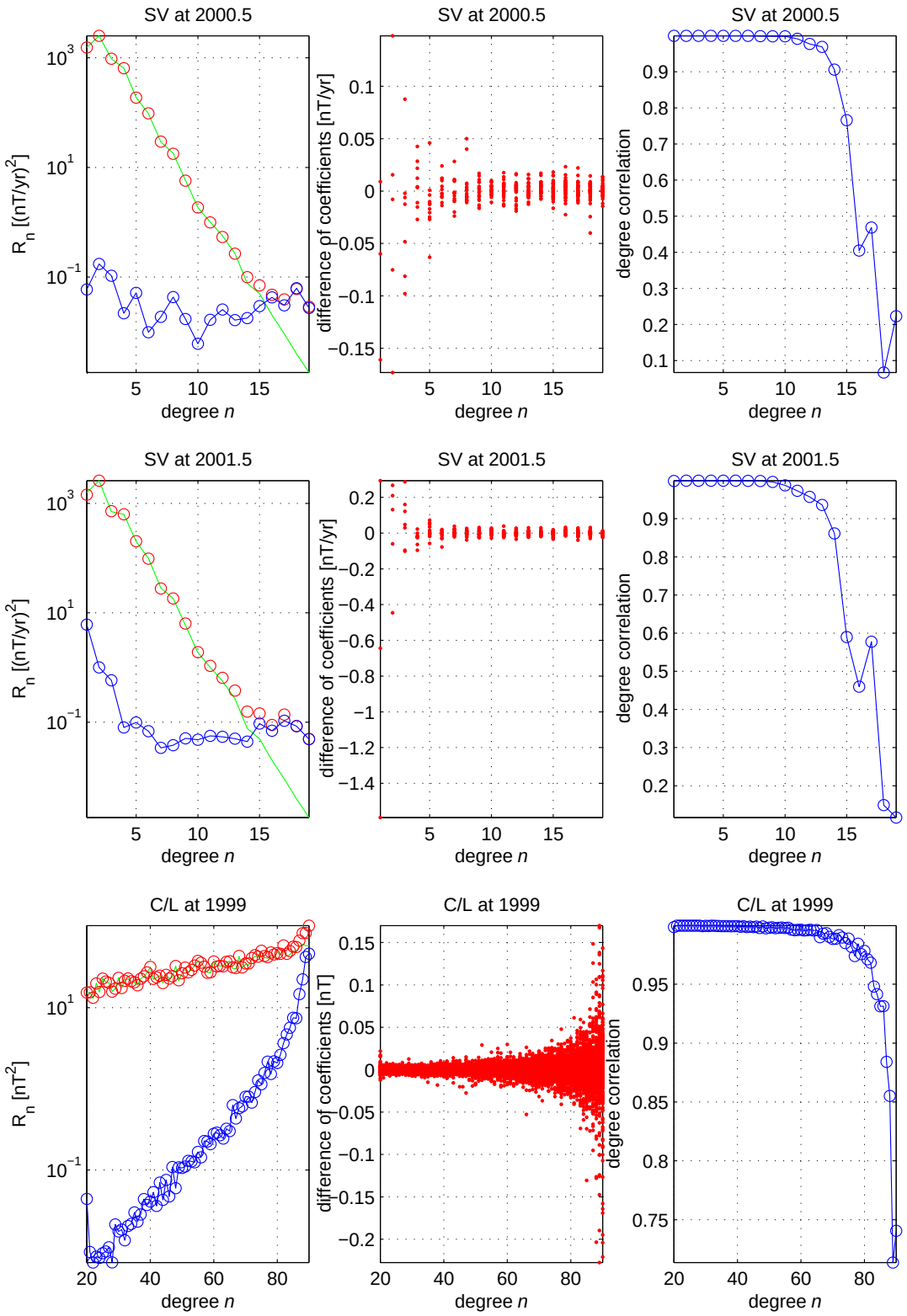

Figure 6.11: Same as Fig. 6.10, but for SV at 2000.5 and 2001.5 and for the core and lithosphere (C/L) at 1999.0 at Earth's surface.

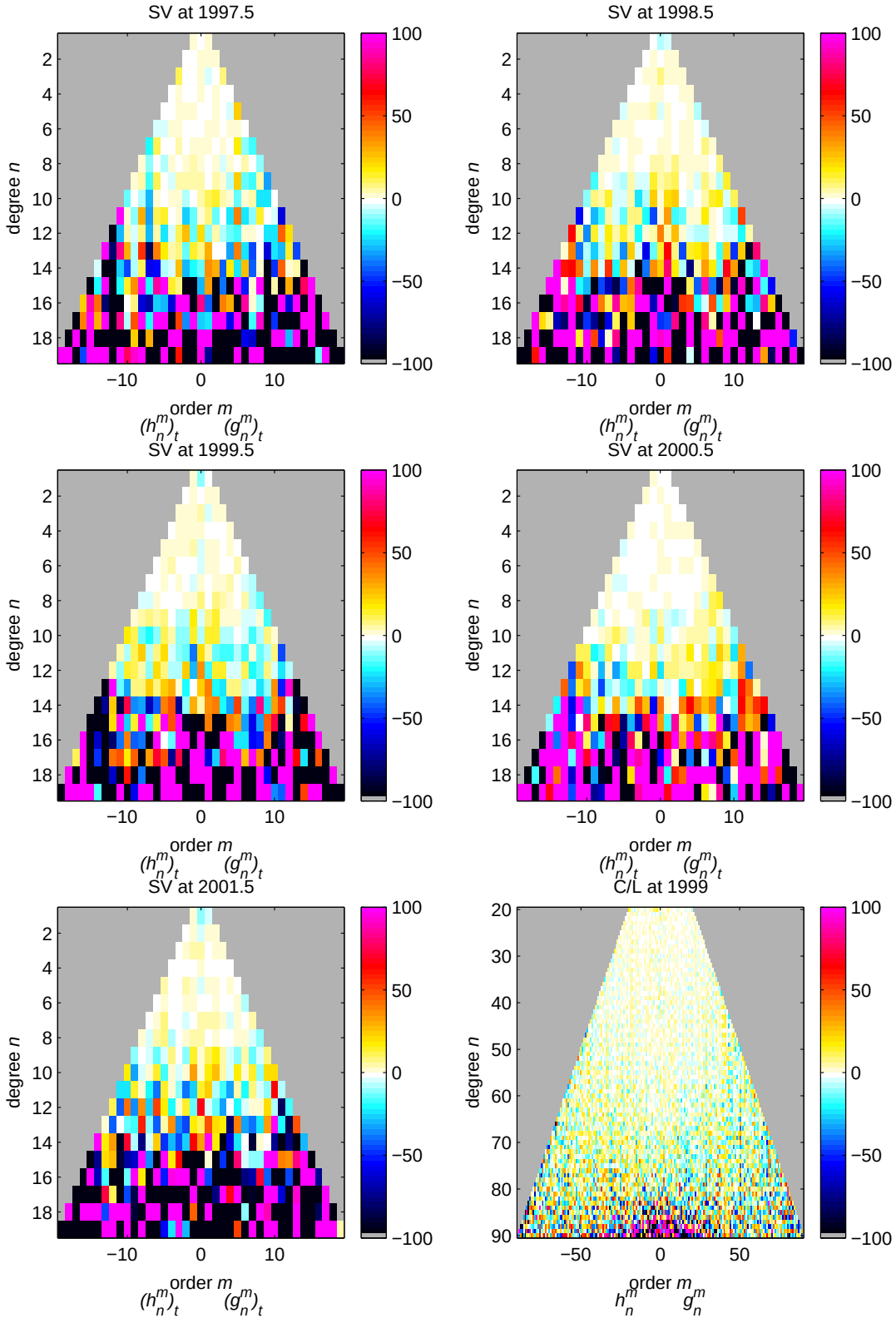

Figure 6.12: Sensitivity matrices for the sw1245 SV and C/L models corresponding to those in 6.10 and 6.11.

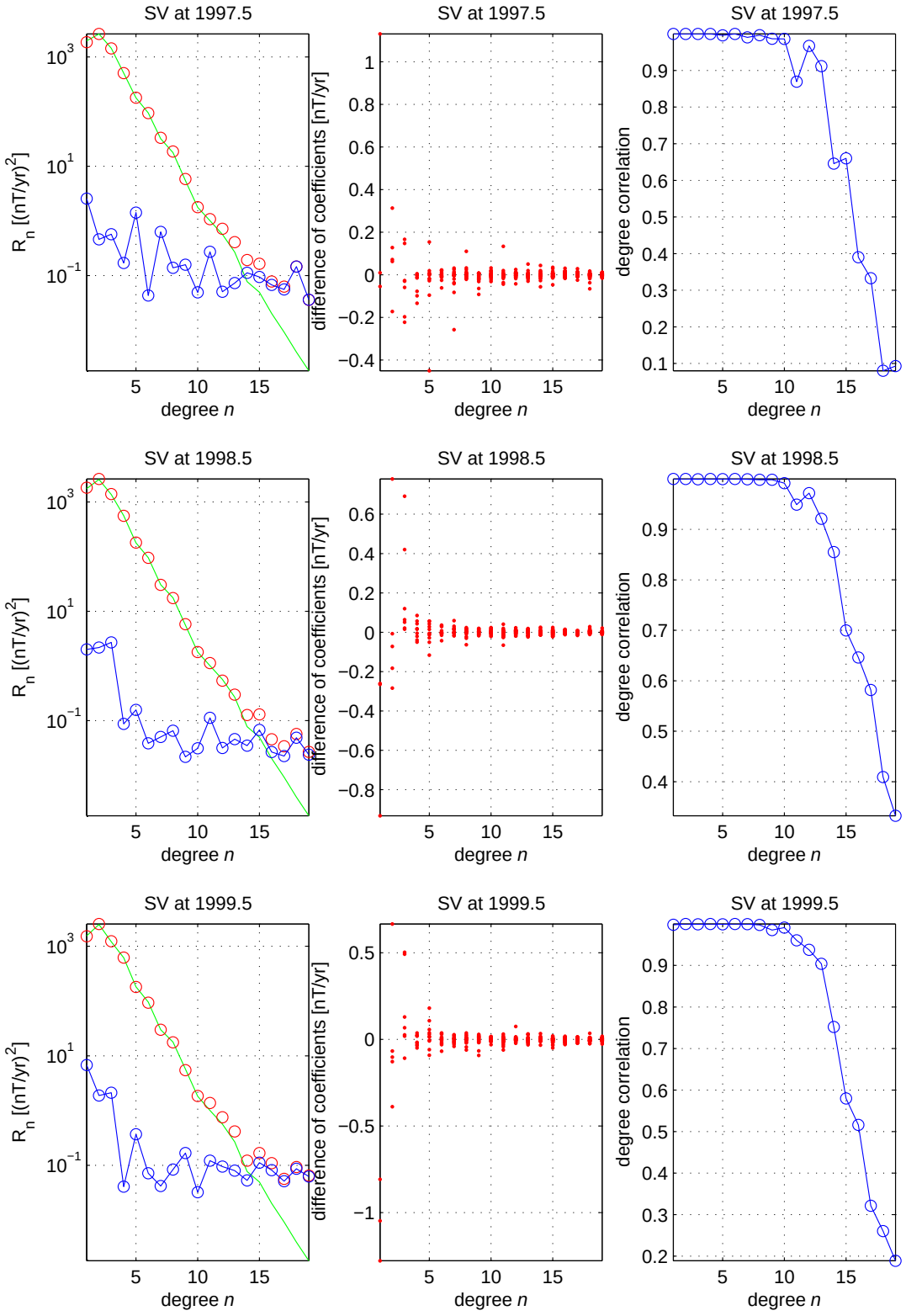

Figure 6.13: Same as Fig. 6.10, but for the sw245 model.

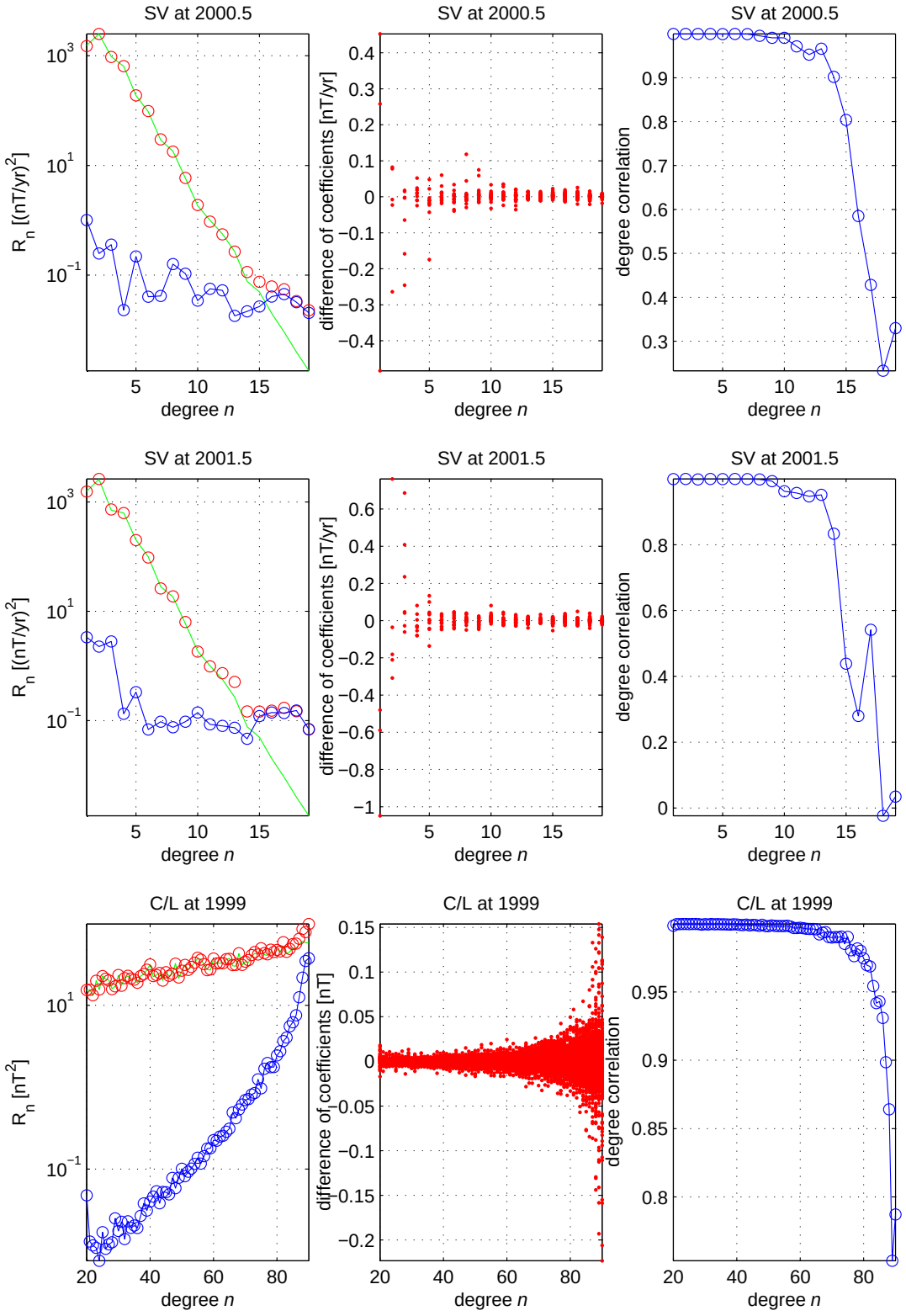

Figure 6.14: Same as Fig. 6.11, but for the sw245 model.

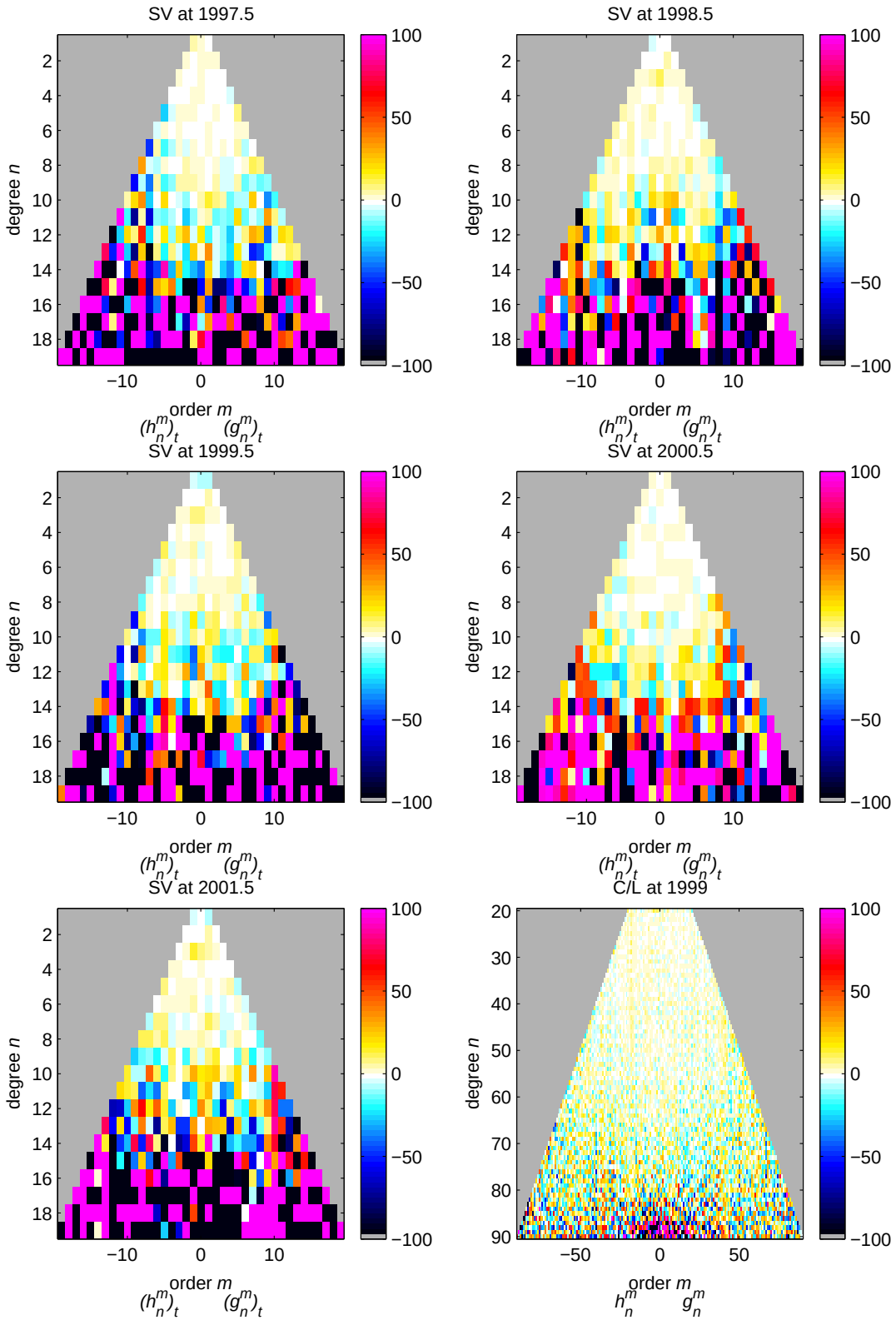

Figure 6.15: Same as Fig. 6.12, but for the sw245 model.

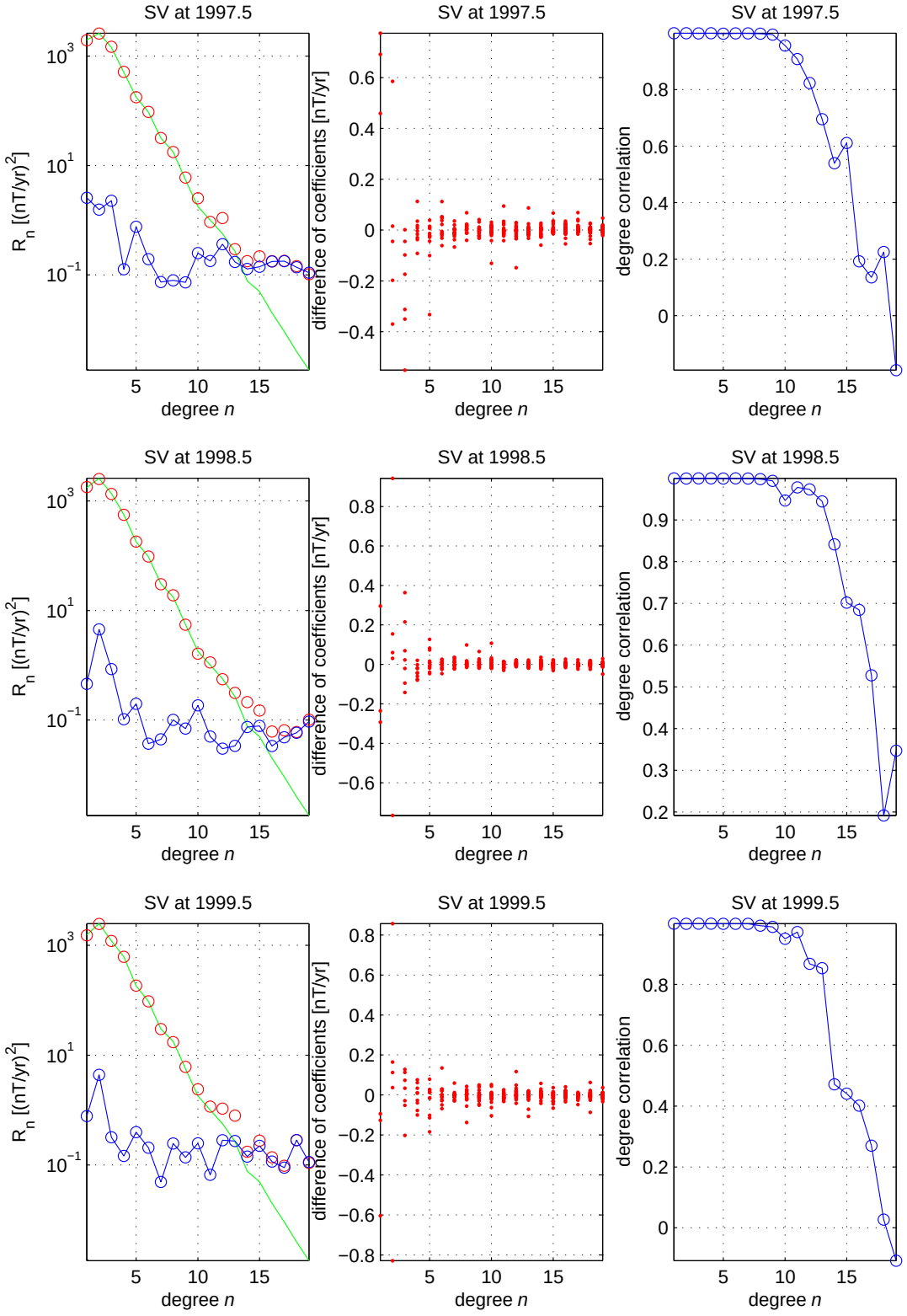

Figure 6.16: Same as Fig. 6.10, but for the sw45 model.

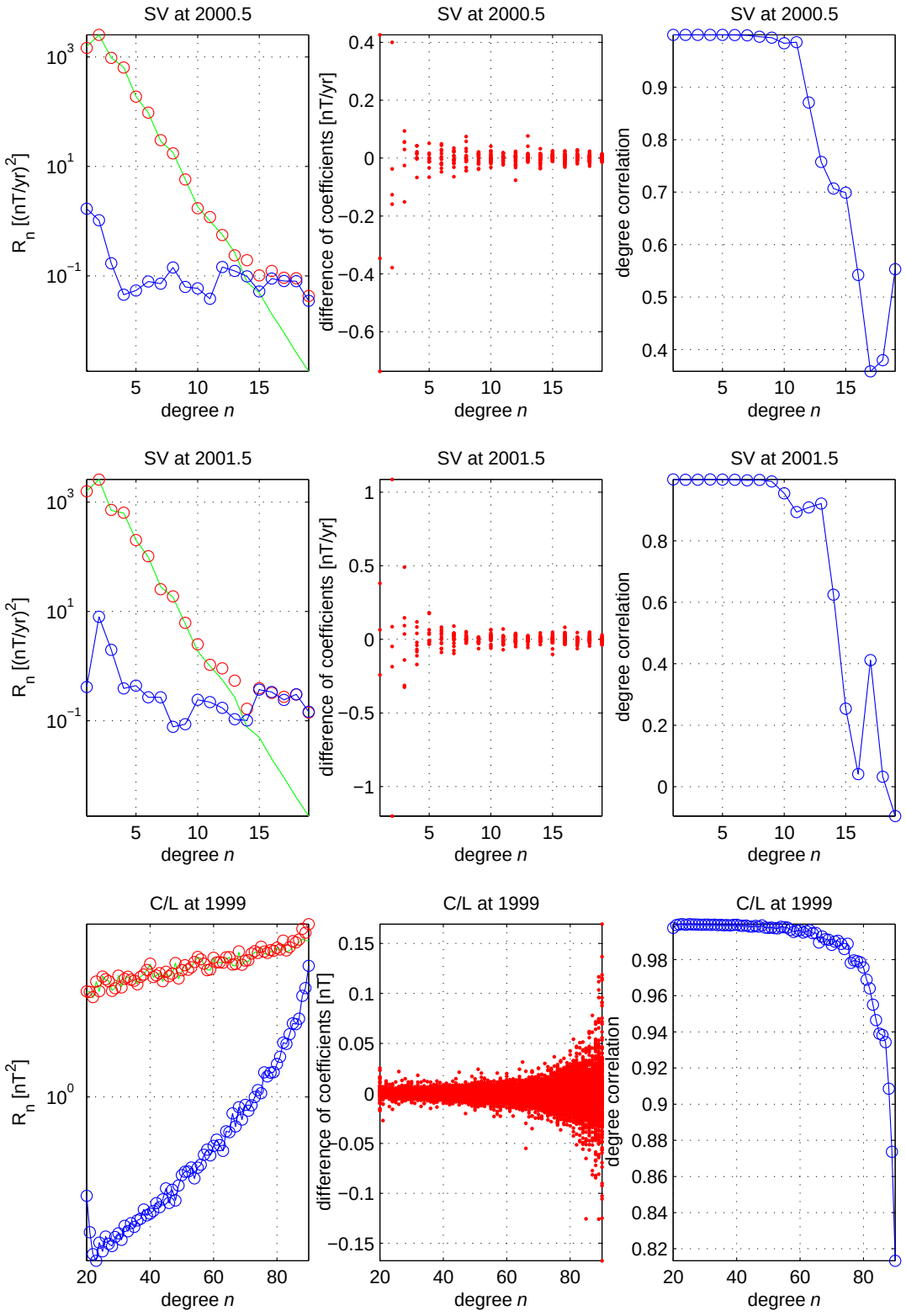

Figure 6.17: Same as Fig. 6.11, but for the sw45 model.

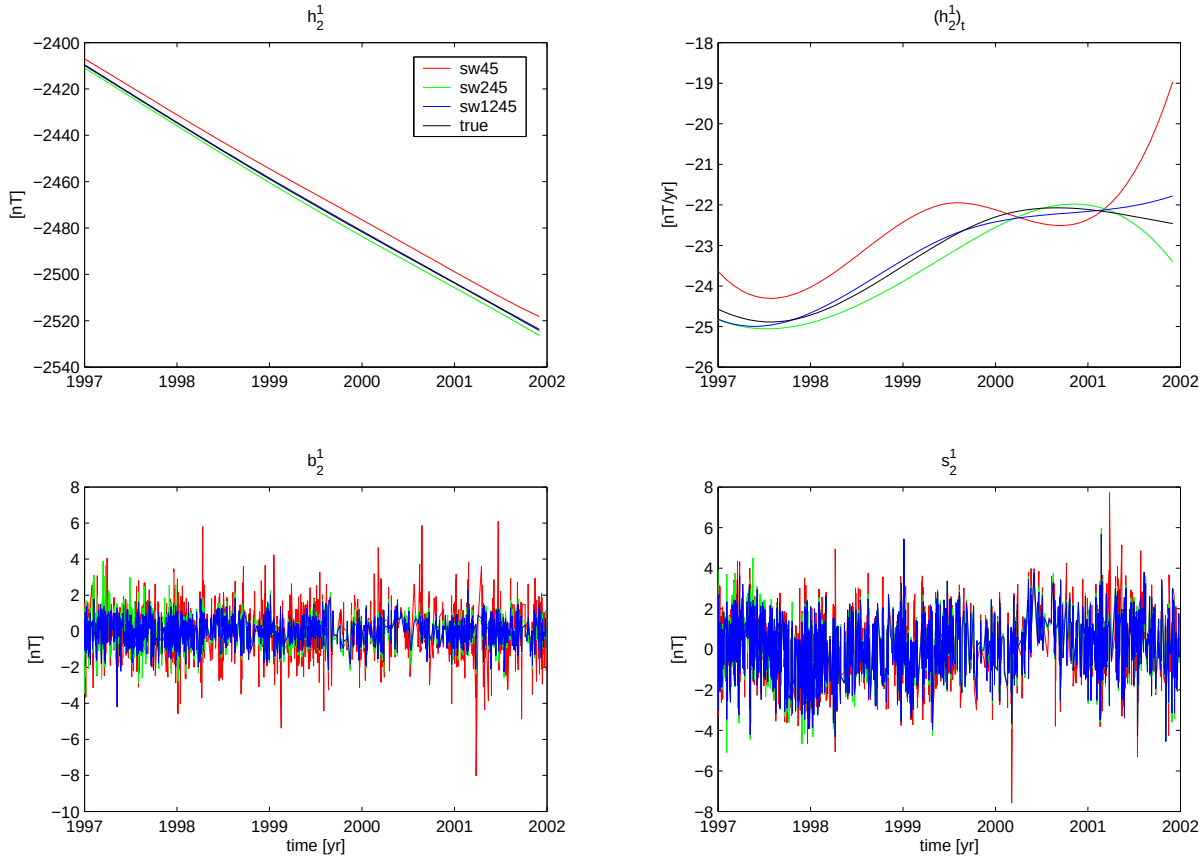

Figure 6.18: Plots of the h_2^1, $(h_2^1)_t$, b_2^1 (induced) and s_2^1 coefficients over the mission envelope resolved by the sw45 model (red), sw245 (green) and sw1245 (blue) models, and the true h_2^1 and $(h_2^1)_t$ coefficients (black).

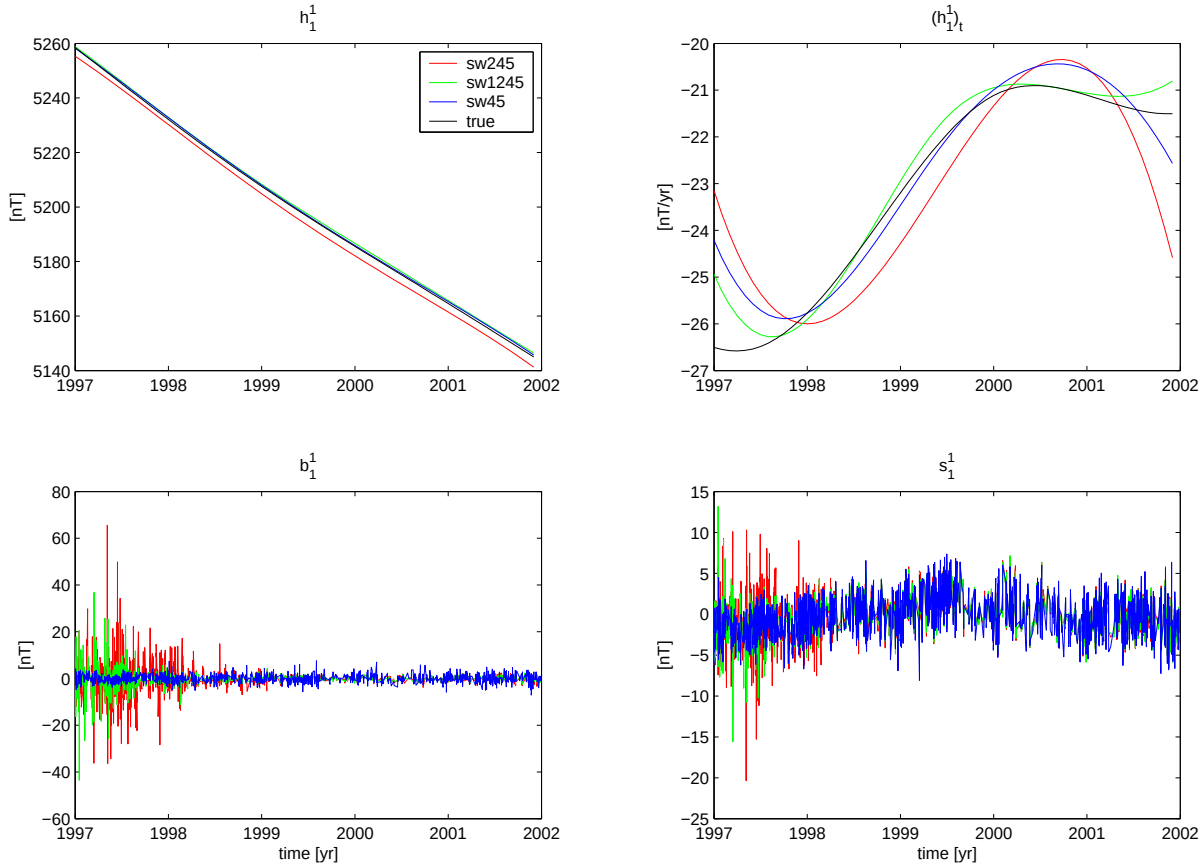

Figure 6.19: Plots of the h_1^1, $(h_1^1)_t$, b_1^1 (induced) and s_1^1 coefficients over the mission envelope resolved by the sw45 model (blue), sw245 (red) and sw1245 (green) models, and the true h_1^1 and $(h_1^1)_t$ coefficients (black).

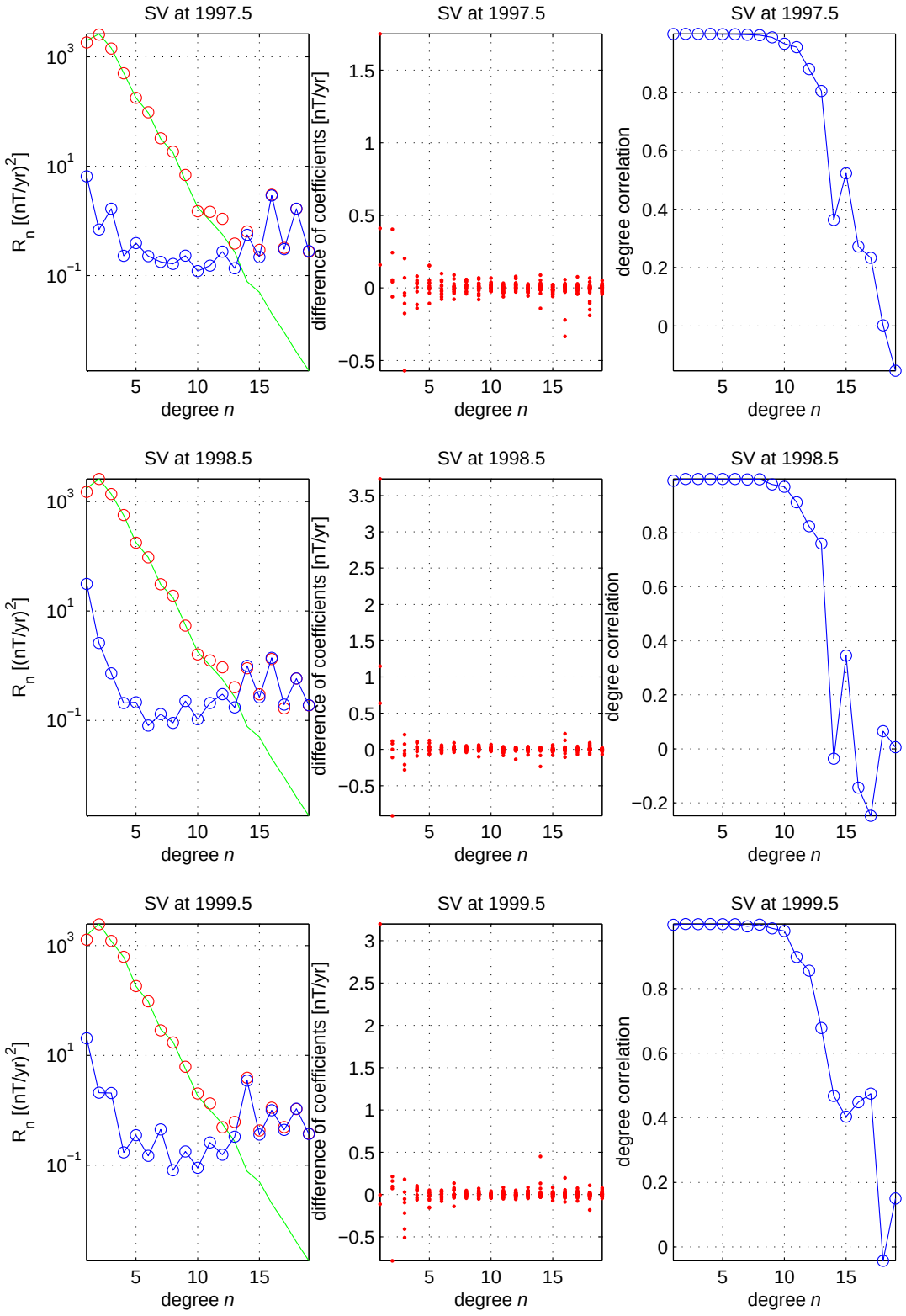

Figure 6.20: Same as Fig. 6.10, but for the sw4 model.

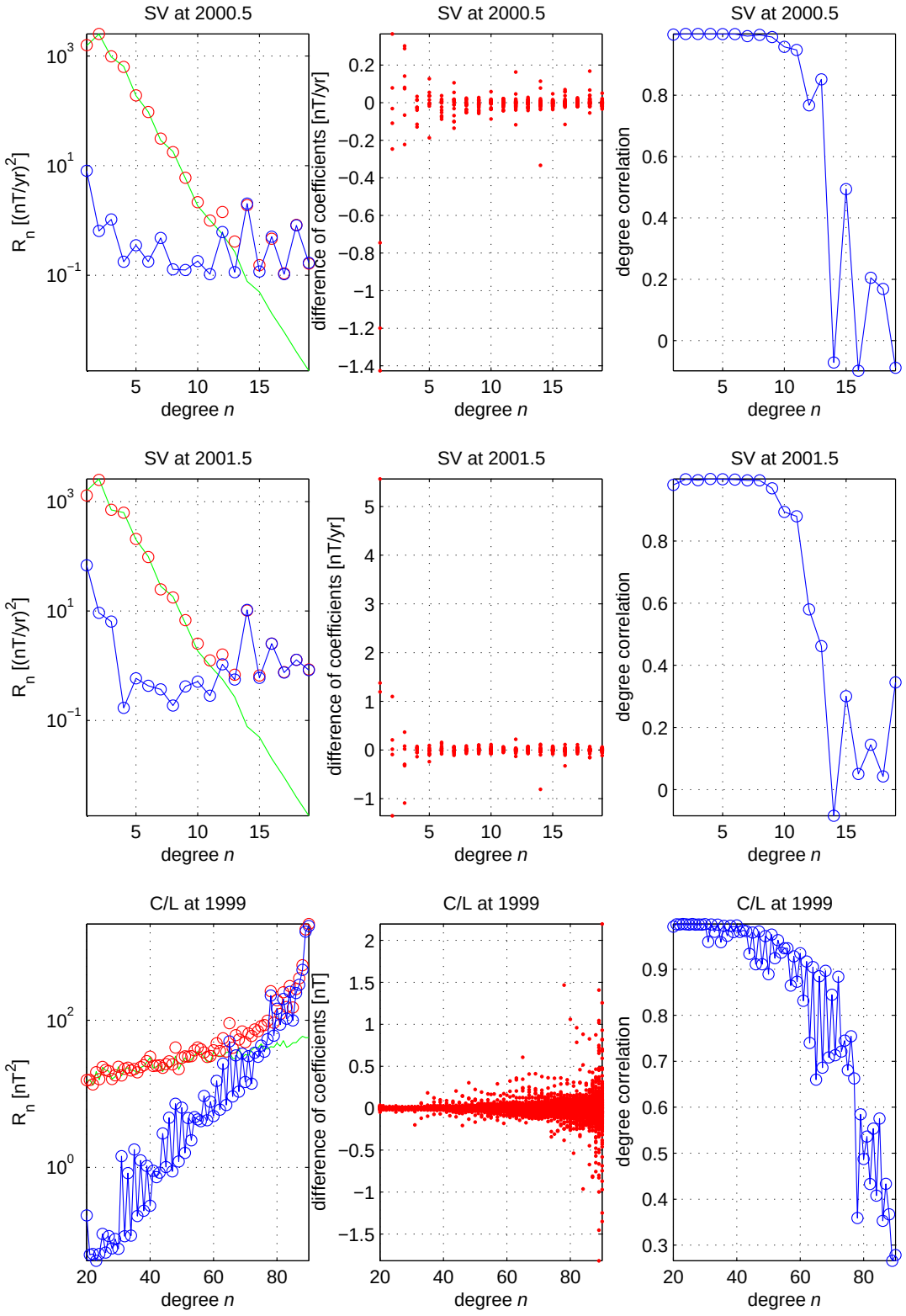

Figure 6.21: Same as Fig. 6.11, but for the sw4 model.

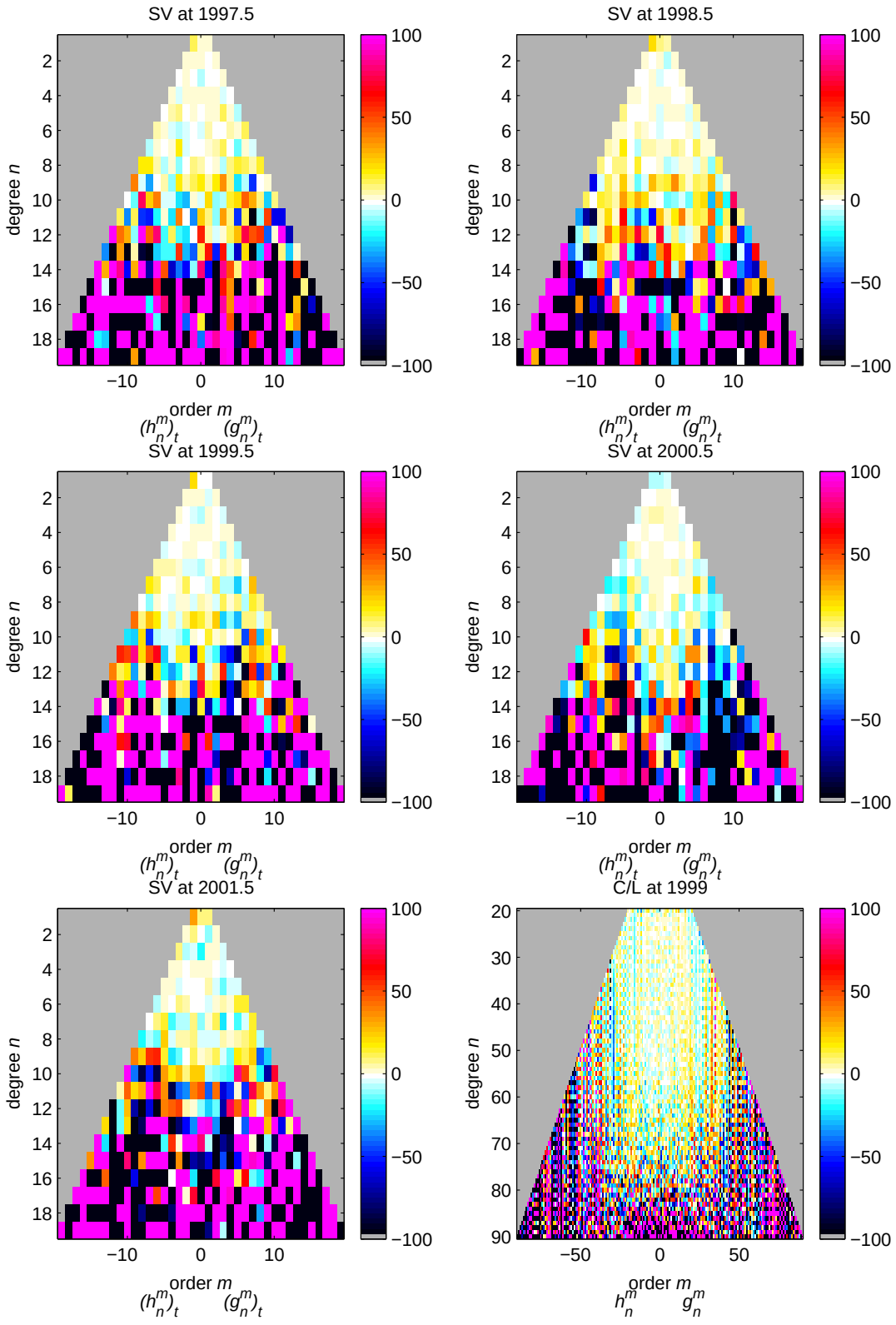

Figure 6.22: Same as Fig. 6.12, but for the sw4 model.

6.2 Lithospheric Field Recovery – Method 1

This section describes the effort to determine the high-degree lithospheric magnetic field using the methods developed by the GeoForschungsZentrum Potsdam. The work is associated with WP 4230 "Lithospheric Field – Method 1".

In the first part (Sections 6.2.1 to 6.2.4) we are describing our attempts to recover the lithospheric field from simulated , "clean" data that only contain the lithospheric signal. This is regarded an important step for testing the reliability of the involved algorithms. The questions to be addressed include an assessment of the consistency of the synthetic data, a check of the ability of the inversion algorithm applied for recovering the spherical harmonic coefficients, and an investigation of the role of the polar gap. The synthetic magnetic data contain features of scale sizes much smaller than have ever been recovered from satellites. It will be interesting to see, to which extend they can be resolved in this inversion. In the second part of this study (Sections 6.2.5 to 6.2.7) we perform the analysis with noise-free data that contain all source contributions. For these two parts data derived from Constellation #1 are used. Further studies, performed as part of Task 3, made use of the data from Constellation #2. The main purpose of those was to find out the benefit of having accompanying spacecraft separated in east-west direction. In addition, instrument noise has been added to the data.

6.2.1 Input Data Characteristics

Since the prime objectives are verifying the suitability of the data set and testing of the inversion approach, only that contribution to the synthetic data set which is attributed to the lithospheric field has been used in this first part. It contains the magnetic field structures derived from spherical harmonic of degree 14 to 120, where the lithospheric magnetisation dominates over the core field contribution. As mentioned before, coefficients above $n = 110$ are tapered to reach zero at $n = 120$. The lithospheric field contribution is assumed to be stationary in time.

Further details, which may be of interest for this study, are that the individual field values are truncated at a resolution of 0.01 nT. The sampling rate of the data set is 1 per min. Although, a spacing between consecutive points of 450 km seems to be quite coarse, a sufficiently high resolution can be achieved when the considered data interval is long enough. For the inversions presented below we used the most favourable part of the mission, the last 400 days of the modelled mission, MJD2000=330 to 730 (November 2000 - December 2001). The data used in this study are taken from one of the low satellites, SW3. This spacecraft traversed the altitude range from 400 km down to 250 km during the considered time span.

A quantity which may be of concern for the investigations performed here, is the size of the polar gap. Due to the inclination of the SW3 spacecraft of 85.4° a circular area with a radius of about 500 km is left unsampled. This again is larger than the half-wavelength of 170 km corresponding to a degree and order 120 model.

6.2.2 Approach used for Data Inversion

The basic method employed here is the well-known algorithm for retrieving spherical harmonic (SH) coefficients from vector measurements well distributed over a sphere. As required, the vector readings of the lithospheric contribution fulfil the Laplace equation. Due to the sampling pattern of a satellite in a near-polar orbit the density of measurement points is much higher at polar latitudes than close to the equator. This disparity is compensated by down-weighting the high-latitude samples with respect to those from equatorial regions. After this treatment all areas (except for the polar gap) contribute equally to the global solution. Since we are dealing with noise-free data, no weighting is used in the inversion. The applied standard inversion algorithm finds a solution by minimising the rms-value of the residuals.

For the inversion we utilized in a first run the full vector information (three components). This contains quite a bit of redundant information. From the mathematical point of view it is sufficient to either use the vertical or the horizontal component. To test this effect all runs were repeated by using only the vertical component.

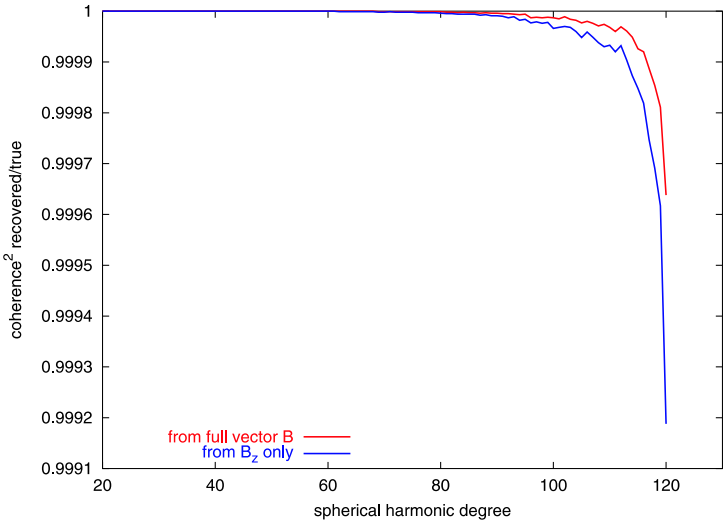

Figure 6.23: Degree correlation between the input and output lithospheric field models

6.2.3 Obtained Lithospheric Field Model from Study 1

Figure 6.23 shows the obtained degree correlation (cf. Eq. 5.2) between the input SH coefficients and the retrieved ones. According to this test both are virtually identical. A difference from unity is obtained only when the truncation beyond degrees 110 sets in. Here we obviously run out of signal. As expected, the full vector solution gives a slightly better result.

It is generally hard to imagine what the high correlation obtained above actually means. A more intuitive way of visualising the fit between input and output fields is to plot the direct differences on a global map. Figure 6.24a shows the results from the full vector solution. Obtained residuals are very small, well below 0.01 nT. In case of the solution with the vertical component, B_z, (cf. Fig. 6.24b) the differences are slightly larger, but still insignificant and evenly distributed. As an interesting feature, now the polar gap becomes visible in both hemispheres.

In a third test the SH coefficients between the original and the recovered model are directly compared. The obtained errors are colour-coded in the sensitivity matrix with degree n versus order m. Figure 6.25a shows the percentage error for the full vector solution. Here the deviations are generally well below 1% except for the degrees just below $n = 120$ where tapering becomes effective. Slightly larger errors are encountered if only the vertical component is used (cf. Fig. 6.25b). Worth noting is the distinct feature for coefficients with order $m = 0$. The somewhat enhanced errors of these zonal terms are caused by the polar gap. This point probably requires special attention in future configuration designs.

6.2.4 Discussion of Results from Study 1

The comparison between the synthetic input data and the retrieved magnetic field model reveals a very close fit of both sets for the case of clean data. The agreement is much better than the maximim error predicted in section 4.3 of the Task 1 Report for the linear 3D interpolation that has been used to create field values from SH terms above $n = 29$.

Several conclusions can be drawn from the obtained results. For example, the truncation of the generated magnetic field data to a resolution of 0.01 nT, which is achievable with state-of-the-art instrumentation, causes no limitation in the recovery of lithospheric signatures up to degree $n = 120$. Also the rather coarse sampling of 1 per min has no negative effect on the solution. The reason for that is, the lithospheric data set considered here is stationary, repeated sampling of all regions gradually fills in the gaps. In future approaches when a full field representation is used as input data with all its temporal variations, we plan to use a denser sampling of the order of one reading per 5 s.

A feature of the input data which effects all the presented results, is the tapering of the spectrum for degrees beyond $n = 110$. No reliable recovery of the magnetic signatures can be obtained at this short

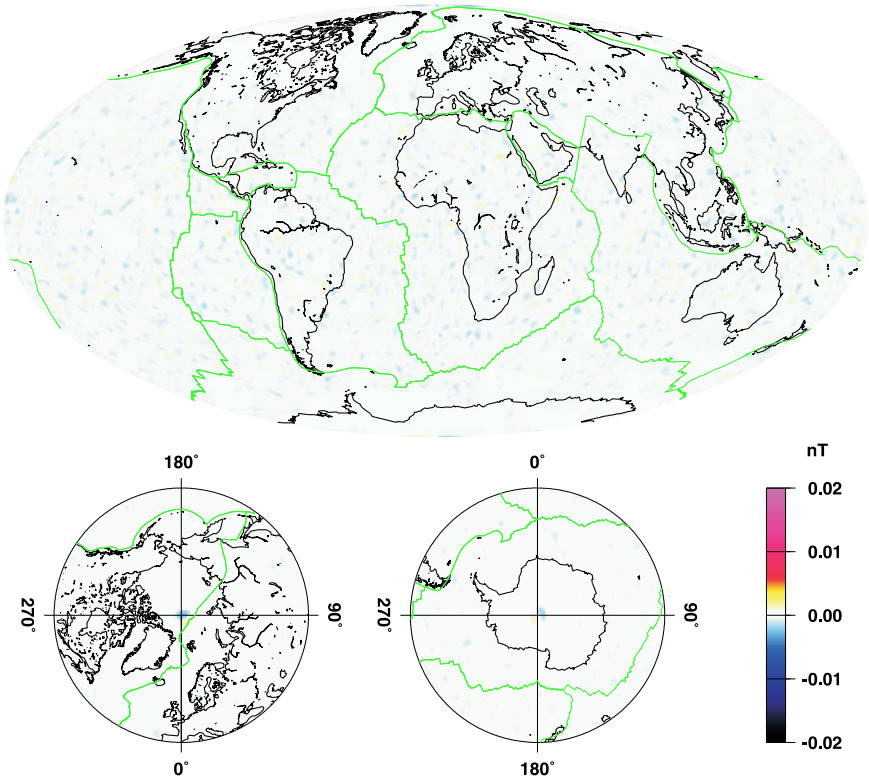

a)

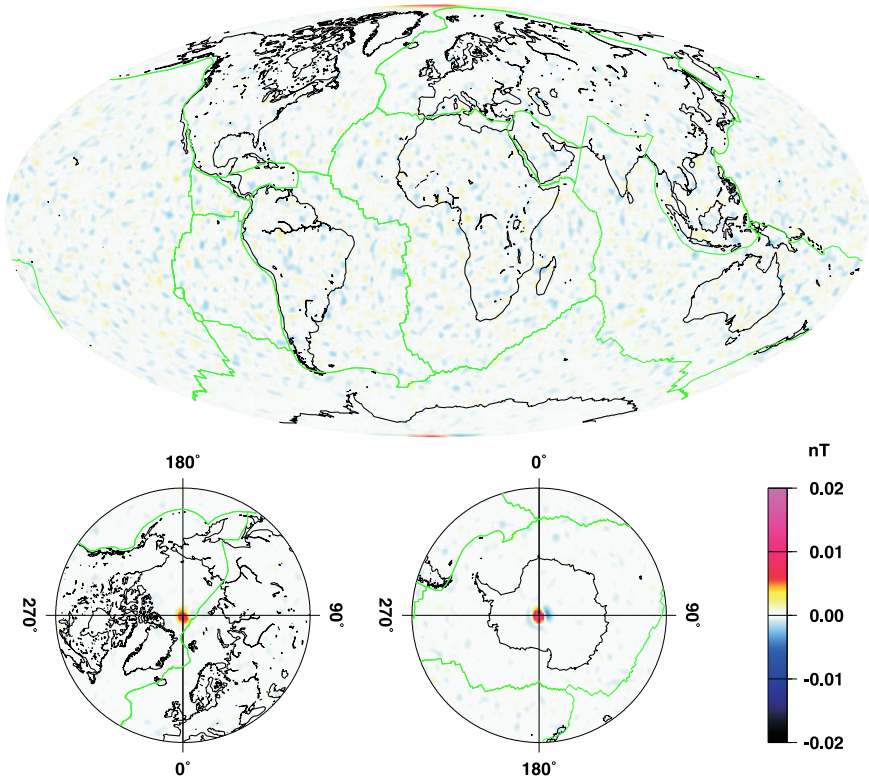

b)

Figure 6.24: a) Global distribution of the difference between the derived model fields and that of the original model. For the inversion all vector components have been considered. b) Same as above, but for a recovered model derived from the vertical component only.

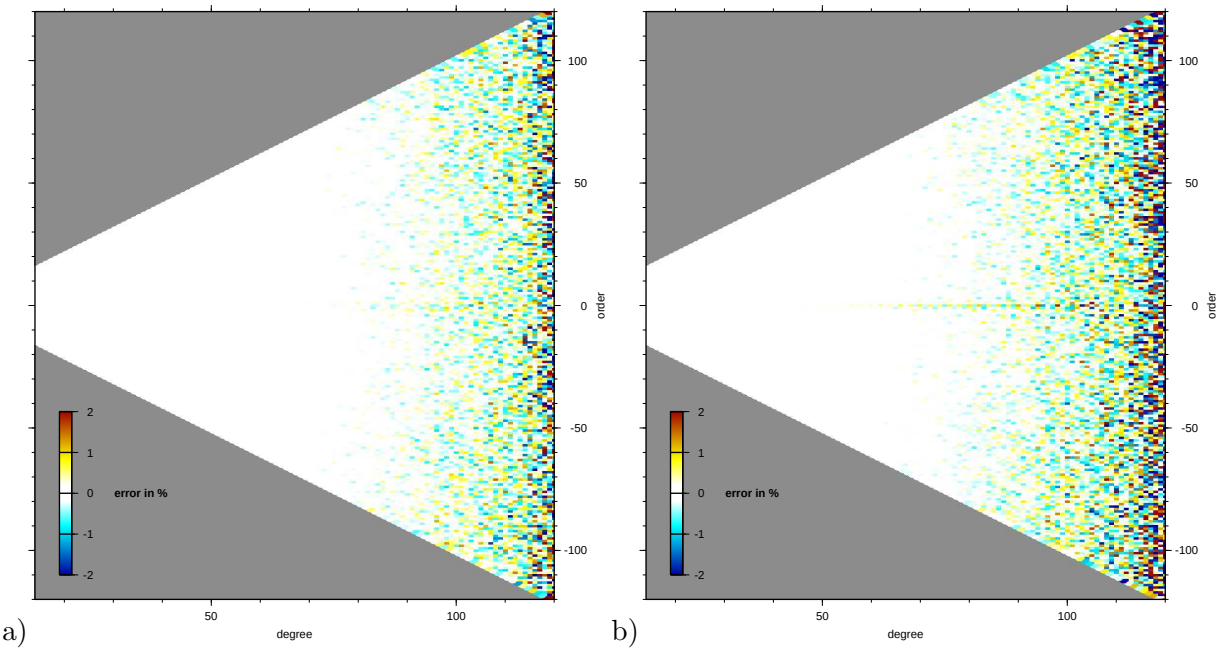

Figure 6.25: a) Sensitivity matrix (cf. Eq. 5.3) showing the difference between derived and the input model Gauss coefficients as relative errors. For the inversion all vector components have been considered. b) Same as above, but derived from the vertical component only.

wavelength end due to the run out of signal. This effect is rather prominent in the sensitivity matrix (cf. Fig. 6.25). Errors above 2% are found only in the degrees beyond $n = 110$. From these findings we may recommend that in future cases the synthetic lithospheric data should go to higher degrees. These last 10 degrees comprise about 20% of all the coefficients. It is not an effective use of computing time, if they do not contribute to the result.

As expected, employing the full magnetic field vector for the inversion gives somewhat better results than limiting the determination of the Gauss coefficients to the vertical component. Quite prominent is the difference in the response to the polar gap. Even though it is comparably large (about 500 km radius) it is hardly discernable in case the full vectors have been considered. When deriving the recovered model from the vertical component larger differences show up in both the global map (Fig. 6.24b) and the spectral sensitivity matrix (Fig. 6.25b). The enhanced errors for coefficients with $m = 0$ are a manifestation of the polar gap.

When retrieving magnetic field models from real satellite measurements it is good practise to use only the field magnitude at polar regions, since the perpendicular (horizontal) components are strongly effected by ionospheric currents. In that respect our solution with the vertical component describes real conditions much better than the one with the full vector. At high latitudes the field direction is almost vertical over a fairly large range. We may conclude that a polar gap of 500 km radius will have adverse effects on the high resolution magnetic field modelling. To make use of the full performance of the swarm mission will requires a size of the polar gap not to exceeding something like 250 km.

6.2.5 Study 2: Lithospheric Field Recovery

For the second study all source terms of the synthetic data set of Constellation #1 are considered. Here we make use of the 5-second data which provide a sufficiently dense sampling of the high-degree lithospheric signals. The purpose of this study is to show how well the lithospheric field can be recovered from the complete, but noise-free data when one or more satellites are involved in the inversion.

In section 6.2.4 we had demonstrated that the lithospheric field can be reconstructed almost perfectly, even with a single satellite, if only the relevant source term is considered. The multi-satellite approach

thus has to be optimized toward an efficient separation of the other source terms. Four satellites are not enough to provide a unique representation of all the terms at any time. We therefore reduce the size of the considered area to a diameter of about 3000 km, assuming that four satellites can provide a local description of the complete external field structure sufficiently well. This approach resulted in certain data selection criteria:

- Only night-time (19:00LT to 05:00LT) passes are considered to minimise the effect of ionospheric currents.
- Only time intervals where the nightside equator crossings of all four satellites are within a sector of 20° in longitude are taken into account.

The second condition is met during the first 200 days of the mission and once again for 400 days roughly centred about the fourth year. We have used both intervals (see section 3.3 for the orbit development). It is not required that the satellites pass the region of interest simultaneously. We allow for a time difference of up to one hour for tracks to be considered in a joint inversion. Time variations taking place on this scale are considered to be small and randomly distributed. This rather generous condition is allowing all four satellites to contribute to the solution on almost each orbit during the considered periods. While the main field is assumed to be known to degree 13 and is subtracted from the synthetic data, the constellation approach is used to characterise the main features of the external field and its induction effect. As argued before, only the low-degree terms are determined which is assumed to be sufficient for a local solution. On an orbit-by-orbit base the following parameters are solved for:

- External magnetic dipole, aligned with the main dipole plus its time derivative (2 parameters)
- An orthogonal external dipole in the orbital plane, which allows for a tilt between the internal and external dipoles (1 parameter)
- The induced counter parts of these two components and the time derivative of the internal dipole (3 parameters)
- The toroidal field contribution, but limited to B_θ component , B_ϕ not used (1 parameter)
- External magnetic quadrupole, axial component (1 parameter)
- Orthogonal quadrupole in orbital plane, allowing for a tilt of the quadrupole (2 parameters)
- The induced counterparts of the quadrupoles (3 parameters)

In a test it was shown that all these parameters can be determined reliably. The magnetic field components resulting from this joint multi-satellite inversion are considered to be long wavelength noise which is subtracted in order to isolate the lithospheric magnetic signal.

6.2.6 Results of the Inversion Study 2

In a first run we tested the algorithm by applying it to a single satellite, the low flying SW3. The spherical harmonic coefficients were solved for degree and order from 14 to 110. The lower-degree terms are dominated by the core magnetic field. Having confirmed that the programme works properly, the same data set was used in a multi-satellite inversion. As expected, the comparison with the original lithospheric field signature is not as good as the one achieved from clean data in the first study. Figure 6.26 shows the degree correlation between the retrieved and input high-degree coefficients of the lithospheric field. A result, surprising at first sight, is that the single-satellite solution gives a better correlation over large parts of the spectrum. The threshold of 0.7 is encountered at degrees around 90 in case of SW3 alone and slightly less than 80 for the four-satellite solution. The degree of field recovery with SW3 is remarkably high and goes beyond the resolution obtained so far by the CHAMP magnetic field measurements. We interpret this as a confirmation for the suitability of our external field filter. The less favourable result obtained by the joint inversion is probably an indication of inappropriate assumptions. Suggestions will be discussed in the next section. Another way of visualising the fit between the original and the recovered model is to plot the local differences on a global map. Figures 6.27a and b show the spatial distribution of the residual on a globe for the single-satellite and the formation solutions, respectively.

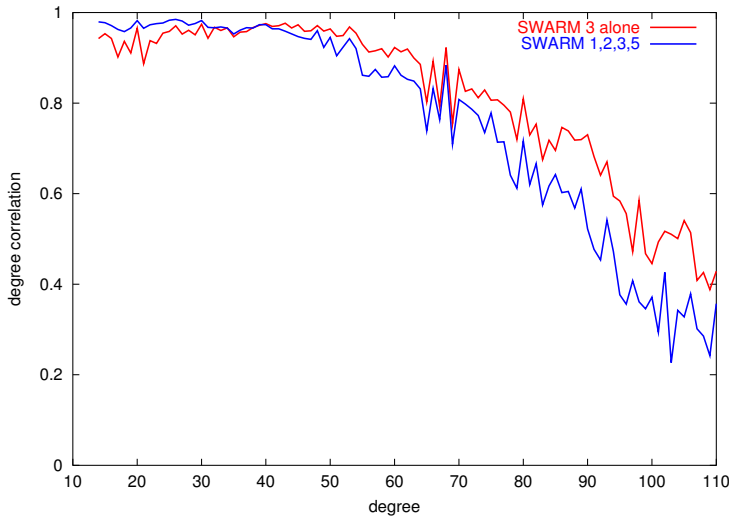

Figure 6.26: The degree correlation between the input and the retrieved lithospheric magnetic field model for a single satellite and a formation approach.

The dominating features are zonal stripes of alternating residuals with amplitudes of up to 5 nT. Their spatial scales correspond to the lower truncation degree of $n = 14$. In case of the *Swarm* constellation solution the stripes of dominating residuals are much weaker. Spots of strong residuals appear in polar regions and in particular at the magnetic poles.

In a third test the retrieved spherical harmonic coefficients are directly compared with the input model. Figures 6.28a and b show the percentage errors for the single and multi-satellite solution respectively. Errors are colour-coded in the sensitivity matrix containing degree n versus order m. The matrices show some interesting structures. At low degrees up to about $n = 50$ the errors are fairly low. For higher degrees they increase significantly. There are prominent error levels at certain values of the order m. They come at multiples of $m = 15$ and can thus be regarded as multiples of the stripes in the residuals (cf. Fig. 6.27). Most pronounced is the peak at $m = 0$. This is at least partly due to the polar gap in measurements.

6.2.7 Discussion of Results from Study 2

This second study is based on noise-free data, but all magnetic field sources included in the synthetic data set are considered in the inversion. Special filters have been applied for rejecting in particular the external field contributions. As expected, the results are not as good as in the first case where only the lithospheric field part was considered. The resolution achieved with the single satellite obtaining correlations above 0.7 for spherical harmonic degrees up to 90 is very satisfying and can be interpreted as a confirmation of the used filter.

In case of the multi-satellite inversion we are searching for a common solution fitting all four satellites at the same time. When looking at Figure 6.26 we see that the constellation solution is better for degrees up to 35. In this wavelength range the filter used with a single satellite obviously removes genuine crustal signal. For higher degrees the constellation has more and more problems in characterising the small-scale features of the external field correctly. There is obviously no common solution which fits the data of all the four spacecraft sufficiently well within an area of 3000 km. This impression is supported by the distribution of the residuals in Figure 6.27. The amplitude of the dominating zonal stripes is greatly reduced in the constellation approach. The problem of single-track line levelling uncertainty, inherent to along-track filtering, can be effectively mitigated in case of multi-satellite solutions. The optimal spacing of the spacecraft for this purpose still has to be determined. It is worth noting that none of the prominent crustal magnetic features (Bangui, Kursk, Kiruna anomalies) are visible on these maps. The crustal field is obviously well recovered, but contaminated by additional signal in that wavelength range.

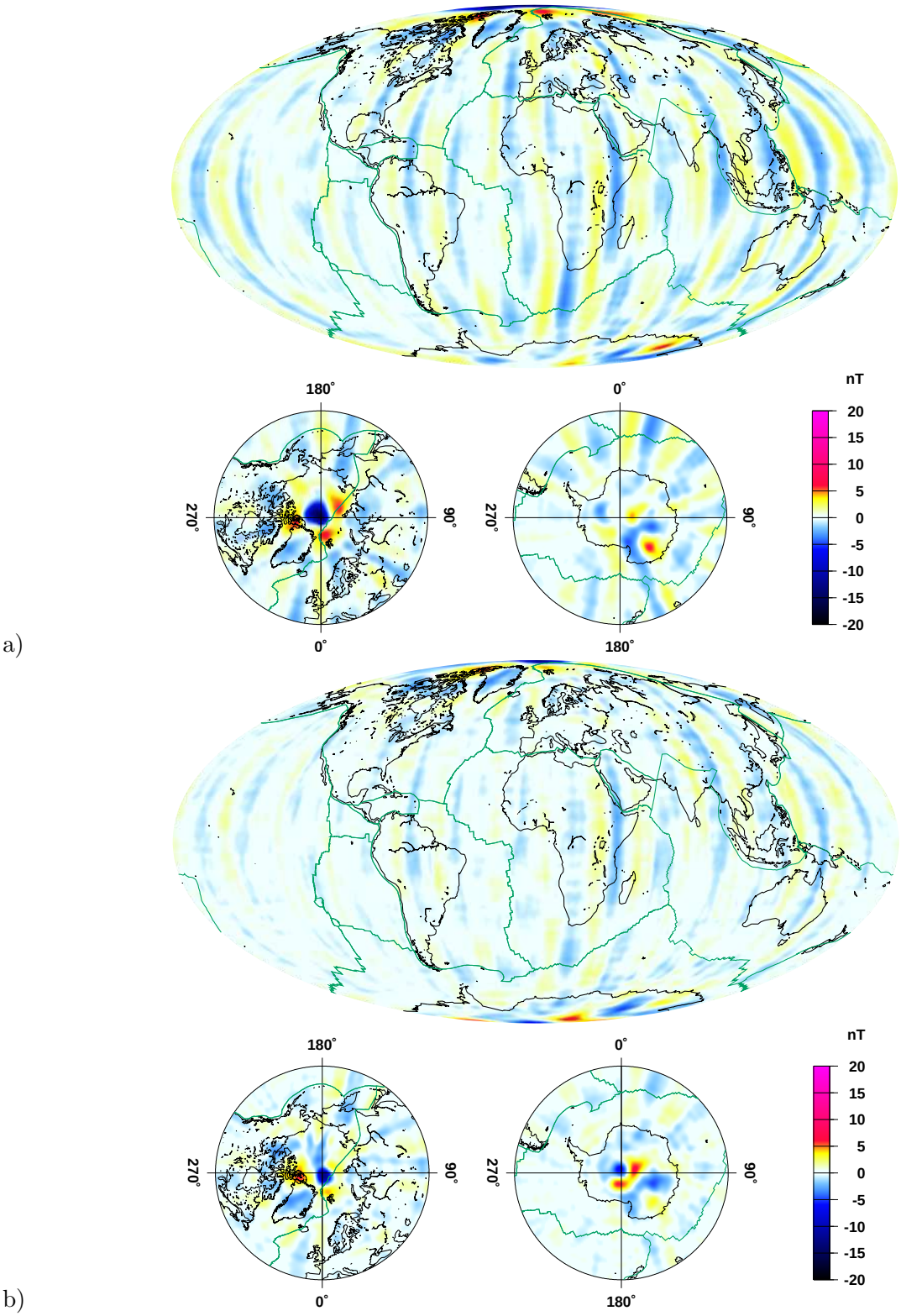

Figure 6.27: Global distribution of residuals between input and derived model. a) Single satellite solution. b) Multi-satellite results. The low-degree zonal terms are quite prominent.

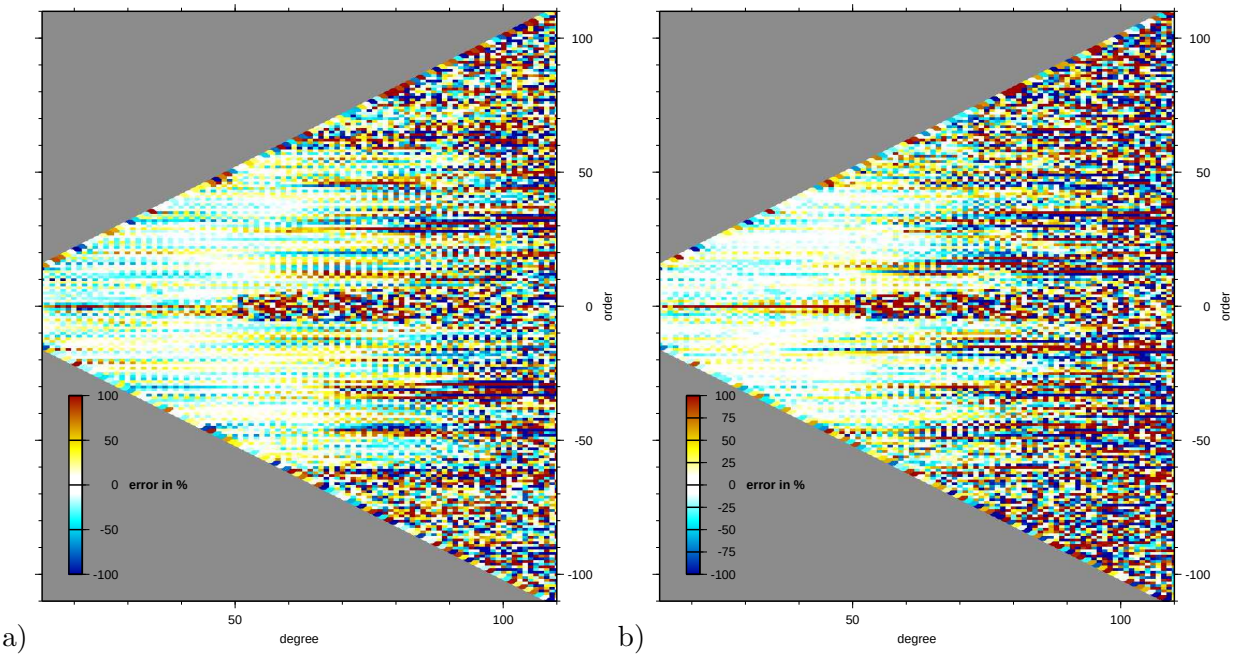

Figure 6.28: Sensitivity matrix showing the difference between the input and the derived Gauss coefficients as relative errors. a) Single satellite solution. b) Multi-satellite results.

Our filter is based on experience with real external magnetic fields and therefore it is focused on the long wavelengths. The synthetic data seem to contain also external fields with a fair amount of short wavelength signal. This is contrary to our experience with CHAMP data, which do not show small scale disturbances in quiet night time data. In future runs this discrepancy should be removed. Then we should be able to demonstrate the full capability of the constellation.

6.2.8 Lithospheric Field Recovery: Task 3

Inspired by the results of the previous study it was decided to try a somewhat different constellation of satellites for sampling the magnetic field. The important change of Constellation #2 is that the spacecraft of the lower pair are now flying side-by-side rather than following each other (see Section 3.3) In this Study 3 the advantages of the new constellation for the lithospheric field recovery will be tested. In addition, the synthetic data used contain in this case also instrument noise (see Section 3.5.4)

6.2.9 Data Selection and Inversion Approach

For this third study the synthetic data generated for the Constellation #2 (Section 3.2.2) are employed. We make use of the 5-sec vector data which are needed for the recovery of the high-degree lithospheric anomalies. All magnetic source terms in the data set are added up. In this case also realistic instrument noise is included. There is one exception from the complete set of source terms. The modelled toroidal field components are not considered, because they do not seem to represent reality too closely. Furthermore, they were identified within Task 2 as one reason for the limited accuracy of the recovered lithospheric field.

Not all the available data have been used. Only periods were considered when ionospheric currents are believed to be weak. Commonly used criteria are a small activity index, $Kp \leq 2$ and the hours of the late night, 22 to 05 local time, when the ionospheric conductivity is low. Data of the whole mission time of 61 months were considered in the selection according to the above mentioned criteria and treated in one inversion run for the retrieval of the lithospheric field.

A major task for recovering the rather weak lithospheric signal is the elimination of all the other

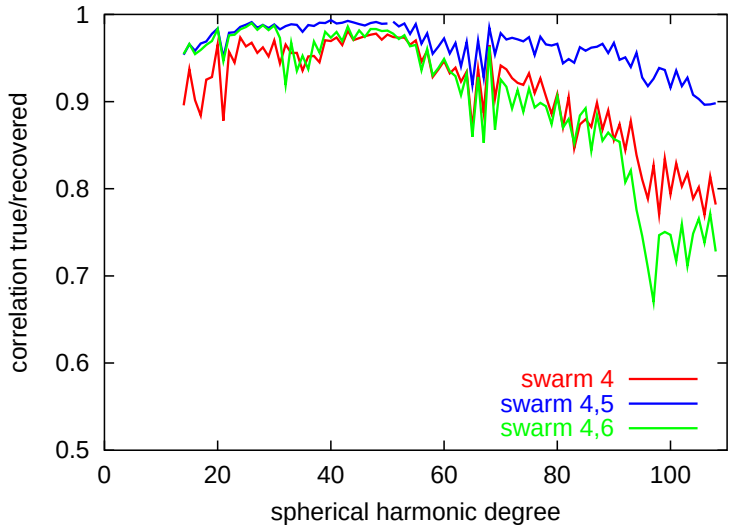

Figure 6.29: Degree correlation between the input model and the retrieved lithospheric field model separately for a single satellite solution and for pairs of satellites.

source contributions. As a first step, a main field model is subtracted. Secular variations up to degree 13 are considered as linear changes with time.

Contributions from the external sources are determined on a track-by-track base. They are resolved up to degree 3. In the same way the induced counter parts are estimated. If several satellites of the constellation are considered in an inversion run, all of them are included in a joint determination of the external contributions.

In cases where two of the lower altitude satellites are used, the vector components and the horizontal gradients of the vector components were employed in the recovery of the lithospheric signal.

6.2.10 Results of the Lithospheric Field Retrieval, Study 3

The questions we wanted to answer with these simulations are among others: What is the effect of realistic instrument noise on the resolution of the models? Which spacing of the satellites within the constellation is optimal for the recovery of the lithospheric anomalies? In order to find answers the same data set was processed several times using a variety of spacecraft combinations. Most instructive results were obtained from the different sets of the satellites in the lower orbit. Adding one or two spacecraft from the higher orbit did not improve the resolution of the high-degree field.

For the lithospheric field recovery the spherical harmonic coefficients were determined for degree and order from 14 to 110. These values are then compared with the SHA coefficients of the input model. One of the possibilities to check the quality of the result is to perform a degree correlation with the input model. Figure 6.29 shows the degree of correlation for three obtained models. Using only one low-flying satellite (SW4) provides already a good recovery of the lithospheric signal. This confirms the findings of the Task 2 results. Adding another satellite improves clearly the model accuracy in the longer wavelength range up to degree 30. The overall gain when considering a second satellite depends quite significantly on the chosen separation. The pair SW4/6 with an east/west separation of 11.25° in longitude provides good performance up to about $n = 30$ where the correlation somewhat drops off. Around these degrees the wavelength of the signal becomes comparable to the spacecraft separation. For degree beyond $n = 40$ the pair SW4/6 does not provide any advantage over the single-satellite solution.

There is a large difference in the case of the closely spaced pair SW4/5 which is separated only by 1.5° in longitude. Here we obtain a significant gain in accuracy over the whole spectrum. The improvement even increases toward higher degrees. At $n = 110$ the correlation between the input and the retrieved model is still above 0.9. In the subsequent assessment we therefore will compare only the result of SW4 with the pair SW4/5.

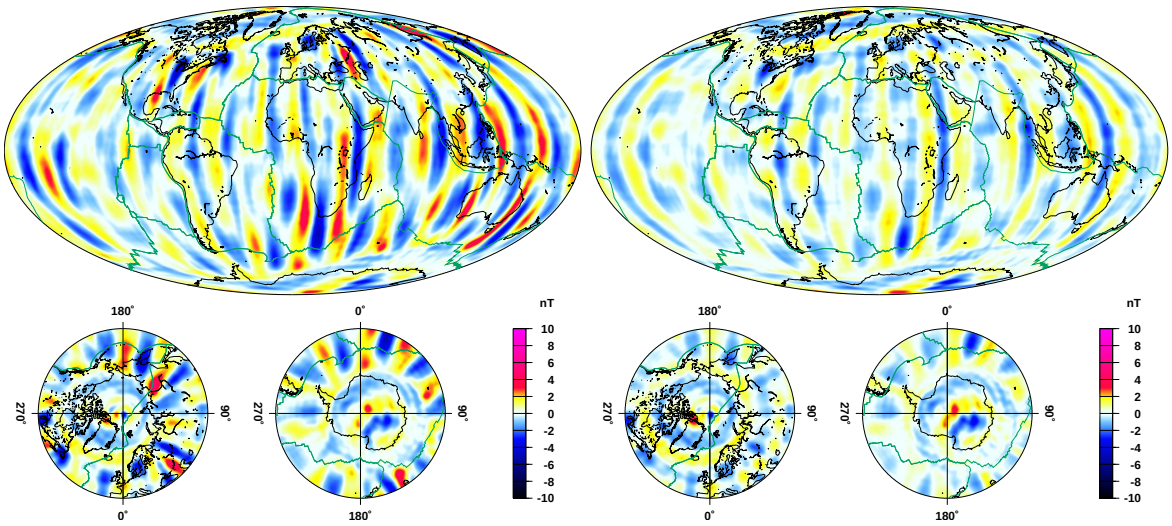

Figure 6.30: Global distribution of residuals between input and derived model, *(left)* solution from satellite SW4, *(right)* solution from satellite pair SW4/5.

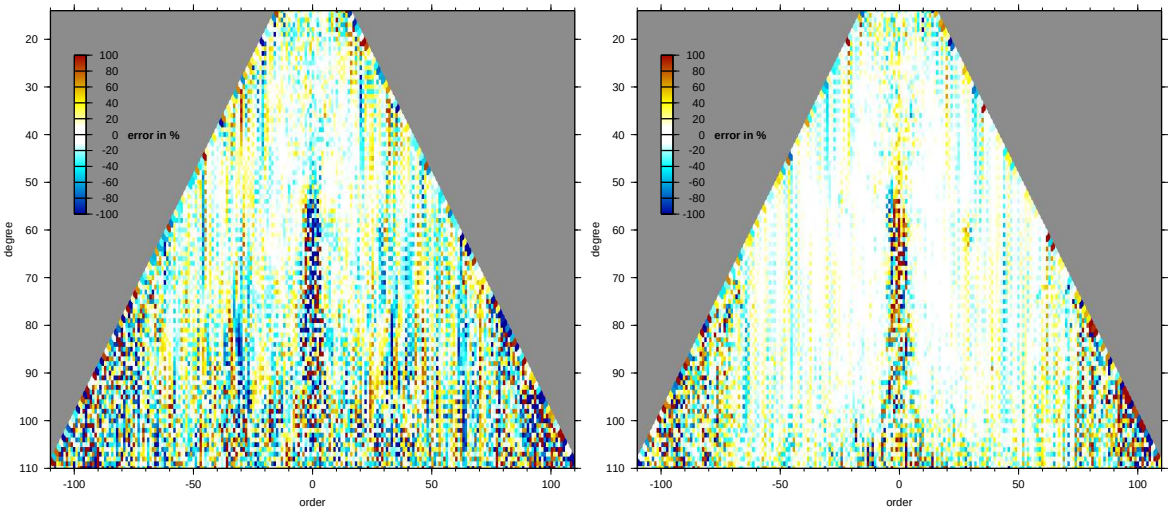

Figure 6.31: Sensitivity matrix showing the difference between input and derived Gauss coefficients as relative error, *(left)* solution from satellite SW4, *(right)* solution from satellite pair SW4/5.

Another way of visualising the fit between the input data and the obtained models is to plot the residuals on a global map. Figure 6.30 shows the results from the single satellite and the closely spaced pair. The dominant residual features are meridional stripes. Their spatial scale is close to the truncation wavelength at degree 15. In the case of the dual-satellite solution the amplitude of the residuals is largely reduced.

A third way of testing the model quality is to compare directly the relative error of each SH coefficient between the obtained model and the input data for the two retrievals. In Figure 6.31 the relative errors are plotted as colour coded boxes in a sensitivity matrix ordered by degree n versus order m. There is clear evidence that the closely spaced pair provides better results at all degrees. Remaining uncertainties are centred around some m values. Remaining uncertainties in the case of the SW4/5 pair are around $m = 0$ and $|m| \sim n$. The larger errors around $m = 0$ are probably caused by ionospheric disturbances in both polar regions. For an improvement of the results a suitable high latitude activity index would be

needed which helps to find the very quiet passes.

6.2.11 Assessment of the Results and High-Degree Test

This third study on the recovery of the lithospheric field is based on rather realistic data including even instrument noise. The quality of the retrieved models is remarkably high. It is demonstrated that the features up to degree 110 can be recovered reliably with an optimised constellation comprising spacecraft flying side-by-side. When comparing it with the second study of Task 2, the omission of the somewhat unrealistic toriodal field contribution has made a big difference.

The other large improvement is achieved when the horizontal gradients of the B-field are also considered in the inversion. Here it is shown that the separation of the spacecraft should be of the order of half the wavelength of the highest degree to be recovered. This is of importance for the design of the constellation. If we aim in the *Swarm* mission at a model resolution of degree and order 120, a separation of about 160 km should be selected. The observational requirement on the constellation resulting from the lithospheric field objective thus would be to have two spacecraft flying side-by-side separated in the east/west direction by 1.5° in longitude.

Motivated by the very promising result of the last study we decided to carry this gradient approach a step further. The inversion is based on the synthetic data set of the high-degree lithospheric model called swarm(05a/04). Details of this model extending up to degree and order 150 are given in Section 3.4.2 and the power spectrum is shown in Figure 3.13. Magnetic field readings were sampled at 5s intervals along the orbits of the lower pair, SW4 and SW7 and equally for the higher pair SW2 and SW3. As has been mentioned in Sec. 3.3.7, for Constellation #2 an additional spacecraft, SW7, was introduced just for this purpose. The orbit of SW7 is artificially kept at 1.5° east of SW4 to maintain an optimal east-west separation for a high-degree recovery.

We aim at recovering the lithospheric signal up to degree and order 140. For this exercise all magnetic field contributions in the synthetic data set have been considered, except for the toroidal field (cf. comments in Sec. 6.2.9). The first step is, as usual, separation of the external field contributions. In a common inversion the Gauss coefficients of the first three spherical harmonic degrees of the internal and external contributions are determined from the readings of SW4 and SW7 on a track-by-track basis and subsequently subtracted. The full vector information of the cleaned data is used to derive the horizontal gradients between the spacecraft SW4 and SW7. Both the vectors themselves and the horizontal gradients of the vector components were employed as separate input data sets for the inversion. A special weighting of the data was used to obtain an equal area distribution on the sphere. In a first inversion the raw distribution of Gauss coefficients was determined. From that an empirical damping matrix was constructed reducing the power of all coefficients which exceed the average amplitude of their vicinity by more than 200%. This is to eliminate spikes in the solution for coefficients that are not well resolved by the data, such as the high degree zonal coefficients which suffer from the polar gap. In a second inversion the final Gauss coefficients are determined.

In order to check the quality of the results a comparison between the retrieved and the input model is performed. Figure 6.32 shows in the left frame the signal spectrum of the input and retrieved models. Both curves track each other very well. The difference spectrum attains significant amplitudes only for degrees beyond 100. The middle panel contains the absolute errors of the individual Gauss coefficients. The differences grow slowly with the degrees. There is a string of larger outliers. These are associated with a constant m value. The right frame shows the degree correlation. It can be seen that the agreement is good (close to 1) over a wide range of degrees. The threshold of 0.7 is passed around degree 130. This is an excellent confirmation of the potential of the field gradient method. A better impression of the degree of details recovered from the crustal signals can be obtained from Figure 6.33 showing the input model on the left and the retrieved map on the right hand side. All these details, especially the ocean bottom stripes come out very clearly. In summary, this additional study has demonstrated the large potential for a detailed lithospheric field recovery when dedicated satellite constellations are available. Employing the field gradients from a properly spaced pair of satellites in the inversion approach is the key factor for the success. The demand on computing power is quite large for such a high-degree solution. To obtain the degree and order 140 model, presented here, requires the equivalent of 3 weeks CPU time on a 8-way SUN Fire V880.

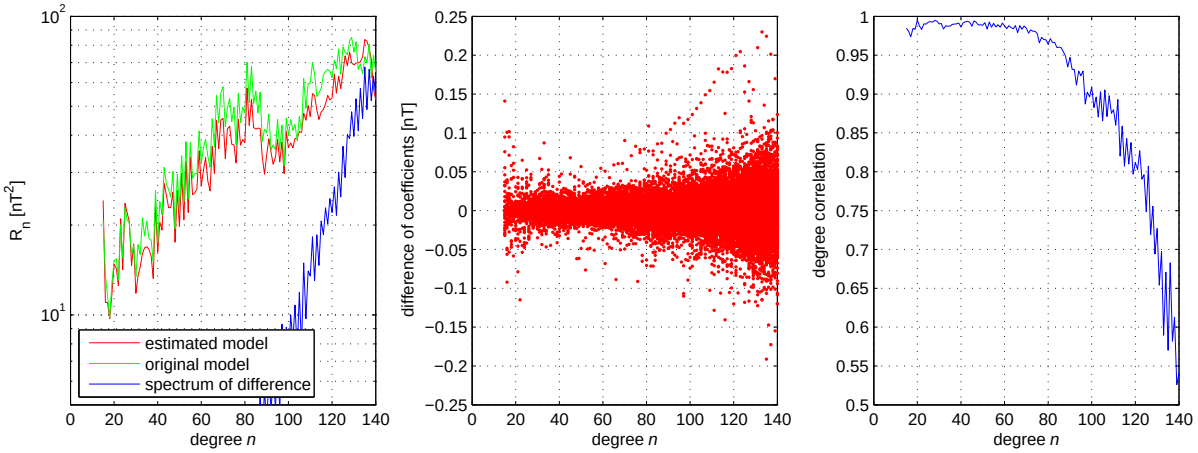

Figure 6.32: Quality of the high-degree retrieval model obtained by the gradient method. True and retrieved signal spectrum, plus error spectrum (*left*); absolute error of Gauss coefficients (*middle*); degree correlation between input and retrieved lithospheric magnetic field model (*right*).

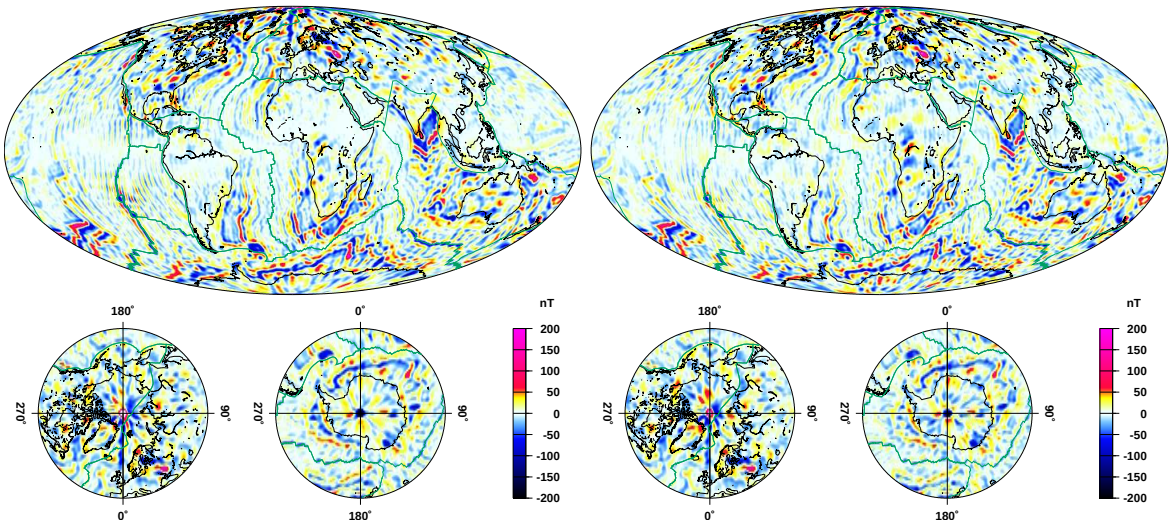

Figure 6.33: Global map of lithospheric magnetisation. High-resolution (degree and order 150) input model *(left)*, recovered lithospheric features utilizing the gradient method *(right)*.

6.3 Core Field and Secular Variation – Method 1

This section describes results obtained by Mioara Mandea and Gauthier Hulot, Institut de Physique du Globe de Paris (IPGP) in WP 4210 "Core surface field and secular variation".

During the course of Task 2, we first analyzed synthetic data from the full set and subsets of Constellation #1, using standard algorithms available in our team, and tested the possibility of recovering the core surface field and its secular variation. As an outcome of those first computations, it was noted that in the context of a mission such as *Swarm*, the method we relied on to construct core surface fields and secular variation models suffered a number of drawbacks, limiting the accuracy of the recovered models. This accuracy was similar to the one reached by BGS, who relied on a similar modeling strategy. Only the Comprehensive Inversion approach jointly used by NASA/Goddard Space Flight Center and DSRI led to much better results. Several suggestions were made that we felt could help improve our method. It was one of our goals during Task 3 to test the extent to which some improvements could indeed be achieved in this way.

Having done this, we next investigated the extent to which our method could discriminate between the various constellations considered for the mission.

6.3.1 Algorithm and Parameters

The modeling is done using selection criteria and inversion algorithms developed by our team. The inversion algorithm uses the least squares method and is based on a code described elsewhere [Langlais and Mandea, 2000, Langlais et al., 2003]. Inclusion of observatory data has only been considered in the course of Task 3, and not in the earlier Task 2 computations. The internal field and its secular variation were calculated up to degree/order 19 and 8 in the context of Task 2, but those number were next increased to 29 and 13 for Task 3. A secular acceleration was otherwise computed up to degree and order 8 except when we considered very short periods of times (2 months). The model also included parameters to describe an external field up to degree 2 (with a D_{st}-dependent part for Task 3). A geographic weighting scheme was otherwise applied to compensate for the polar concentration of the data (a weight proportional to the sine of the colatitude was applied to each data).

6.3.2 Data selection

Geographical and local-time selection *Satellite data.* To limit the influence of external field variations (or to produce a realistic data distribution whenever no external signal is included in the synthetic data to be analysed), only night-side data (between 22:00 and 06:00 Local Time) have been considered: in such a way contributions from ionospheric currents at middle and low latitudes were reduced. At high absolute dipole latitude (± 50), only intensity data have been used. Vector data were taken for dipole latitudes equatorward of ± 50 (in this range of latitude no scalar data are included). In addition, the data was also homogenized. In this process we started by randomly sorting a maximum of 5 measurement locations per 5x5 bin. The next bin was obtained by translation of the previous one by 2.5x2.5 in latitudinal and longitudinal directions. This main homogenization applied for one satellite and a three-month period of data was considered as the "basic" homogenization. All the other combinations were obtained from the basic one, depending on the number of satellites and the time-span considered in each simulation.

Observatory data (only in the context of Task 3). All observatory data were considered. However, in order to avoid the dayside current systems and to keep the quietest available period, only data between 01:00 and 03:00 Local Time were selected.

Geomagnetic activity In order to take into account the magnetic activity, we relied on a filtering of data based on Kp and RC index for the satellite data, and on Kp and D_{st} index for the observatory data. Considering a particular satellite data with associated time t (in hour), the criteria used were:

$$\begin{array}{lll} Kp(t) \leq 2^- & \text{and} & \delta Kp(t \pm 3) \leq 2^0 \\ \mid RC(t) \mid \leq 10nT & \text{and} & \delta \mid \frac{dRC(t)}{dt} \mid \leq 3nT/h \end{array}$$

The same selection was applied for the observatory data, using D_{st} index instead of RC index.

These criteria are more restrictive than those used for other models (e.g. the Ørsted Initial Field Model), however the resulting dataset was large enough to allow the high degree and order spherical harmonic models to be derived.

6.3.3 Mission configuration

For the present report, only the most relevant results are being presented. Those correspond to missions of various durations and satellite configurations.

Duration For Task 2, results have been obtained for simulated missions lasting one year (1997), two years (1997-1998), or four years (1997-2000).

For Task 3, results have been obtained for simulated missions lasting 2 months, 6 months, and 2 years. We especially focused on our ability to recover some useful information when very short periods of time are considered, which is the type of situation which could turn out to be sensitive to the choice of the constellation. With this respect, our results complement usefully those presented by BGS, who focused on longer periods of 3 and 5 years.

Satellite configuration For Task 2 and for each corresponding period of measurement defined above, results have been obtained when relying on data acquired by either (satellite numbers as defined for constellation 1):

i) One satellite on a high orbit (*Swarm* 1);
ii) One satellite on a low orbit (*Swarm* 3);
iii) Four satellites, as given by the full constellation 1.

For Task 3 and for each corresponding period of measurement defined above, results have been obtained with data acquired by either (satellite numbers as defined for constellation 2):

i) One satellite on a low orbit (*Swarm* 4);
ii) Two satellites on a low orbit, orbiting next and close to each other and one satellite at high altitude (*Swarm* 145);
iii) Four satellites, same as the previous but with two antipodal satellites on the high orbit (*Swarm* 1245);
iv) Two satellites on a low orbit, orbiting next but quite away from each other, and two satellites on a high orbit, again next but quite away from each other (*Swarm* 1346).

6.3.4 Field sources

The strategy tested in our inversions is one which consists in recovering the core field and its secular variation, with as little as possible modelisation of the other sources, the signature of which is minimised mainly by the selection procedure. In the context of Task 2, we tested the extent to which contributions from non-core sources could alter the quality of the recovered core field and secular variation models. For that purpose, we focused on the analysis of the following synthetic data sets:

a) "Core": core field and secular variation;
b) "Solid Earth": core field, secular variation and lithospheric field;
c) "All sources": all possible components.

Note that noise was not considered in the course of Task 2.
In the context of Task 3, all sources and instrumental noise were systematically considered, except for some late computations.

6.3.5 Task 2 Results

In what follows, results are being provided in the form of figures displaying the energy spectra of the misfit of the model we computed, with both the field of internal origin and the secular variation used to

produce the synthetic data (source field and source secular variation). More precisely, for each mission duration (one, two or four years), and for each type of field sources ("Core", "Solid Earth", "All sources") used to create the synthetic data, we produced two figures, one displaying the spectrum of the misfit between the source field and the field of internal origin we recover, the other displaying the spectrum of the misfit between the source secular variation and the secular variation we recover. In both cases, comparisons are being made for quantities estimated at the central epoch of the mission (1997.5; 1998.0, or 1999.0). Finally, on each of those figures, results for each of the three satellite configurations are simultaneously considered (single *Swarm* 1 high orbit satellite, single *Swarm* 3 low orbit satellite, full constellation). For reference, the spectrum of the source secular variation is also systematically plotted. We did not plot the spectrum of the source field which always lies above the misfits.

Test with only core field and secular variation This case amounts to test our code if we were to gather data from a *Swarm* mission orbiting a special "ideal" Earth with just a core geodynamo and no source of noise. This geodynamo would produce a time-varying field only up to degree 19, with little energy in degrees 14-19 (by default, the source field is set at zero at epoch 1999.0 beyond degree 13). Errors found in our recovered model can then be interpreted as being the result of the finite amount of data, and of the differences in the parameterization used in our model and that of the source model which produced the synthetic data. Most important is the fact that the temporal variation in the source model is governed by B-splines, with high temporal derivatives for all degrees up to degree 13, whereas our modelling only assumed a simple temporal behaviour.
Figures 6.34-6.37 show that in all cases considered here, the core field is extremely well recovered. The situation is also very good for the secular variation. In all cases, and not surprisingly, we see that the single low satellite configuration always does better than the single high satellite configuration, especially for high degree coefficients, the full constellation 1 configuration always doing the best. Of particular interest is the comparison of the quality of the secular variation recovered from one year of data, compared to two years of data (Figures 6.35 and 6.37). We clearly see that waiting for two years degrades the quality of the low degree secular variation, but improves the high degree secular variation (note that all of the secular variation is properly recovered in that case). The reason for this is that waiting for a longer period of time makes it easier for the code to detect the changes due to the secular variation (those changes are then larger), but waiting too long makes it possible for higher temporal derivatives in the field to kick in and distort the temporal behaviour of the secular variation. One year of data is sufficient to resolve the low degree secular variation, but not the high degree secular variation. By going to two years, we start seeing the mismatch between the temporal representation of our model and the source model for the low degrees, which leads to a poorer low degree secular variation, but improve the quality of the high degree secular variation. Those issues could be resolved with the help of higher order temporal derivatives in our code.

Solid Earth data This case tests our code if we were to gather data from a *Swarm* mission orbiting an "ideal" Earth with a core geodynamo, a lithospheric field, but no external and induced fields and no source of noise. This Earth would produce a time-varying field up to degree 19, and a static field up to degree 120. Compared to the previous case, we now expect to further experience aliasing effects, linked to possible misinterpretation of the small scale lithospheric field for which we do not invert. Figures 6.38-6.43 show the results of those tests.
Let us first comment on the recovery of the field itself (Figures 6.38, 6.40 and 6.42). First we note that all satellite configurations are basically leading to the same results, all of which are in fact excellent in terms of accuracy (those error spectra are all extremely low). Second, we see that the best models seem to be recovered when one or two years of data are being used. Both those results can readily be explained. Aliasing is more or less occurring in a systematic matter, so that adding more data does not help improving the model. For low degrees however, this aliasing effect is low, and the leading effect is the one we discussed in the previous case, temporal behaviour misrepresentation (compare Figure 6.40 with Figure 6.34).
For the secular variation, we again see the effect of temporal misrepresentation for the low degrees (compare low degrees of Figures 6.41 and 6.35), but the situation is very different for the high degrees. Clearly, the single high satellite does worst, the single low satellite does better, the full constellation

does best. Also, the longer the mission, the better the results. This can be understood as aliasing (due to the static lithospheric field) behaving more like random noise for the secular variation than for the field itself (which would rather see it as a bias). Hence getting more data (either by waiting longer, or by having more satellites) helps improve the secular variation model. Finally, waiting for a longer period helps the signal from the secular variation to build up.
Those results shows that not modelling the full lithospheric field in the inversion procedure, can alter our ability to recover the secular variation beyond degree 13. But they also show that a constellation configuration can contribute to mitigating this effect. Here, with four years of data, a secular variation up to degree 15 can be recovered.

All sources data This final case tests our code if we were to gather data from a *Swarm* mission orbiting an "ideal" Earth with all sources but no noise. Figures 6.44-6.49 show the results of those tests. Non-Solid Earth sources significantly degrades our capacity to recover the core field and its secular variation. As far as the field itself is concerned, this is not so much a concern, as we are well below the amplitude of the signal itself. Note nevertheless that relying on more data or different satellite configurations does not change the result for the main field, probably because much of the external signal is somehow mapped as a systematic contribution to the model. This reveals the limits of the selection procedure we rely on to get rid of those contributions. Some systematic signal is left in the data we invert for.
The issue is more serious for the secular variation, the highest degrees of which can no longer be recovered. As in the previous case, however, the satellite configuration and duration of the mission play a role. When only one or two years of data are considered, the single high satellite mission does worst, and the single low satellite and full constellation configurations do about the same. Clearly, by not adequately modelling the external field, our code fails to take advantage of the constellation. The secular variation is recovered only up to degrees 9, 10 or 11 when computed over a period of one, two or four years.

Conclusions Several conclusions can be drawn from this Task 2 study.
First, is the fact that the modelling strategy we relied on to carry the present study clearly reveals its limits. Those limits are most serious for the secular variation we recover. When all signal sources are considered, even without any source of noise, the secular variation during the mission is at best recovered up to degree 11. This suggests that more elaborate modelling strategy should be implemented, including observatory data, involving better magnetospheric corrections and also inverting for some simplified ionospheric field.
Those results also reveal the impact of not modelling the small scale lithospheric field, when attempting to recover the core field and its secular variation. Although this impact is much smaller than the impact of external sources, it does introduce a limitation which we would eventually have to face. A much weaker, but not to be ignored, limitation also arises because of higher temporal derivatives.
More generally, it is fair to conclude that in order to achieve the goal we intend to achieve with *Swarm*, a simple modelling strategy such as the one we relied on during Task 2 may no longer be used. Some form of modelisation of, or correction for, the non-geodynamo sources must be included in the inversion. This suggests that we at least :

i) make use of more elaborate external field modelisation,
ii) make use of observatory data,
iii) model more of the medium to small scale lithospheric field.

An interesting additional possibility would be to also try and take advantage of lithospheric and external field models recovered by other teams to correct the data and reduce the impact of non-geodynamo sources. Those possibilities have been considered in the context of Task 3.

6.3.6 Task 3 Results

In what follows, as in the previous section, results are being provided in the form of figures displaying the energy spectra of the misfit of the model we computed, with both the field of internal origin and the secular variation used to produce the synthetic data (source field and source secular variation). Several

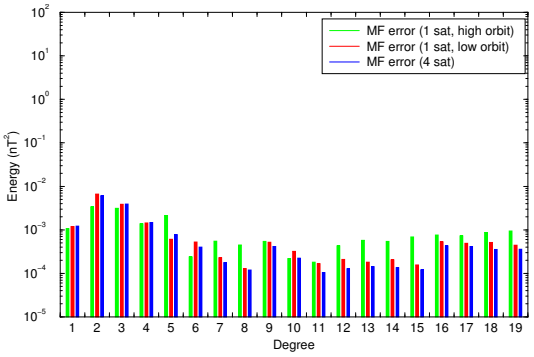

Figure 6.34: Errors for a 2-year period of measurements, considering the core field only.

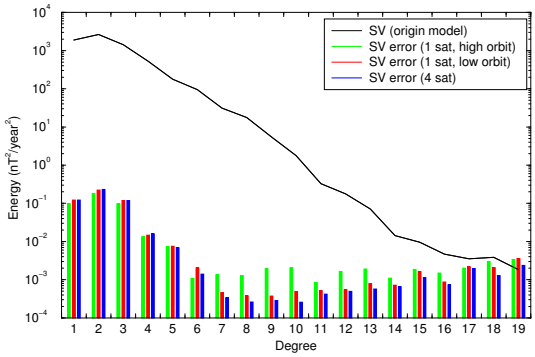

Figure 6.35: Secular variation errors for a 2-year period of measurement, considering the core field only.

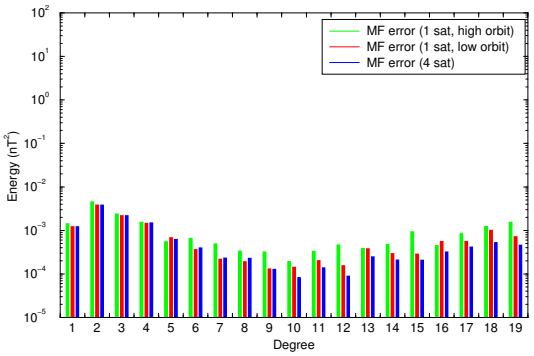

Figure 6.36: Errors for a 1-year period of measurements, considering the core field only.

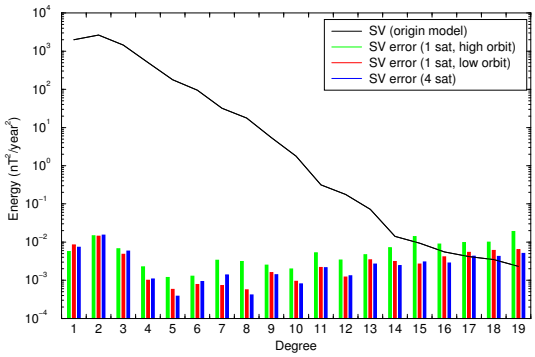

Figure 6.37: Secular variation errors for a 1-year period of measurement, considering the core field only.

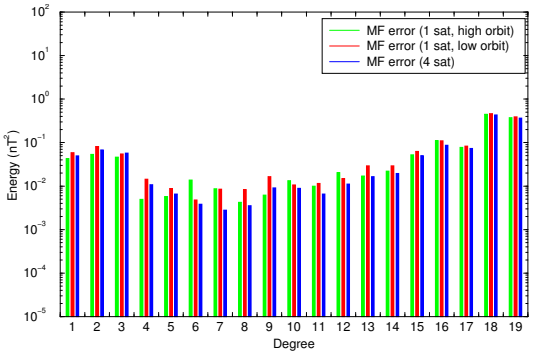

Figure 6.38: Errors for a 4-year period of measurements, considering core and lithospheric fields.

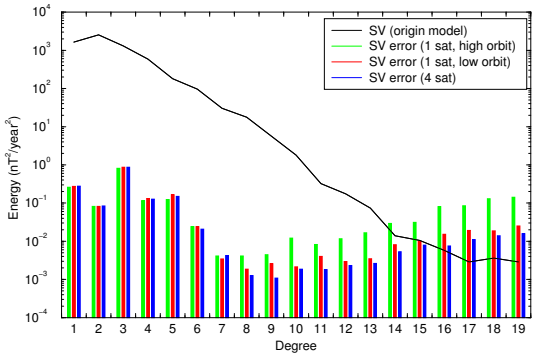

Figure 6.39: Secular variation errors for a 4-year period of measurement, considering core and lithospheric fields.

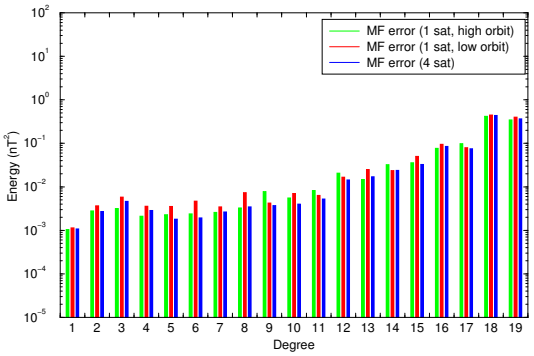

Figure 6.40: Errors for a 2-year period of measurements, considering core and lithospheric fields.

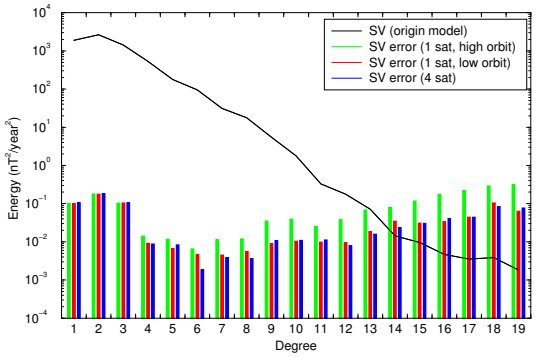

Figure 6.41: Secular variation errors for a 2-year period of measurement, considering core and lithospheric fields.

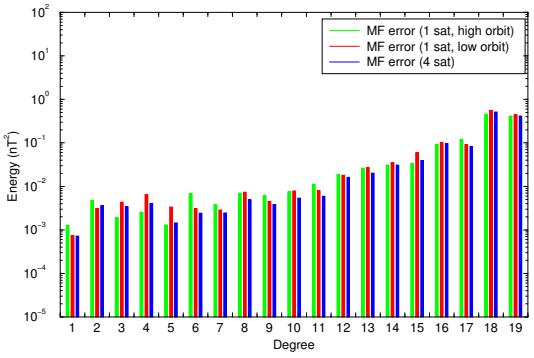

Figure 6.42: Errors for a 1-year period of measurements, considering core and lithospheric fields.

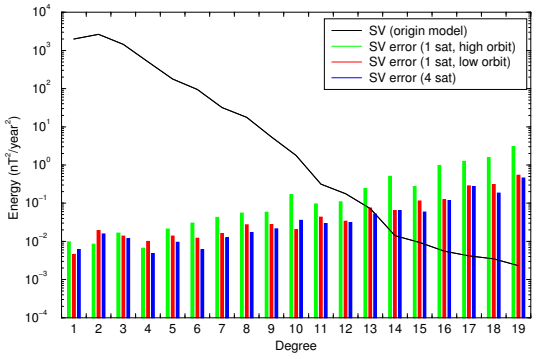

Figure 6.43: Secular variation errors for a 1-year period of measurement, considering core and lithospheric fields.

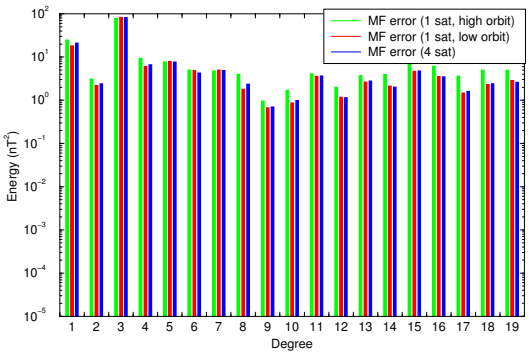

Figure 6.44: Errors for a 4-year period of measurements, considering core, lithospheric and external fields.

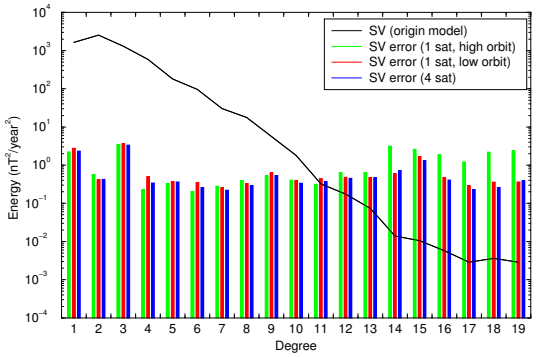

Figure 6.45: Secular variation errors for a 4-year period of measurement, considering core, lithospheric and external fields.

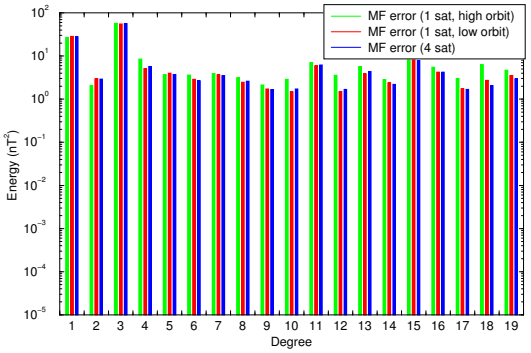

Figure 6.46: Errors for a 2-year period of measurements, considering core, lithospheric and external fields.

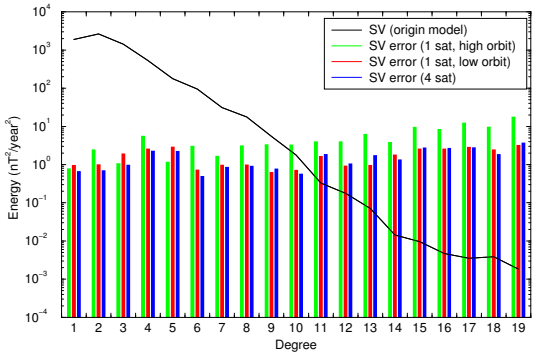

Figure 6.47: Secular variation errors for a 2-year period of measurement, considering core, lithospheric and external fields.

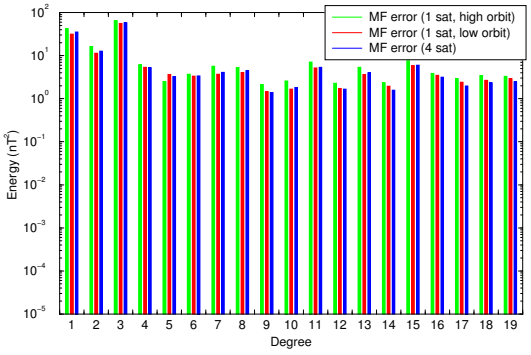

Figure 6.48: Errors for a 1-year period of measurements, considering core, lithospheric and external fields.

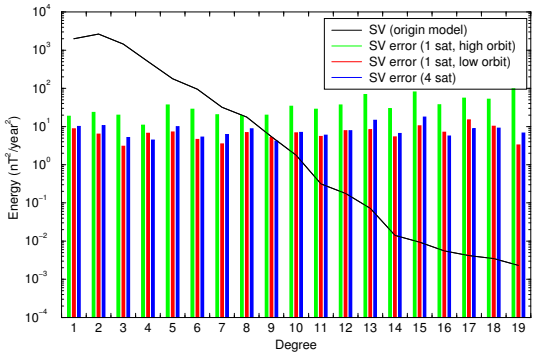

Figure 6.49: Secular variation errors for a 1-year period of measurement, considering core, lithospheric and external fields.

results from different computations based on the same data, are shown on the same plots to illustrate the impact of the choice of a constellation and on parameters. For reference, the spectra of the source secular variation and of the source field are also systematically plotted.
In a first series of tests and following the results of Task 2, it was checked and confirmed that the use of a better description of the external field (the D_{st}-dependent part), together with a higher (29 in place of 19) degree (better describing the crustal field) indeed brought some improvement. This led us to systematically adopt those parameters.
Next we turned to the three following issues: the possibility of introducing some crustal correction, the impact of observatory data, the choice of constellation.

Crustal correction and Observatory data In the course of Task 2, we noticed that some errors arose in our models because of the unmodelled signal of the crustal field. We suggested that a way of avoiding those errors could be to correct for the crustal signals as predicted from a crustal model derived independently from the same data-set. Stefan Maus from GFZ, provided us with one such model derived from the data of constellation SW1245 for the whole period. This model covers the degrees 14 to 60, and is tapered off starting at degree 50. We ran a number of inversions for the same constellation SW1245 comparing the results when a crustal correction based on Stefan Maus's model from degree 30 to degree 60, was included or not. We considered a time span of 6 months and also compared the case when observatory data was included or not. Figures 6.50-6.51 show the results, for the internal field and the secular variation.
Consider first the case without any crustal correction. It clearly appears that the inclusion of observatory data brings some improvement in the low degrees of the models, but deteriorates the quality of the high degrees. This we attribute to two effects: some contributions of the ionospheric signal, and some small scales ("crustal" bias) our modeling strategy cannot account for. This is exactly the situation for which a crustal correction could help improve the models. Unfortunately, and as is also clearly seen, introducing those corrections did not bring any significant improvement. This disappointing result we believe is likely caused by the fact that the crustal field model we used for the correction does not represent enough of the small scales that actually went into the forward model (and which in fact seems to make most of the crustal biases seen by the observatories). Thus, we must conclude that, at least as far as our modeling strategy is concerned, correcting for crustal signal does not bring any significant improvement.

Choosing a constellation We next considered the issue of choosing a constellation. Three cases were considered in some details, and for each case the results for the internal field and for the secular variation are shown. One with 2 years of data (Figures 6.52-6.53), one with 6 months of data (as in the previous tests, Figures 6.54-6.55), the last one with only 2 months of data (Figures 6.56-6.57).
The case for 2 years shows little difference between the three constellations considered, which we also compared to the case of a single low satellite, although we do see some better results in the case of constellation SW1346. In all cases, the secular variation is recovered up to degree 10.
The case for 6 months does not show more of a discriminating result, although again, constellation SW1346 appears to do a slightly better job. In that case the secular variation can be recovered up to degree 6.
As a matter of fact, it is only when one considers the case for 2 months that a somewhat significant difference can be found between the constellations, again in favor of constellation SW1346. In that case, when combined with observatory data, the data from the constellation would make it possible to recover the secular variation up to degree 4, only.

Not considering the external toroidal field contribution The synthetic data provided by DSRI (CM4 code) contains all sources. But towards the end of this study, it was noted that the external toroidal field contribution had likely been overestimated in the forward code. Because of this we also briefly considered the case when the external toroidal field was omitted. Figures 6.58-6.61 show the results for the constellations SW1245 and SW145, for respectively 6 and 2 months. Those constellations were considered despite the fact that our study showed a slight preference for constellation SW1346, because they had been shown to be the best suited for the purpose of recovering the crustal field. Not including the external toroidal field contribution clearly leads to a better recovery of the secular variation.

6.3.7 Conclusions

There are several conclusions we may finally draw from both Tasks.
As an outcome of Task 2, it was already concluded that a modeling strategy mainly based on data selection with little modeling of the non-core sources (an approach which had proved quite successful for the analysis of data recovered from a single satellite), no longer seems to be appropriate for the purpose of taking advantage of a constellation of satellites. Some of the problems arise because this strategy fails to properly account for the crustal signal. Unfortunately, correcting for this crustal signal with the help of a crustal field model derived independently from the same data, did not significantly alleviate those problems. The biggest problems however, came from the external field signal. Part of this signal was better taken into account in the course of Task 3. But it is clear that in the future, only a strategy along the lines of the comprehensive approach will be able to take full advantage of a constellation such as that of *Swarm*. Despite those limitations, results from both Tasks show some advantages of a constellation over a single satellite mission. This was best seen in the course of Task 2 (recall Figures 6.39, 6.41 and 6.43). This study cannot be used to actually decide which constellation would be best, but is consistent with the results derived from the much better suited comprehensive modelling approach.

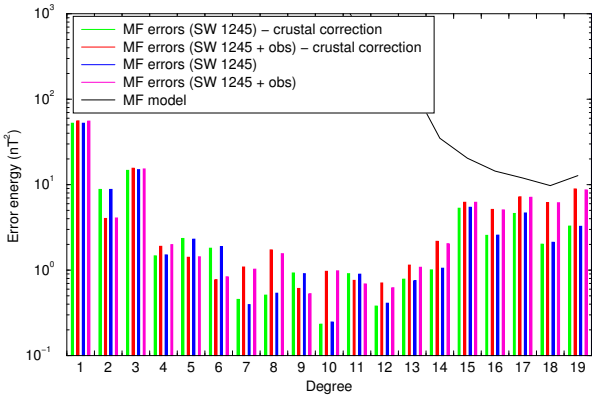

Figure 6.50: Internal field errors for a 6-month period of measurements, considering all sources of data and the instrumental noise. The internal field is calculated up to $N = 29$, the secular variation up to N =13, the secular acceleration up to N =8. For comparison the crustal corrections are also applied.

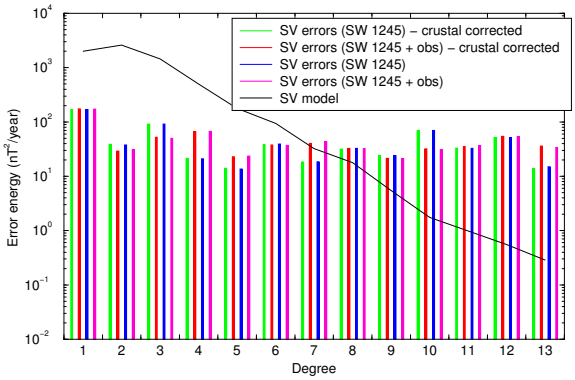

Figure 6.51: Secular variation errors for a 6-month period of measurements, considering all sources of data and the instrumental noise. The internal field is calculated up to $N = 29$, the secular variation up to N =13, the secular acceleration up to N =8. For comparison the crustal corrections are also applied.

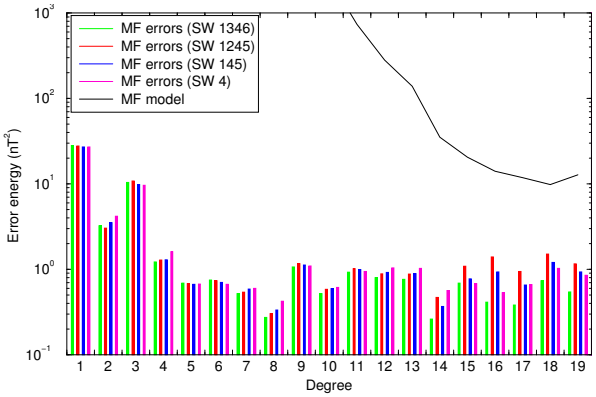

Figure 6.52: Internal field errors for a 2-year period of measurements, considering all sources of data and the instrumental noise. The internal field is calculated up to $N = 29$, the secular variation up to N =13, the secular acceleration up to N =8.

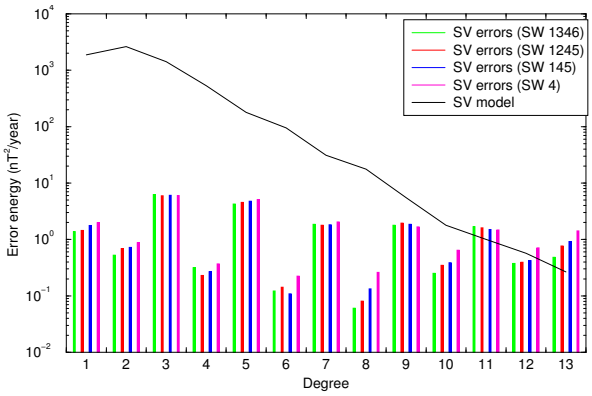

Figure 6.53: Secular variation errors for a 2-year period of measurements, considering all sources of data and the instrumental noise. The internal field is calculated up to $N = 29$, the secular variation up to N =13, the secular acceleration up to N =8.

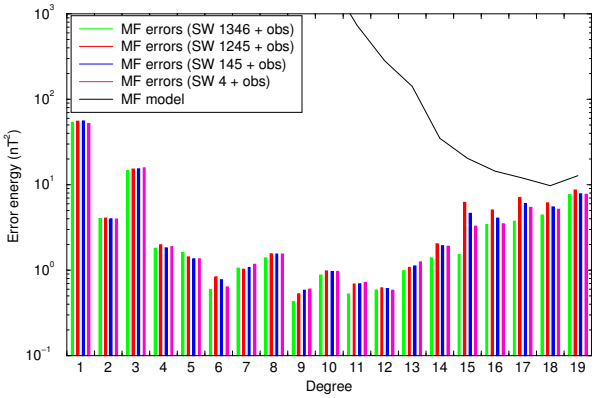

Figure 6.54: Internal field errors for a 6-month period of measurements, considering all sources of data and the instrumental noise. The internal field is calculated up to $N = 29$, the secular variation up to N =13, the secular acceleration up to N =8.

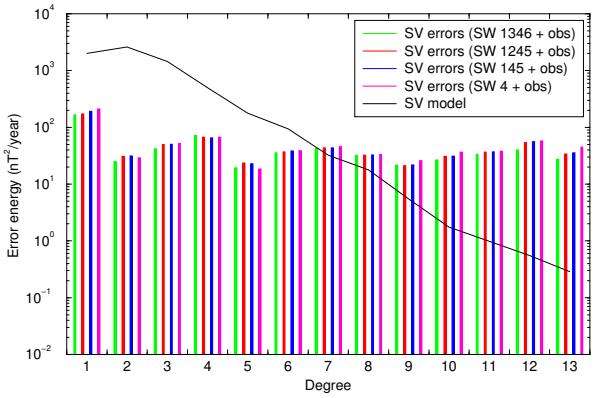

Figure 6.55: Secular variation errors for a 6-month period of measurements, considering all sources of data and the instrumental noise. The internal field is calculated up to $N = 29$, the secular variation up to N =13, the secular acceleration up to N =8.

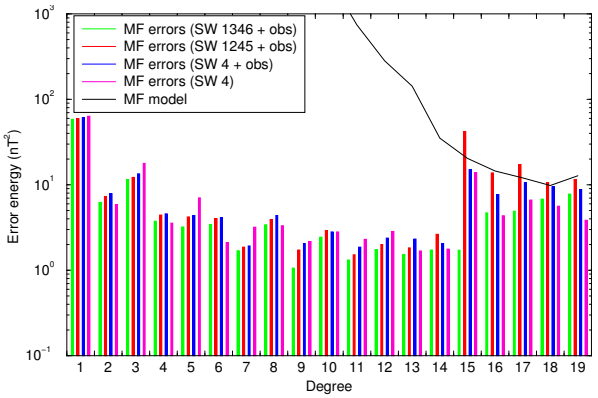

Figure 6.56: Internal field errors for a 2-month period of measurements, considering all sources of data and the instrumental noise. The internal field is calculated up to $N = 29$, the secular variation up to N =13, the secular acceleration up to N =0.

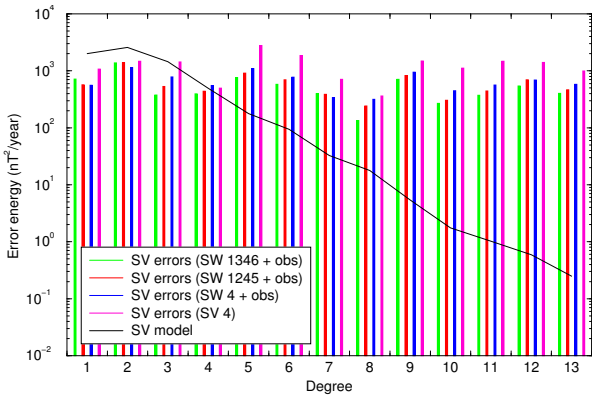

Figure 6.57: Secular variation errors for a 2-month period of measurements, considering all sources of data and the instrumental noise. The internal field is calculated up to $N = 29$, the secular variation up to N =13, the secular acceleration up to N =0.

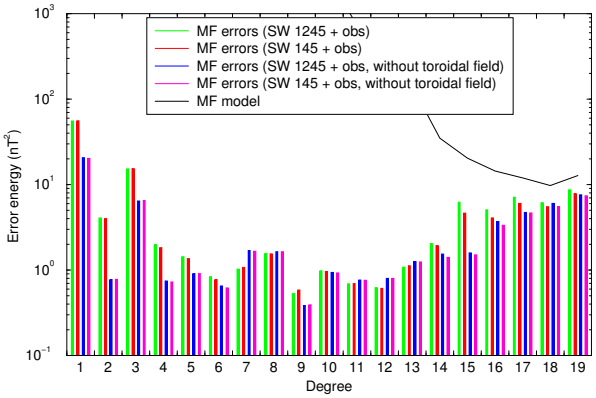

Figure 6.58: Internal field errors for a 6-month period of measurements, considering all sources of data (except the toroidal field if precised) and the instrumental noise. The internal field is calculated up to $N = 29$, the secular variation up to N =13, the secular acceleration up to N =8.

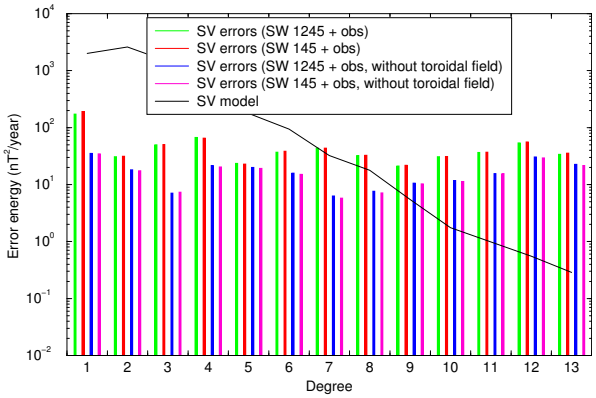

Figure 6.59: Secular variation errors for a 6-month period of measurements, considering all sources of data (except the toroidal field if precised) and the instrumental noise. The internal field is calculated up to $N = 29$, the secular variation up to N =13, the secular acceleration up to N =8.

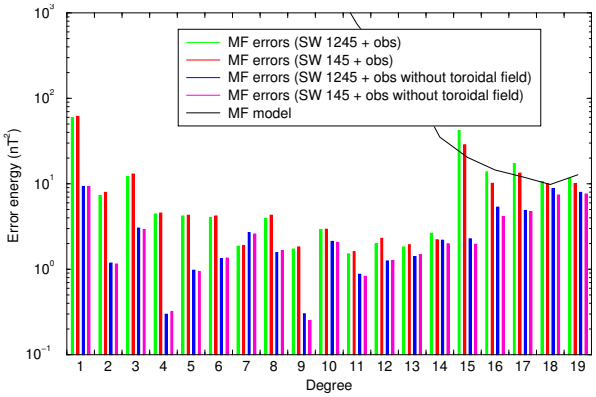

Figure 6.60: Internal field errors for a 2-month period of measurements, considering all sources of data (except the toroidal field if precised) and the instrumental noise. The internal field is calculated up to $N = 29$, the secular variation up to N =13, the secular acceleration up to N =0.

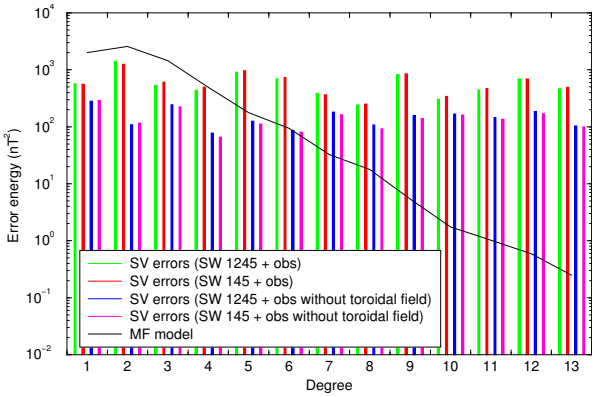

Figure 6.61: Secular variation errors for a 2-month period of measurements, considering all sources of data (except the toroidal field if precised) and the instrumental noise. The internal field is calculated up to N =29, the secular variation up to N =13, the secular acceleration up to N =0.

6.4 Core Field and Secular Variation – Method 2

This section describes results obtained by Vincent Lesur, Alan Thomson and Susan Macmillan, of the British Geological Survey, Edinburgh, UK, in relation to WP 4220: "Earth Surface Main Field and Secular Variation".
These results were obtained in two steps. Firstly we investigated the degree to which we were able to recover the underlying known main and secular variation field models from a "noise-free" data set and, secondly, we tried to estimate the most suitable satellite constellation for resolving the main field and its secular variation. In the following the first step is referred to as "task 2" and the second step as "task 3".
For these tasks we constructed a synthetic data set from one, two or four satellites, in constellation #1 for task 2, and constellation #2 for task 3, and used either one, two or five years of data. We investigated synthetic satellite data where the underlying model contained only the core field and its secular variation, data where only the core, crustal, and large-scale magnetospheric sources were involved, and data where all the sources in the original model were included.
Our modelling technique included an internal field model and its linear secular variation up to spherical harmonic degree 19 and, where appropriate, quadratic or cubic time variation up to degree 13. For a better resolution of the main field model and its secular variation, models of the magnetospheric field, and the fields it induced in the Earth, were used. The variation in time of these fields included annual and semi-annual dependencies and the very rapid variations in time were controlled by the Dst or RC index. We anticipate that with such a modelling technique we cannot recover the underlying model to a very high accuracy when all the sources of the geomagnetic field are present in the synthetic data set. The main limiting factor is the complexity in space and time of the ionospheric and magnetospheric fields and their induced counterparts. However similar modelling techniques are currently used by many research groups in geomagnetic field modelling.
The next section describes our data selection criteria and modelling techniques that are common to both tasks. The following two sections then describe the data sets, models and results specific to each task.

6.4.1 Data filtering and modelling technique

In all the data selections we filtered the data according to (with justification in parentheses): local times 2300-0600 (avoidance of day-side and dusk-side current systems); $Kp < 1^+$ (current three hour period – quiet magnetosphere); $Kp < 2^-$ (previous three hour period); $-10 < Dst < +10$ (current hour – quiet magnetosphere); $-15 < Dst < +15$ (previous hour); interplanetary magnetic field data (ACE satellite) with $-1 < B_z < +5$ (minimise field aligned currents), $|B_y| < 3, |B_x| < 10$ nT, and the solar wind velocity $V_{sw} < 450$ km/s. We comment that these filter options were set with rather narrow pass bands to minimise contributions from un-modelled sources and to aid the recovery of the underlying model. Full vector data are used within 60 degrees of the geomagnetic equator for task2 and 55 degrees for task3. Scalar data are used outside these limits.
The parameterisation uses spherical harmonics and has similarities with the parameterisation described in Olsen [2002] where the magnetic field vector is presented as the gradient of a scalar potential (see equation 2.1). The internal field and its secular variation were modelled up to spherical harmonic degree 19. Quadratic time variations, for up to a three year data span, or cubic time variations, for a five year data span, were introduced up to degree 13. The external field was modelled up to degree 2 with a Dst or RC index and annual/semi-annual time dependency. The internal induced magnetic field was set proportional to the external Dst or RC dependency (with factor 0.27).
Model solutions were obtained by iterative least-squares with a time dependent tesseral data weighting (i.e. dependent on data number, for a given time span, in an equal-area tessera equivalent to a 5 degree square at the equator). All data were given the same 2 nT uncertainty, together with a dependence on the sun zenith angle of $3(1 + \cos\kappa)$ (for night-side data κ is larger than 90°).

6.4.2 Task 2: Inverting noise-free data

We investigate here the degree to which we are able to recover the underlying known main and secular variation field models for epoch 1999.5 using one or five years of data. We first start from a "noise-free"

	Scalar data	Vector data	Total number
Selection 2-1	2431	4494	15913
Selection 2-2	11215	23982	83161
Selection 2-3	23753	53088	183017
Selection 2-4	95592	210802	727998

Table 6.2: Number of data depending on the selection.

	Model 2-0	Model 2-1	Model 2-2	Model 2-3	Model 2-4	Model 2-5	Model 2-6	Model 2-7	Model 2-8
Selections	2-2	2-1	2-2	2-1	2-2	2-3	2-4	2-3	2-4
Satellites	1,2,3,4	3	1,2,3,4	3	1,2,3,4	3	1,2,3,4	3	1,2,3,4
Years	1999	1999	1999	1999	1999	1997 to 2001	1997 to 2001	1997 to 2001	1997 to 2001
Sources	*m*	*mcx*	*mcx*	*all*	*all*	*mcx*	*mcx*	*all*	*all*
int + sv	19	19	19	19	19	19	19	19	19
quad sv	13	13	13	13	13				
cubic sv						13	13	13	13
ext		2	2	2	2	2	2	2	2
annual/semi-annual		2 *int&ext*	2 *int&ext*	2 *int&ext*	2 *int&ext*	2 *int &ext*	2 *int&ext*	2 *int&ext*	2 *int&ext*
RC		*ext* 1	*ext* 1	*ext* 1 + induced	*ext* 1 + induced	*ext* 1	*ext* 1	*ext* 1 + induced	*ext* 1 + induced

Table 6.3: Model definition and associated data sets for task 2. In this table *int* and *ext* stand for internal and external gauss coefficients respectively, *sv* stands for secular variation and *quad* for quadratic. The numbers in the bottom 6 rows of the table give the maximum spherical harmonic degree used, the minimum always being one.

synthetic data set built from the core field alone and then look at the effect of including the other sources.

Data selection and model parameterisation

Four different selections of the satellite data were made. The first two data selections used only year 1999 data, with either satellite 3 data only (selection 2-1), or data from the four satellites of constellation #1 (selection 2-2). We selected 1999 because of the optimal local time separation of the constellation satellites i.e. approximately 6 hours apart, despite the relative high level of geomagnetic activity towards the end of the year. The two other selections used data for years 1997 to 2001 with again only satellite 3 data (selection 2-3) or data from the four satellites (selection 2-4). We use the ring current proxy *RC* rather than *Dst*, since *Dst* is part of the synthetic data generation algorithm. The number of data values depending on the selection criteria used is given in Table 6.2.

Satellite data sets were compiled depending not only on the above selection criteria but on the sources that contribute to the synthetic data. We have used three different source combinations to build the data sets: the core field including the secular variation (sources "*m*"), the core field with the secular variation, crustal field and external field (sources "*mcx*") and ultimately, all the sources of the underlying model (sources "*all*").

A total of nine models were investigated and are presented in Table 6.3.

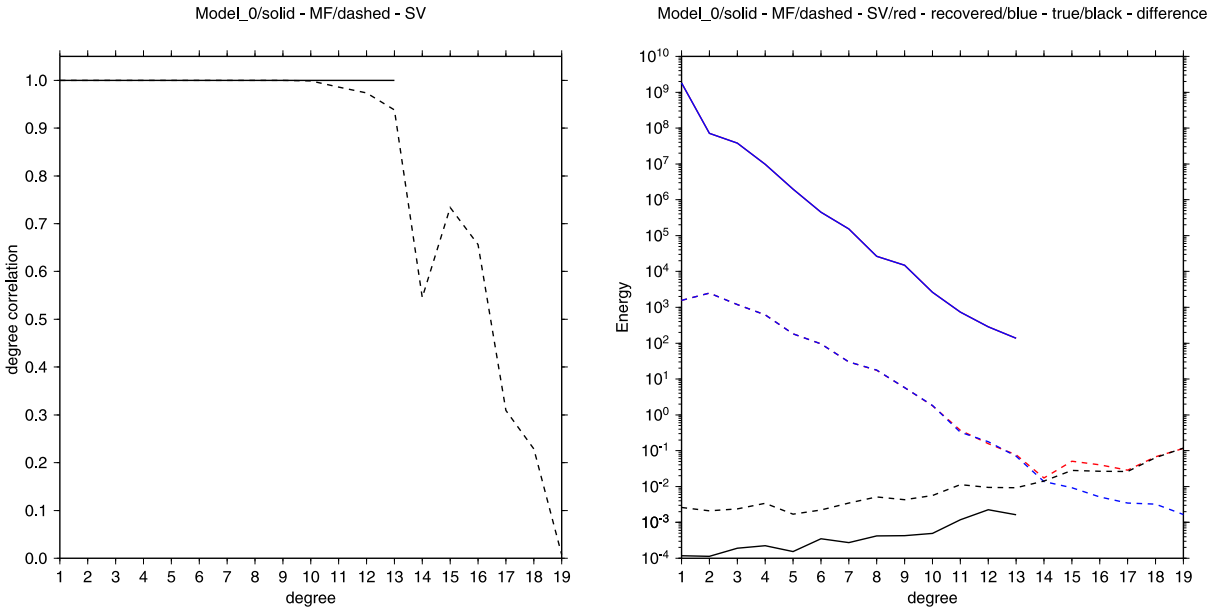

Figure 6.62: Degree correlation plot and power spectra of the Gauss coefficients and their secular variations as estimated from model 2-0.

Results

Model 2-0 data set covers only the year 1999 and is almost "noise free" because the model we try to estimate differs from the underlying model only by the *sv* parameterisation (our model contains quadratic sv whereas the underlying model uses cubic splines). Figure 6.62 shows the degree correlation plot and the power spectra for model 2-0. The maximum degrees to which the recovered model are compatible (defined by degree correlation > 0.7) with the underlying models are given in Table 6.4. The square root of the sum over all the degrees of the power spectra of the differences (*sqspd*) is 0.1 nT for the core coefficients and 0.6 nT/year for their *sv*. It is clear that the fit to the original model is excellent. The slight drop of the *sv* degree correlation for degree 10 to 13 can be corrected if data from more than one year are used.

Models 2-1 to 2-4 are built using one year of data. Satellite 3 only (selection 2-1) does not provide enough data to robustly solve for models as complex as models 2-1 and 2-3 and some regularisation is needed. However models 2-2 and 2-4 can be solved and their degree correlation and power spectra plots are shown in Figures 6.63 and 6.64. The maximum degree to which these models are compatible and their *sqspd* are given in Table 6.4. All these results show that the poor representation of the external fields has a strong impact on the parameter estimation, but the core field coefficients, and the associated *sv* up to degree 7 or 8 are recovered with good accuracy. The discrepancy between the underlying model and model 2-4 for degrees 1 and 2 (see Figure 6.64) is due to the internal annual and semi-annual parameters that are poorly constrained with our data distribution. Introducing observatory data can reduce this discrepancy.

Most of the above problems are solved for models 2-5 to 2-8 when 5 years of data are used. Figures 6.63 and 6.64 present their degree correlation and power spectra plots. The maximum degrees to which these models are compatible and their *sqspd* are given in Table 6.4. Over such a long period of time, the effect of the external fields tend to average out, leading to better results for the static Gauss coefficients over degree 13 and reasonable agreement between the *sv* coefficients up to degree 10. Over five years the quantity of data is such that the main field and sv models up to degree 10 are well resolved even with one satellite.

Finally, Figure 6.65 shows maps of differences between the underlying model and model 2-8 for each of the three components of the magnetic field. The maps of differences for the static Gauss coefficients (the main field) are dominated by the difference associated with the zonal degree 3 Gauss coefficient which is

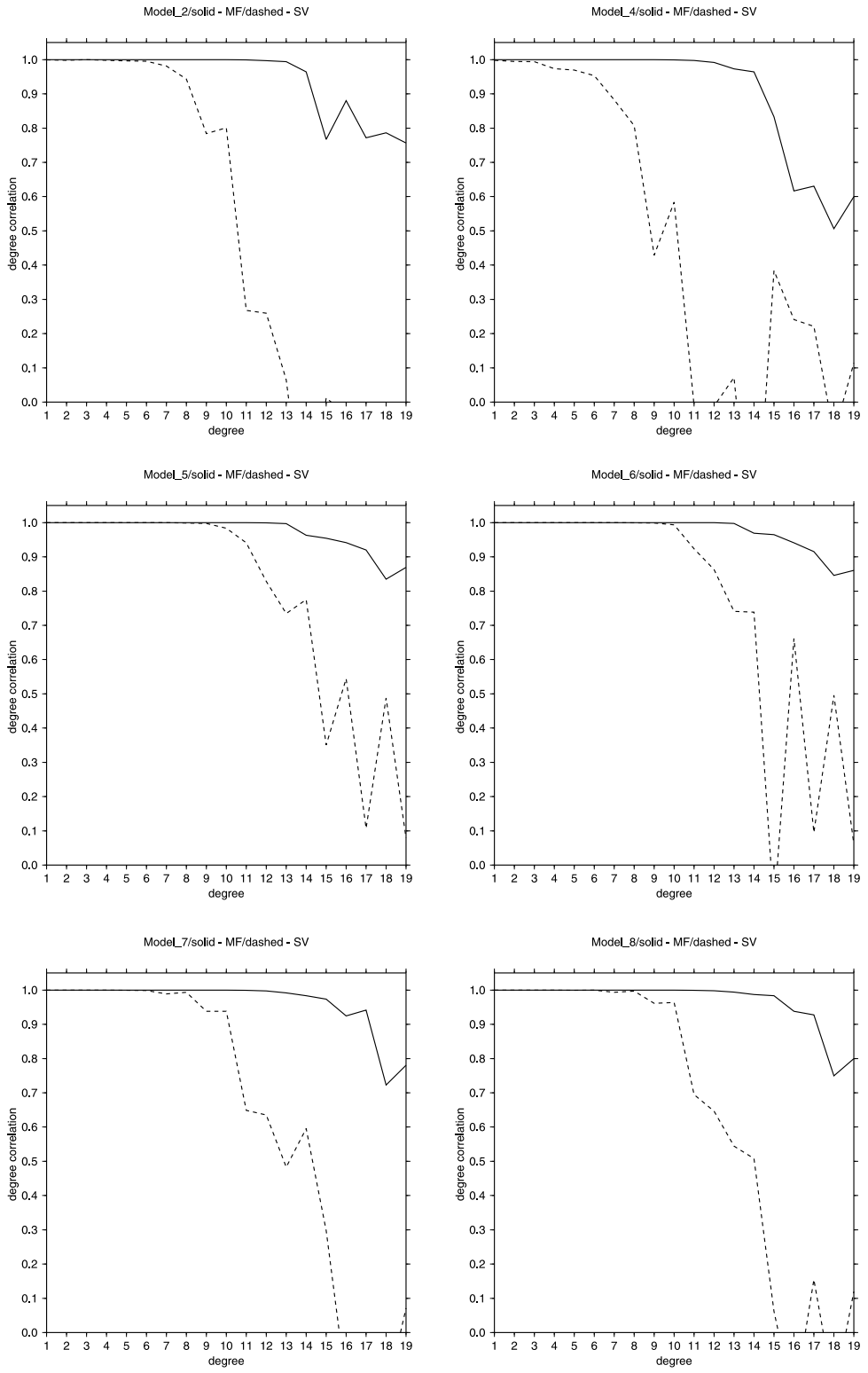

Figure 6.63: Degree correlation plots of the Gauss coefficients and their secular variations up to degree 20. Presented are the models 2-2, 2-4, 2-5, 2-6, 2-7 and 2-8.

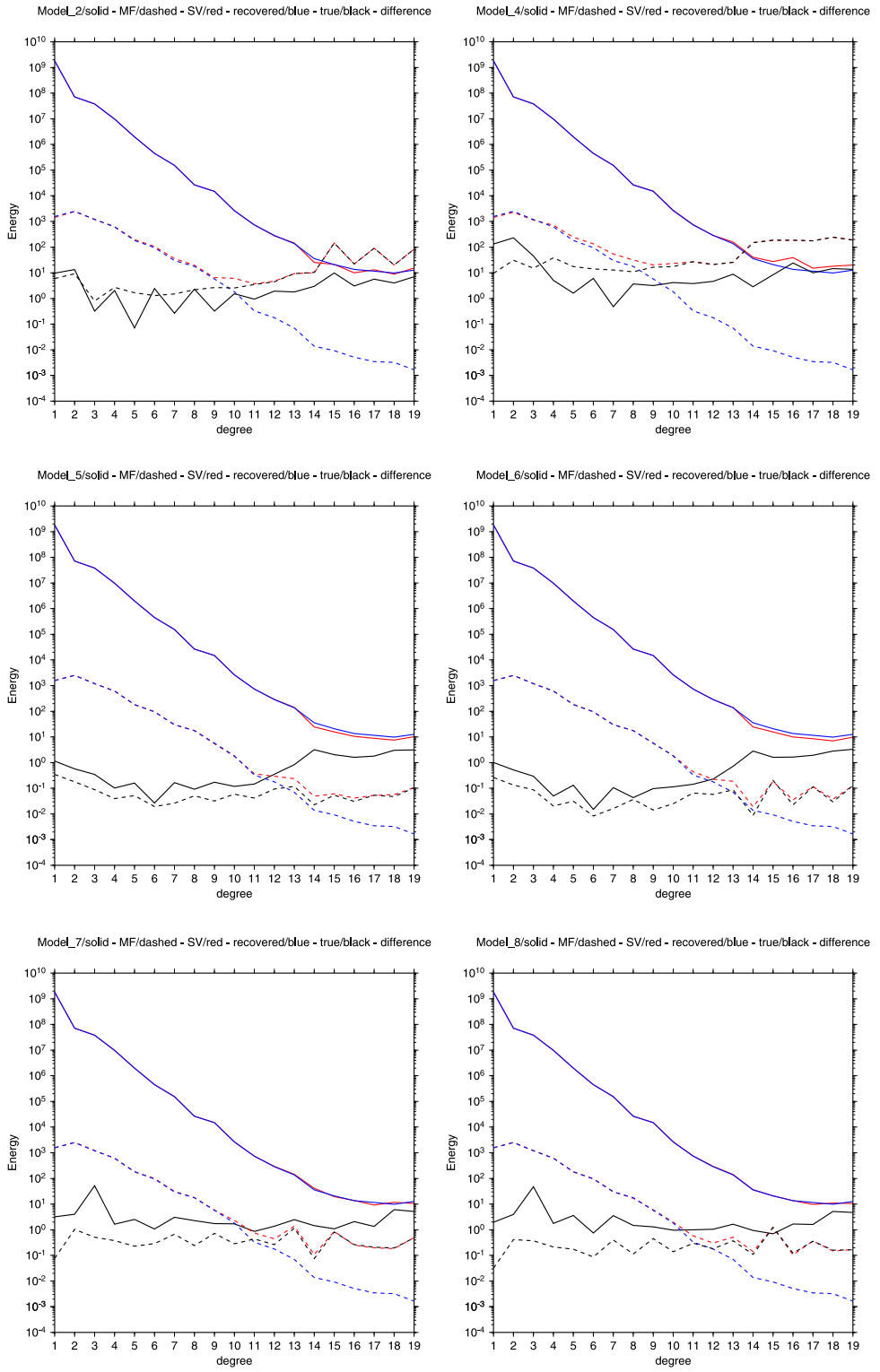

Figure 6.64: Power spectra of the Gauss coefficients, their secular variations and their differences relative to the underlying model. Presented are the models 2-2, 2-4, 2-5, 2-6, 2-7 and 2-8.

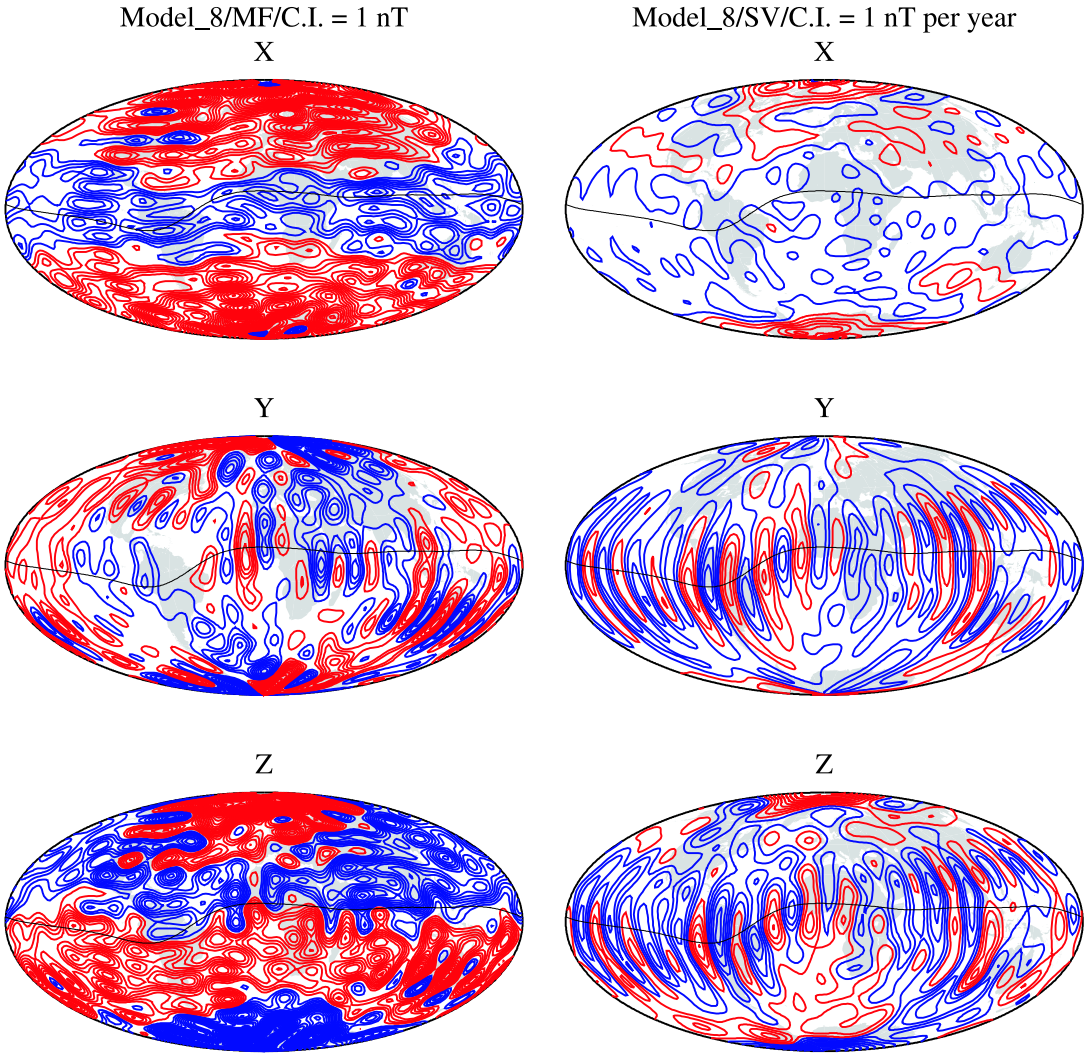

Figure 6.65: Maps of the Main field and sv model differences in the three components of the geomagnetic field.

Model		2-0	2-2	2-4	2-5	2-6	2-7	2-8
Maximum degrees	Mainfield	13	19	15	19	19	19	19
	sv	13	10	8	14	14	10	10
sqspd	Mainfield (nT)	0.1	8.3	22.9	4.4	4.2	9.8	9.3
	sv (nT/year)	0.6	20.5	37.2	1.2	1.2	2.9	2.3

Table 6.4: Maximum degree to which the models are compatible with the underlying models and their *sqspd*.

under-estimated by more than 3 nT in model 2-8 relative to the underlying model. Similarly, the map of differences associated with the *sv* is dominated by one sectorial coefficient at degree 15 giving this "Backus effect"-like pattern. These erroneous coefficient values also affect the power spectra plots in Figure 6.64.

	Model 3-0	Model 3-1	Model 3-2	Model 3-3	Model 3-4
Selection	3-0	3-1	3-2	3-3	3-4
Satellites	1,2,4,5	1,2,4,5	1,3,4,6	1,2	1,3
Years	1997 to 2001	1997 to 2001	1997 to 2001	1997 to 1998	1997 to 1998
Instrument noise	*no*	*yes*	*yes*	*yes*	*yes*

Table 6.5: Model definitions and associated data sets for task 3. The sources and model parameterisations are the same as for model 2-8 in Table 6.3.

6.4.3 Task 3: Constellation choice

We investigate here what would be the most appropriate satellite constellation to generate a data set that would allow the recovery of the underlying known main and secular variation field models, in the presence of instrumental noise.

Data selection, weighting and model parameterisation

Five data selections were made. The data were filtered as described in Section 6.4.1 and selected over five years for satellites 1, 2, 4 and 5 (which we refer to as selection 3-1) or satellites 1, 3, 4 and 6 (selection 3-2) in constellation #2. Selection 3-0 is then the same as selection 3-1, but without the instrumental noise. Selections 3-3 and 3-4 use data from years 1997 and 1998 only and include data from satellites 1 and 2, or 1 and 3, respectively.
The model parameterisation is the same as for model 2-8 above, but here we use the Dst index in place of the RC index to describe the rapid variations of the magnetospheric fields. Table 6.5 summarises the models produced for task 3.

Satellite combination 1245 and 1346

In this section we examine how well we are able to recover the core field Gauss coefficients and their sv from models 3-1 and 3-2. Both of these models were built using 1999.0 as the reference epoch. Figures 6.66 and 6.67 present the degree correlation plots and the power spectra for models 3-1 and 3-2. For both models, the results are not as good as those presented under task 2. This is very likely to be due to the increased complexity of the magnetospheric and induced field models used to build the synthetic data set of task 3, and also the increased power of the sv terms in the underlying model. However, if we compare models 3-1 and 3-2, results are better for the latter. The maximum degrees to which the recovered models are compatible (again defined by degree correlation > 0.7) with the underlying models are given in Table 6.6 together with the *sqspd*. Also given are the values for model 3-0. The results for models 3-0 and 3-1 are almost the same, showing that the addition of instrumental noise has a negligible effect on our main field recovery.
In order to understand why there is such an improvement in changing from model 3-1 to model 3-2 we plot in Figure 6.68 the *sqspd* for both as a function of time. Not only are the *sqspd* values not at a minimum for 1999.0 as we would have expected, but the difference between model 3-1 and 3-2 is much larger over the two first years. It is very likely that the improvements observed in model 3-2, compared with model 3-1, are mainly due to the use of data from satellite 3 in place of satellite 2 during the first two years. With the model parameterisation that we have used, the lower satellites are not as "good" for determining the secular variation since they have a higher level of crustal "noise" and their paths are changing rapidly with time.

Satellite combination 12 and 13

Figure 6.69 and Figure 6.70 present the degree correlation plots and the power spectra plots for models 3-3 and 3-4 respectively. The maximum degree where the recovered models are compatible with the underlying models and their *sqspd* are given in Table 6.4.
It is relatively easy to understand why the results for model 3-4 are better than for model 3-3. Satellites 1 and 2 are flying half an orbit apart and they are never together in the narrow local time window

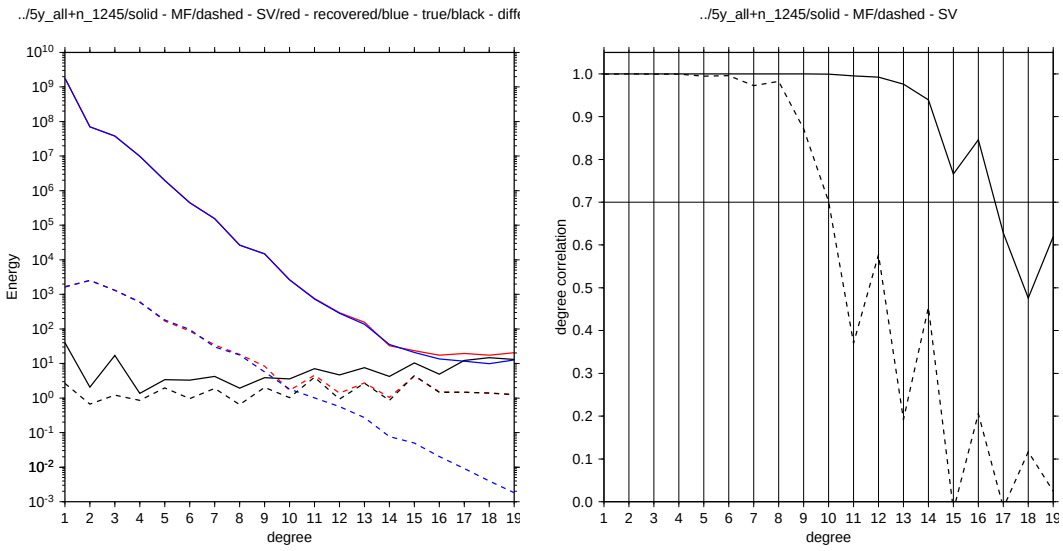

Figure 6.66: Degree correlation plot and power spectra of the Gauss coefficients and their secular variations as estimated from model 3-1.

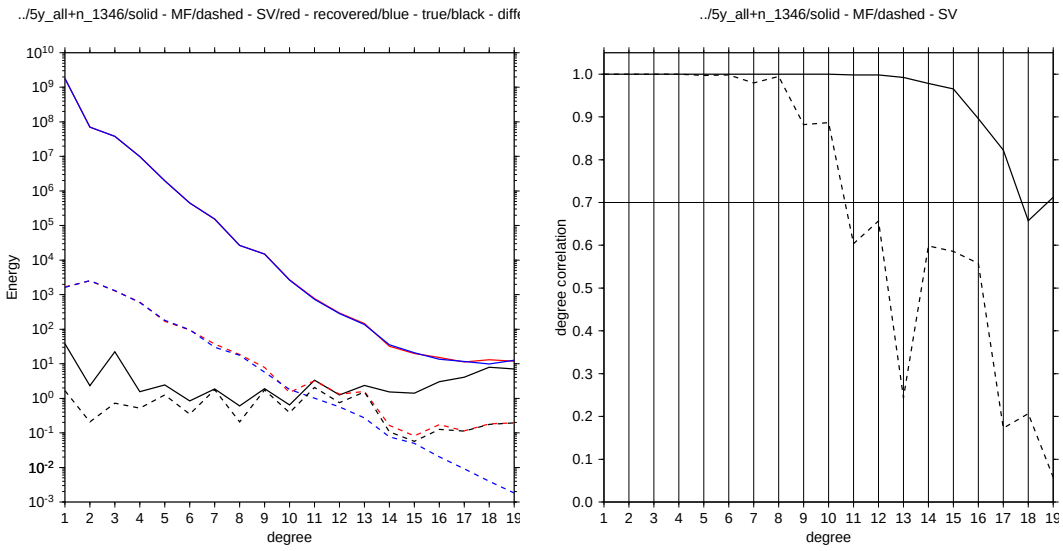

Figure 6.67: Degree correlation plot and power spectra of the Gauss coefficients and their secular variations as estimated from model 3-2.

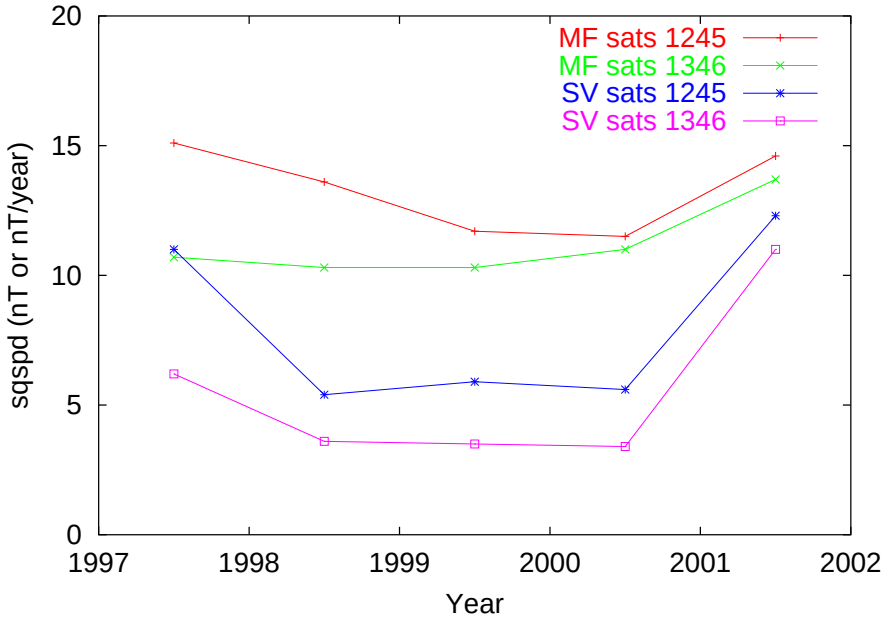

Figure 6.68: Variation of the *sqspd* with time calculated for the main field and its *svsqspd* for models 3-1 and 3-2.

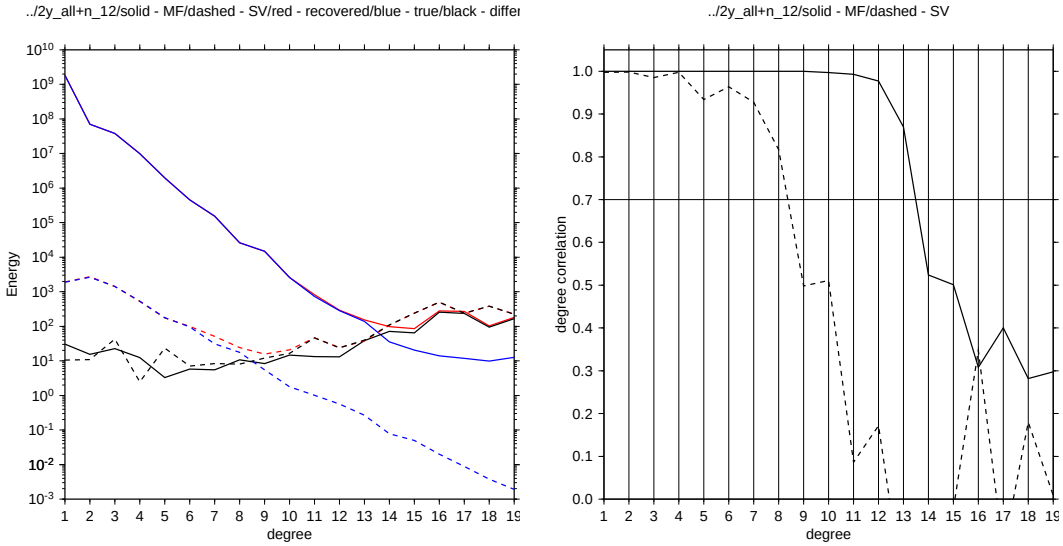

Figure 6.69: Degree correlation plot and power spectra of the Gauss coefficients and their secular variations as estimated from model 3-3.

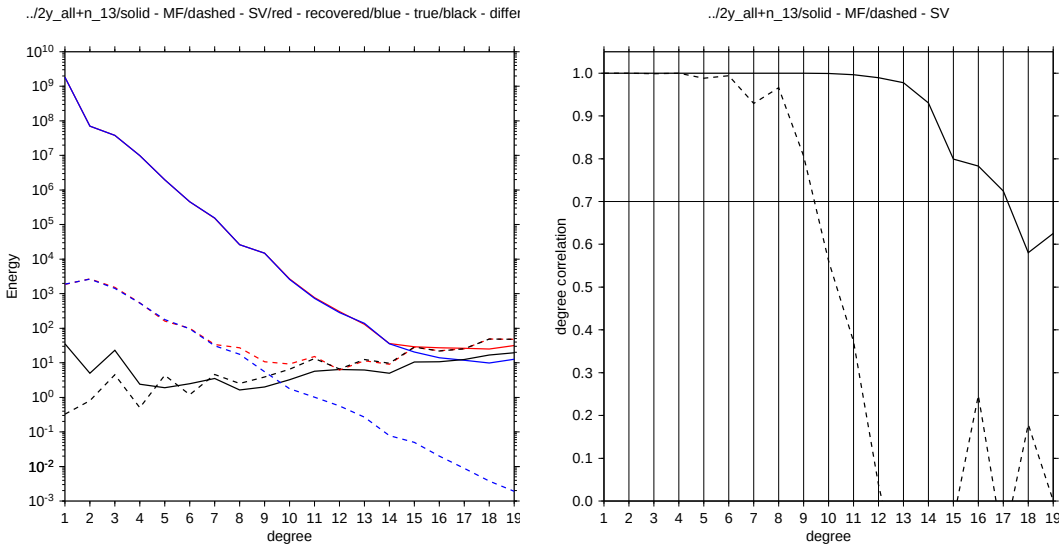

Figure 6.70: Degree correlation plot and power spectra of the Gauss coefficients and their secular variations as estimated from model 3-4.

Model		3-0	3-1	3-2	3-3	3-4
Maximum degrees	Mainfield	16	16	17	13	17
	sv	10	10	10	8	9
sqspd	Mainfield (nT)	12.6	12.6	10.2	32.9	13.2
	sv (nT/year)	5.6	5.7	3.7	44.1	15.6

Table 6.6: Maximum degree to which the models are compatible with the underlying models and their *sqspd*.

specified as part of our selection criteria. Unless we model the ionospheric field and use day-side data there is therefore no advantage in such a constellation. There isn't much more information for main-field and *sv* modelling in the combined data set of satellites 1 and 2 than there is in the satellite 1 data set alone. Furthermore, satellites 1 and 2 are surveying almost the same longitude keeping the data in very narrow band around 15 constant meridians. With such a distribution in space there is no possibility of recovering model coefficients of high spherical harmonic orders. In contrast, satellites 1 and 3 are always together in our narrow local time window and are surveying twice as many discrete meridians. We can, with satellites 1 and 3, take full advantage of a constellation. However, high altitude satellites are not optimal for modelling the crustal field and further satellites at lower altitude need to be included to complete the constellation.

6.4.4 Conclusion

Our studies have shown:

- We are able to recover the underlying model parameters to a high accuracy when noise free data are provided.
- Progress must be made in the parameterisation of external fields to be able to fully appreciate the

quality of the data provided by the swarm constellation.

- When data over several years are used, a better resolution of internal static Gauss coefficients, and their associated secular variation, is obtained.
- The instrumental noise has no visible effect on our ability to recover the main field model and associated secular variation.
- Over five years the main field and its secular variation is better resolved with the satellite combination 1346 than with the combination 1245 of constellation #2.
- With our modelling approach, the best satellite combination should include satellites flying parallel to one another rather than half an orbit apart.

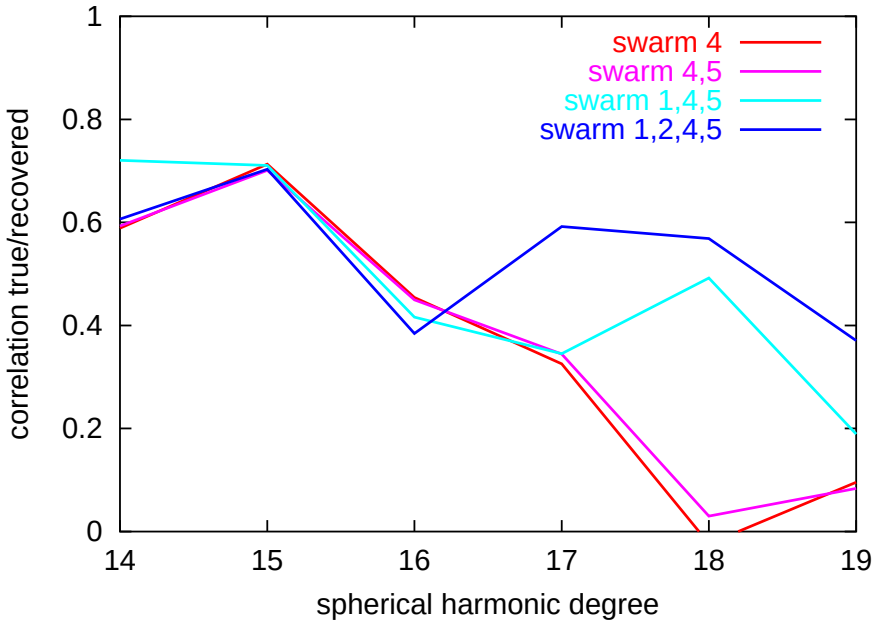

Figure 6.71: Degree correlation between input and recovered model of the high-degree secular variation. An increasing number of satellites in the *swarm* constellation improves the result.

6.5 High-Degree Secular Variation

The group at GFZ Potsdam has been dealing with the high-degree features beyond $n = 14$ in the context of the *swarm* End-to-End System simulator. These include the lithospheric anomalies and the ocean signals. For that reason we applied also our processing approach to the high-degree part ($n = 14$ to 19) of the secular variation. Main purpose is to study the potential of a constellation mission in resolving this varying part of the magnetic field.

6.5.1 Data selection and processing approach

For this task all the magnetic field components that are part of the Constellation #2 data set, including noise, have been added up. For the processing only data from very quiet periods have been selected, $Kp \leq 1$. The local time interval considered here is limited to 20 - 06 LT. Magnetic field vector data have been used for all latitudes.
Several field contributions have been removed before the determination of the secular variation was performed. First a main field model with linear SV up to degree 13 was subtracted. Furthermore, the ocean signal was removed. The external contributions and their induced counterparts are accounted for on an orbit-by-orbit base. All spacecraft passing SW4 within an hour at longitudes not further away than 50° are considered for that procedure. The low-degree external field components were estimated from these measurements, using the data of all these satellites in a single solution. The cleaned data from the whole mission period of 5 years is included in a recovery of the secular variation.
The procedure described above has been repeated several times using an increasing number of satellites from the *swarm* constellation. The quality of the recovery is tested using the degree correlation between the input and the derived model. Figure 6.71 shows the performance of the recovered model for four different satellite constellations. In case only one of the lower satellites is used (SW4) the correlation continuously decreases and disappears at $n = 18$. Adding the closely spaced accompanying spacecraft, SW5, does not change the situation. The inclusion of one of the upper satellites (SW1) helps already a bit to improve the correlation. Considering all four satellites makes a significant difference. Now the secular variation up to the highest degree can be recovered. We regard this as a convincing demonstration of the potential to retrieve the details of the temporal changes with the proposed constellation.

6.6 Mapping of 3-D Conductivity Anomalies in the Mantle - Method 1

The following two sections describe results obtained by Alexei Kuvshinov (DSRI), Pascal Tarits (CNRS/IUEM), T. Sabaka (NASA/Goddard Space Flight Center) and Nils Olsen (DSRI) in relation to WP 4410: "3-D Mantle Conductivity".

The study of lateral variability in the physical properties of Earth's mantle using geophysical methods provides insight into geodynamic processes such as mantle convection, the fate of subducting slabs and the origin of continents. One example is global seismic tomography [e.g. Li and Romanowicz, 1995, Woodhouse and Trampert, 1995, Su and Dziewonski, 1997, Ritsema et al., 1999, Bijwaard and Spakman, 2000, Deschamps et al., 2002], the products of which can be interpreted in terms of cratonic roots, mantle plumes, and slab graveyards.

The goal of geomagnetic induction studies is to identify complementary large-scale spatial variations (3-D structures) in the electrical conductivity of the mantle. This is interesting since induction data reflect the connectivity of constituents such as graphite, fluids, partial melt, and volatiles – all of which may have profound effect on rheology and, eventually, mantle convection and tectonic activity. In contrast, seismology provides information on bulk mechanical properties. Traditionally, land-based data [e.g. Roberts, 1984, Schultz, 1990, Egbert and Booker, 1992, Olsen, 1998, Neal et al., 2004] have been used to sense lateral mantle conductivity variations, but this task is rather challenging, since the observatories are sparsely and very irregularly distributed on the globe (e.g., oceanic regions are almost free from observations) and, moreover, the data quality is strongly variable. Satellite-borne measurements provide an intriguing and unique source to improve our knowledge about 3-D variations of electrical conductivity in the Earth's mantle owing to a good spatio-temporal coverage with data of uniform quality.

With this great interest in 3-D induction studies from space it is surprising to find that so far there are no successful examples to map 3-D structures from satellite data. Using realistic 3-D induction time-domain modeling approaches (see details of the 3-D model adopted and numerical approach described in section 3.5.2) we demonstrate here that the present single satellite missions are hardly able to resolve deep 3-D structures, even on a regional scale. However, we found that the multi-satellite (*Swarm*) mission may recover deep-seated anomalies in the mantle on the basis of analysis of geomagnetic response functions (C-responses).

6.6.1 Geomagnetic transfer functions

Traditionally, the geomagnetic depth sounding (GDS) method [Schmucker, 1985] is used to infer 1-D mantle conductivity depth profiles and to detect lateral variations of conductivity in the mantle. The GDS method is based on the determination, analysis and interpretation of transfer functions like the C-response, which, in its general form, is defined as

$$C(\omega, r, \theta, \phi) = -\frac{B_r(\omega, r, \theta, \phi)}{\nabla_{\mathbf{H}} \cdot \mathbf{B}_{\mathbf{H}}(\omega, r, \theta, \phi)} \tag{6.4}$$

with

$$\nabla_{\mathbf{H}} \cdot \mathbf{B}_{\mathbf{H}}(\omega, r, \theta, \phi) = \frac{1}{r \sin\theta} \left\{ \frac{\partial (B_\theta) \sin\theta}{\partial \theta} + \frac{\partial B_\phi}{\partial \phi} \right\} \tag{6.5}$$

being the tangential divergence of $\mathbf{B_H} = (B_\theta, B_\phi)$. Note that $|C|$ is a measure of the "effective" depth of penetration of the electromagnetic (EM) field into the conducting Earth. By determining C-responses at a number of frequencies (by means of time series analysis (TSA) of the corresponding time series of B_r and $\nabla_{\mathbf{H}} \cdot \mathbf{B_H}$ at specific sites) one can invert the responses into conductivity-depth profiles [cf. Olsen, 1998] beneath these sites. Recognizing that the periods used in the GDS method typically span a few hours to months, the derived C-responses probe upper and mid mantle conductivities in the depth range from 100 to 1000 km or so. As an example, Figure 6.72 shows the real (left) and imaginary (right) parts of the C-responses of local 1-D conductivity profiles from three different regions of the 3-D Earth model constructed (see model description in section 3.4.3). The period range is 1 to 39 days. The green curves present C-responses for the continental 1-D conductivity profile with a surface conductance of 400 S,

whereas the red and blue curves show responses for 1-D conductivity profiles in oceanic regions with and without deep seated conductors, respectively. An oceanic conductance of 18000 S has been assumed. As seen from the figure, the maximum difference between continental and oceanic responses is at a period of 1 day, where the relative difference between the responses reach 130%. Also, the real, C_r, and imaginary, C_i, parts of the oceanic C-responses show different behavior with respect to the inclusion of the deep conductor in the oceanic 1-D profile. At a period of 1 day the manifestation of the deep conductor in C_r is very weak; C_r with and without the deep conductor almost coincides. At longer periods, C_r of the oceanic 1-D profile without the deep conductor reaches the continental value: their difference at a period of 14 days does not exceed 7%. With increasing period the relative difference between C_r of the 1-D profiles with and without deep seated conductor increases, reaching a maximum value of 40% at a period of 7 days. For the imaginary part the manifestation of the deep seated conductor in C_i is maximal at a period of 1 day, decreasing with increasing period. Further, in general, the real part of the C-responses are at least three times larger compared to C_i in the considered period range, and C_r is more sensitive to the presence of a deep conductor.

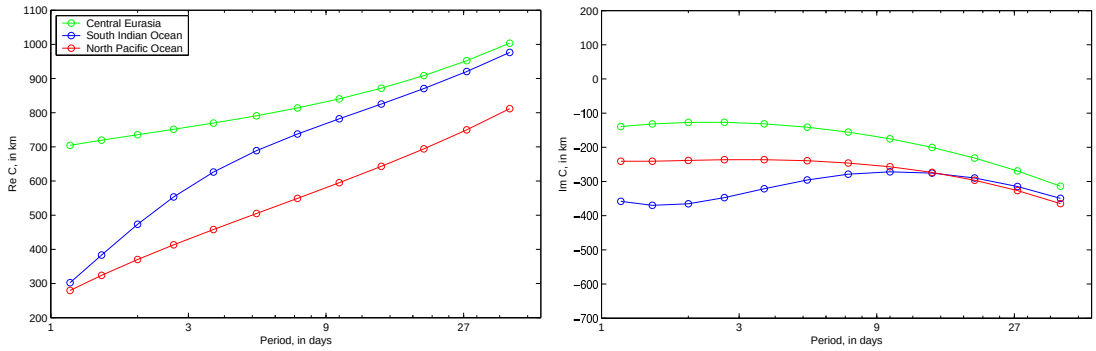

Figure 6.72: Real (left) and imaginary (right) parts of C-responses calculated for local 1-D conductivity profiles for three different regions.

These 1-D results suggest that a regional deep seated conductor (see lower panel of Figure 3.16) might be detectable in the C-responses at periods longer than a few days. It should be stressed, however, that the results shown in Figure 6.72 are obtained from 1-D conductivity models. If one considers 3-D Earth models – 3-D deep regional heterogeneities overlaid by realistic oceans and continents –, excited by realistic external source field that includes contributions from spherical harmonic other than $P-1^0$, (cf. [Olsen and Kuvshinov, 2004]), it is probably rather difficult to infer 3-D mantle structures from C-responses.

Indeed, only in the case of a 1-D Earth and the exciting external fields are described by low degree spherical harmonics, the C-responses are asymptotically independent from the source geometry [cf. Schmucker, 1985] and hence only a function of frequency and of the conductivity distribution. Since the main source of magnetospheric variations in the GDS period range is of large scale (at least at non-polar latitudes), only external coefficients, $q_n^m(t), s_n^m(t)$, of relatively low n (say, $n \leq 3$) are necessary to describe the spatial behavior of the source field. However, in the presence of conductivity inhomogeneities the C-responses lose their invariance with respect to the source geometry. Thus, only realistic 3-D Earth models excited by realistic sources can answer the question whether it is possible to detect and map lateral mantle heterogeneities using a GDS approach.

Given the sparse and irregular distribution of observatory sites it is difficult to determine accurately the horizontal field gradient. Only satellite missions provide a chance to determine C-responses on a regular grid. However, in contrast to ground observations, the satellites move with a speed of a few km per second and thus they measure a mixture of temporal and spatial changes of the magnetic field. In the next section we will show how this problem might be solved. We will present a scheme for the determination of C-responses on a regular grid using satellite magnetic data.

6.6.2 Recovery of C-responses from magnetic satellite data

Let's assume that we have magnetic fields observations $B_r^{(j)}(t_i, r_i^{(j)}, \theta_i^{(j)}, \phi_i^{(j)})$, $B_\theta^{(j)}(t_i, r_i^{(j)}, \theta_i^{(j)}, \phi_i^{(j)})$, $B_\phi^{(j)}(t_i, r_i^{(j)}, \theta_i^{(j)}, \phi_i^{(j)})$, from a constellation of satellites. Here $t_i = i\Delta_i, i = 1, 2, ..., N_d, j = 1, 2, ..., N_s$, where Δ_i is the sampling rate, N_d is the number of samples, and N_s is the number of satellites. Note that in general the sampling rate (and hence the number of samples) may vary from satellite to satellite, and that scalar data, as well as observatory data, can be added.
At satellite altitude the magnetic field can be derived from scalar magnetic potential as $\mathbf{B}(t) = -\nabla V(t)$, where V is approximated by a spherical harmonic expansion as

$$V(r,\theta,\phi,t) = a\sum_{n=1}^{N_e}\sum_{m=0}^{n}\left[(q_n^m(t)\cos m\phi + s_n^m(t)\sin m\phi)\left(\frac{r}{a}\right)^n\right]P_n^m(\cos\theta)+$$

$$\sum_{k=1}^{N_i}\sum_{l=0}^{k}\left[(g_k^l(t)\cos l\phi + h_k^l(t)\sin l\phi)\left(\frac{a}{r}\right)^{k+1}\right]P_k^l(\cos\theta). \tag{6.6}$$

Here $q_n^m(t), s_n^m(t)$ and $g_k^l(t), h_k^l(t)$ are time series of the expansion coefficients of the external and internal parts of the potential, r, θ, ϕ are spherical coordinates with $a = 6371.2$ km as the mean Earth's radius and θ and ϕ as geographic colatitude and longitude, P_n^m and P_k^l are the associated Legendre functions. The magnetic field components follow from this potential expansion as

$$B_r(r,\theta,\phi,t) = -\sum_{n=1}^{N_e}\sum_{m=0}^{n}\left[n(q_n^m(t)\cos m\phi + s_n^m(t)\sin m\phi)\left(\frac{r}{a}\right)^{n-1}\right]P_n^m(\cos\theta)+$$

$$\sum_{k=1}^{N_i}\sum_{l=0}^{k}\left[(k+1)(g_k^l(t)\cos l\phi + h_k^l(t)\sin l\phi)\left(\frac{a}{r}\right)^{k+2}\right]P_k^l(\cos\theta), \tag{6.7}$$

$$B_\theta(r,\theta,\phi,t) = -\sum_{n=1}^{N_e}\sum_{m=0}^{n}\left[(q_n^m(t)\cos m\phi + s_n^m(t)\sin m\phi)\left(\frac{r}{a}\right)^{n-1}\right]\frac{dP_n^m(\cos\theta)}{d\theta}-$$

$$\sum_{k=1}^{N_i}\sum_{l=0}^{k}\left[(g_k^l(t)\cos l\phi + h_k^l(t)\sin l\phi)\left(\frac{a}{r}\right)^{k+2}\right]\frac{dP_k^l(\cos\theta)}{d\theta}, \tag{6.8}$$

$$B_\phi(r,\theta,\phi,t) = -\sum_{n=1}^{N_e}\sum_{m=0}^{n}\left[(s_n^m(t)\cos m\phi - q_n^m(t)\sin m\phi)\left(\frac{r}{a}\right)^{n-1}\right]\frac{m}{\sin\theta}P_n^m(\cos\theta)-$$

$$\sum_{k=1}^{N_i}\sum_{l=0}^{k}\left[(g_k^l(t)\sin l\phi - h_k^l(t)\cos l\phi)\left(\frac{a}{r}\right)^{k+2}\right]\frac{l}{\sin\theta}P_k^l(\cos\theta). \tag{6.9}$$

This means that one can reconstruct time series (of sampling rate, Δ_C) of the external and internal coefficients using a least-square (LS) approach. This scheme has successfully applied by Olsen et al. [2003b] to calculate 1-D responses. Once the coefficients, $q_n^m(t), s_n^m(t)$ and $g_k^l(t), h_k^l(t)$, are determined, time series of B_r and $\nabla_{\mathbf{H}}\cdot\mathbf{B}_{\mathbf{H}}$ are reconstructed at some regular grid at the Earth's surface by spherical harmonic synthesis (SHS) using equation (6.7) and the equation below.

$$\nabla_{\mathbf{H}}\cdot\mathbf{B}_{\mathbf{H}}(r,\theta,\phi,t) = \sum_{n=1}^{N_e}\sum_{m=0}^{n}\left[n(n+1)(q_n^m(t)\cos m\phi + s_n^m(t)\sin m\phi)\left(\frac{r}{a}\right)^{n-1}\right]P_n^m(\cos\theta)+$$

$$\sum_{k=1}^{N_i}\sum_{l=0}^{k}\left[k(k+1)(g_k^l(t)\cos l\phi + h_k^l(t)\sin l\phi)\left(\frac{a}{r}\right)^{k+2}\right]P_k^l(\cos\theta). \tag{6.10}$$

By applying time-series analysis (TSA) to reconstructed time series of B_r and $\nabla_{\mathbf{H}}\cdot\mathbf{B_H}$, $C(\omega, r, \theta, \phi)$ is estimated using eq. 6.4). Then, C can be inverted to obtain images of the conductivity distribution in the Earth interiors. Note, however, that the last issue is out of the scope of this study.

Figure 6.73 summarizes the scheme of C-response determination from satellite magnetic signals. There are some problems that need further investigations, for example the optimal sampling rate, Δ_C, that should be used for the determination of $q_n^m(t), s_n^m(t)$ and $g_k^l(t), h_k^l(t)$. However, sampling rate should be much larger than the initial sampling rate of the satellite constellation, $\Delta_C \gg \Delta_i$, in order to provide good space coverage of the satellite data. Two important questions that we address in the next section are 1) at what periods is a signature of deep seated anomalies detectable in C-responses?, and 2) what is the minimum value of N_i, for which the geometry of a deep seated anomaly can be detected in the C-responses.

6.6.3 Model studies using a reduced scheme

In this section we assume that time series of the external and internal coefficients are available (how they might be determined will be discussed later). Hence we ignore the first step (LS) of the scheme of Figure 6.73. We use the realistic time series, $q_n^m, s_n^m (n = 1-3,\ m = 0, 1, ..., n)$ and $g_k^l, h_k^l (k = 1, 2, ..., 45,\ l = 0, 1, ..., k)$, which have been derived to produce magnetic fields due to magnetospheric sources for a given three-dimensional (3-D) spherical conductivity model of the Earth (see sections 3.4.3 and 3.5.2 for details). Based on this set of coefficients, time series of B_r and $\nabla_{\mathbf{H}}\cdot\mathbf{B_H}$ have been calculated on a regular grid of $5^\circ \times 5^\circ$ resolution (this grid will be used in all model studies hereafter). The sampling rate, Δ_C, and the length of the time series, L, were chosen to be 6 hours and 3 years (1999-2001) respectively. As an example, Figure 6.74 shows the time series of B_r (left panel) and $\nabla_{\mathbf{H}}\cdot\mathbf{B_H}$ (right panel) for the year 2000, obtained at a site in Central Eurasia.

By performing a TSA of $B_r(t)$ and $\nabla_{\mathbf{H}}\cdot\mathbf{B_H}(t)$ (using the scheme presented in Olsen [1998]), C-responses have been estimated on a regular grid in the period range from 1.8 days to 29.5 days. Figure 6.75 presents maps of real and imaginary parts of C at periods of 1.8, 7.8, 15, and 29.5 days, respectively It can be seen from the Figure that the deep-seated regional anomaly (the geometry of which is shown on the Figures by red line) is masked by the ocean at periods shorter than 1.8 days . The most prominent manifestation of the anomaly is observed in the real part of the C-responses at a period of 7.8 days, with gradual decay of the effect toward longer periods. The anomalous behavior of C in the dip-equatorial region is due to the fact that B_r as well as $\nabla_{\mathbf{H}}\cdot\mathbf{B_H}$ are close to 0 (due to the geometry of the source, dominated by the first zonal harmonic in geomagnetic system of coordinates), which makes the numerical estimation of C unstable in this region. Squared coherency between $B_r(t)$ and $\nabla_{\mathbf{H}}\cdot\mathbf{B_H}(t)$ drops below 0.6 which means that the response functions in this region should be rejected or used with extreme care. Nevertheless, the Figure demonstrates that deep-seated regional structures can be detected and mapped.

However, these results have been obtained with all available internal coefficients, $M_i = N_i(N_i+2)$, with $N_i = 45$. In reality one probably will not be able to determine time series of coefficients up to such a high degree. Figure 6.76 presents response maps at a period of 7.8 days that have been obtained from various different numbers of internal coefficient. The left and right panels present maps for $N_i = 9$ and $N_i = 5$, respectively. The results for $N_i = 9$ are almost as good as those obtained from the full spectrum ($N_i = 45$) (cf. panels for $T = 7.8$ days on Figure 6.75). Even for $N_i = 5$ the anomaly is clearly identified in the C-responses.

There is no manifestation of local subsurface targets (plumes and subduction zone) which, along with the deep-seated regional anomaly, are included in the 3-D conductivity model used for synthesizing the data (see their geometry and location in the central panel of Figure 3.16). The main reason for this is that at the considered periods it is difficult to resolve structures in the depth range between a few km and a few hundreds km.

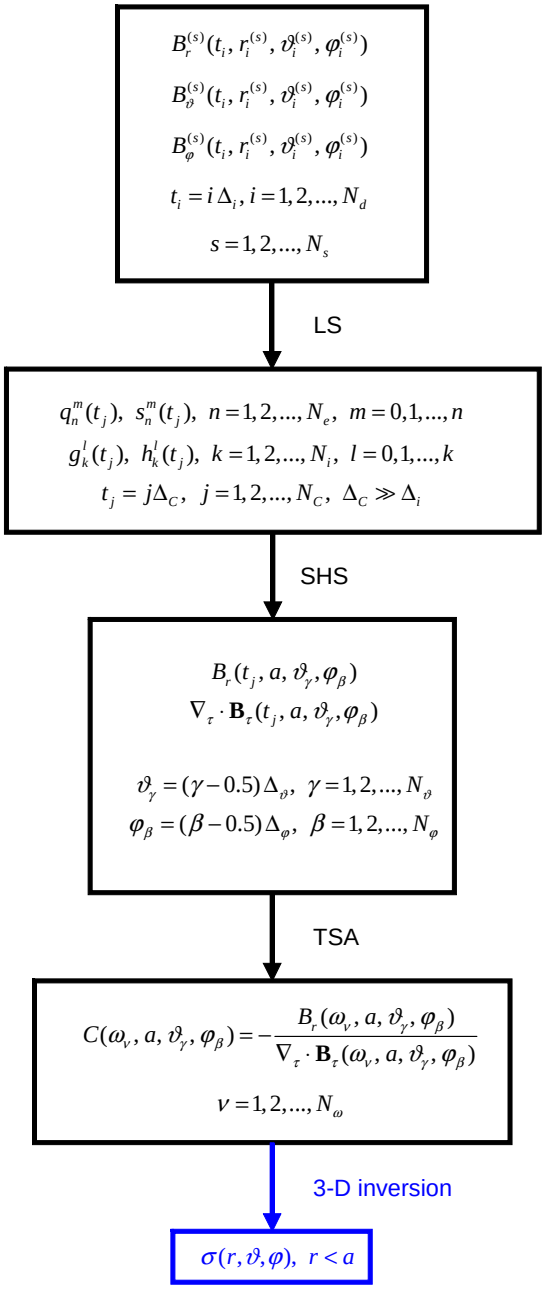

Figure 6.73: Scheme describing recovery of C-responses from satellite magnetic signals. LS means least-square approach, SHS - spherical harmonic synthesis, TSA - time series analysis.

6.6.4 Model studies using the full recovery scheme of recovery and "clean" data

So far our model studies are based on the reduced scheme of C-responses recovery. In this section we present results obtained with the full scheme, starting from the processing of satellite magnetic data (first step in Figure 6.73). We assume that the data are "clean", i.e. free from other field contributions (such as the main field, lithospheric field, ionospheric variations as well as instrumental noise). Hence we only use the part of the synthetic data that contain the magnetospheric contribution and its induced counterpart (see sections 3.4.3 and 3.5.2 for details of deriving these data). The aim of these studies is to investigate whether we are able to recover 3-D C-responses that are consistent with the "true" responses obtained in the previous section. Figure 6.77 presents the results for two cases: data from one single satellite (*Swarm 4*; left panel) data, and data from a constellation of three satellites (*Swarm 2+4+5*; right panel). We used *Swarm* data of 1-min sampling rate (experiments with a 5 sec sampling rate did not show visible improvements of the results). The sampling rate of the resulting coefficients, the length of the time series, and the number of internal coefficients were chosen to 6 hours, 3 years (1999-2001) and 35 coefficients ($N_i = 5$) respectively. Results are shown for a period of 7.8 days. From the Figure one can conclude that only the constellation data allows to recover 3-D "low-order" C-responses. By comparing the right panels of Figures 6.76 and 6.77 it is obvious that the recovered C-responses are consistent in geometry with the "true" responses.

Figure 6.78 confirms this quantitatively, demonstrating the relative differences, $|C^{(r)} - C^{(t)}|/|C^{(t)}|$, between he recovered, $C^{(r)}$, and the true responses, $C^{(t)}$, in the period range between 3 and 15 days for three sites with different conductivity-depth profiles. The location of these sites is shown by green circles in the left lower panel of Figure 6.77. These differences are about 20% for the North Pacific Ocean site, and less than 10% for sites located in the South Indian Ocean and in Central Eurasia. For comparison the Figure also shows the relative differences for the case when the recovery is done using data of a single satellite. The relative differences are unsatisfactory large, larger than 40% at the longest period of 15 days and exceeding 100% at a period of 3 days. The single satellite results are closer to the multiple satellites results as period increases, indicating that the 3-D effect in the C-responses is weaker at longer periods. Hence single satellite data may be adequate to obtain C-responses of a 1-D conductivity.

Next we attempt to improve the image of deep conductor geometry in C-responses by increasing the number of internal coefficients for the description of $B_r(t)$ and $\nabla_{\mathbf{H}} \cdot \mathbf{B}_{\mathbf{H}}(t)$. There is a trade-off between the number of coefficients M_i to be resolved, and the sampling rate of the resulting series, Δ_C. In order to resolve the coefficients with higher degree n and order m, one has to choose a smaller sampling rate in order to provide good spatial coverage of the satellite data. For the next series of calculations the number

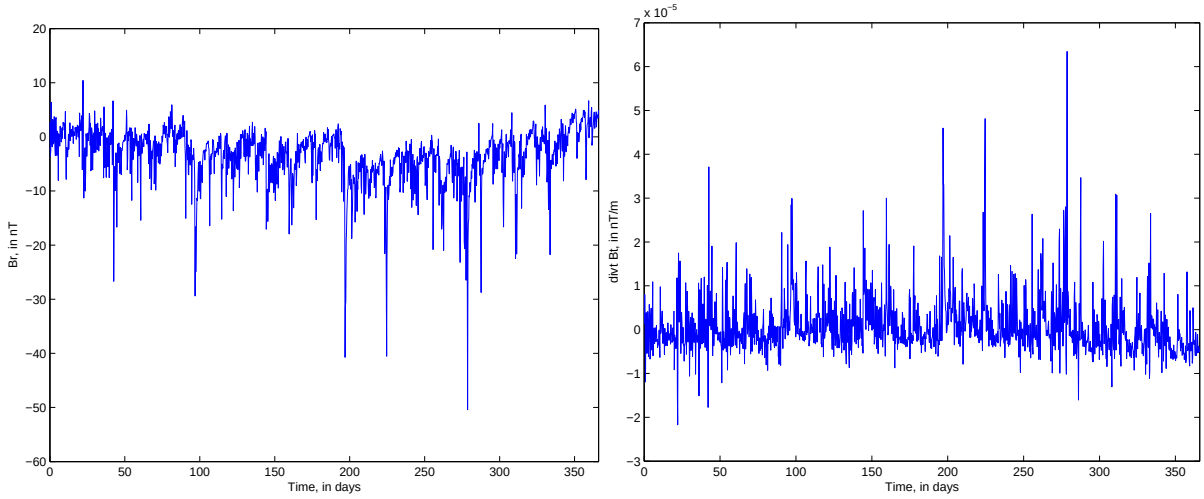

Figure 6.74: Time series of B_r (left panel) and $\nabla_{\mathbf{H}} \cdot \mathbf{B}_{\mathbf{H}}$ (right panel) for the year 2000, obtained at a site in Central Eurasia.

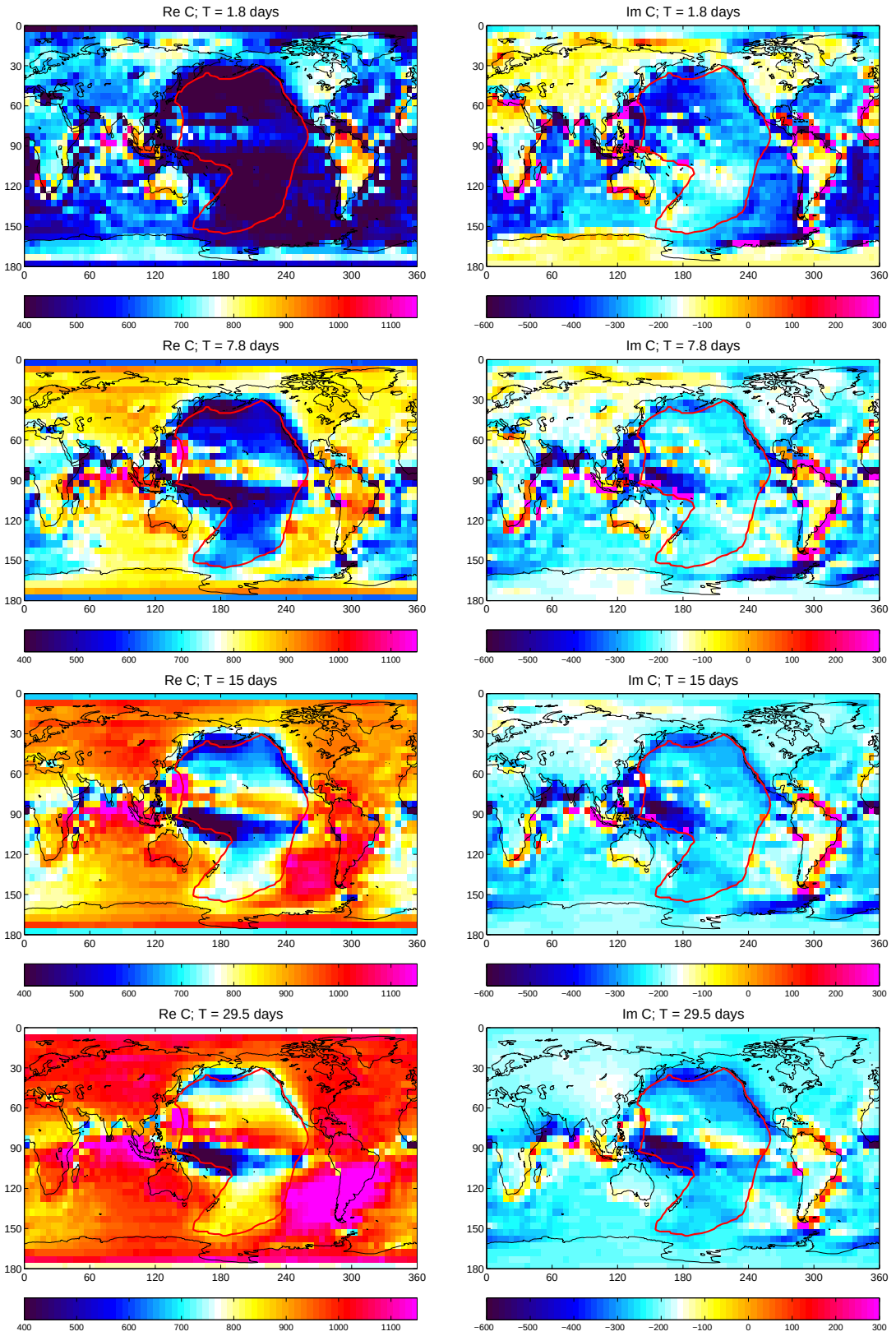

Figure 6.75: Real and imaginary parts of C-responses at periods of 1.8, 7.8, 15 and 29.5 days, obtained with the use of reduced scheme of recovery (with $N_i = 45$).

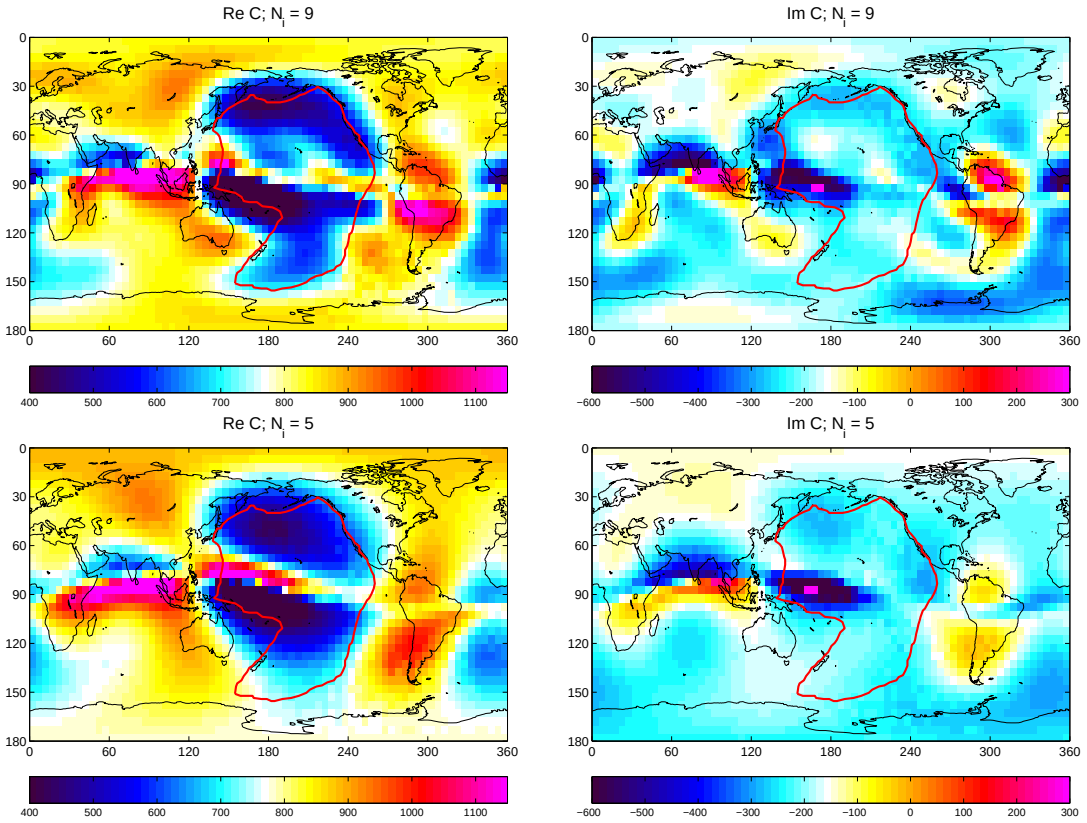

Figure 6.76: Real and imaginary parts of C-responses at a period of 7.8 days, obtained with $N_i = 9$ (top) and 5 (bottom), respectively.

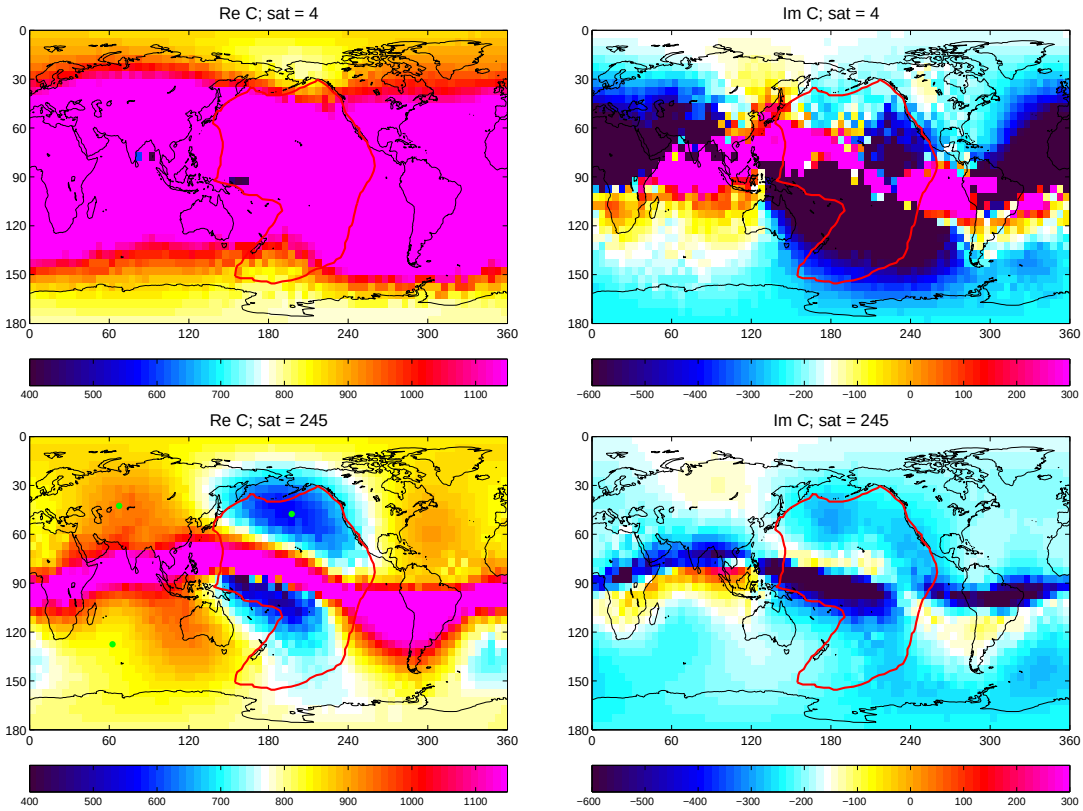

Figure 6.77: Real and imaginary parts of C-responses at a period of 7.8 days, obtained using the full scheme of recovery but "clean" data. Top and bottom panels present the results obtained using a single satellite (*Swarm 4*) and a constellation of three satellites (*Swarm 2+4+5*).

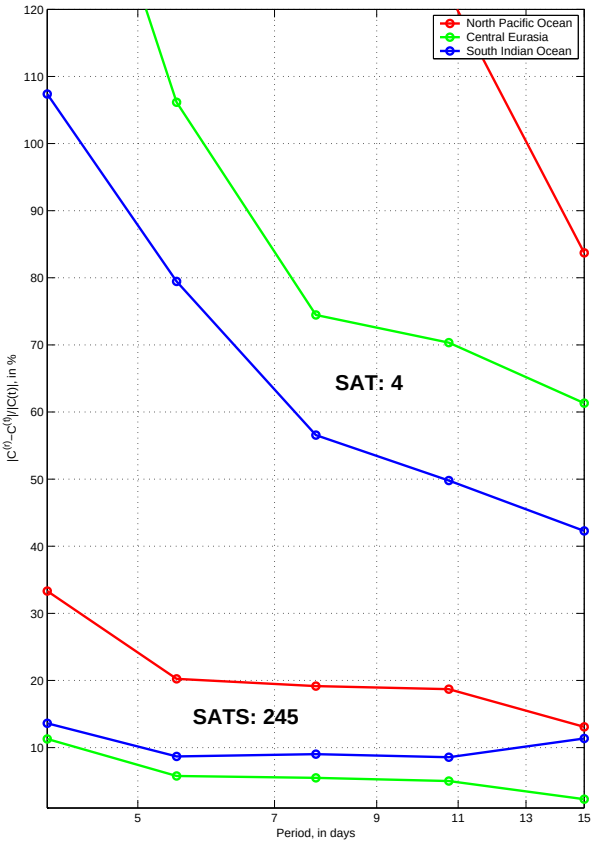

Figure 6.78: Relative difference, $|C^{(r)} - C^{(t)}|/|C^{(t)}|$, in %, between recovered, $C^{(r)}$, and true responses, $C^{(t)}$, in the period range between 3 and 15 days for three sites. "SAT: 4" and "SATS: 245" stands for results obtained from a single satellite (4) and from a constellation (245).

of internal coefficients, M_i, was chosen to 99 ($N_i = 9$). Sampling rate was 12 hours, with the same length (3 years; 1999-2001) of time series analyzed. Figure 6.79 shows the C-responses at a period of 8 days (slight shift in the period is due to th different sampling rate). With $M_i = 99$ and $\Delta_C = 12$ hours the C-responses maps become slightly more generalized (cf. lower panels on Figure 6.77), but the geometry of the anomaly in South Pacific Ocean is now more clearly identified.

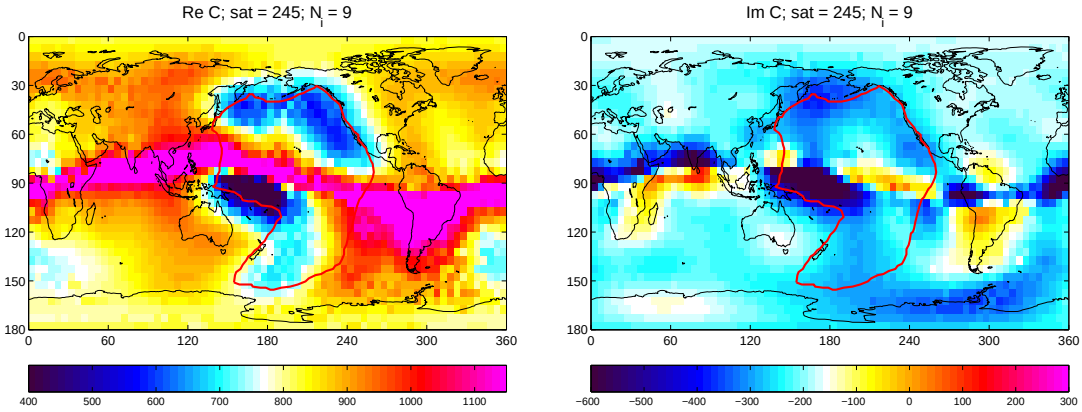

Figure 6.79: Real and imaginary parts of C-responses at a period of 8 days, obtained with the use of the full scheme of recovery, with processing of "clean" data from constellation 245 ($M_i = 99$, $\Delta_C = 12$ hours; see details in the text).

6.6.5 Model studies using full scheme of recovery and "real" data

Finally we investigated the possibility of recovering C-responses from satellite data containing all source contributions (core field, lithospheric field, magnetospheric and ionospheric variations plus induced counterparts, as well as instrumental noise). The comprehensive inversion (CI) scheme has been used to determine $q_n^m(t), s_n^m(t)$ and $g_k^l(t), h_k^l(t)$. As in the previous section, the sampling rate, the length of the time series, and the number of internal coefficients were chosen to 6 hours, 3 years (1999-2001) and 35 coefficients ($N_i = 5$) respectively. Figure 6.80 shows maps of the recovered C-responses at a period of 7.8 days. It is remarkable that the C-responses recovery from the "real" satellite data are almost as close to the true responses as those found from "clean" data (cf. lower panels on Figure 6.77).

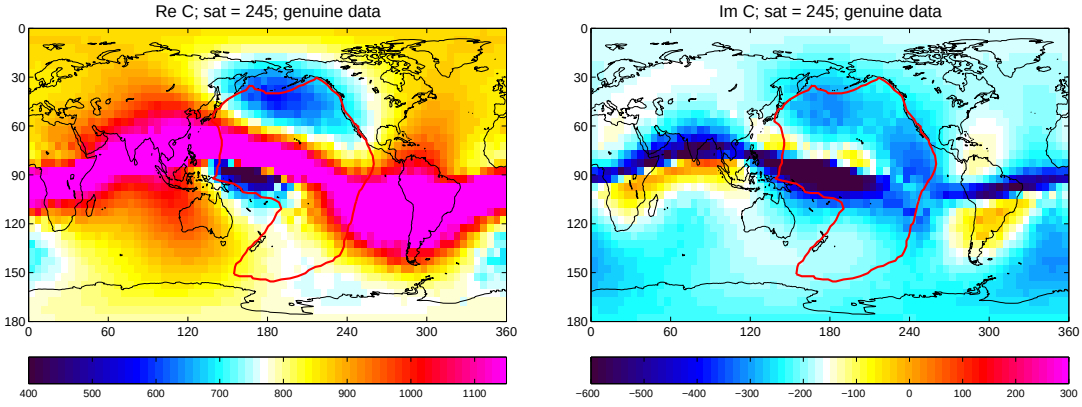

Figure 6.80: Real and imaginary parts of C-responses at a period of 7.8 days, obtained with the use of full scheme of recovery but using "real" data.

6.6.6 Conclusions

For the first time it has been demonstrated that C-responses obtained at a regular grid can be used to infer regional deep-seated conductivity anomalies. These C-responses can be successfully recovered from satellite magnetic data from a constellation of satellites.
We found several areas where the proposed recovery scheme needs improvement: For instance, to obtain more accurate time series of external and induced coefficients using constrained least-squares, and application of improved time series analysis schemes.
Ultimately the C-responses at a regular spatial grid and at a set of periods should serve as input for sophisticated 3-D inversion to be elaborated for obtaining 3-D quantitative images of the conductivity distribution in the Earth's interior.

6.7 Mapping of 3-D Conductivity Anomalies in the Mantle - Method 2

Recovery of electrical conductivity in the earth is possible from satellite magnetic data provided that the earth response to induction by magnetospheric sources can be characterized. The satellite records a continuous time series of the geomagnetic field that mixes the time and spatial varying part of the transient field. The approach proposed here is complementary to the C-response derivation. The difference is that the frequency dependency of the inducing and induced fields is explicitly included in the analysis. The vector spherical harmonic notation of [Phinney and Burridge, 1973] is used to represent the magnetic field. Let $\mathbf{B}(r,\theta,\varphi)$ with components $(B_r, B_\theta, B_\varphi)$ be a vector function of position in the spherical coordinate system $(\hat{\mathbf{e}}_r, \hat{\mathbf{e}}_\theta, \hat{\mathbf{e}}_\varphi)$, r is the distance from the Earth's center, θ is the colatitude and φ is the longitude. The generalized spherical harmonic (GSH) vector canonical basis is [e.g., Phinney and Burridge, 1973]

$$\begin{bmatrix} \hat{\mathbf{e}}^+ \\ \hat{\mathbf{e}}^0 \\ \hat{\mathbf{e}}^- \end{bmatrix} = \begin{bmatrix} \frac{1}{\sqrt{2}}(\hat{\mathbf{e}}_\theta - i\hat{\mathbf{e}}_\varphi) \\ \hat{\mathbf{e}}_r \\ \frac{-1}{\sqrt{2}}(\hat{\mathbf{e}}_\theta + i\hat{\mathbf{e}}_\varphi). \end{bmatrix} \tag{6.11}$$

In this basis, the vector $\mathbf{B}$ has the form

$$\mathbf{B}(r,\theta,\varphi) = \sum_{-1,0,1}^{N} B^N(r,\theta,\varphi)\hat{\mathbf{e}}^N, \tag{6.12}$$

and its GSH expansion is, using the Greek letter α to refer to the degree and order (l,m)

$$\mathbf{B}(r,\theta,\varphi) = \sum_{-1,0,1}^{N}\sum_{l=0}^{\infty}\sum_{m=-l}^{l} B^{N\alpha}(r)Y^{N\alpha}(\theta,\varphi)\hat{\mathbf{e}}^N. \tag{6.13}$$

Here $Y^{N\alpha}(\theta,\varphi) = P^{N\alpha}(\cos\theta)e^{im\varphi}$ are generalized spherical harmonics (GSHs) [Phinney and Burridge, 1973], normalized so that

$$\int_0^{2\pi}\int_0^{\pi} Y^{N\alpha}(Y^{N\alpha})^* \sin\theta d\theta d\varphi = \frac{4\pi}{2l+1}, \tag{6.14}$$

where $(Y^{N\alpha})^*$ is the complex conjugate of $Y^{N\alpha}$. Note that the $B^{0\alpha}$ are the GSH coefficients of the radial component of the vector $\mathbf{B}$. We introduce the following definition for the non radial GSH components of the vector $\mathbf{B}$

$$\begin{aligned} B^{P\alpha} &= \Omega_l(B^{+\alpha} + B^{-\alpha}) \\ B^{T\alpha} &= \Omega_l(B^{+\alpha} - B^{-\alpha}), \end{aligned} \tag{6.15}$$

where $\Omega_l = \sqrt{l(l+1)/2}$, and $B^{P\alpha}$ and $B^{T\alpha}$ are the GSH spheroidal (or poloidal) and toroidal components of the vector $\mathbf{B}$.
Let $B^N(\mathbf{r},t)$ be one component of the field $\mathbf{B}$ measured by a satellite at $\mathbf{r} = (r,\theta,\varphi)$ and time t. At each time, the field may be expanded into spherical harmonics P_l^{Nm} of degrees and orders l, m and a Fourier series of harmonics $e^{i\omega t}$ at frequency ω

$$B^N(\mathbf{r},t) = \sum_{lm\omega} b_l^{Nm}(\omega)P_l^{Nm}(\cos\theta)e^{im\varphi}e^{i\omega t}, \tag{6.16}$$

where $b_l^{Nm}(\omega)$ is the time and space spectral component of B^N, and N ranges from -1, 0, +1.
The general solution of equation 6.16 is

$$b_{l'}^{Nm'}(\omega') = \sum_t \int_S B^N(\theta,\varphi,t)P_{l'}^{Nm'}(\cos\theta)e^{-im'\varphi}e^{-i\omega' t}dS, \tag{6.17}$$

where S is the surface of the sphere of radius r.
The satellites sample B^N continuously at θ_t, φ_t, t. As a result, equation 6.16 may only be approached. The constellation of satellites provide at instant t a crude estimate of the integral over S in addition

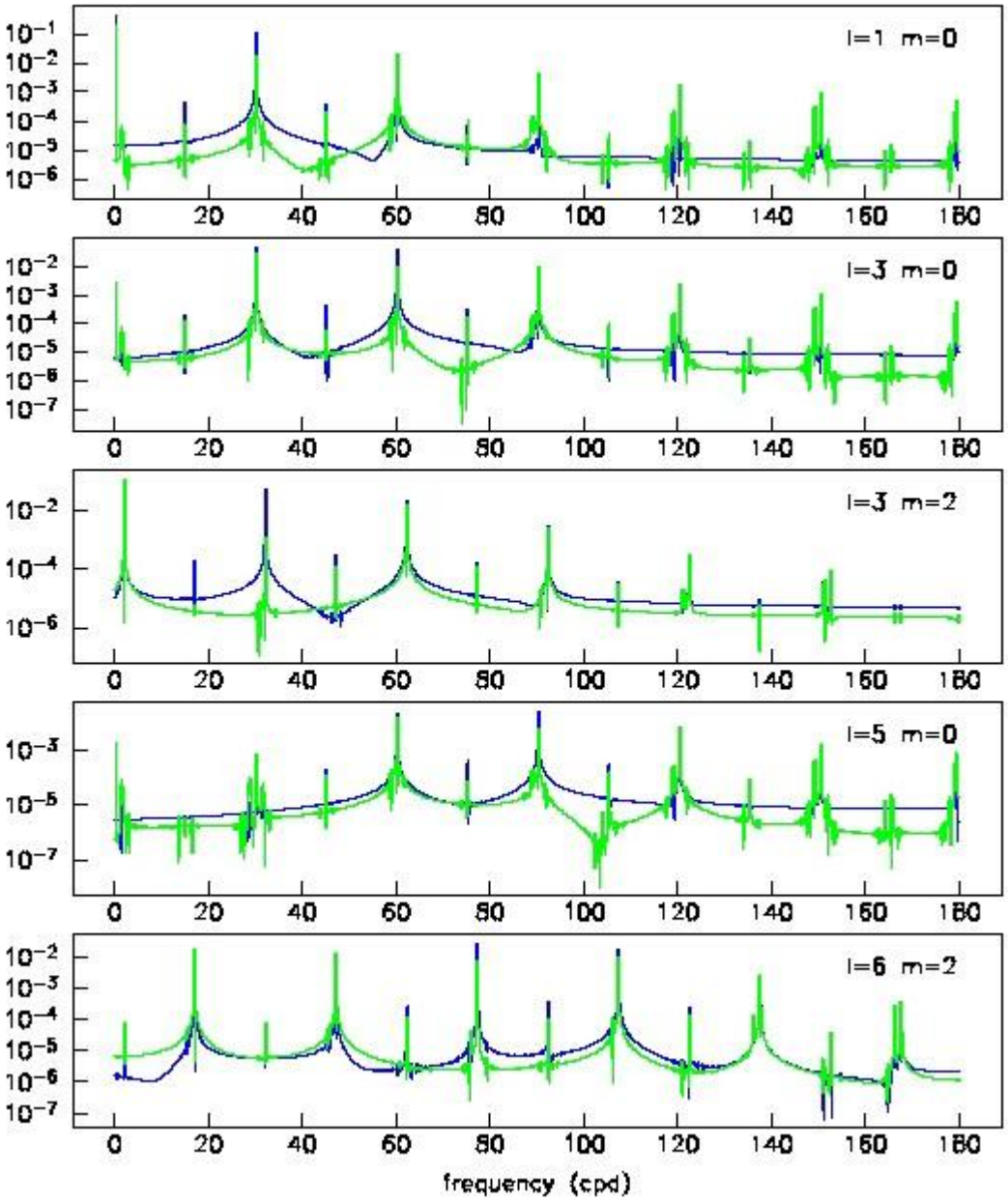

Figure 6.81: Spectrum versus frequency (in cycle per day) of $\hat{b}^P$ (in blue) and $\hat{b}^0$ in green for five different set of degrees and orders. The field B^N is proportional to $P_1^{N0}\cos(2\pi f_0 t)$ with f_0=0.17 cpd.

of repeated sampling of the field over time. Here for sake of simplicity, we do not take into account the variation in r between satellites. The generalization to real constellations with satellites at different altitude is straightforward.
We propose to approach equation 6.17 by

$$\hat{b}_{l'}^{Nm'}(\omega') = \sum_t [\sum_{ns} B^N(\theta_t^{ns}, \varphi_t^{ns}, t) P_{l'}^{Nm'}(\cos\theta_t^{ns}) e^{-im'\varphi_t^{ns}} \sin\theta_t^{ns}] e^{-i\omega' t}, \tag{6.18}$$

where ns is the number of available satellites.

The value $\hat{b}$ is the inverse Fourier transform of the term between brackets in equation 6.18. In Figure 6.81, $\hat{b}$ is obtained for different degrees and orders for a data set made of a single frequency (here 0.17 cpd) and a single geometry (P_1^0). What Figure 6.81 shows is how the signal is spread over other frequencies and spherical harmonic (SH) degrees and orders by the satellite sampling (here the orbits of SWARM1 for the year 2000 are used). The coefficient $\hat{b}$ combines b values of different l, m, ω.
The approach proposed here is based on the characterisation of the $\hat{b}$ values without having to explicitly determine the actual linear combination of b coefficients. I define b_l^{Pm} and $\hat{b}_l^{Pm}$ according to equation 6.15. The coefficients b^0 and b^P are linearly related with

$$b_l^{0m}(\omega) = \sum_{l'm'} A_{ll'}^{mm'}(\omega) b_{l'}^{Pm'}(\omega). \tag{6.19}$$

The maximum degrees l and l' are controlled by the number of inducing source terms and the conductivity heterogeneity. There is no need to specify them at this stage. The quantity $A_{ll'}^{mm'}$ is a function of the source geometry and the conductivity distribution. It can be modeled by 3-D solvers using unit sources and 3-D conductivity models. However, only $\hat{A}_{ll'}^{mm'}$ can be determined from the satellite magnetic data. $\hat{A}$ verifies

$$\hat{b}_l^{0m}(\omega) = \sum_{l'm'} \hat{A}_{ll'}^{mm'}(\omega) \hat{b}_{l'}^{Pm'}(\omega), \tag{6.20}$$

and is a combination of A values. This combination is a direct function of the sampling mode for the data (or equivalently for the orbit).
Equation 6.20 can be solved by singular value decomposition (SVD) and the $\hat{A}$ values are obtained along the eigenvectors corresponding to the non-zero (or significant) eigenvalues. A band averaging approach is used. Here the analysis was carried out up to a maximum degree $l = 7, m = -l, l$. The results on the data set SWARM3 and SWARM4 for year 2000 reveals that at frequencies less than 1 cycle per day (cpd), one eigenvalue explains 99 % of the variance. The corresponding eigenvector is dominated by the degree 1. We denote as $\tilde{A}_{lm}$ the projection of $\hat{A}$ for degree l and order m along the eigenvector. The spatial representation of $\tilde{A}$ is obtained at a frequency ω from

$$\tilde{A}(\theta, \varphi, \omega) = \sum_{lm} \tilde{A}_{lm}(\omega) P_l^{0m}(\cos\theta) e^{im\varphi}, \tag{6.21}$$

and is shown in Figure 6.82 at 0.6 cpd. In Figure 6.83, $\tilde{A}$ is shown without the terms of degree 1. The resulting transfer function describes well the 3-D conductivity structures built into the model. Two features dominate the geometry of the transfer function, the coast effect and the deep mantle conductor beneath the Pacific ocean. The other localized features (the subduction, the plume and the rift) are not seen because of the small maximum degree of the SH expansion ($l_{max} = 7$).

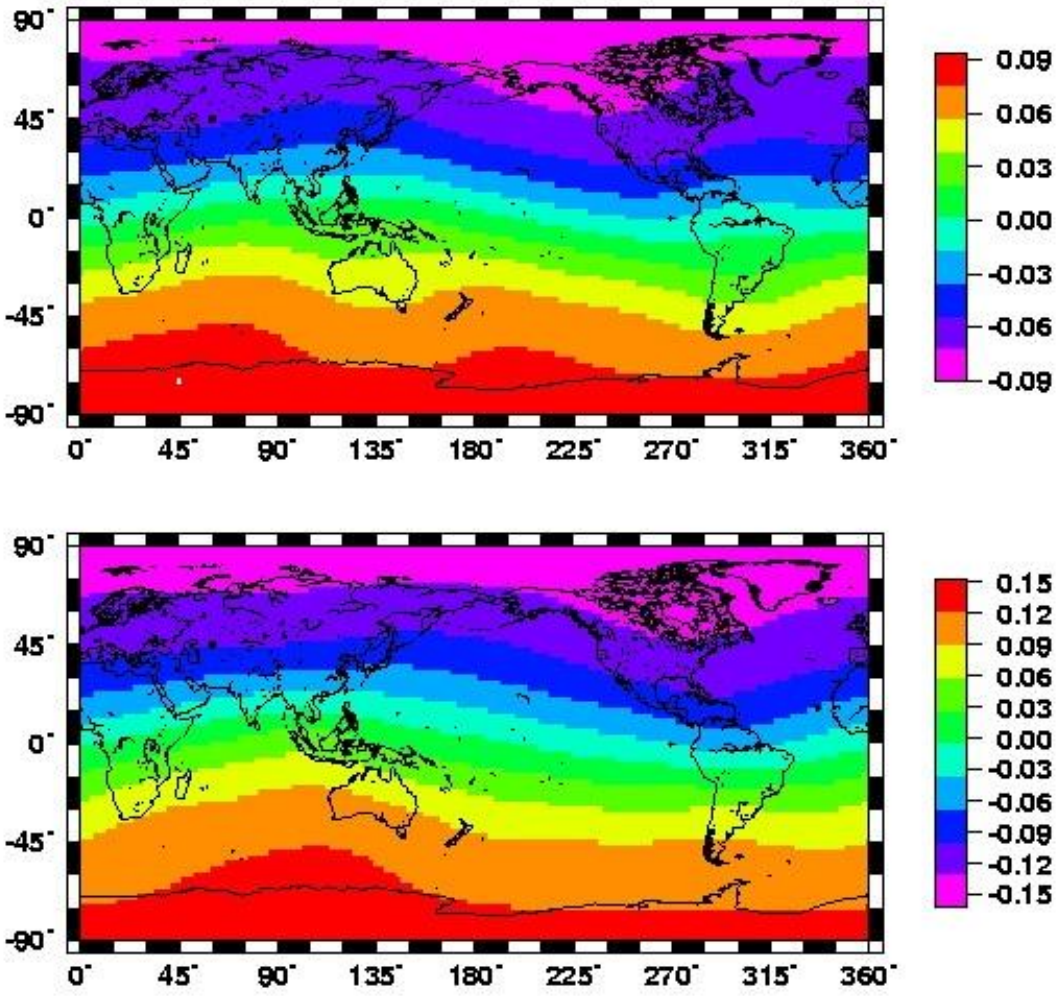

Figure 6.82: Real (upper panel) and imaginary (lower panel) parts of the transfer function $\tilde{A}$ between $\hat{b}^0$ and $\hat{b}^P$ along the principal eigen vector of the $\hat{b}^P$ cross-spectrum matrix. The maximum degree of the SH expansion in equations 6.18 and 6.20 used for this example is $l = 7$.

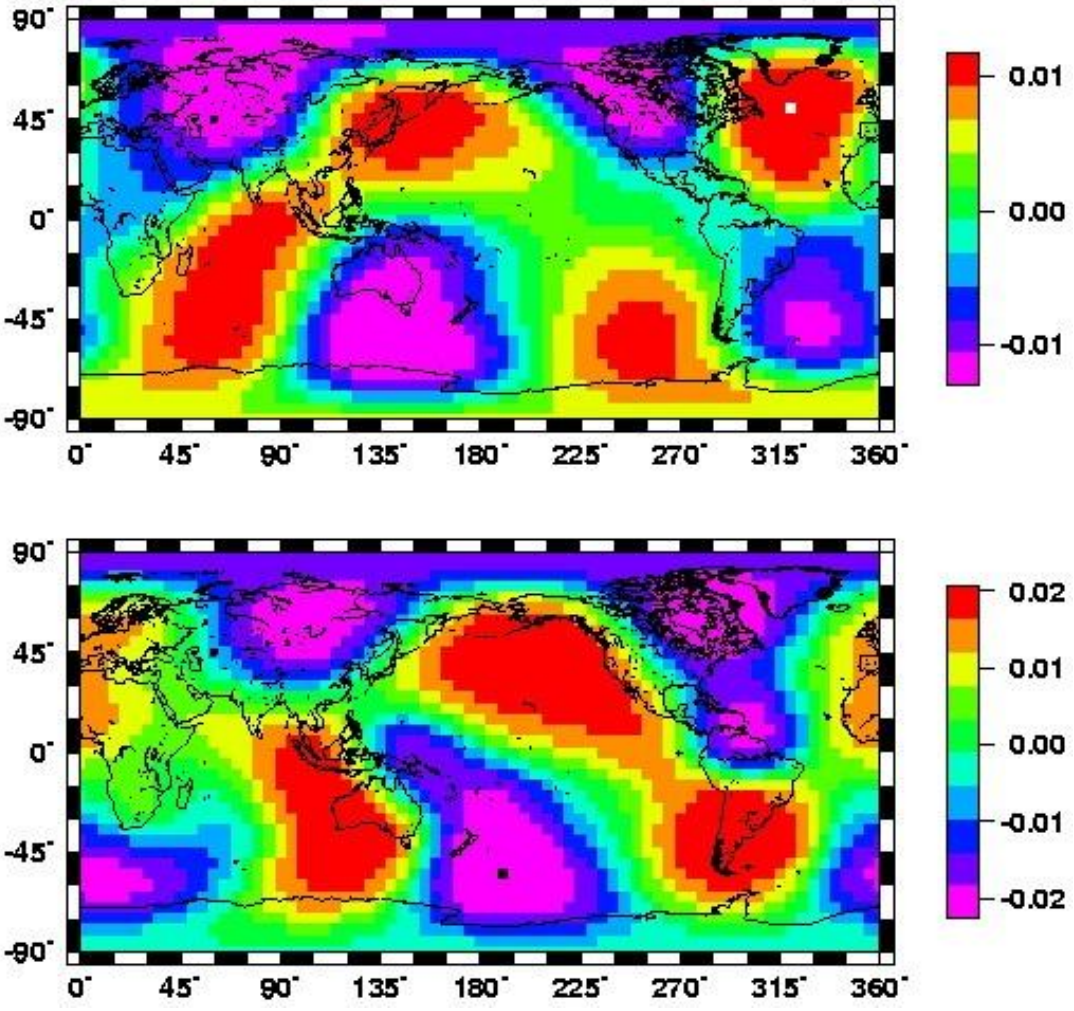

Figure 6.83: Same as in 6.82 but without the terms $l = 1, m = -l, l$.

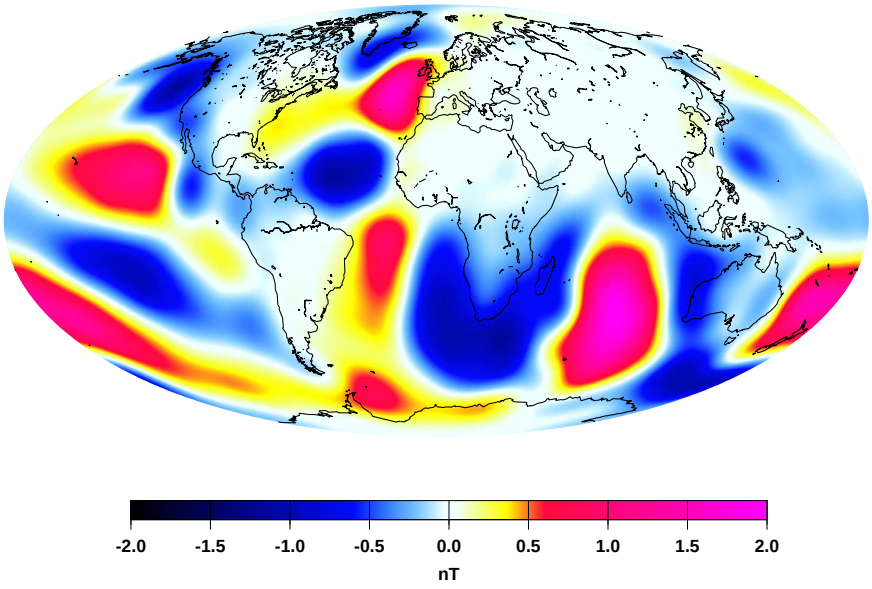

Figure 6.84: Magnetic signature of the M2 ocean tide at 400 km altitude. This field distribution is valid for the situation when the Moon is above the Greenwich meridian.

6.8 Recovery of the Ocean magnetic Signal

This section describes the efforts of the GeoForschungs Zentrum Potsdam to fulfill the tasks of WP4420 "Contributions due to Ocean Flows". The study is based on the synthetic magnetic field data set for the *swarm* Constellation #2. These data include the magnetic signatures of the M2 ocean tides. This periodically varying, Moon-driven signal is rather small compared to the other contributions. To give an impression, the field distribution is shown in Figure 6.84 for a certain Moon phase. Peak amplitudes are about 2 nT.
A main field model including secular variation and a lithospheric field model are subtracted before starting to recover the ocean-related fields. For the inversion only data from the night-time hours 20 to 05 LT of moderately quiet days, $Kp \leq 3$ are employed. The contribution of external sources are again determined on an orbit-by-orbit base. The approach is the same as used for the high-degree secular variation (section 6.5). All satellites considered in a constellation are included in a common solution for the external and induced fields. In case of the ocean signals we had, however, to go up to degree 4 with our external field filter to recover a reasonable part of the weak ocean signal.

6.8.1 Results of the Inversion

The inversion runs for retrieving the tidal signal were repeated several time for different numbers of satellites in the constellation. Before discussing the results it is instructive to look at the power spectrum of the signal strength. Figure 6.85 shows both the spectrum of the input data and the retrieved signal. The spectrum of the tidal signal exhibits a strong peak at degree 5. Beyond that it slopes off quite rapidly until it reaches an almost constant level at $n = 10$. The retrieved signal is much smaller than the input for the first ten degrees. This may be surprising but is the consequence of the external field filter. At the same time it can be seen that the attenuation of the signal is reduced considerably, if more spacecraft are included in the retrieval.
To judge the quality of the recovered tidal signal we performed a degree correlation again. It is evident from the results shown in Figure 6.86 that the external field filter takes away all the long wavelength signal up to degree 4. A significant correlation is obtained for degrees 5 and higher. The results obtained with three and four satellites are highly superior to the ones with two or less for degrees up to $n = 15$. For higher degrees the signal is very weak so that it is probably hard to distinguish it from the other contributions.

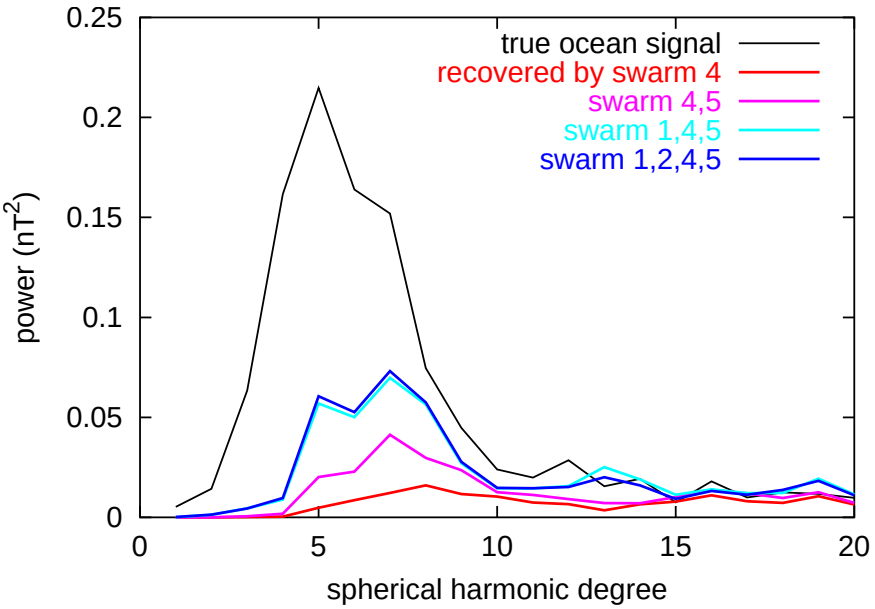

Figure 6.85: SHA power spectrum of the M2 ocean tide signal. Displayed are the input signal and the part of it that is recovered with a varying number of spacecraft in a constellation.

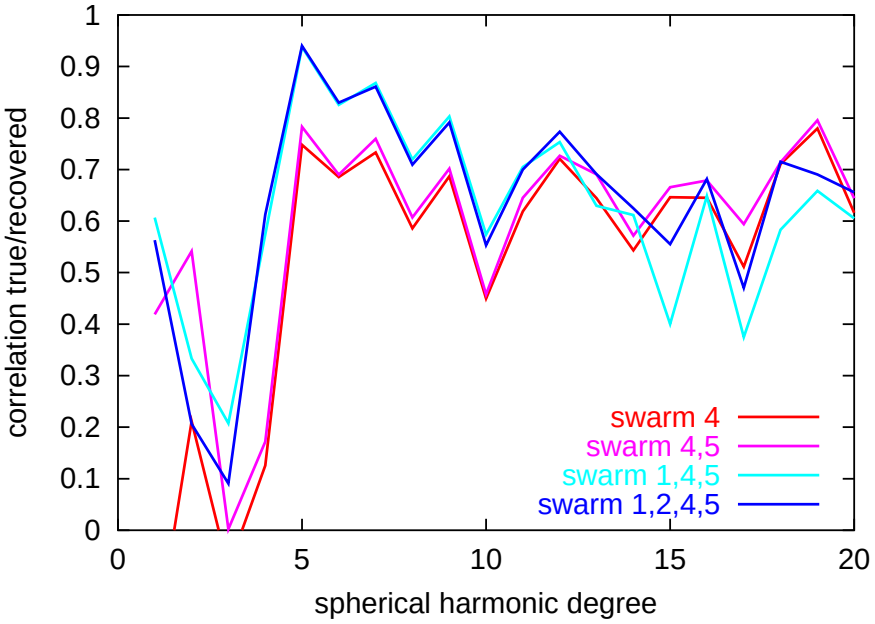

Figure 6.86: Degree correlation between input and recovered model of the M2 ocean tidal signal. Constellations of three or four satellites provide much improved results.

6.8.2 Discussion of Results

The recovery of the ocean tidal signal did not turn out to by a simple task. Special efforts were required to obtain an appreciable result. First we had to increase the number of considered data points by relaxing the selection criteria. The acceptable Kp-range was extended from 2 to 3. Another step was to make the external field filter more restrictive. Usually signals up to degree 2 are rejected. In this case the number had to be increased to 4 to get a reasonable fit in the higher parts of the spectrum. The penalty of this measure is the loss of the main part of the signal, as seen in Figure 6.85. From our experience of M2 ocean tide recovery in the CHAMP data we know that the standard external field filter up to degree 2 is sufficient. It thus may be concluded that the synthetic data set used here contains higher degree external field components which are not compatible with the real spectral distribution.
In spite of these imperfections the simulator results demonstrate favourably the potential of a constellation of four satellites in recovering the ocean circulation signal.

Chapter 7

Assessment

The results of the magnetic field recovery approaches described in Chapter 6 are used in this chapter to demonstrate the advantage of the proposed *Swarm* constellation #2. For this assessment we will focus on the following primary research objectives of the *Swarm* mission:

- Lithospheric field
- Core field and secular variation
- 3D mantle conductivity

Data accuracy of each of the *Swarm* satellites (1 nT of the vector components, 0.3 nT of the field intensity) will be superior to that of any previous and present satellite mission (accuracy of the vector components 2-5 nT) by at least a factor of 2. The reason for this is the unique triple-head star imager concept in combination with the ultra-stable optical bench that connects star imager and vector magnetometer, and the improved in-flight calibration possibility that the *Swarm* constellation will allow for.
This data accuracy improvement leads to improved magnetic field modeling. However, probably even more important than the improved single-satellite data accuracy is the **constellation concept**, which allows for better separation of the space-time structure of the various magnetic field contributions and thereby better field separation.
Analyzing data from two instead of one satellite will double the number of data points, and from that one might expect an improvement of the results by a factor of $1/\sqrt{2} = 1.41$ (This holds if the data are statistically independent). According to this argument, the combination of data from three satellites would improve the results by a factor of $\sqrt{3} = 1.73$. However, as will be demonstrated now, the actual improvement obtained with the *Swarm* mission is much higher than these values, indicating that advantage has been taken of the constellation during the data analysis.

7.1 Performance related to lithospheric field

The black curve of the left panel of Fig. 7.1 shows the degree signal, i.e. the square root of the degree variance, of the lithospheric vector field at ground. The degree errors of models derived from MAGSAT and CHAMP combined with Ørsted, are included (dashed blue lines). The error exceeds the signal beyond degree 30 for MAGSAT and beyond degree 60 for the present CHAMP model. The difference between CHAMP and MAGSAT models is due to significantly improved data accuracy and due to the longer observational period. Future CHAMP data collected at 300 km altitude will probably allow extending this model to degree 70 or so.
The magenta curve shows the error of a model derived from single *Swarm* satellite data obtained at an altitude of about 300 km towards the end of the mission (cf. Section 6.2.10). Compared to present state-of-the-art models, this curve indicates the improvement that one will get from the higher accuracy of the level 1b products of the *Swarm* mission. Combining data from the two side-by-side flying lower *Swarm* satellites A and B (see Figure 3.3 and Table 3.3 for the orbit characteristics of the satellites) provides a significantly improves field recovery at higher degrees. The green curve shows the three-satellite solution (*Swarm* A, B and C) that can be obtained using existing approaches [Sabaka et al., 2002, Maus et al., 2002] taking advantage of the East-West gradient measured by *Swarm A + B*. This optimal 3-satellite model is obtained from the results of the *Comprehensive Inversion* (cf. section 6.1) and of the Gradient method (cf. Section 6.2). The co-estimation of external and induced fields results in much improved crustal field recovery for degrees below 80. The fourth satellite (yellow curve) does not improve crustal field recovery significantly.
Figure 7.2 shows the lithospheric radial magnetic component at ground derived from a state-of-the art crustal model up to degree 60, left panel, and the improvement (field models up to degree 130) that *Swarm* will provide, right panel. This will bridge the existing gap between satellite models and data from ground, airborne and marine surveys.

7.2 Performance related to core field and secular variation

No other satellite missions are presently planned for the year 2010+. Hence without *Swarm* satellite data, models of the time change of the magnetic field at the beginning of the next decade have to be

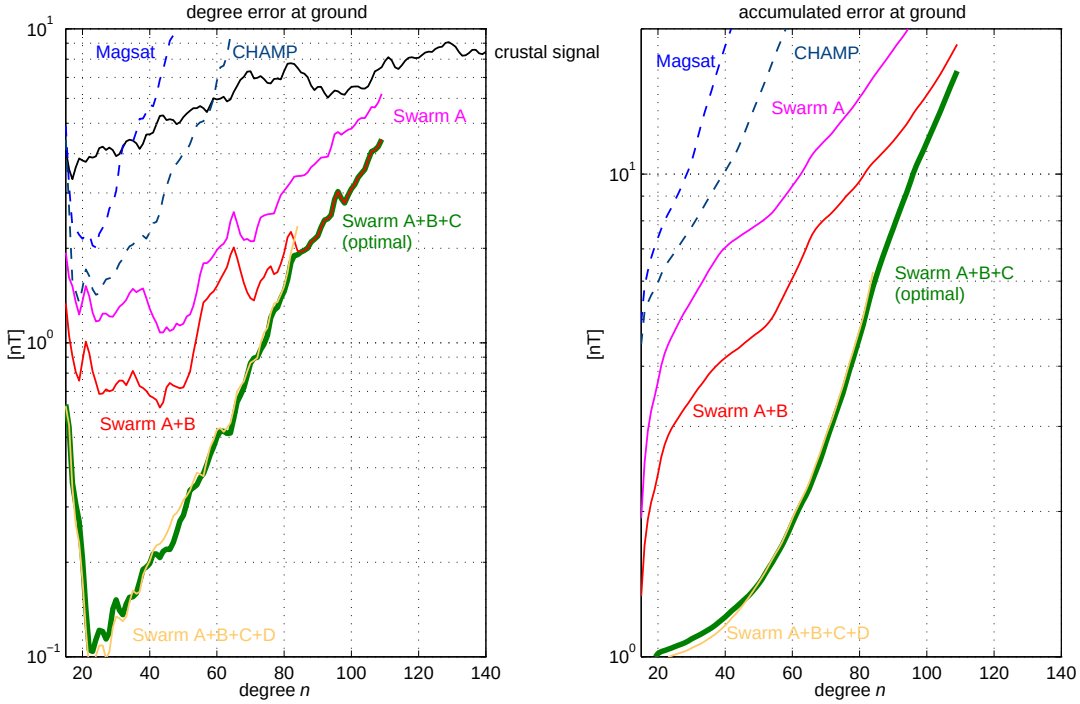

Figure 7.1: Left: Degree error (at the Earth's surface) of the lithospheric field recovery for different satellite combinations and approaches. Black curve presents lithospheric signal as given by the synthetic model swarm(06a/04). Right: accumulated error, i.e. the square root of the sum (from degree 14 to n) of the degree variances.

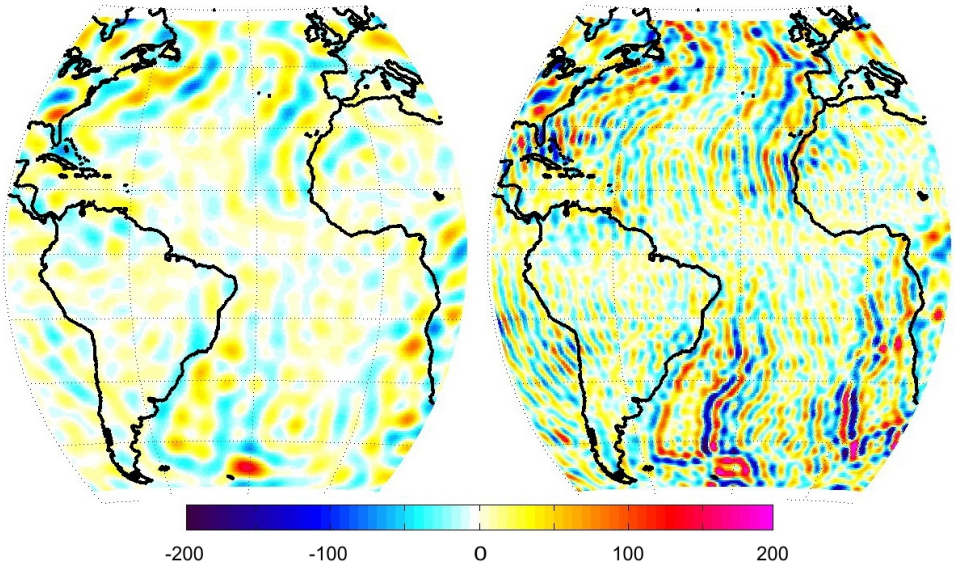

Figure 7.2: B_r (in nT) at ground for $n \leq 60$ (present state, left panel) and $n \leq 130$ (*Swarm* result, right panel).

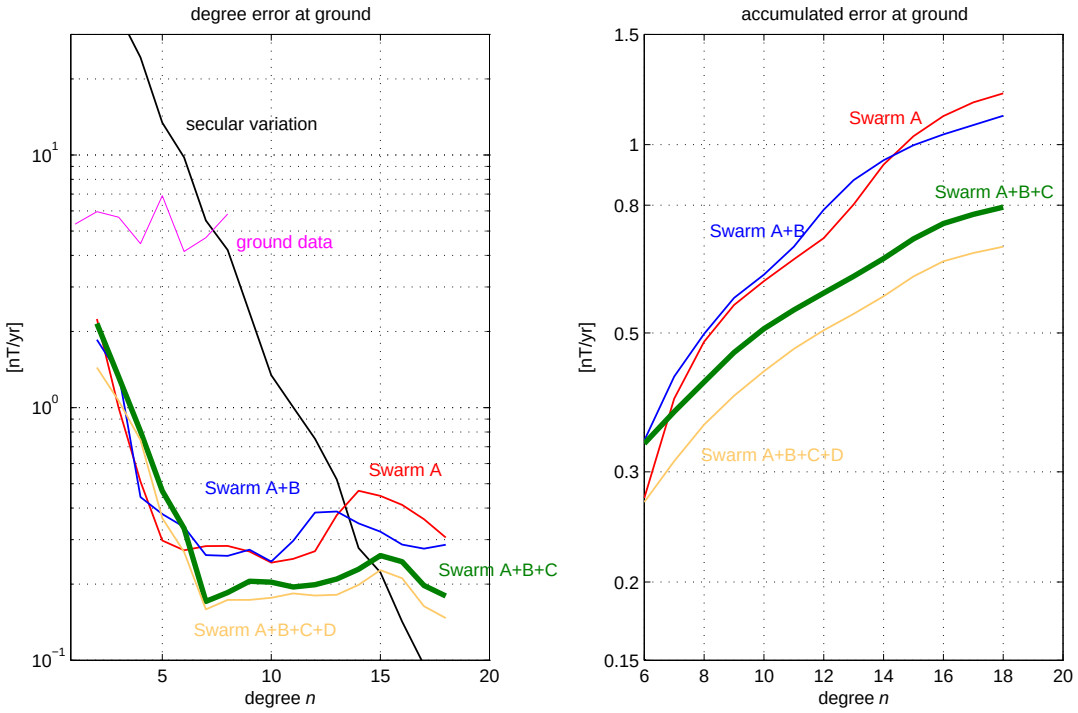

Figure 7.3: Degree error of the secular variation for different satellite combinations approaches. Black curve presents secular variation signal.

based on magnetic observatory data. This allows for deriving field models only up to degree 8, indicated by the magenta curve in Fig. 7.3. Models derived from single-satellite missions will reduce the degree error typically by one order of magnitude. The proposed constellation with 3 *Swarm* satellites allows determining secular variation models up to degree 15, with half the degree error obtainable with a single satellite. This result has been found by means of the Comprehensive Inversion approach described in section 6.1.

The short-term fluctuations of the secular variation can be improved with data from a constellation. Models derived from Ørsted data, over two-month intervals, show that secular variation cannot be directly obtained on this short time scale, due to the limited geographical distribution of a single satellite [Langlais et al., 2003]. However, the increased geographical coverage available from the proposed satellite constellation will allow recovering core field and secular variation simultaneously up to degree 14.

7.3 Performance related to 3-D Mantle conductivity

Magnetic field variations with periods of a few hours to 30 days sense mantle conductivity in the depth range between about 400 and 1000 km. *Swarm* will for the first time allow for a global determination of 3D structures in the electrical conductivity of the mantle, as has been demonstrated in sections 6.6 and 6.7. The key for this is the simultaneous observation of the magnetic field variations at different local times, resulting in models of the time-space structure of inducing magnetospheric and ionospheric fields. This can be achieved in the important signal period range of a few days down to a horizontal scale of 8000 km, corresponding to degree 5.

The C-response [Schmucker, 1985] of a location is a transfer function that connects the vertical component of the magnetic field variation and the horizontal derivatives of the horizontal components; its frequency dependence contains information on the variation of conductivity with depth in the surrounding of that location. The real part of the C-response indicates the depth of the induced currents; regions with

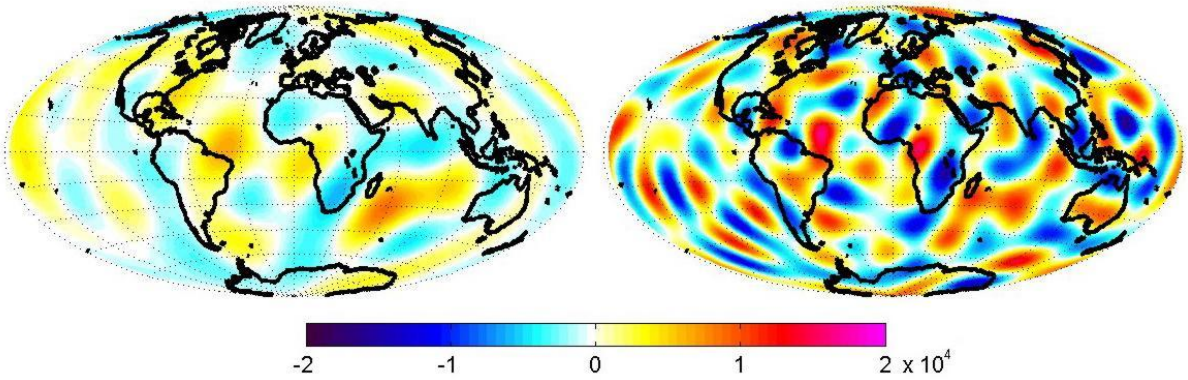

Figure 7.4: Secular Variation of B_r (in nT/yr) at the Core-Mantle-Boundary for $n \leq 8$ (model from ground data only, left panel) and $n \leq 14$ (*Swarm* result, right panel).

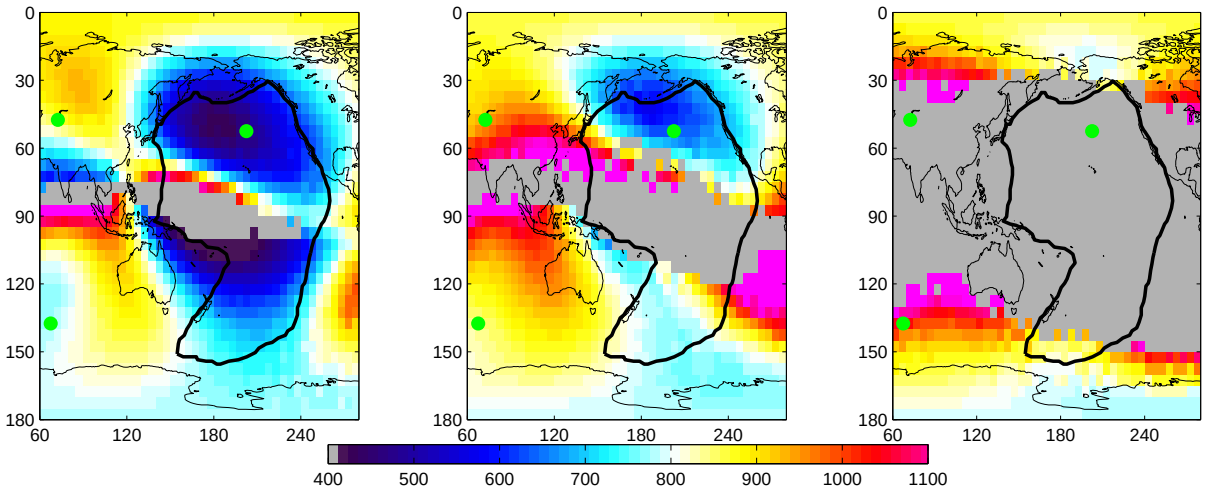

Figure 7.5: Maps of the real part of the C-response for a period of 7 days. The thick black curve indicates the boundaries of a hypothetical conductivity anomaly at 400 km depth. True values (left); estimated ones using 3 satellites (centre); and estimated ones from one single satellite (right). Regions in which squared coherency is below 0.6 are excluded and shown in grey.

reduced real parts indicate shallower induced currents, as shown in the left part of Fig. 7.5, which shows the true value of the real part that has been used as input for the simulation. The centre part of the figure demonstrates a successful detection of a conductivity anomaly beneath the Pacific with 3 *Swarm* satellites; a detection using single satellites (right panel) is not possible.

This demonstrates the ability of *Swarm* to detect regions of enhanced conductivity at 400 km depth, the boundary of which is indicated by the thick black line. External field variations of 7-day period induce currents that are normally flowing at about 800-900 km depth; they will, however, be shallower beneath the Pacific, since they tend to flow in regions of higher conductivity.

Three specific locations, marked in green in Fig. 7.5, are selected, because they represent different regimes for the mantle environment. The frequency-dependence of the C-response for these locations is shown in the left part of Fig. 7.6; as expected, the real part increases with period, since variations at longer periods penetrate deeper into the mantle. The right panel shows the error in the recovered C-response from 1 and 3 satellites, respectively. The recovery is shown in relation to the original model responses for these locations in Fig. 7.5. The relative errors in the right panel of this figure show a drastic improvement for three satellites, down to approximately 10% of the expected responses, whereas the single-satellite

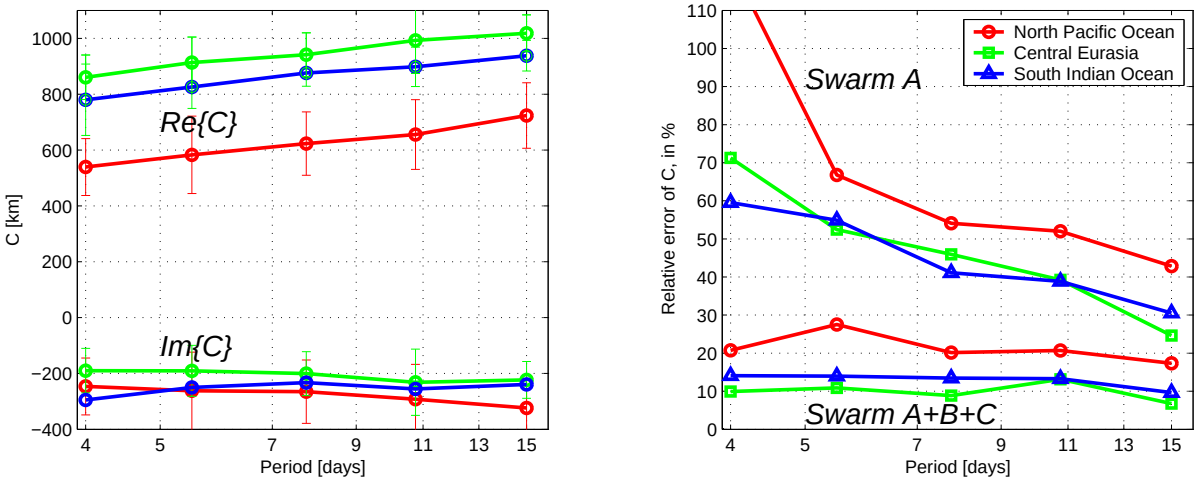

Figure 7.6: Single site C-response estimation using 3 satellites against true values and error bars (left). The locations of these sites are shown by the green dots in Figure 7.5. The relative error of C-response estimation for a single satellite and the proposed 3 satellites constellation solutions are shown as well (right).

solutions perform poorly. Since the model does not contain inhomogeneities in the lower mantle, the error of the single satellite solution is less at longer periods, but still larger than the 3-satellite solution by a factor of at least 2.

7.4 Constellation performance

In the table below the main findings related to the primary objectives are summarized. Given the fact that the single-satellite performance requirements are met, the proposed three satellites constellation will lead to a drastic improvement in the desired models. The relative improvement of the fourth satellite appears to be marginal in relation to these objectives. However, specific scientific investigations related to the external field could benefit from such a fourth satellite, but this was not studied during Phase A, in the End-to-End Mission Simulator. From the analysis of the results for three satellites it appears possible to recover the signals up to the finest scales, which is necessary to achieve the research goals for *Swarm*. The performance of the models at ground level and satellite level is shown in Table 7.1. Overall the two-satellite performance does not meet these requirements.
The experience gained from the existing missions and the extensive detailed scientific studies of various constellation scenarios, which were performed in parallel with the Phase A studies, have very convincingly demonstrated that a dedicated mission like *Swarm* is bound to bring significant advances in many science fields from the deep core to the external environment of the Earth. The constellation concept of *Swarm* will furthermore provide measurements that can be used for completely new investigations and methodology developments. Some of the most promising new science areas within the field of geomagnetism include studies of the fine-scale of the core and lithospheric fields, determination of the 3-D conductivity of the mantle, the fine-structure of the field aligned currents and their surprisingly large effect on the density variations in the upper atmosphere.

			without *Swarm**	1 satellite (A)	2 satellites (A+B)	3 satellites (A+B+C)	4 satellites (A+B+C+D)
Lithospheric Field	At ground	Degree error, *n*=60 [nT]	6.8	2.0	1.5	0.50	0.50
		Accumulated error, *n*=14-60 [nT]	23.2	11.3	8.5	2.0	2.0
		Degree error, *n*=110 [nT]	N/A	6.3	4.4	4.4	4.4
		Accumulated error, *n*=14-110 [nT]	N/A	29	20	16	16
	At 400 km altitude	Degree error, *n*=110 [nT]	N/A	0.0072	0.0052	0.0052	0.0052
		Accumulated error, *n*=14-110 [nT]	3.80	2.91	2.58	0.41	0.39
	altitude independent	Relative error, *n*=60 [%]	117	34	26	4.1	4.1
		Degree correlation, *n*=60	0.58	0.94	0.97	0.996	0.996
		Relative error, *n*=110 [%]	N/A	67	47	47	47
		Degree correlation, *n*=110	N/A	0.74	0.87	0.88	0.88
Secular Variation	At ground	Degree error, *n*=8 [nT/yr]	2.3	0.28	0.26	0.18	0.17
		Accumulated error, *n*=6-8 [nT/yr]		0.52	0.50	0.42	0.36
		Degree error, *n*=14 [nT/yr]	N/A	0.47	0.35	0.22	0.20
		Accumulated error, *n*=6-14 [nT/yr]	N/A	0.99	0.94	0.65	0.57
	At 400 km altitude	Degree error, *n*=14 [nT/yr]		0.176	0.132	0.086	0.075
		Accumulated error, *n*=6-14 [nT/yr]	N/A	0.47	0.45	0.34	0.30
	Altitude independent	Relative error, *n*=8 [%]	32	6.7	6.2	4.4	4.1
		Degree correlation, *n*=8		0.996	0.998	0.999	0.999
		Relative error, *n*=14 [%]	N/A	168	126	82	71
		Degree correlation, *n*=14	N/A	0.59	0.69	0.80	0.82

Table 7.1: Expected performance related to primary objectives of the mission.

* For lithosphere it means best present day models (CHAMP and Ørsted). For secular variation it is based upon the ground observatory network available at the time of *Swarm*.

Chapter 8

Conclusions and Outlook

The purpose of the *Swarm* End-to-End Mission Simulator described in this report was to build a virtual (simulated) mission in order to analyze the key system requirements, particularly with respect to the number of *Swarm* satellites and their orbits, related to the science objectives of *Swarm*.
During the study several methods for the production and analysis of synthetic *Swarm* data have been developed, implemented and tested, in order to optimize the choice of the constellation of *Swarm* satellites that would best achieve the science objectives of the mission.
Two constellations have been studied: Constellation # 1 was the 4-satellite constellation from the original *Swarm* proposal [Friis-Christensen et al., 2002]. Based on the experience gained with this constellation we designed and analyzed Constellation #2. While the two lower satellites follow each other in constellation #1, they fly side-by-side, separated by, say, 1.5° in longitude, thereby allowing for the first time measuring of the East-West gradient of the magnetic field.
A full mission simulation was performed for each constellation. Start-time of the four-year simulations was set to January 1, 1997, one full solar cycle (11 years) before the planned mission, in order to use realistic indices of the Earth's environment. Synthetic magnetic field values were generated based upon a combination of existing and simulated models for all relevant contributions (chapter 3). Synthetic data and errors for a total of six different satellites were generated for the complete mission lifetime (190 million satellite positions), which amounted to 10,950 files (2.42 MB each), requiring 26.5 GB per constellation run. Out of these six satellites, different constellations of 1, 2, 3 and 4 satellites were selected and the success in recovering the original models was analyzed for each constellation. It turned out that the modified 3- and 4-satellite constellations provide significantly improved scientific return compared to the first constellation.
Several independent methods were applied in the simulation environment to analyze various aspects of the model estimation in relation to different numbers of satellites, different constellations, and realistic noise sources. The comprehensive inversion (section 6.1), which contains parameterization of all relevant sources, has been chosen as the primary approach for field recovery and error analysis.
Based on the experience gained during this study, the following topics are recommended for future studies

- As the mechanical stability of the optical bench assembling the VFM and ASC is crucial for the accuracy of the magnetic vector data, an integrated study on sophisticated testing of the VFM/ASC package and developing of methods for pre-flight determination of the VFM/ASC alignment angles is recommended. This also includes the development of approaches for determining the precise dating of the measurement from the various instruments.
- Present approaches for in-flight calibration of alignment are single-satellite methods which do not take advantage of the constellation aspect of *Swarm*. While the single-satellite aspect turned out to be sufficient for the in-flight calibration of the VFM (cf. section 4.1), it is expected that a multi-satellite approach would heavily improve the in-flight alignment. This should be investigated.
- More sophisticated methods for utilizing observations of the magnetic field gradient (measured by the two lower *Swarm* satellites) in geomagnetic modeling should be investigated.
- *Swarm* will allow for the first time to detect the signature of large-scale 3-D inhomogeneities in the electrical conductivity of the mantle. In this study the impact of these mantle inhomogeneities on the transfer functions estimated from *Swarm* data was studied. The next logical step would be to develop methods for imaging (mapping) of 3-D mantle inhomogeneities, a first step toward a full 3-D inversion of mantle conductivity.

Bibliography

H. Bijwaard and W. Spakman. Non-linear global P-wave tomography by iterated linearized inversion. *Geophys. J. Int.*, 110:251–266, 2000.

S. Constable and G. Heinson. Hawaiian hot-spot swell structure from seafloor MT sounding. *Tectonophysics*, 389:111–124, 2004.

F. Deschamps, J. Trampert, and R. Snieder. Anomalies of temperature and iron in the uppermost mantle inferred from gravity data and tomographic models. *Phys. Earth Planet. Int.*, 129:245–264, 2002.

J. Dyment and J. Arkani-Hamed. Contribution of lithospheric remanent magnetization to satellite magnetic anomalies over the world's oceans. *J. Geophys. Res.*, 103:15423–15442, July 1998.

ECSS. Space engineering. ECSS-E-10-04A - Space Environment (21 January 2000), European Cooperation for Space Standardization, Secretariat, ESA-ESTEC, Requirement & Standards Division, Noordwijk, The Netherlands, 2000. URL `www.ecss.nl`.

G. D. Egbert and J. R. Booker. Very long period magnetotellurics at tucson observatory: implication for mantle conductivity. *J. Geophys. Res.*, 97:15099–15112, 1992.

S. Erofeeva and G. Egbert. Efficient inverse modelling of barotropic ocean tides. *J. Ocean. Atmosph. Technol.*, 19:183–204, 2002.

M. Everett, S. Constable, and C. Constable. Effects of near-surface conductance on global satellite induction responses. *Geophys. J. Int.*, 153:277–286, 2003.

C. Fox Maule, M. Purucker, and N. Olsen. The magnetic crustal thickness of Greenland. In C. Reigber, H. Lühr, P. Schwintzer, and J. Wickert, editors, *Earth Observation with CHAMP, Results from Three Years in Orbit*. Springer Verlag, 2005.

E. Friis-Christensen, H. Lühr, and G. Hulot. *Swarm* - a constellation to study the dynamics of the Earth's magnetic field and its interactions with the Earth system. DSRI Report 1/2002, Danish Space Research Institute, Copenhagen, 2002.

A. E. Hedin. MSIS-86 thermospheric model. *J. Geophys. Res.*, 92:4649–4662, 1987.

R. V. Hogg. An introduction to robust estimation. In R. L. Launer and G. N. Wilkinson, editors, *Robustness in Statistics*, pages 1–17. Academic Press, San Diego, Calif., 1979.

P. Knocke, J. Ries, and B. Tapley. Earth radiation pressure effects on satellites. In *Proc. AIAA/AAS AstrodynamicsConference*, Minneapolis, Minn, August 1988.

A. V. Kuvshinov, D. B. Avdeev, O. V. Pankratov, S. A. Golyshev, and N. Olsen. Modelling electromagnetic fields in 3D spherical Earth using fast integral equation approach. In M. S. Zhdanov and P. E. Wannamaker, editors, *3D Electromagnetics*, chapter 3, pages 43–54. Elsevier, Holland, 2002.

A. V. Kuvshinov and N. Olsen. 3D modelling of the magnetic field due to ocean flow. In C. Reigber, H. Lühr, P. Schwintzer, and J. Wickert, editors, *Earth Observation with CHAMP, Results from Three Years in Orbit*. Springer Verlag, 2005.

A. V. Kuvshinov, H. Utada, D. Avdeev, and T. Koyama. 3-D modelling and analysis of *Dst C*-responses in the North Pacific ocean region, revisited. *Geoph. J. Int.*, 60 (2):505–526, doi: 10.1111/j.1365–246X.2005.02477.x, 2005.

R. A. Langel and W. J. Hinze. *The magnetic field of the Earth's lithosphere: The satellite perspective.* Cambridge University Press, 1998.

B. Langlais and M. Mandea. An IGRF candidate main geomagnetic field model for epoch 2000 and a secular variation model for 2000-2005. *Earth, Planets and Space*, 52:1137–1148, 2000.

B. Langlais, M. Mandea, and P. Ultre-Guerard. High-resolution magnetic field modeling: application to Magsat and Ørsted data. *Phys. Earth Planet. Int.*, 135:77–91, 2003.

G. Laske and G. Masters. A global digital map of sediment thickness. *EOS Trans. AGU*, 78:F483, 1997.

X. D. Li and B. Romanowicz. Global mantle shear velocity model developed using nonlinear asymptotic coupling theory. *J. Geophys. Res.*, 101:22245–22272, 1995.

S. Maus, M. Rother, K. Hemant, H. Lühr, A. V. Kuvshinov, and N. Olsen. Earth's crustal magnetic field determined to spherical harmonic degree 90 from CHAMP satellite measurements. *Geophys. J. Int., submitted*, 2005.

S. Maus, M. Rother, R. Holme, H. Lühr, N. Olsen, and V. Haak. First scalar magnetic anomaly map from CHAMP satellite indicates weak lithospheric field. *Geophys. Res. Lett.*, 29(10), 2002.

D. D. Mc Carthy. IERS technical note 21, IERS conventions. Technical report, IERS, 1996.

J. Merayo, P. Brauer, F. Primdahl, J. R. Petersen, and O. V. Nielsen. Scalar calibration of vector magnetometers. *Meas. Sci. Technol.*, 11:120–132, 2000.

H. Nataf and Y. Ricard. 3SMAC: an a priori tomographic model of the upper mantle based on geophysical modeling. *Physics of the Earth and Planetary Interiors*, 95:101–122, May 1996.

S. L. Neal, R. L. Mackie, J. C. Larsen, and A. Schultz. Variations in the electrical conductivity of the upper mantle beneath North America and the Pacific Ocean. *J. Geophys. Res.*, 105:8229–8242, 2004.

N. Olsen. Estimation of *C*-responses (3 h to 720 h) and the electrical conductivity of the mantle beneath Europe. *Geophys. J. Int.*, 133:298–308, 1998.

N. Olsen. A model of the geomagnetic field and its secular variation for epoch 2000 estimated from Ørsted data. *Geophys. J. Int.*, 149(2):454–462, 2002.

N. Olsen and A. V. Kuvshinov. Modelling the ocean effect of geomagnetic storms. *Earth, Planets and Space*, 56:525–530, 2004.

N. Olsen, L. Tøffner-Clausen, T. J. Sabaka, P. Brauer, J. M. G. Merayo, J. L. Jørgensen, J.-M. Léger, O. V. Nielsen, F. Primdahl, and T. Risbo. Calibration of the Ørsted vector magnetometer. *Earth, Planets and Space*, 55:11–18, 2003a.

N. Olsen, S. Vennerstrøm, and E. Friis-Christensen. Monitoring magnetospheric contributions using ground-based and satellite magnetic data. In C. Reigber, H. Lühr, and P. Schwintzer, editors, *First CHAMP Mission results for Gravity, Magnetic and Atmospheric Studies*. Springer Verlag, 2003b.

R. Phinney and R. Burridge. Representation of the elastic-gravitational excitation of a spherical earth model by generalized spherical harmonics. *Geophys. J. R. astr. Soc.*, 34:451–487, 1973.

M. E. Purucker and J. Dyment. Satellite magnetic anomalies related to seafloor spreading in the South Atlantic Ocean. *Geophys. Res. Lett.*, 27:2765–2768, doi:10.1029/1999GL008437, Sept. 2000.

A. D. Richmond. Ionospheric electrodynamics using magnetic Apex coordinates. *J. Geomagn. Geoelectr.*, 47:191–212, 1995.

T. Risbo. Fourier transform summation of legendre series and d-functions. *Journal of Geodesy*, 70: 383–396, 1996.

T. Risbo, P. Brauer, J. M. G. Merayo, O. V. Nielsen, J. R. Petersen, F. Primdahl, and I. Richter. Ørsted pre-flight magnetometer calibration mission. *Measurement Science and Technology*, 14:674–688, May 2003.

J. Ritsema, H. J. van Heijst, and J. H. Woodhouse. Complex shear velocity structure imaged beneath Africa and Iceland. *Science*, 286:1925–1928, 1999.

R. G. Roberts. The long-period electromagnetic response of the earth. *Geophys. J. R. astr. Soc.*, 78: 547–572, 1984.

R. Robinson and P. Vondrak. Measurements of e region ionization and conductivity produced by solar illumination at high latitudes. *J. Geophys. Res.*, 89:3951 – 3956, 1984.

T. J. Sabaka and N. Olsen. Comprehensive modelling of the Earth's magnetic field: Current status and future prospects. In P. Stauning, editor, *Proceedings of the 4th OIST conference*, Copenhagen, Denmark, 2003.

T. J. Sabaka, N. Olsen, and R. A. Langel. A comprehensive model of the quiet-time near-Earth magnetic field: Phase 3. *Geophys. J. Int.*, 151:32–68, 2002.

T. J. Sabaka, N. Olsen, and M. Purucker. Extending comprehensive models of the Earth's magnetic field with Ørsted and CHAMP data. *Geophys. J. Int.*, 159:521–547, doi: 10.1111/j.1365–246X.2004.02421.x, 2004.

U. Schmucker. Magnetic and electric fields due to electromagnetic induction by external sources. In *Landolt-Börnstein, New-Series, 5/2b*, pages 100–125. Springer-Verlag, Berlin-Heidelberg, 1985.

A. Schultz. On the vertical gradient and associated heterogeneity in mantle electrical conductivity. *Phys. Earth Planet. Interiors*, 64:68–86, 1990.

W. J. Su and A. M. Dziewonski. Simultaneous inversions for 3-D variations in shear and bulk velocity in the mantle. *Phys. Earth Planet. Int.*, 100:135–156, 1997.

J. Woodhouse and J. Trampert. Global upper mantle structure inferred from surface wave and body wave data. *EOS Trans.*, page F422, 1995.